

JAERI - M
93-181

REACTOR ENGINEERING DEPARTMENT ANNUAL REPORT

(April 1, 1992 — March 31, 1993)

September 1993

Department of Reactor Engineering

日 本 原 子 力 研 究 所
Japan Atomic Energy Research Institute

JAERI-Mレポートは、日本原子力研究所が不定期に公刊している研究報告書です。
入手の問合わせは、日本原子力研究所技術情報部情報資料課（〒319-11茨城県那珂郡東海村）あて、お申しこしてください。なお、このほかに財団法人原子力弘済会資料センター（〒319-11 茨城県那珂郡東海村日本原子力研究所内）で複写による実費頒布をおこなっております。

JAERI-M reports are issued irregularly.

Inquiries about availability of the reports should be addressed to Information Division
Department of Technical Information, Japan Atomic Energy Research Institute, Tokai-mura, Naka-gun, Ibaraki-ken 319-11, Japan.

©Japan Atomic Energy Research Institute, 1993

編集兼発行 日本原子力研究所
印刷 いばらき印刷㈱

Reactor Engineering Department Annual Report
(April 1, 1992-March 31, 1993)

Department of Reactor Engineering

Tokai Research Establishment
Japan Atomic Energy Research Institute
Tokai-mura, Naka-gun, Ibaraki-ken

(Received August 30, 1993)

This report summarizes the research and development activities in the Department of Reactor Engineering during the fiscal year of 1992 (April 1, 1992-March 31, 1993).

The major Department's programs promoted in the year are the assessment of the high conversion light water reactor, the design activities of advanced reactor system and development of a high energy proton linear accelerator for the engineering applications including TRU incineration.

Other major tasks of the Department are various basic researches on the nuclear data and group constants, the developments of theoretical methods and codes, the reactor physics experiments and their analyses, fusion neutronics, radiation shielding, reactor instrumentation, reactor control/diagnosis, thermohydraulics and technology developments related to the reactor physics facilities.

The cooperative works to JAERI's major projects such as the high temperature gas cooled reactor or the fusion reactor and to PNC's fast reactor project were also progressed.

The activities of the Research Committee on Reactor Physics are also summarized.

Keywords: Reactor Engineering Department Annual Report, Advanced Reactor System, Nuclear Data, Group Constants, Reactor Physics, Thermohydraulics, Fusion Neutronics, Radiation Shielding, Reactor Instrumentation, Reactor Control/Diagnosis

Board of Editors for Annual Report: Yoshida, H. (Chief Editor), Nakagawa, M. (Associated Chief Editor), Akino, F., Iijima, S., Ikeda, Y., Hasegawa, K., Okazaki, M., Sakamoto, Y., Suzudo, T., Watanabe, H. and Yagi, H.

Editorial Assistants: Yamano, H.

平成4年度原子炉工学部年報

日本原子力研究所東海研究所
原子炉工学部

(1993年8月30日受理)

本報告は、平成4年度における原子炉工学部の研究活動状況を取りまとめたものである。

原子炉工学部において、まとまった規模で行われた活動は、高転換軽水炉の検討評価、新型炉概念設計研究及びTRU消滅処理のための大強度陽子線形加速器の計画である。基礎基盤研究としては、核データと群定数、炉理論とコード開発、炉物理の実験と解析、核融合ニュートロニクス、放射線遮蔽、原子炉計測・計装、原子炉制御・診断、伝熱流動、及び炉物理施設技術開発等がある。また、高温ガス炉及び核融合等原研のプロジェクトへ協力する研究及び、動燃事業団との高速炉の共同研究も進めた。さらに、本報告は、炉物理に関する研究委員会活動も取りまとめた。

東海研究所：〒319-11 茨城県那珂郡東海村白方字白根2-4

原子炉工学部年報編集委員会：

吉田 弘幸（委員長）、中川 正幸（副委員長）、秋濃 藤義、飯島 進、池田裕二郎、長谷川和男、
岡崎 元昭、坂本 幸夫、鈴木 知明、渡辺 秀明、八木 秀之、
山農 宏之（事務局）

Contents

Foreword

1. Nuclear Data and Group Constants	1
1.1 Measurements on the Cross Sections for ^{94}Mo (n, p) & ^{95}Mo (n, np) ^{94}Nb , ^{158}Dy (n, p) ^{158}Tb , ^{182}W (n, n α) $^{178\text{m}2}\text{Hf}$ and ^{187}Re (n, 2n) $^{186\text{m}}\text{Re}$ Reactions at 14 MeV Region	2
1.2 Measurement of Neutron Activation Cross Sections at 9.1, 10.1, 11.1. and 11.8 MeV Using ^1H (^{11}B , n) ^{11}C Neutron Source at TANDEM Facility at JAERI	5
1.3 Beta Half-lives of $^{102\text{m}}\text{gRh}$	8
1.4 Modification of Self-shielding Factor Table of Au-197 in the SRAC System	11
1.5 Benchmark Calculations for ^{235}U Cross Section of ENDF/B-VI	14
1.6 Analysis of Bulk Shielding Experiments on Large SS316 Assemblies by DOT3.5 with FENDL Multigroup Library	17
2. Theoretical Method and Code Development	20
2.1 Benchmark Calculations for a Three-dimensional Transport Code Based on the Double Finite Element Method	21
2.2 Development of Coupled Neutron-photon Module for Vectorized Continuous Energy Monte Carlo Code	24
2.3 Reactivity Worth Calculations of Rotating Control Drums for Space Reactors	27
2.4 Whole Core Calculations of PWR by Monte Carlo Techniques	30
2.5 Development of Intelligent Reactor Design System IRDS (4)	33
3. Reactor Physics Experiment and Analysis	36
3.1 Mock-up Experiments of Metallic-fueled LMFBR in FCA Assembly XVI-2	37
3.2 Measurement of Capture to Fission Ratio (C8/F) by γ -ray Spectroscopy of Fuel Plate in FCA Assembly XVII-1	39
3.3 Measurement and Analysis of Mn-55 Capture Rate Distribution in FCA Assembly XVII-1	42
3.4 Measurement of Doppler Effect up to 2000°C in MOX-LMFBR Mockup Core FCA Assembly XVII-1	45
3.5 Analysis of Doppler Effect Measurement by PEACO-X Code	48
3.6 Measurement of Effective Delayed Neutron Fraction at FCA	51
3.7 Measurement of Reactivity Worth of the Multiple Burnable Poison Rods in the VHTRC-4 Core	54
3.8 HTGR Water Ingress Simulation Experiment at VHTRC-4 Core	57
3.9 Measurement of Axial Power Distribution in the VHTRC-6 Core	60

3.10	Measurement of Reaction Rate Ratio (C28/F) in Fuel Compact at VHTRC-6 Core	62
3.11	Benchmark Calculation of the Lead Cooled Fast Reactor Critical Assembly BFS-61	64
3.12	Studies on Production and Utilization of U-233 Fuel in Thermal Reactors	67
4.	Advanced Reactor System Design Studies	70
4.1	A Design Study of Lead-cooled Fast Breeder Reactor with Nitride-fuel Assembly	71
4.2	Concept of Passive Safe Reactor SPWR (System-integrated PWR)	74
4.3	A New Concept of Once-through Type Plutonium Burning	77
4.4	A Concept of Passive Safety Light Water Reactor System Requiring Reduced Operational and Maintenance Efforts	80
4.5	A Study on Possibility of a Reactor with Highly-load Following Capability	83
5.	Fusion Neutronics	86
5.1	Benchmark Experiment on Copper Slab Assembly Irradiated by D-T Neutrons	87
5.2	Influence of Calculation Parameters in Analyses for Blanket Neutronics Experiments of JAERI/USDOE Collaborative Program	90
5.3	Integral Tests of the JENDL Activation File and the REAC*3 Libraries for Fusion Applications	93
5.4	Development of Measurement Technique for Neutron Spectrum in Energy Region of eV in Large Assemblies	96
5.5	Second International Comparison on Measurement Techniques of Tritium Production Rate for Fusion Neutronics Experiments	99
5.6	Improvement of Neutron Measurement Technique for DD Plasma Diagnostics in Magnetic Confinement Fusion Device (2)	102
5.7	Measurement of Recoiled Activities from Al, Fe, Ni, Zr, Nb, Mo and SS-304 due to Neutron Sputtering at 14.9 MeV and Their Systematics	105
5.8	14 MeV Neutron Generation Characteristics of FNS Tritium Target —Measurement of Tritium Depth Profile—	108
6.	Radiation Shielding	111
6.1	Neutron Shielding Experiments at TIARA	112
6.2	HIL086R: Revised Version of Neutron-photon Multigroup Cross Section Library HIL086 for Neutron Energies up to 400MeV	115
6.3	Evaluation of Fluence to Dose Equivalent Conversion Factors for High Energy Radiations	118
6.4	Response of LiF TLDs to 10-40 keV Monoenergetic Photons from Synchrotron	121
6.5	Survey Calculation for Bulk Shielding Experiments —Effects of Void and Special Material—	123
7.	Reactor and Nuclear Instrumentation	126
7.1	Computer Program for Emission Rate Calculation of Neutrons from (α , n) Reactions in Arbitrary Compounds and Mixtures	127

7.2	Detection Possibility of ^{244}Cm in High Level Radioactive Wastes from Reprocessing Process	129
7.3	Radiation Effects of Opto-electronic Materials	132
7.4	Beam Profile Monitor Using Inverse Estimation Method of Current Distribution from Magnetic Fields by Genetic Algorithm	135
7.5	AC Magnetic-flux Penetration in a Sample Disk-type Sintered $\text{Bi}_2\text{Sr}_2\text{CaCu}_2\text{O}_x$ under Low Magnetic Fields Applied by a Planar Coil	138
7.6	Electric and Magnetic Characteristics of Co-Fe-Si-B Based Amorphous Wire and its Application to a Multivibrator-type Magnetometer at Low Temperature	141
7.7	Directional Detection of Current Dipoles by a Hybrid System of Superconducting Plates and a Magnetic Sensor	144
8.	Reactor Control, Diagnosis and Robotics	147
8.1	Application of H_∞ Control Theory to Power Control of a Nonlinear Reactor Model ...	148
8.2	An Analytical Study of Nonlinear Reactor Dynamics Based on Bifurcation Theory ...	151
8.3	Multivariate Autoregressive Analysis of Power Oscillation in NSRR	153
8.4	Noise Analysis for Plant Dynamics Identification of Nuclear Ship Mutsu	155
8.5	Benchmark Analysis of Acoustic Noise Signals for Sodium/Water Reaction Detection	157
8.6	Neutron-fuzzy Methodology for Sodium Leak Detection in LMFBRs	159
8.7	A Practical Module for Manipulator Mechanism Analysis	162
8.8	A Method for Improving Resolution of Ultrasonic Object Location	163
9.	Heat Transfer and Fluid Dynamics	166
9.1	Assessment of REFLA/TRAC Code for System Behavior during Reflood Phase in a PWR LOCA with CCTF Data	167
9.2	Analysis of Multidimensional Thermal-hydraulic Behavior in Core during Reflood Phase of PWR-LOCA with REFLA/TRAC Code	170
9.3	Applicability of REFLA/TRAC Code to a Small-break LOCA of PWR	173
9.4	Analyses for LOCA Experiments of ROSA-II Test Using REFLA/TRAC Code	176
9.5	Improvement of Models in COBTA-TF Code for Liquid Entrainments in Film-mist Flow	179
9.6	Visualization of Boiling Two-phase Flow and CHF Phenomenon with Real Time Neutron Radiography	182
9.7	DNBR Analysis under Circulation Pump Seizure Accident for SPWR	185
9.8	Experimental Investigation on Non-uniform One-phase Flow in Lower Plenum Through Perforated Plate	188
10.	Development of Proton Linear Accelerator and Transmutation Target System	191
10.1	A Progress in the High Intensity Proton Linear Accelerator Development	192

10.2 Development of a High Brightness Hydrogen Ion Source for the Basic Technology Accelerator	
—Beam Test at an Acceleration Voltage of 100 kV—	195
10.3 Development of a Radio Frequency Quadrupole for the Basic Technology Accelerator	
—Study on an LEBT, Thermal Considerations and Mechanical Design—	198
10.4 Development of a Drift Tube Linac for the Basic Technology Accelerator	
—Measurement of the Quadrupole Magnets—	201
10.5 Improvements of the Spallation Cascade Code NMTC/JAERI	204
10.6 Benchmark Calculations with Intranuclear Cascade Evaporation Model for Intermediate Energy Proton Induced Spallation Reactions	207
10.7 Integral Spallation Experiment with a Lead Assembly Irradiated with 500 MeV Protons	210
10.8 Neutron Measurement for (p, xn) Reaction with Protons of GeV Range	213
10.9 Neutronics and Thermal Hydraulics Calculations of Targets for the Proton Accelerator Driven TRU Transmutation System	216
10.10 Conceptual Design Study on Accelerator-driven Minor Actinide Transmutation System	219
11. Facility Operation and Technique Development	222
11.1 Operation Report of FCA	223
11.2 Operation Report of VHTRC	224
11.3 Operation Report of FNS	225
11.4 Operation Report of Heat Transfer and Fluid Flow Facility	226
12. Activities of the Research Committee on Reactor Physics	227
Publication List	230
Appendix I Department of Reactor Engineering Organization Chart	241
Appendix II Abbreviations	243

Foreword

The annual research activities of the Department of Reactor Engineering, Japan Atomic Energy Research Institute, during the fiscal year 1992 (April 1992 - March 1993) are presented in this report. The research activities of the Department had covered the broad area including fission reactor physics, fusion reactor neutronics, shielding, reactor instrumentation and control, thermohydraulics, nuclear energy systems analysis and intense accelerator technology.

The total number of people working in the department has been 117. The Department was funded from JAERI expenditures amounted to about 1284 million yen for the fiscal year 1992, excluding nuclear fuel costs and personnel expenses. About 483 million yen have been also provided by research contracts with external organizations; Science and Technology Agency (STA) for non-destructive measurement technology of transuranic elements (TRU) and for the large scale reflood test program and the thermal hydraulic demonstration test for HCLWR and Power Reactor and Nuclear Fuel Development Corporation (PNC) for fast reactor physics.

The research activities were conducted in the following nine laboratories:

- Reactor System Laboratory,
- Fast Reactor Physics Laboratory,
- Thermal Reactor Physics Laboratory,
- Reactor Instrumentation Laboratory,
- Reactor Control Laboratory,
- Accelerator Engineering Laboratory,
- Heat Transfer and Fluid Flow Laboratory,
- Fusion Reactor Physics Laboratory and
- Shielding Laboratory

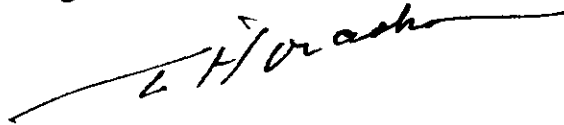
with the support of Reactor Physics Facility Operation Division. The Department has managed the Research Committee on Reactor Physics and the Research Committee on Advanced Reactors.

The project-related research program by the Department has been:

- (1) Design study of advanced reactors

- (2) Development of technology for partitioning and transmutation of nuclear wastes including R&D of the high intensity proton linear accelerator
- (3) Development of Very High Temperature Gas-cooled Reactor (VHTR)
- (4) Engineering research for fusion reactors

Activities by the Department in fiscal year 1992 have contributed to the essential progress in the field of reactor engineering.

A handwritten signature in black ink, appearing to read 'T. Hiraoka', with a long horizontal stroke extending to the right.

Toru Hiraoka, Director

Department of Reactor Engineering

1. Nuclear Data and Group Constants

Efforts on the measurement of long-lived radioactivity production cross sections at 14 MeV energy region has been continued at FNS. In this fiscal year, cross sections of the $^{94}\text{Mo}(n,p)^{94}\text{Nb}$, $^{95}\text{Mo}(n,np)^{94}\text{Mo}$, $^{158}\text{Dy}(n,p)^{158}\text{Tb}$, $^{182}\text{W}(n,n'\alpha)^{178\text{m}2}\text{Hf}$ and $^{187}\text{Re}(n,2n)^{186\text{m}}\text{Re}$ reactions were subjected. As a result, it was concluded that accuracy of data for the $^{94}\text{Mo}(n,p)^{94}\text{Nb}$, $^{95}\text{Mo}(n,np)^{94}\text{Mo}$ and $^{182}\text{W}(n,n'\alpha)^{178\text{m}2}\text{Hf}$ reactions satisfied the requirement from data needs. It revealed, however, that the measurement of the $^{158}\text{Dy}(n,p)^{158}\text{Tb}$ reaction suffered from a strong interference of ^{158}Tb produced via the $^{159}\text{Tb}(n,2n)^{158}\text{Tb}$ reaction due to a impurity of Tb in the Dy sample. It was also found that further cooling time more than 2 years were needed to reduce strong interference radioactivities for the measurement of the $^{187}\text{Re}(n,2n)^{186\text{m}}\text{Re}$ reaction. In addition to the 14 MeV energy region, the activation cross section measurements at an energy region from 9 to 13 MeV were conducted using $^1\text{H}(^{11}\text{B},n)$ neutron source available TANDEM accelerator of JAERI. Cross sections of nine reactions important for dosimetry applications were measured at 9.1, 10.1, 11.1 and 11.9 MeV. The effectiveness of the $^1\text{H}(^{11}\text{B},n)$ neutron source was demonstrated. In addition to the cross section measurement, half-lives of $^{102\text{m}}\text{Rh}$ and $^{102\text{g}}\text{Rh}$ were measured. The half-life of $^{102\text{g}}\text{Rh}$ isotope in question is to be revised extensively based on the new experimental data.

A precise study was carried out on the self-shielding factor table (f-table) for $^{197}\text{Au}(n,\gamma)^{197}\text{Au}$ reaction implemented in the SRAC system. A new self-shielding factor table was obtained with the PEACO routine in the SRAC system, by calculating hyper fine energy mesh neutron spectrum, on the one-dimensional cylindrical or slab geometry. The newly created f-table was compared with the original one in the SRAC system. As a result, there was no serious difference between the new and original f-tables.

In response to the question for underestimation in calculations with JENDL-3 library for k_{eff} in the uranium fueled cores TRX-1 and 2, and for the ration of epithermal to thermal ^{235}U fission rate, adequacy of the cross section of ^{235}U was investigated through the analysis of benchmark cores of TRX, BAPL and TCA with the SRAC code system. When the cross section of ^{235}U in the resolved energy region less than 2.2 keV was replaced with that of ENDF/B-VI, the calculation gave an excellent agreement with the experiment. It was suggested that the cross section of ^{235}U in JENDL-3 should be reevaluated by taking into the results.

Multigroup cross section library FENDL (Fusion Evaluated Data Library) was processed by using a TRANSX-2 processing code for the transport calculation with DOT3.5. The adequacy of data was examined by comparing the results with FENDL and FUSION-J3 based on the JENDL-3. Although there was a general agreement between calculations with FENDL and FUSION-J3 as long as the analysis of a SS-316 shielding experiments, two problems in the FENDL library were pointed out in terms of photon production cross sections and treatment of self-shielding table.

(Yujiro Ikeda)

1.1 Measurements on the Cross Sections for $^{94}\text{Mo}(n,p)$ & $^{95}\text{Mo}(n,np)$ ^{94}Nb , $^{158}\text{Dy}(n,p)$ ^{158}Tb , $^{182}\text{W}(n,n\alpha)$ $^{178\text{m}2}\text{Hf}$ and $^{187}\text{Re}(n,2n)$ $^{186\text{m}}\text{Re}$ Reactions at 14 MeV Region

Y. Ikeda and C. Konno

In response to the further data need in the summary document of the last RCM¹⁾ in November 1991, cross sections for $^{94}\text{Mo}(n,p)$ & $^{95}\text{Mo}(n,np)$ ^{94}Nb , $^{158}\text{Dy}(n,p)$ ^{158}Tb , $^{182}\text{W}(n,n\alpha)$ $^{178\text{m}2}\text{Hf}$ and $^{187}\text{Re}(n,2n)$ $^{186\text{m}}\text{Re}$ reactions at the 14 MeV energy region have been measured by performing a new irradiation experiment in 1991 using enriched isotopes or re-counting of samples which were irradiated in 1989. Although the summary document gave a status for $^{94}\text{Mo}(n,p)$ ^{94}Nb as adequate and no more data required, contribution of $^{95}\text{Mo}(n,np)$ reaction to ^{94}Nb production is of important and no experimental data has been reported. The present measurement aimed at discriminating contributions from both reactions of $^{94}\text{Mo}(n,p)$ ^{94}Nb and $^{95}\text{Mo}(n,np)$ ^{94}Nb by using isotopic enriched samples. For the measurement of the $^{182}\text{W}(n,n'\alpha)$ $^{178\text{m}2}\text{Hf}$ reaction, an enriched sample was also used because of low activity yield, the cross section of which was expected to be less than several tens μ barn according to the previous investigation. 2) For the reaction of $^{158}\text{Dy}(n,p)$ ^{158}Tb and $^{187}\text{Re}(n,2n)$ $^{186\text{m}}\text{Re}$, we have tried to determine the cross sections by counting the samples irradiated in 1989, putting longer cooling time.

The neutron source of FNS and irradiation configuration in 1989 were described somewhere in detail.²⁾ The new irradiation in 1991 lasted for 288,000 seconds with total D-T neutron yield of 2.74×10^{17} at the target. The Mo samples were placed at 10° and 90° with respect to incident d+beam direction. The ^{182}W sample was placed at 10° . The neutron flux was monitored by using the $^{93}\text{Nb}(n,2n)$ $^{92\text{m}}\text{Nb}$ reaction with 459 ± 10 mb at 14 MeV region.

The results for the present measurements were summarized in **Table 1.1.1** along with data in the literature. The decay data except the half-life of ^{158}Tb were taken from Table of Radioactive Isotopes.³⁾ The contributions of the $^{95}\text{Mo}(n,np)$ ^{94}Nb reaction to the ^{94}Nb productions were subtracted even though the enriched isotopes were used. Insufficient γ -ray counting statistics dominated experimental errors for each measurement. This was due to the use of small amounts of samples being about 50 to 60 mg. The uncertainty of half-life ($\pm 6.1\%$) was the secondly large error contributor. The present data are in good agreement within experimental errors with data previously reported^{2,4)} as shown in **Table 1.1.1**. **Figure 1.1.1** gives a mass dependency of (n,p) cross sections at 14.8 MeV for Mo isotopes. The data measured at FNS⁵⁾ are used as the cross sections for $^{95}, ^{96}, ^{97}, ^{98}\text{Mo}$. The systematic trend supports the adequacy of presently measured cross section values. As noted in the last summary document of the RCM, it is confirmed that there is no urgent need for this cross section at 14 MeV. The contributions of $^{94}\text{Mo}(n,p)$ ^{94}Nb were subtract from the ^{94}Nb

production using isotopic abundance data as in the $^{94}\text{Mo}(n,p)^{94}\text{Nb}$ case. The mass dependency of cross sections at 14.8 MeV for Mo isotopes is also shown in Fig. 1.1.1. Also data other than $^{95}\text{Mo}(n,np)^{94}\text{Nb}$ are referred from data at FNS. The large error is due to the γ -ray counting statistics. However, the systematic trend suggests that the present data gives the reasonable range of cross sections. The present results demonstrated that due to the appreciably large cross section at 14.8 MeV, the $^{95}\text{Mo}(n,np)^{94}\text{Nb}$ reaction should be taken into account for the long-lived activity production as well as $^{94}\text{Mo}(n,p)^{94}\text{Nb}$. After 3.6 year cooling, γ -lines of ^{158}Tb were clearly observed in a γ -ray spectrum. The cross section for the $^{158}\text{Dy}(n,p)^{158}\text{Tb}$ reaction was derived from the γ -ray peak counts measured. The results shown in Table 1.1.1, however, gave unreasonably large value more than one order of magnitude. From the reaction systematics, the cross section should be around 10 mb. The IRK evaluation¹⁾ also indicated that cross section should be less than 100 mb. The previous measurement at FNS gave cross sections of 100 ± 80 mb. The value was still very tentative because of extremely poor counting statistics. The present new measurement gave much better counting statistics with $\pm 11\%$. We concluded that there must be some error source in the present measurement. This situation could be explained by the impurity of Tb in the Dy sample. Assuming there was some amount of impurity of Tb in a Dy sample and 10 mb for $^{158}\text{Dy}(n,p)$ reaction cross section, at least 200 ppm of Tb should be there to give the ^{158}Tb activity corresponding to the count rate. Unfortunately, there was no data for the impurity composition in the Dy material used. A data of 250 ppm of Tb in Dy, which was available in some literature, was remarkably consistent with the estimation. If the sample constituent is carefully measured by some chemical analysis, we would say that there is no need to have expensive enriched ^{158}Dy sample any more as long as this assumption is true. Nevertheless, it is still recommended to pursue a measurement with enriched sample of ^{158}Dy . Using enriched sample, still very poor counting statistics for the γ -ray line of $^{178\text{m}2}\text{Hf}$. This is simple due to the extremely low reaction cross section being less than 0.1 mb.^{1,2)} Nevertheless, slight improvement was achieved in the measurement with the enriched sample in comparison with the last one using sample with natural abundance. The cross sections determined in the present measurement agreed with in experimental error with the previous data. The results is shown in Table 1.1.1. It was concluded that it is needed that we have to wait for 2 to 3 year to reduce interference activities (^{184}Re [$T_{1/2}=165$ d] and ^{182}Ta [$T_{1/2}=115$ d]). In order to avoid unnecessary controversial discussion on the data with large uncertainty. The long-lived activity allow unlimited cooling time as long as we keep this in our mind.

References

- 1) "Conclusion and Recommendation" in the Summary Report of 2nd IAEA-RCM for "Activation Cross Sections for the Generation of Long-Lived Radionuclides of Importance in Fusion Reactor Technology" at Vienna, 11-12 November 1991.

- 2) Ikeda, Y., et al. : "Measurements of Long-Lived Activation Cross Sections by 14 MeV Neutrons at FNS," Proc. Int. Conf. on Nuclear Data for Science and Technology, Jülich, Germany, 13-17 May, 1991, pp 364-366.
- 3) Browne, E. and Firestone, R. B., Shirley, V. S., Editor : "Table of Radioactive Isotopes," A Wiley-Interscience Publication, John Wiley & Sons, 1986.
- 4) Greenwood, L. R., et al. : Phys. Rev. C 35, 76 (1987).
- 5) Ikeda, Y., et al. : JAERI-1312 (1988).

Table 1.1.1 Results of measured cross sections

Reaction	Cross section (mb)		Reference values	
	14.1 MeV	14.8 MeV	Energy (MeV)	(mb)
$^{94}\text{Mo}(n,p)^{94}\text{Nb}$	58 \pm 12	54 \pm 9	14.1	44 \pm 18 a)
			14.5	48 \pm 20 a)
			14.8	58 \pm 17 a)
			14.8	53.1 \pm 5.3 b)
$^{95}\text{Mo}(n,np)^{94}\text{Mo}$	12 \pm 7	21 \pm 9	-----	-----
$^{158}\text{Dy}(n,p)^{158}\text{Tb}$		620 \pm 85	14.8	100 \pm 80 a)
		(10 - 20)*	14 - 15	<100 c)
$^{182}\text{W}(n,n'\alpha)^{178\text{m}2}\text{Hf}$		0.026 \pm 0.013	14.8	0.014 \pm 0.008 a)
			14.9	< 0.04 d)

a) Ikeda; Ref. 2), b) Greenwood; Ref. 4), c) IRK evaluation; Ref. 1),

d) KRI measurement; Ref. 1), * Estimation assuming 250 ppm Tb impurity in the Dy sample

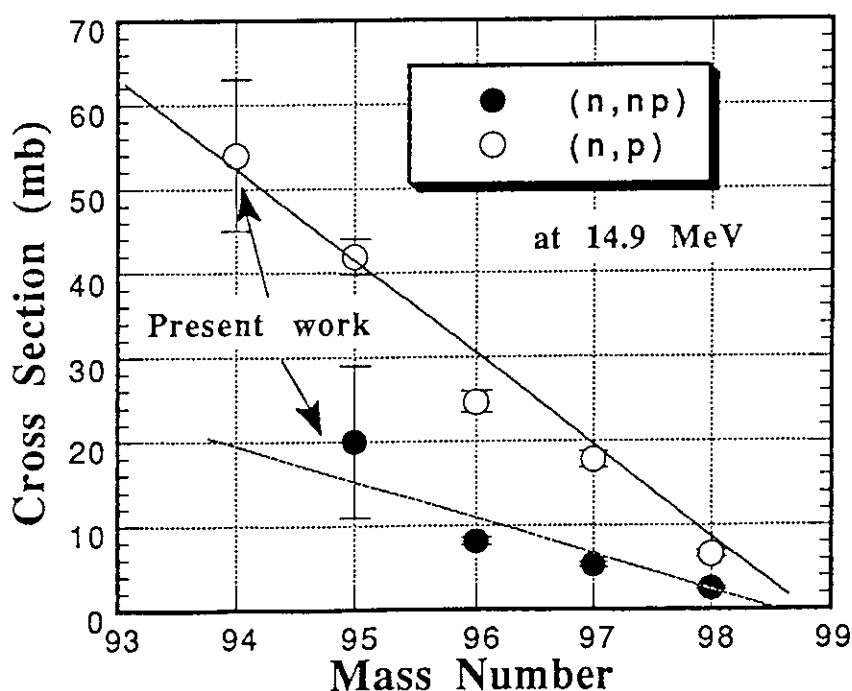


Fig. 1.1.1 Cross sections of $^{94}\text{Mo}(n,p)^{94}\text{Nb}$ and $^{95}\text{Mo}(n,np)^{94}\text{Nb}$ along with other (n,p) and (n,np) cross sections at 14.9 MeV for different molybdenum isotopes.

1.2 Measurement of Neutron Activation Cross Sections at 9.1, 10.1, 11.1, and 11.8 MeV Using $^1\text{H}(^{11}\text{B}, n)^{11}\text{C}$ Neutron Source at TANDEM Facility at JAERI

Y. Ikeda, S. Chiba, T. Fukahori, K. Hasegawa, M. Mizumoto, S. Meigo
and H. Maekawa

The continuous program on activation cross section measurements for important dosimetry reactions at an energy range from 9 to 13 MeV has been under way by using a neutron source incorporated with $^1\text{H}(^{11}\text{B}, n)^{11}\text{C}$ reaction.¹⁾ The present report gives the most recent results of the cross section measurements.

The neutron energies applied were 9.1, 10.1, 11.1 and 11.8 MeV which corresponded to ^{11}B beams with energies of 55, 57, 60 and 63 MeV, respectively, incident into a $^1\text{H}_2$ gas target. In addition to the irradiation with gas in, separate irradiation with gas out was performed for each energy in order to subtract the parasitic neutrons due to interaction of ^{11}B beam with the target structure. The neutron spectra in the forward direction with respect to the ^{11}B beam direction were measured with the TOF technique incorporated with two NE213 scintillation spectrometers. Figure 1.2.1 shows net neutron spectra for 10.1 and 11.8 MeV. Obviously, they look broadened at the peak energy regions. This was attributable to insufficient time resolution in the TOF measurement. Stacked foils of Ti, V, Fe, Co, Zn, Zr and Nb sandwiched with both Al and Au monitor foils were irradiated at a distance of 100 mm from the center of target cell for 11 hours for runs with gas in and for 3 to 4 hours with gas out. After irradiation for each run, activities were measured with Ge detectors and reaction rates were deduced Fig. 1.2.1. Neutron spectra at 10.1 and 11.8 MeV by performing necessary corrections in terms of decay times, natural abundance, detector efficiency, γ -ray self absorption, and so forth. The neutron flux was determined from the reaction rate of monitor reaction of $^{27}\text{Al}(n, \alpha)^{24}\text{Na}$, the cross section value of which was taken from IRDF-90²⁾. The neutron flux at each foil was derived by interpolating reaction rates of $^{27}\text{Al}(n, \alpha)^{24}\text{Na}$ on both front and rear sides. The spectra were used not only in the determination of mean reaction energy, but also in the correction for the low energy neutron component to the net reaction rate of interest. Fortunately, the correction for the low energy neutron contribution was not serious because of rather high threshold energy of almost all reactions, except for $^{64}\text{Zn}(n, p)^{64}\text{Cu}$. Most dominant experimental error arose in the reaction rate due to poor statistics of γ -ray counts. This was simply because of low neutron yields in the present operation of ^{11}B beam.

The present results are summarized in Table 1.2.1. The presently measured cross sections of $^{59}\text{Co}(n, \alpha)^{56}\text{Mn}$, $^{90}\text{Zr}(n, p)^{90\text{m}}\text{Y}$, $^{93}\text{Nb}(n, \alpha)^{90\text{m}}\text{Y}$ and $^{197}\text{Au}(n, 2n)^{196}\text{Au}$ are plotted in Figs. 1.2.2 to 1.2.5, along with comprehensive evaluations and experimental data in the literature. Although the experimental errors are large due to low activity production by weak $^1\text{H}(^{11}\text{B}, n)$ source strength, the new experimental values are of importance in this particular energy region.

References

- 1) Ikeda, Y., et al. :Proc. Intl. Conf. on Nucl. Data for Sci. & Technol., Jülich, Germany, 13-17 May 1991 (issued in 1992: Editor S. M. Qaim) pp. 294-296.
- 2) Kocherov, N. P. and Vonach, H.: "The International Reactor Dosimetry File (IRDF-90)," Proc. of the Seventh ASTM-EURATOM Symp. on Reactor Dosimetry, Strasbourg, France, 27-31 August (1990) pp357-361.

Table 1.2.1 Results of Cross Section Measurements

Reaction	Cross Section (mb)			
	9.1 MeV	10.1 MeV	11.1 MeV	11.8 MeV
$^{48}\text{Ti}(n,p)^{48}\text{Sc}$	26.0 ± 2.1	-----	-----	-----
$^{51}\text{V}(n,\alpha)^{48}\text{Sc}$	4.9 ± 2.0	4.2 ± 1.0	9.1 ± 1.2	
$^{56}\text{Fe}(n,p)^{56}\text{Mn}$	58.0 ± 5.0	73.6 ± 5.4	86.9 ± 5.2	94.5 ± 6.0
$^{59}\text{Co}(n,\alpha)^{56}\text{Mn}$	12.8 ± 1.8	18.6 ± 1.7	19.8 ± 1.5	21.6 ± 2.5
$^{64}\text{Zn}(n,p)^{64}\text{Cu}$	$287. \pm 30.$	$282. \pm 23.$	$288. \pm 18.$	$293. \pm 31.$
$^{90}\text{Zr}(n,p)^{90m}\text{Y}$	$2.1(+2.9, -1.0)$	5.7 ± 1.6	6.8 ± 2.0	9.8 ± 2.1
$^{93}\text{Nb}(n,2n)^{92m}\text{Nb}$	$29. \pm 11.$	94.5 ± 8.7	$242. \pm 27.$	$357. \pm 20.$
$^{93}\text{Nb}(n,\alpha)^{90m}\text{Y}$	2.3 ± 1.1	3.0 ± 1.4	2.9 ± 0.7	3.5 ± 0.8
$^{197}\text{Au}(n,2n)^{196}\text{Au}$	$379. \pm 40.$	$1124. \pm 45.$	$1680. \pm 100.$	$1976. \pm 110.$
$^{27}\text{Al}(n,\alpha)^{24}\text{Na} *$	73.83	89.03	109.06	115.87

* Monitor Reaction; Cross section data are referred from IRDF-90

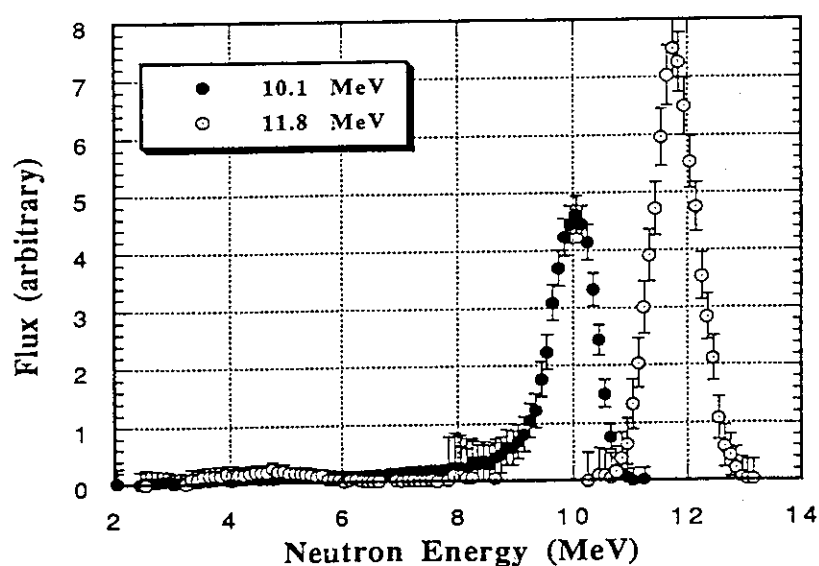
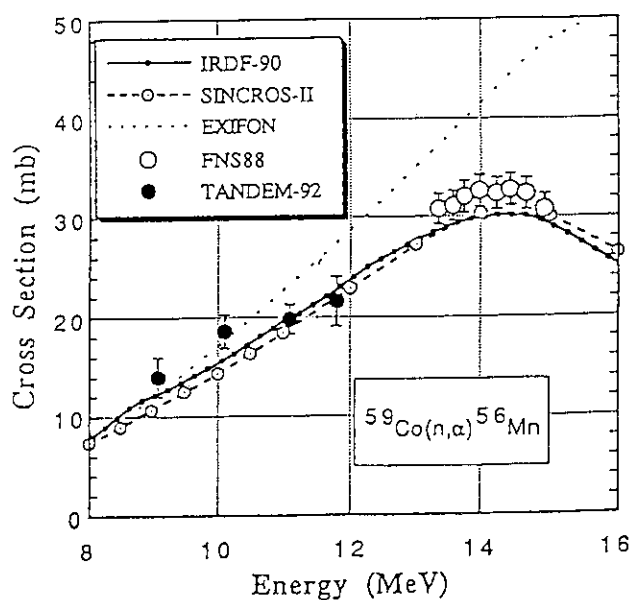
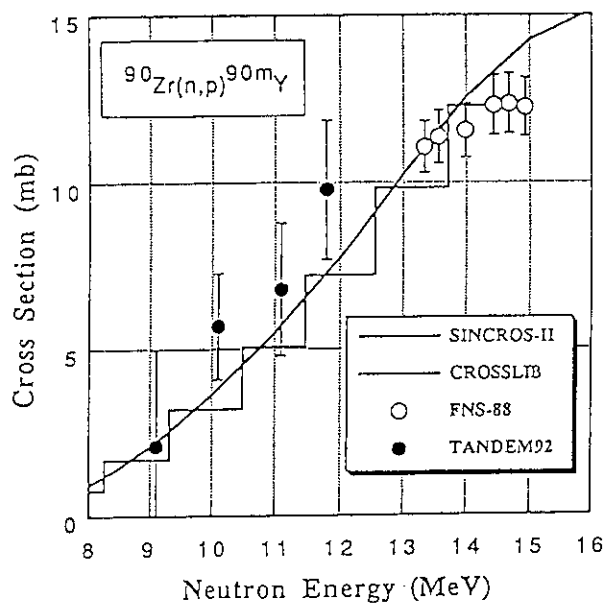
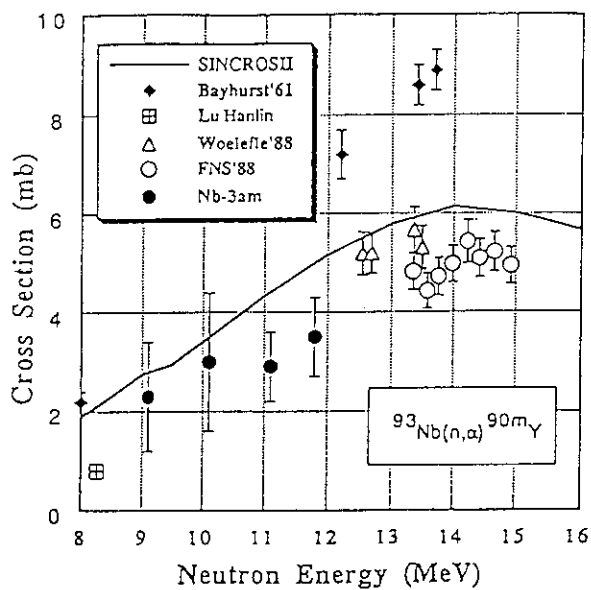
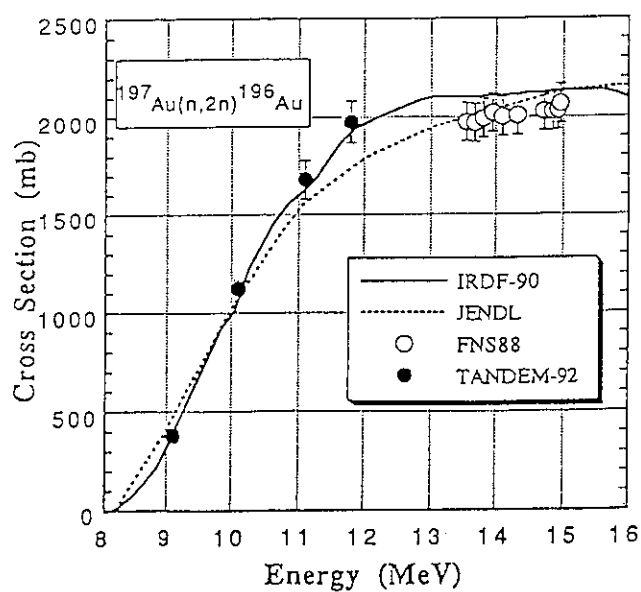


Fig. 1. 2.1 Neutron spectra at 10.1 and 118 MeV measured with TOF technique.

Fig. 1.2.2 Cross section of $^{59}\text{Co}(n,\alpha)^{56}\text{Mn}$ Fig. 1.2.3 Cross section of $^{90}\text{Zr}(n,p)^{90\text{m}}\text{Y}$ Fig. 1.2.4 Cross section of $^{93}\text{Nb}(n,\alpha)^{90\text{m}}\text{Y}$ Fig. 1.2.5 Cross Section of $^{197}\text{Au}(n,2n)^{196}\text{Au}$

1.3 Beta Half-lives of $^{102m,g}\text{Rh}$

A. Tanaka*, M. Asai*, H. Yamamoto*, Y. Ikeda, H. Maekawa and K. Kawade*

The previous values of the half-lives of ^{102m}Rh and ^{102g}Rh were ~ 2.9 y and 207 ± 3 d, respectively ¹⁾. There were few measurements of the half-life of ^{102m}Rh and no evaluation of uncertainty was reported. These values were measured with GM counters, scintillation counters and β -ray spectrometer. In this work, we followed the change of the γ -ray intensities in the decay of $^{102m,g}\text{Rh}$ with an HPGe detector to determine the precise half-lives. In addition, gamma singles and γ - γ coincidence measurements were performed with HPGe detectors in order to propose a more detailed decay scheme. In gamma singles measurement, a 115 % Ge detector was used to obtain high detection efficiency.

A natural Rh foil of 50 μm thickness was irradiated for 32 hours with d-T neutrons at the FNS facility in JAERI to produce $^{102m,g}\text{Rh}$ by the $^{103}\text{Rh}(n,2n)$ reaction. No chemical separation was performed. The measurements were started after a cooling time of six months, so that the contribution of short-lived components was negligible. The sample was divided into two and each sample was used for half-life measurement and γ - γ coincidence measurement, respectively.

The sample was fixed between acrylic plates together with Al foil which had ^{133}Ba on its surface. The ^{133}Ba source was used for the check of the possible change in source-to-detector distance for the long experimental period. Gamma-ray spectrum was measured with a 20 % Ge detector for 24 hours every one month. The arrangement of the detector and the sample is shown in Fig. 1.3.1. The source in the acrylic holder was attached to the acrylic spacer at 5 cm from the detector. After the measurement was done, the source was removed every time. In this case, it is very important to ensure that the sample is attached at the same position. In this work, a γ -ray of 356.0 keV from ^{133}Ba source was used for the correction of the distance.

Gamma singles measurements were performed with 20 % and 115 % Ge detectors. In the case of 115 % Ge detector, a Pb plate of 2.5 cm thickness was placed between the source and the detector to detect high energy gamma-rays effectively and to reduce sum coincidence effects. The γ - γ coincidence measurement was performed with 20 % and 23 % Ge detectors and a LEPS (low energy photon spectrometer).

Fig. 1.3.2 shows the decay curves of the gamma-rays from $^{102m,g}\text{Rh}$ after correction with ^{133}Ba . The half-lives of $^{102m,g}\text{Rh}$ have been determined to be 3.76 ± 0.10 y for ^{102m}Rh and 206 ± 3 d for ^{102g}Rh , respectively, which are weighted mean values of two or four gamma-rays in each curve. Present values are compared with previous ones in Fig. 1.3.3. There is a good agreement with the previous values of 210 ± 6 d²⁾, 206 ± 3 d³⁾ and $205 \pm$

*Department of Nuclear Engineering, Nagoya University

10 d⁴) for ^{102g}Rh , while the present value indicates a longer half-life compared with the previous ones of 1057 d⁵) and 2.1 ± 0.9 y⁶) for ^{102m}Rh .

In addition to the half-life measurement, γ -ray spectroscopy was performed to establish a new decay scheme of ^{102}Rh . Two new γ -rays of 865.5 and 1493.6 keV are observed. The 865.5 keV γ -ray was observed in coincidence with the γ -rays of 631.3 and 1103.2 keV, but the 1493.6 keV γ -ray was observed only in singles measurements. Based on the present study, a decay scheme is proposed.

References

- 1) Frenne, D. de and Jacobs, E. : Nuclear Data Sheets 63, 373 (1991).
- 2) Minakawa, O. : Phys. Rev. 60, 689 (1941).
- 3) Hisatake, K. : J. Phys. Soc. Japan 16, 1280 (1961).
- 4) McGowan, F. K. and Stelson, P. H. : Phys. Rev. 123, 2131 (1961).
- 5) Born, P., Veefkind, A., Elsenaar, W. H. and Blok, J. : Physica 29, 535 (1963).
- 6) Hisatake, K., Matsuo, S. and Kawakami, H. : J. Phys. Soc. Japan 20, 1107 (1965).

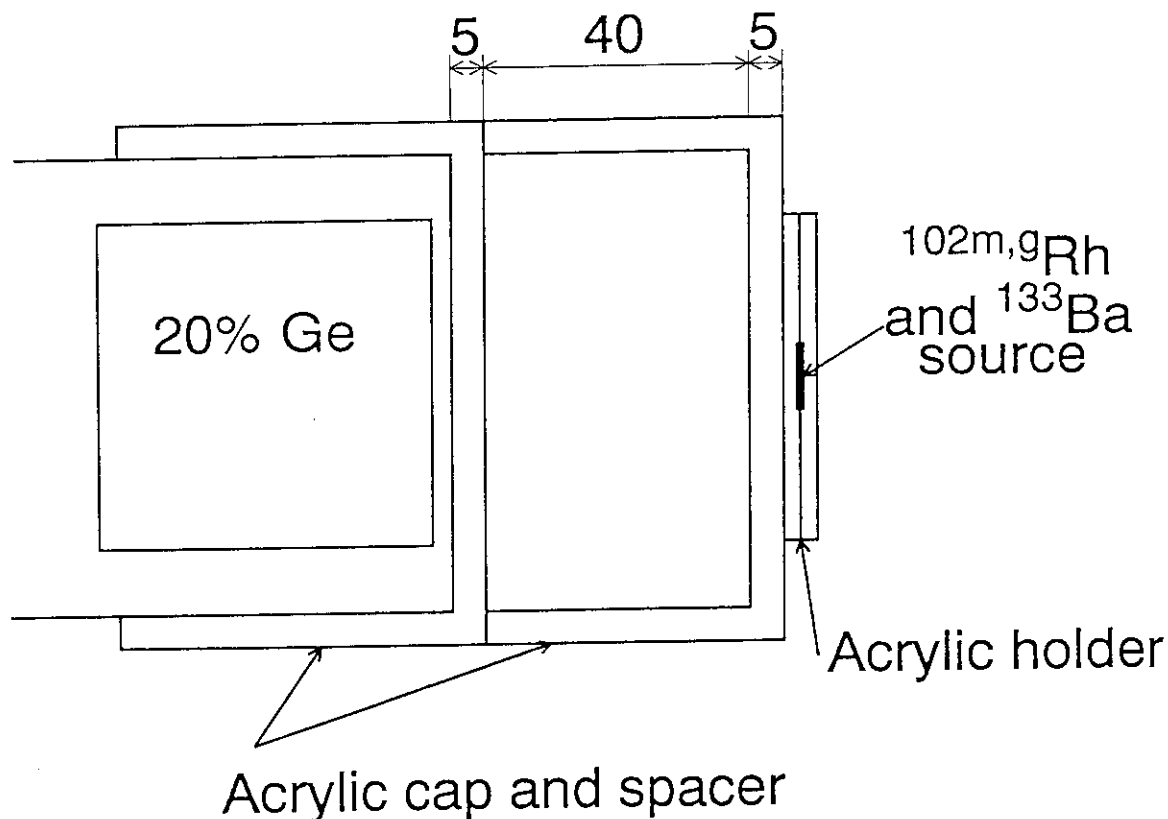


Fig. 1.3.1. Source and detector arrangement in half-life measurement. The sample was attached to the spacer with a tape in each measurement.

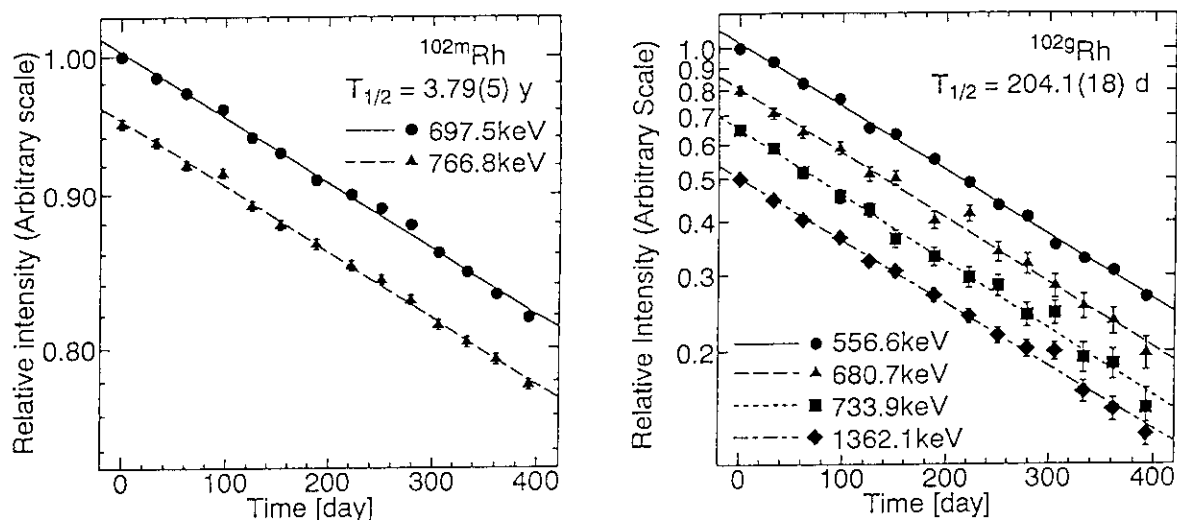


Fig. 1.3.2. Decay curves of the γ -rays from $^{102m,g}\text{Rh}$.

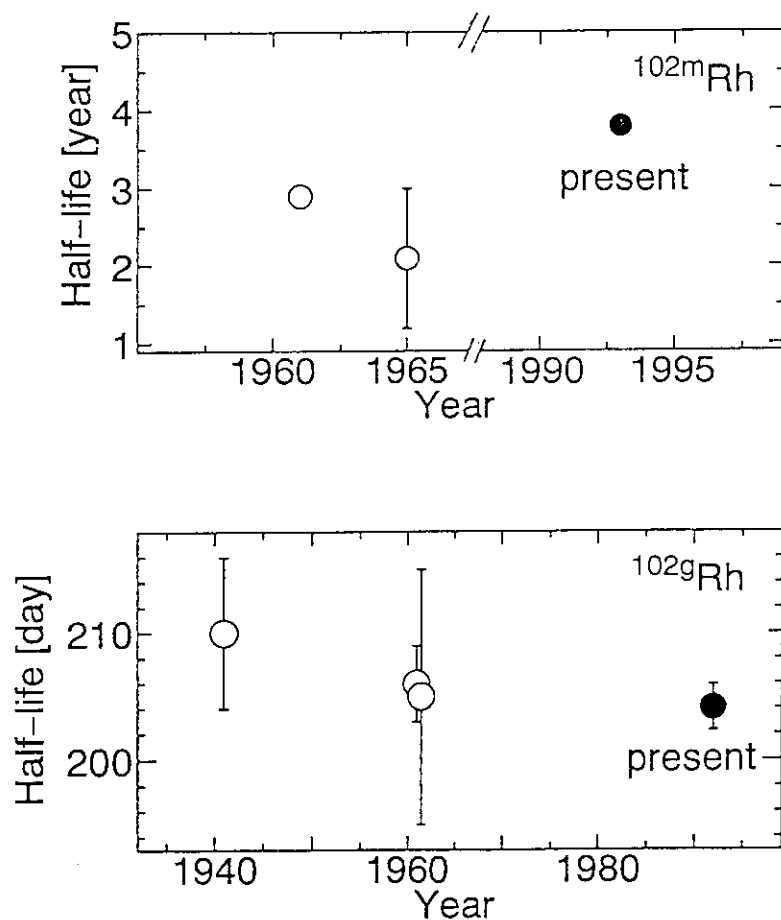


Fig. 1.3.3. Comparison of half-lives with previous values.

1.4 Modification of Self-shielding Factor Table of Au-197 in the SRAC System

H.Akie and K.Tsuchihashi

It has been pointed out that the self-shielding factor table(f-table) of Au-197 in the SRAC system is possibly not accurate, from the results of the analyses of Au activation experiment performed at KUCA. The self shielding factor in the SRAC library was evaluated as the ratio of the effective cross section in a homogeneous mixture of Au-197 with a material of background cross section σ_0 , to the infinite dilution cross section. The effective cross section of light and medium weight nuclides was simply obtained by averaging with the following weighting spectrum :

$$\phi = \phi_0 / (\sigma_f + \sigma_0) \quad , \quad (1)$$

where ϕ_0 is the combination of the fission and 1/E spectra. It seems that the shielding factor table calculated in such a way has two problems to be used for experimental analysis of Au activation, that 1) in activation experiments, Au is usually irradiated in the heterogeneous forms of wire or foil, and 2) the effective cross section calculated with the weighting spectrum in Eq.(1) is assumed to be not accurate especially in the resonance energy range. For these reasons, a new self-shielding factor table of Au-197 was obtained with the PEACO routine in the SRAC system, by calculating a hyper fine energy mesh neutron spectrum on the one-dimensional cylindrical or slab geometry. Comparing the original and the new f-tables, the accuracy of the self-shielding factor of Au-197 was studied.

The PEACO calculations were made for the cylindrical geometry of Au-197 surrounded by water, and for the slab geometry of Au-197 inserted between water region, that simulate Au wire and foil, respectively. The diameter d (for wire) and the thickness t (for foil) of the Au region were selected so that σ_0 becomes 10^{-1} , 10^0 , 10^1 , ... and 10^6 barns from the equivalence relation

$$\sigma_0 = \frac{g(c)(1-c)}{N \cdot l} \quad , \quad (2)$$

where $l=d$ or $2t$, $c=0.0$, $g(c)=1.2$ and N is the atomic number density of Au-197 (5.9×10^{22} atoms/cm³).

The new shielding factors for the capture cross section of Au-197 calculated with

PEACO are compared in Fig.1.4.1 with the original f-table in the 59th SRAC energy group, in which the largest resonance of Au-197 at 4.9eV is located. The new shielding factors for wire and foil are seen to shift from the original value, and to differ from each other. Thus, for the calculations of Au wire and foil, two corresponding f-tables were created.

Figure 4.1.2 shows the capture rate distributions of the Au wire of 0.5mm diameter placed in a one-dimensional core with reflector, calculated with the original and the new f-tables. Furthermore, the capture rates of the same wire above 1eV are shown in Fig.4.1.3 that simulate the reaction rate of the Au wire with Cd cover. It can be said from these figures that the reaction rate difference between the calculations with the new and the original f-tables is very small. The reaction rate ratios of Au without/with Cd cover(Cd ratios) calculated with these f-tables also agree very well. It is concluded that the f-table of Au-197 in the SRAC library is not the cause of the discrepancy between the experiment and the calculation that has been observed in the analyses of the Au activation experiments.

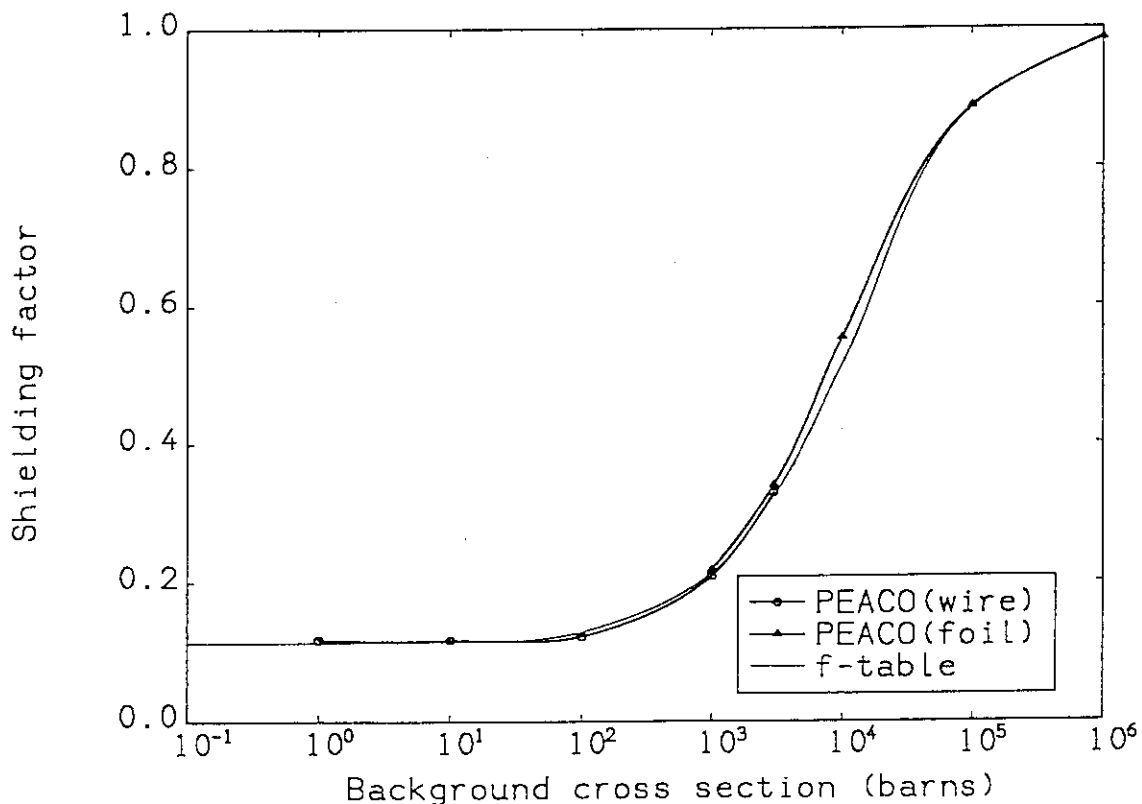


Fig. 1.4.1 Comparison of the original and the new f-table of Au-197 in the 59th energy group of the SRAC library(3.93 – 5.04eV)

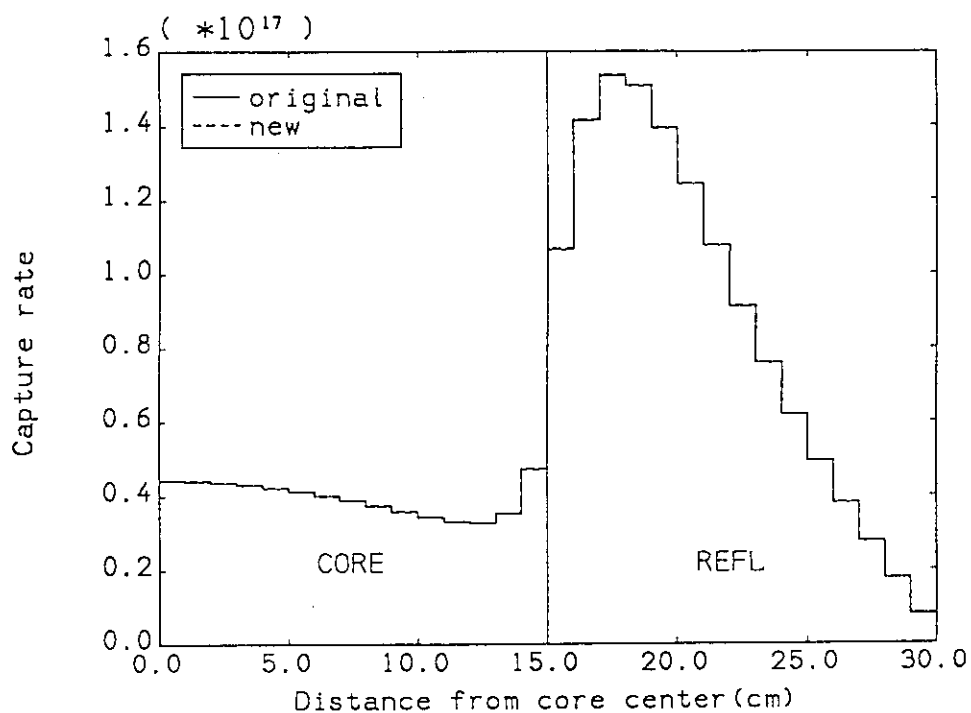


Fig. 1.4.2 Capture rate distributions of Au wire of 0.5mm diameter in a one-dimensional core with reflector obtained with the new and the original f-table

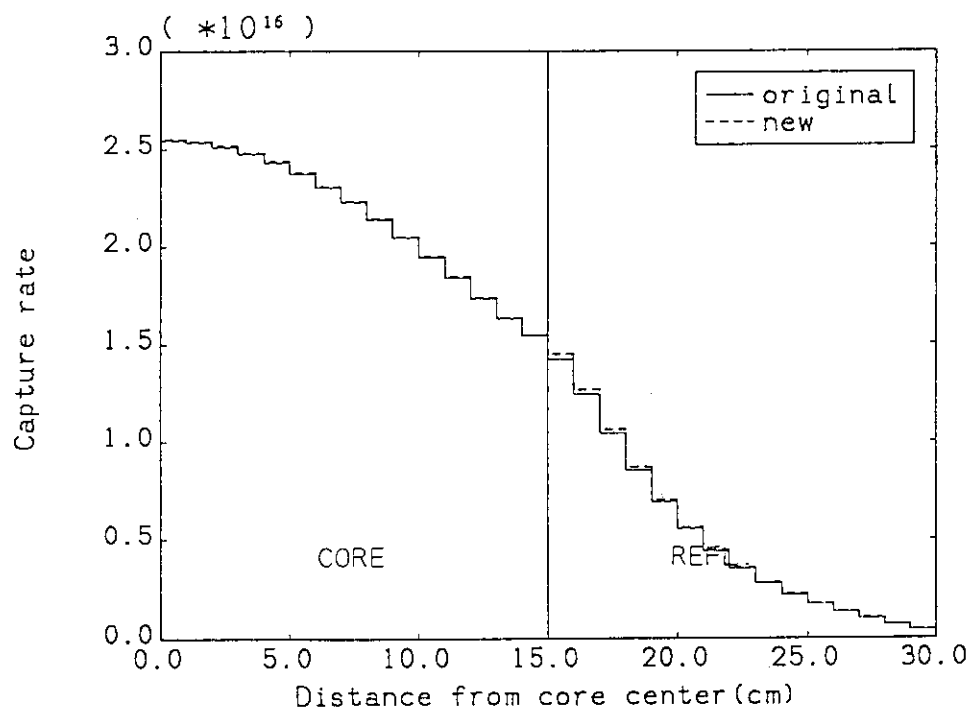


Fig. 1.4.3 Distributions of the capture rate above 1eV of Au wire(0.5mm diameter) in a one-dimensional core calculated with the new and the original f-table

1.5 Benchmark Calculations for ^{235}U Cross Section of ENDF/B-VI

H. Takano, H. Akie, T. Mori and K. Kaneko**

In the previous thermal benchmark tests¹⁾ of JENDL-3, it was found that very accurate neutronic calculation by a continuous energy Monte Carlo code VIM underpredicted k_{eff} by 0.8 % for the uranium fueled cores TRX-1 and 2²⁾. Furthermore, the ratio of epithermal to thermal U-235 fission rate was underestimated.¹⁾ To make a feedback to the nuclear data of JENDL-3, the cross sections data of U-235 are investigated.

In Table 1.5.1 are compared the thermal cross sections and resonance integrals for U-235 obtained from the various nuclear data files. From this table, the capture resonance integral of JENDL-3 is the largest among those of other files, and especially the difference between JENDL-3 and ENDF/B-VI data amounts to 14 %. The fission resonance integral of JENDL-3 is smaller than those of other files. Furthermore, in Fig.1.5.1 are shown the comparison of capture group cross sections calculated from JENDL-3 and ENDF/B-VI. The large differences between two data files are observed in the energy range from 10 eV to 10 keV. In JENDL-3, the resolved resonance region is below 100eV, and in ENDF/B-VI, on the other hand, it is below 2.2 keV.

The effect on k_{eff} due to the difference in U-235 cross sections between JENDL-3 and ENDF/B-VI was studied by calculating the benchmark cores of TRX, BAPL²⁾ and TCA³⁾ with the SRAC code. The results are shown in Table 1.5.2. The results calculated by replacing U-235 cross sections of JENDL-3 to ENDF/B-VI data in the resolved region below 2.2 keV are in very good agreement with the experiments. The U-235 cross sections of JENDL-3 will be reevaluated on the basis of the present results.

References

- 1) Takano H. et al.: "Thermal Reactor Benchmark Calculations for JENDL-3," JAERI-M 92-125, p11 (1992).

**The Japan Research Institute, Ltd., Tokyo

- 2) " Benchmark Specification," ENDF-202, BNL-10302 (1972).
- 3) Turuta H. et al.:" Critical Sizes of Light-Water Moderated UO_2 and $\text{PuO}_2\text{-UO}_2$ Lattices," JAERI 1254 (1978).

Table 1.5.1 Comparison of thermal cross sections and resonance integrals for U-235

	JENDL-3	ENDF/B-VI	JEF-1	ENDF/B-V	ENDL-82
2200m/sec cross section (barns)					
capture	96.0	99.8	98.4	98.4	100.9
fission	584.0	584.3	583.5	583.9	602.0
resonance integral (barns) : 0.5 eV - 20 MeV					
capture	152.0	132.9	139.3	139.2	139.8
fission	275.0	278.6	281.9	281.7	284.0

Table 1.5.2 The effect of U-235 cross sections of ENDF/B-VI on k_{eff}

Core	JENDL-3	B/VI-UR	B/VI-R
TRX-1	0.993	0.994	0.996
TRX-2	0.996	0.996	0.998
BAPL-1	0.995	0.995	0.998
BAPL-2	0.996	0.996	0.998
BAPL-3	0.997	0.997	0.999
TCA150	0.994	0.994	0.998
TCA183	0.996	0.996	1.000
TCA248	0.995	0.995	0.998
TCA300	0.999	0.999	1.001

Note: The B/VI-UR shows the results calculated by replacing U-235 cross section of JENDL-3 to ENDF/B-VI data in the unresolved region above 2.2 keV, and the B/VI-R shows the results obtained by replacing the data in the resolved region below 2.2 keV.

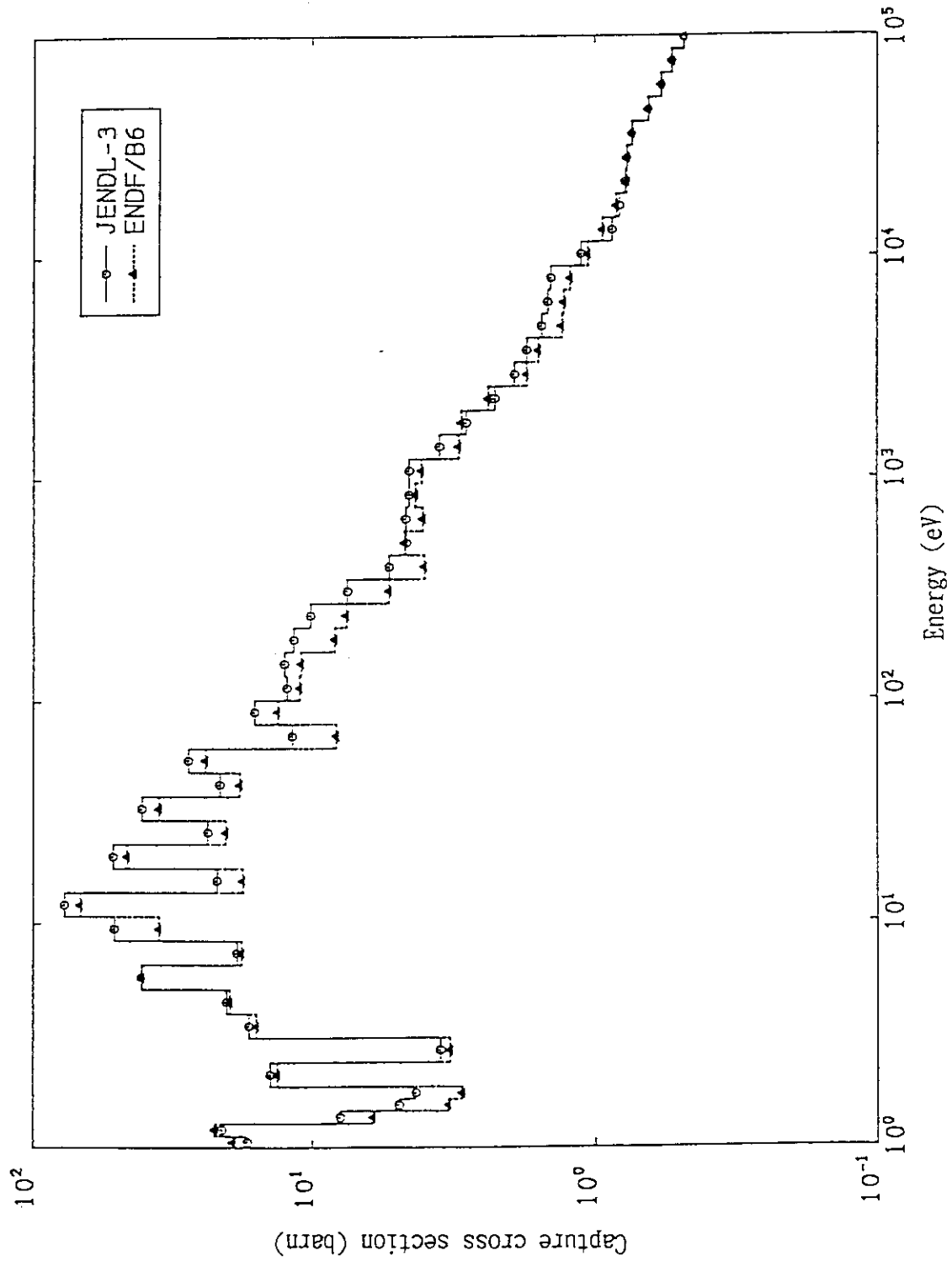


Fig. 1.5.1 Comparison of U-235 capture cross sections for JENDL-3 and ENDF/B-VI

1.6 Analysis of Bulk Shielding Experiments on Large SS316 Assemblies by DOT3.5 with FENDL Multigroup Library

J. Pulpan* and H. Maekawa

The Fusion Evaluated Nuclear Data Library (FENDL)¹ is the project initiated at the International Atomic Energy Agency (IAEA) to promote international cooperation on the development of International Thermonuclear Experimental Reactor (ITER) and other fusion technology related activities².

The FENDL multigroup library was prepared by NJOY 91.38³ from FENDL-1.1⁴ which was selected from evaluated nuclear data files ENDF/B-VI, JENDL-3, EFF-2 and BROND. The selection was performed by the IAEA Advisory Group Meetings organized by the Nuclear Data Section (NDS) of IAEA⁴. The multigroup data for each isotope/element are distributed by NDS-IAEA in the MATES format. The group structure of VITAMIN-J (175 neutron and 42 photon energy groups) is used in the FENDL multigroup library. The TRANSX-2 code is designed for preparation of the problem dependent on transport tables from the MATES files distributed.

A series of the shielding experiments is being performed at FNS/JAERI. The neutron and photon spectra, fission-rates and activation rates are planned to measure at several positions of the three bulk shielding assemblies made from stainless steel^{5,6}. The analysis of the experiments has been done by the two dimensional discrete-ordinate code DOT3.5 with the FUSION-J3 library⁷ and by the MCNP-3B code with the FSXLIB-J3 library⁸.

The aim of this work was to perform the data testing of the FENDL library by analyzing above three bulk shielding experiments and by comparing its results with another well established library, i.e., JENDL-3. The group constant tables used in the calculation were prepared from the FENDL multigroup library by the TRANSX-2 code. The neutron spectra calculated with FENDL are compared with the previous DOT3.5 analysis with the FUSION-J3 library. The analytical results based on both libraries are also compared with the measured ones. Typical results are shown in Figs. 1.6.1 and 1.6.2.

The neutron spectra obtained with infinite-dilution FENDL library agree well with those obtained with FUSION-J3, except for the energy interval 5-11 MeV and energy region below 1 keV. The disagreement of neutron spectra in energy interval 5-11 MeV are caused by different basic nuclear data. The measurement by an NE213 spectrometer agrees better with the FUSION-J3 calculation at this interval than those with FENDL. The difference between both

* STA fellow from Institute of Radiation Dosimetry,
Czech Academy of Sciences, Prague, Czech Republic

calculated neutron spectra below 1 keV is explained by the omission of molybdenum in the FENDL mixing table for SS316 type stainless steel. The FENDL library should include molybdenum cross section in the future version. The good agreement is found between the C/E values of reaction rates calculated from FENDL and FUSION-J3 sets of neutron spectra.

The two problems of processing codes remain even after several changes in the source program:

- 1) The photon production cross sections are not processed correctly by NJOY91.38 for files in the ENDF-6 format.
 - 2) The TRANSX-2 code does not produce self-shielded cross section tables correctly.
- The next recommendation is reduction of the number of neutron group changing the group structure from the VITAMIN-J to some other with the same or smaller energy interval.

Though the preliminary existing bugs in the processing code NJOY91.38, and the post-processing BBC and TRANSX are completed, the FENDL multigroup library distributed as the MATES files will be a useful data base for preparation of the transport tables for discrete ordinate codes. Its flexible conception (self-shielding, different temperatures) makes it suitable for fusion applications.

References

- 1) Goulo V. (Ed.): "Fusion Evaluated Nuclear Data Library (FENDL)-Proceedings of the IAEA Specialists' Meeting on FENDL," INDC(NDS)-223/GF, International Atomic Energy Agency (Aug. 1989).
- 2) Pashchenko A. B. and Muir D. W. (Compilers): "FENDL-2 and Associated Benchmark Calculations," INDC(NDS)-260, International Atomic Energy Agency (March 1992).
- 3) MacFarlane R. E., et al.: "NJOY91.38: A Code System for Producing Pointwise and Multigroup Neutron and Photon Cross Sections from ENDF/B Evaluated Nuclear Data," PSR-171, Radiation Shielding Information Center, Oak Ridge National Laboratory, July 1992.
- 4) Ganesan S. and Muir D. W.: "FENDL Multigroup Libraries," IAEA-NDS-129, International Atomic Energy Agency, July 1992.
- 5) Konno C., et al.: "Bulk Shielding Experiments for ITER/EDA R&D (I) Large SS316 Assemblies," To be published in JAERI-M report.
- 6) Konno C., et al.: "Bulk Shielding Experiments for ITER/EDA R&D (II) Large SS316/water Assembly," To be published in JAERI-M report.
- 7) Maki K., et al.: "Nuclear Group Constant Set FUSION-J3 for Fusion Reactor Calculation Based on JENDL-3," JAERI-M 91-072 (April 1991) (In Japanese).
- 8) Kosako K. Oyama Y., Maekawa H.: "FSXLIB-J3: MCNP Continuous Energy Cross Section Library Based on JENDL-3, JAERI-M 91-187 (Oct. 1991).

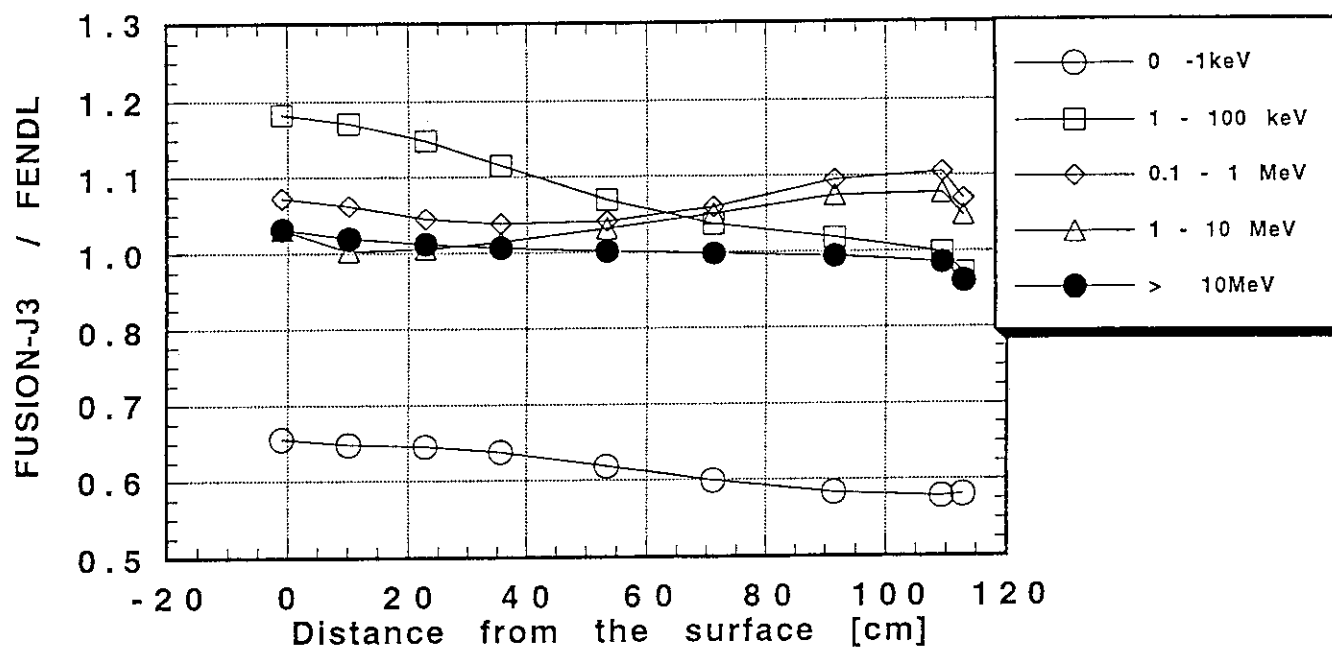


Fig. 1.6.1 Ratio of integrated neutron fluxes calculated with JENDL and FENDL libraries for Assembly SUS#2.

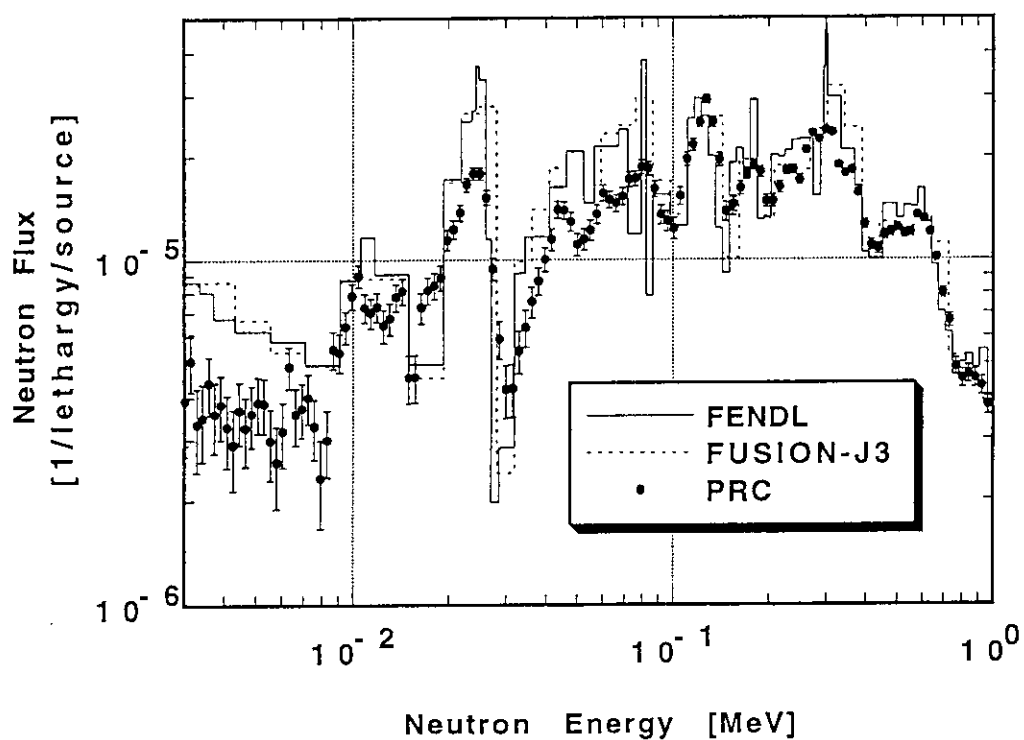


Fig. 1.6.2 Comparison of Calculated Spectra with those measured by proton-recoil proportional counters (36 cm depth in Assembly SUS#2).

2. Theoretical Method and Code Development

A validation work of a 3-D transport code based on the double finite element method was carried out. The results of benchmark calculations showed validity of the method. Further effort is concentrated on economizing the use of computer resources.

Development of vectorized Monte Carlo codes for general use: GMVP working with group cross sections, and MVP working with continuous energy ones has been continued. These codes achieve a higher computation speed by a factor of 10-20 for neutron transport problems compared with the conventional scalar codes. Solution of coupled neutron-photon problems became available. The execution of a demonstration problem by MVP shows a computation speed higher by a factor of 27 compared with the MCNP code. To demonstrate the performance of these codes, two analyses were carried out. One is related to the neutronics design of space reactor where rotating control drums embedded in the radial reflector are used. To validate the reactivity worth calculation based on an R-Z model, which has been conventionally adopted in conceptual design work, whole core calculations with 3-D realistic geometry were performed by the GMVP module. Results show that the R-Z model overestimates the reactivity worth of control drums by about 20 %. The other is also the whole core calculations for a commercial size PWR. The geometry of core was precisely represented in a pin-by-pin model by using the rectangular multiple lattice capability. A run with one million neutron histories gave the variance of 0.03 - 0.05% for k_{eff} and that of about 2% for assembly power with the computation time of 14 minutes by the FACOM VP2600.

Successive effort has been devoted to develop the Intelligent Reactor Design System (IRDS) which will serve for feasibility study and pre-conceptual design of new type reactor. A flow of design process by IRDS was executed on a SUN workstation. The frame structure of Design Model was modified to cover the thermal-hydraulics field. The design information of 17 reactors in operation or under planning was compiled in Design Data Base with the same frame structure of Design Model. It will serve to construct user's design concept. Design Task is driven by selecting window menu. All input data for simulation module is automatically prepared by taking numerical data from Design Model. Simulation calculation is executed on a workstation with simplified models. Visualization of output data is available by a graphical user interface. Thus, a prototype of IRDS has been realized.

(Keichiro Tsuchihashi)

2.1 Benchmark Calculations for a Three-dimensional Transport Code Based on the Double Finite Element Method

T. Fujimura

A neutron transport code DFEM has been developed for multilateral prism geometry¹⁾ and the benchmark calculations have been performed for its validation. The results are given in comparison with those of other solution methods.

A double finite element method is used as the solution algorithm, in which the space and angle finite elements are employed. To simplify the fine mesh calculations, linear basis functions are applied to the spatial variable and step functions to the angular variables. The treatment of the angular variables is somewhat different from that of the S_n method¹⁾ and it is referred to as an F_n approximation. In addition, a remedial scheme has been incorporated to avoid the truncation errors at reflective boundaries.

Ray effect problem

Since we used an S_n -like method, the ray effect is first examined. Figure 2.1.1 shows a well-known problem given by Lathrop²⁾. The one-group, P_0 , fixed source problem in x-y geometry was solved by applying reflective conditions to the bottom and top boundaries. The scalar flux along the line $y=1.875\text{cm}$ is compared with TWOTRAN-II³⁾. Briggs, et al. discussed the ray effect mitigation by their S_n -like finite element method²⁾, and they stated that their method mitigated the ray effects, though their flux deviates considerably from the S_n results. On the contrary, in the present results overall shape of the scalar flux agrees well with the S_n ones, while the mitigation was very little as seen in Fig. 2.1.2.

Small LWR problem

In order to compare the present method with other ones, we adopt the small LWR problem in NEACRP benchmarks proposed by Takeda, et al.⁴⁾. In this problem, the control rod is withdrawn (void), and is inserted in Cases 1 and 2, respectively. Table 2.1.1 shows the results of k_{eff} and control rod worth obtained by various three-dimensional codes⁴⁾. They are the extrapolated values to zero mesh intervals. In general, the angular mesh effect is significant in void region and the spatial mesh effect is significant in control rod region. This tendency is also seen clearly in the DFEM, F_2 , Case 1 and F_4 , Case 2 results. Difference in

the latter case comes mainly from the insufficient extrapolation.

As for the comparison of the fluxes along the line across the control rod position⁴⁾ in Case 2, the effect of angular mesh is not so significant, but the F_2 fluxes of both energy groups around the core center is larger than those of other methods. This means that the F_2 calculation is insufficient even with fine spatial mesh as is clearly seen in the ray effect problem. On the contrary, the F_4 calculation greatly improved the flux shape even with coarser spatial mesh.

The present method has been validated through the benchmark calculations. Main subjects to be studied further are the improvements of the management of coefficient matrices and the acceleration of convergences.

References

- 1) Fujimura T.: Proc. of the Seminar on Software Development in Nuclear Energy Research, JAERI-M 85-017 (1984) (in Japanese).
- 2) Briggs L. L., et al.: Nucl. Sci. Eng., **57**, 205 (1975).
- 3) Lathrop K. D. and Brinkley F. W.: LA-4848-MS (1973).
- 4) Takeda T. and Ikeda H.: J. Nucl. Sci. Technol., **28**, 656 (1991).

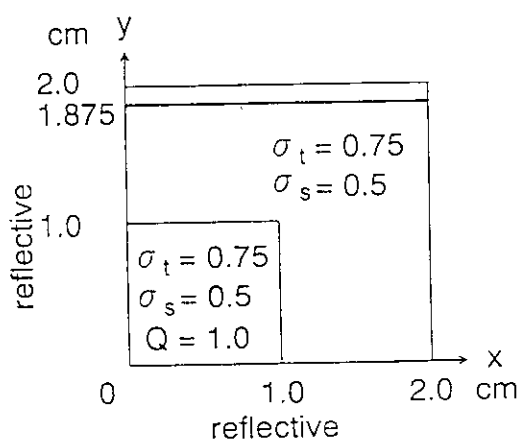


Fig. 2.1.1 Illustration of ray effect problem.

(The flux is plotted along the bold line.)

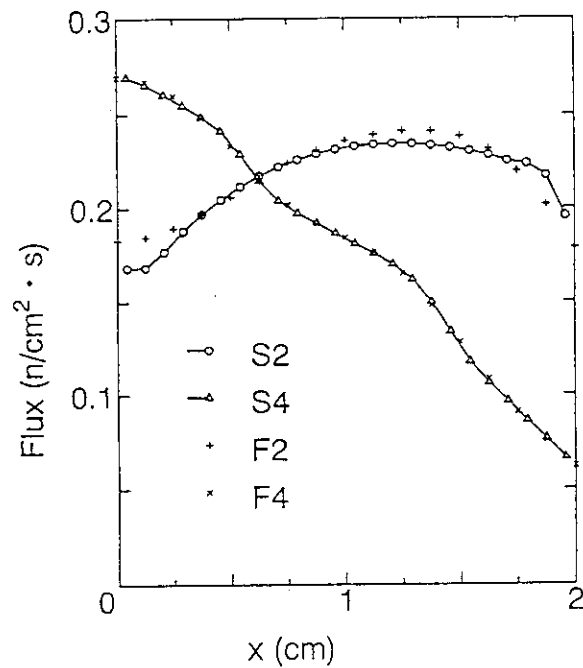


Fig. 2.1.2. Comparison of fluxes in ray effect problem at $y=1.875$ cm.

"SN" means the 24×24 spatial mesh, S_n results by TWOTRAN-II and "FN" means the $(16 \times 16 \times 1)$ element, F_n results by DFEM.

Table 2.1.1 Comparison of k_{eff} 's of a small LWR problem⁴⁾

Method	Case 1	Case 2	CR-worth
Monte Carlo	0.9778	0.9624	1.64E-2
P_n	0.9766	0.9630	1.45E-2
S_n	0.9772	0.9623	1.58E-2
DFEM F_2	0.9763 (-0.15)*	0.9626 (0.02)	1.46E-2 (-10.98)
DFEM F_4	0.9772 (-0.06)	0.9639 (0.16)	1.41E-2 (-14.02)

* The numbers in parentheses are the percent differences from the Monte Carlo method.

2.2 Development of Coupled Neutron-photon Module for Vectorized Continuous Energy Monte Carlo Code

T. Mori, M. Nakagawa and M. Sasaki*

Development of a vectorized continuous energy Monte Carlo code MVP¹⁾ has been continued. This code achieved a higher computation speed by a factor of 10-20 for neutron transport problems compared with conventional scalar codes. In the present work, a new module to analyze coupled neutron-photon transport problems has been developed to extend its applicability to shielding calculations.

The new module includes two calculation tasks: (1) generation of secondary photons from neutron-induced reactions and (2) collision analysis of photon reactions. The first task is a part of collision analysis of neutron reactions, of which the calculation flow is shown in Fig. 2.2.1. This figure shows the flow of neutrons queued in the neutron collision stack and a temporary substack for photon-producing neutrons. Each subtask indicated by double boxes is simultaneously processed for many neutrons queued in the stack, which can be efficiently vectorized. The second task is carried out based on the two models: a simple model applicable to high energy photons and a general detailed model, both of which are similar to those in MCNP 3A²⁾. These models have been vectorized on the basis of the event-based algorithm, and installed into MVP.

In order to increase the vectorization efficiency, the following techniques are adopted:

- (1) Spatial tracking of photons and neutrons is simultaneously carried out since the same tracking algorithm can be applicable to both particles.
- (2) The collision analysis of photons is separated from the other tasks, and is treated as an independent task which has its own stack.
- (3) Secondary photons are generated during the collision analysis of neutrons.

As a result of the present implement, the basic calculation tasks of MVP becomes the following seven ones: "Source generation", "Flight analysis", "Next zone search", "Lattice treatment", "Reflection treatment", "Collision analysis of neutrons" and "Collision analysis of

*Japan Research Institute, Ltd., Tokyo

photons".

To evaluate performance of the present module, we solved a neutron-photon coupled problem in an iron cylinder of 20 cm radius and 20 cm thickness into which 14 MeV mono-directional neutrons enter. The result and the performance of MVP are compared with those of MCNP in Table 2.2.1. The MVP code achieved a vectorization ratio of 99 % and a computation speed higher by a factor of about 27 compared with the MCNP code.

References

- 1) Mori T., Nakagawa M. and Sasaki M.: J. Nucl. Sci. Technol. 29, 325 (1992).
- 2) Briesmeister J.F.(ed.): LA-7396 M, Rev. 2 (1986).

Table 2.2.1 Comparison of performance between MVP and MCNP

	MVP ¹⁾	MCNP
CPU/source-neutron(μ s)	87.6	1726.7
No. of generated photons/source-neutron	3.7	2.6
Total weight of generated photon	4.85	4.82
CPU/track (μ s) ²⁾	2.58	69.0
Ratio of computation speed	26.7	1.0
Vectorization ratio (%)	99	----

1) 5000 neutron/batch, size of particle bank=13,000

2) No. of tracks = No. of collision and boundary crossing events

PHOTON PRODUCTION (P. P.)

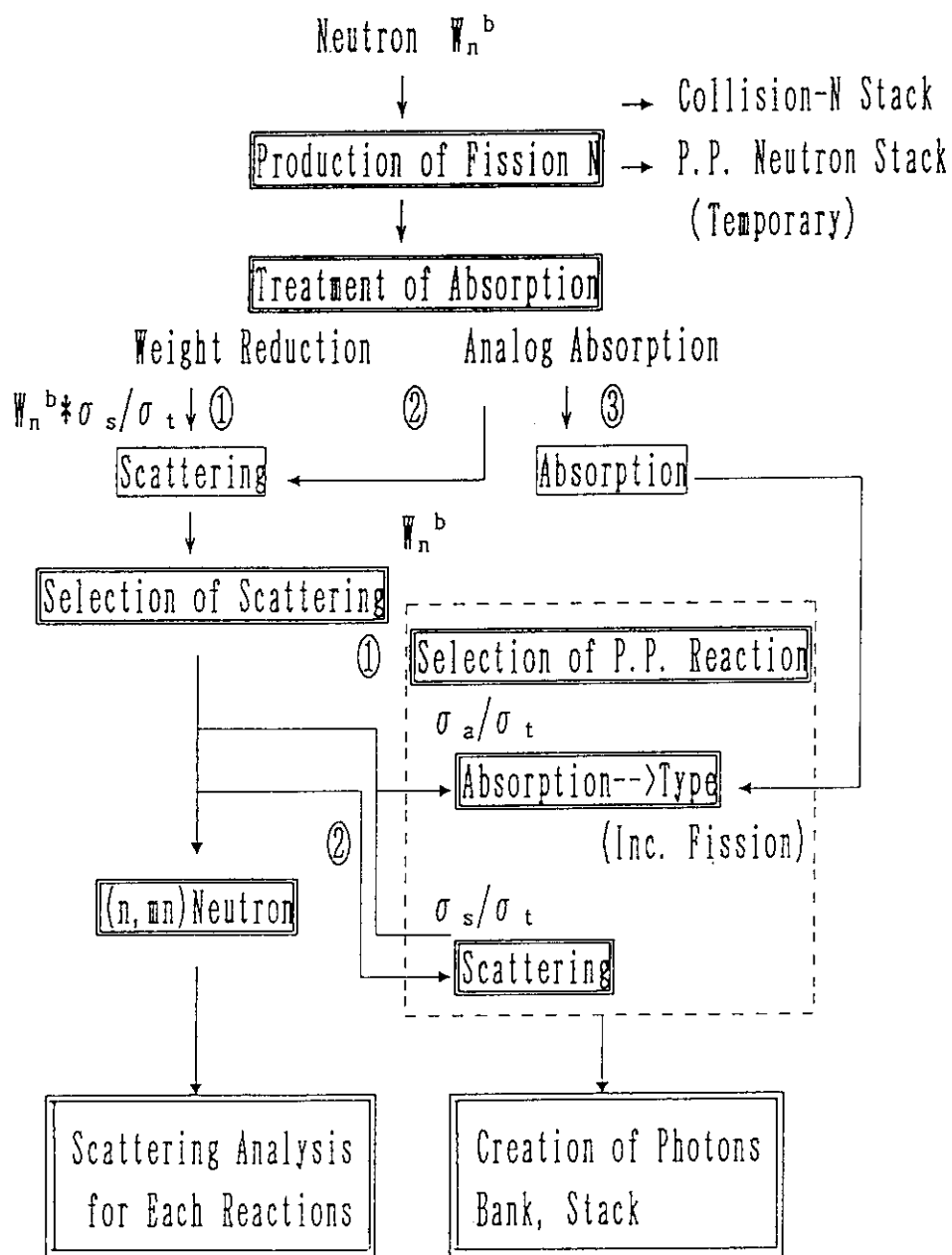


Fig. 2.2.1 Calculation flow of collision analysis of neutrons by which secondary photons are generated

2.3 Reactivity Worth Calculations of Rotating Control Drums for Space Reactors

T. Mori and K. Tsuchihashi

Several conceptual design studies of space reactors have planned to use rotating control drums as a reactivity control device.¹⁾ In the present work, the accuracy of reactivity worth calculation based on an R-Z model, which has been conventionally adopted in conceptual design work, has been studied by comparison with 3-D Monte Carlo calculations.

As a reference reactor, we selected a reactor consisting of a homogeneous core of 54.5 cm height and 28 cm radius with upper and lower BeO reflectors of 20 cm thickness, radial thermal shield and a radial BeO reflector where 12 control drums are located, as shown in Fig. 2.3.1. A reference model for 3-D Monte Carlo calculation precisely takes into account this geometry. In an R-Z model, two extreme cases, where all B_4C absorbers in control drums are directed outward or inward, are modelled by smearing B_4C absorbers into a part of BeO radial reflector region of 3 cm thickness or 2.44 cm thickness, respectively. Smeared region volumes are the same between the two cases.

The 3-D Monte Carlo calculations were carried out by using the GMVP vectorized Monte Carlo code²⁾, and the 2-D R-Z calculations were performed with the GMVP code (transport, Monte Carlo), the TWOTRAN-II code (transport, P_0S_8 approximation) and the CITATION code (diffusion). The cross sections of 15 energy groups (thermal: 5 groups, fast: 10 groups) produced by the SRAC system³⁾ were commonly used by all the codes.

Figure 2.3.2 shows the variation of relative reactivity worth with the change of B_4C absorber direction calculated by the 3-D model. From this figure, it can be seen that there is no significant difference between the cases with 12 and 18 control drums, and that both results show typical "S" curves. Accordingly, we can say that it is possible to estimate roughly reactivity worth of control drums in any direction by interpolating those in outward and inward directions which can be obtained by the 2-D R-Z calculations. The results of 3-D and 2-D R-Z calculations are summarized in Table 2.3.1. The R-Z calculation underestimates the k_{eff} values in all cases, especially in the cases with inward-directed control drums. As a result, reactivity worth of control drums is over estimated by 17 % and 25 % by the R-Z transport and diffusion calculations, respectively.

References

- 1) for example, H. Yasuda et.al.: JAERI-M 90-149, p.85 (1990).
- 2) Nakagawa M., Mori T. and Sasaki M.: Nucl. Sci. Eng., 107, 58 (1991).
- 3) Tsuchihashi K. et. al.: JAERI 1302 (1986).

Table 2.3.1 Comparison of the results (case of 12 control drums)

Absorber direction	Effective multiplication factor and reactivity worth (deviation from reference solution by GMVP ¹⁾ (%))			
	CITATION	R-Z Model TWOTRAN	GMVP	Reference Model GMVP
keff outward	1.0349	1.0400	1.0389±0.04% ²⁾	1.0422±0.04%
	(-0.70)	(-0.21)	(-0.32)	(0.0)
inward	0.9846	0.9917	0.9915±0.04%	1.0011±0.04%
	(-1.60)	(-0.94)	(-0.96)	(0.0)
Reactivity worth (%Δk/k')	-0.0494 (25.)	-0.0468 (19.)	-0.0460±1.2% (17.)	-0.394±1.3% (0.)

1) Calculation by GMVP with 2,000,000 histories, which used CPU time of 3~4 m. on VP-2600 supercomputer.

2) 1 standard deviation

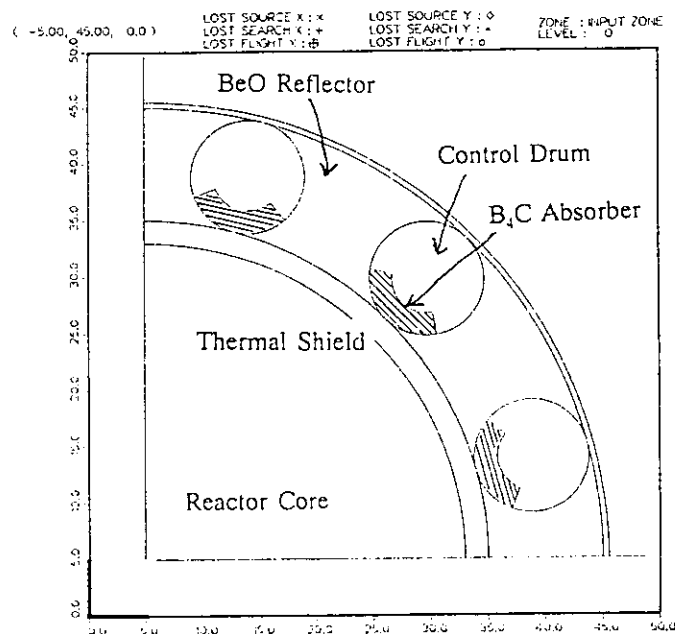


Fig. 2.3.1 Cross sectional view of reference core with 12 control drums

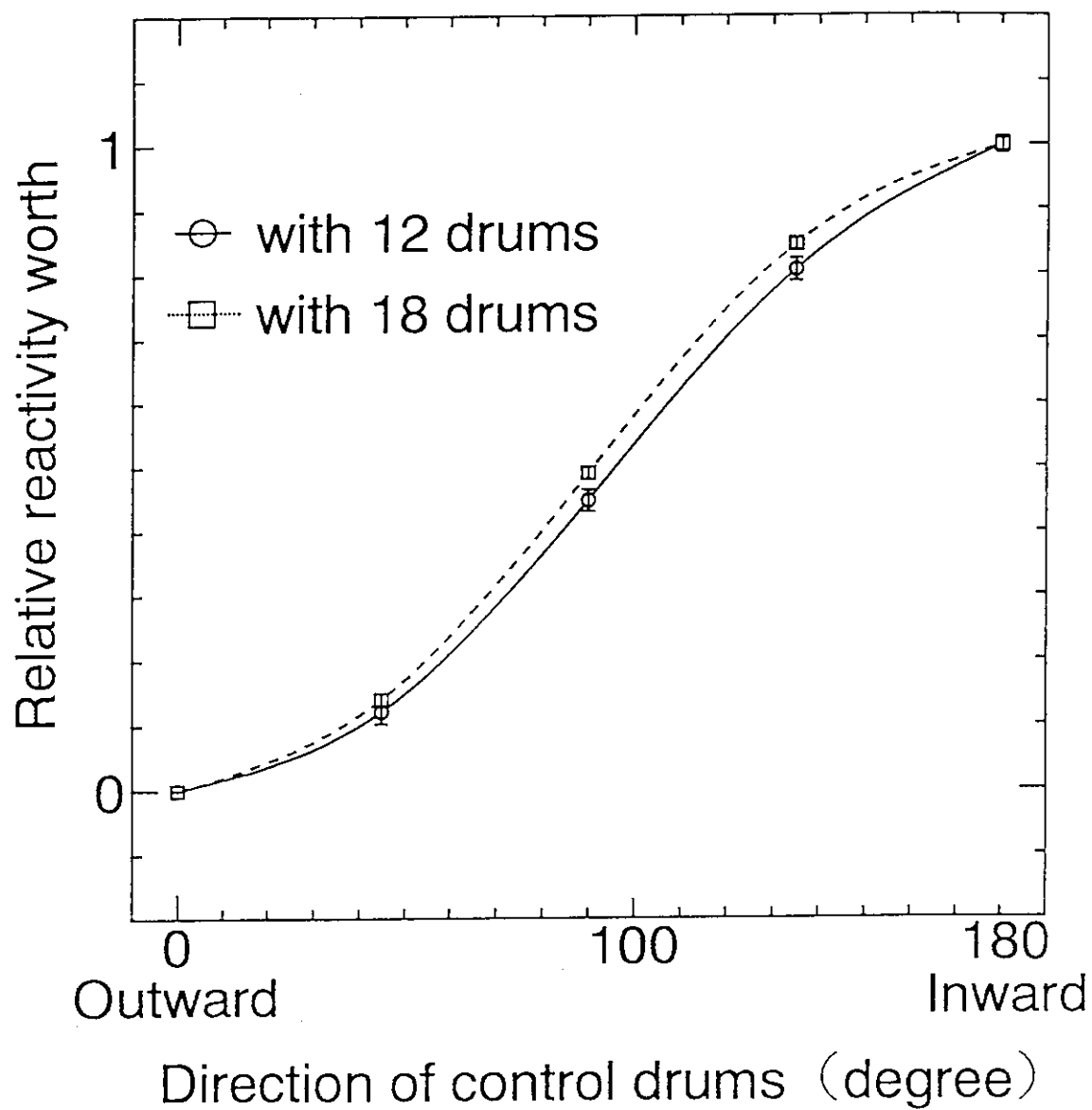


Fig. 2.3.2 Relative reactivity worth of control drums

2.4 Whole Core Calculations of PWR by Monte Carlo Techniques

Masayuki Nakagawa and Takamasa Mori

Whole core calculations have been performed for a commercial size PWR by using vectorized Monte Carlo codes¹⁾. The calculated parameters were k_{eff} , control rod worth, power distribution and so on. Monte Carlo calculations were carried out by the use of the vectorized codes, GMVP²⁾ for the multigroup model and MVP³⁾ for the continuous energy one. The geometry of core was precisely represented in a pin by pin model by using the rectangular multiple lattice capability which can reduce the work required for input data preparation and also computation time by a factor of about two.

The nuclear data used is JENDL-3. MVP uses its own nuclear data library, which includes pointwise cross sections and tables or functions for sampling secondary energy and angle. The unresolved resonance region is treated by the probability table method. The SRAC system⁴⁾ was used to generate four group cross sections for each material by collapsing from the 107 group structure. We modeled a core used in a commercial type four loop 1160 MWe reactor. Temperatures of core constituents correspond to those at the full power stage. The core at the beginning of cycle consists of 2.1, 2.6 and 3.1% enriched ^{235}U fuel assemblies. The reactor core including the core barrel is modeled as precisely as possible. The total numbers of fuel assemblies and fuel pins are 193 and 55777, respectively. Each assembly has 24 control rod channels and a channel for a detector. As chemical shim, boric acid is diluted into water except for control rod channels. A nearly critical core was realized with 2,000 ppm natural boron content.

The eigenvalues of the critical and the control rod inserted cores were calculated. The results are shown in Table 2.4.1. The number of neutron histories is one million for all the cases. The batch size (the number of histories per batch) is 10000 for all the cases. The variances (1σ) of k_{eff} values are 0.04 – 0.05% by the continuous energy model and ~0.03% for the four group model. The latter method gives smaller variances though the same number of histories were tracked. In any case, the variance is small enough. The variances of control rod worths are 3 – 4% where the absolute value of worth is $1.58\% \Delta k/k'$.

The four group model gives smaller eigenvalues for all the cores compared with those

by the continuous energy model. At the critical core, the difference is $0.6\% \Delta k$. Considerable parts of this difference arise in the fine group (107 groups) cell calculation stage. The control rod worth is also underestimated by this method, but the difference is almost within the statistical error. The power distributions of assembly and fuel pin are compared in Table 2.4.2. These values are shown for radial direction from the center to the right boundary. Pin power was calculated for a single pin within each assembly. The variance of assembly power is within 2% while that of pin power ranges 7 ~ 12%. The differences between two models are given in relative values to the continuous energy model. The assembly powers calculated by two models agree within about 2σ uncertainty with each other. The pin power shows still large differences up to ~10% due to large variances but these differences are almost within 1σ uncertainty.

The computation time consumed by the continuous energy model is 14 min (without cross section tally) for 1 million histories and larger by a factor of 2 compared with that by the few group model. The speedup by vectorization (cpu time ratio of scalar calculation to vector one) is a factor of 12 ~ 14 in the present runs. This factor is similar between the continuous energy and the few group models. If we assume target design accuracies for k_{eff} , assembly and pin powers, and CR worth as 0.1, 1, 2 and 2%, respectively, those can be achieved within one hour computation except for pin power, for which higher computation speed, about 10 times, is desired. If a core configuration becomes complex, for example, a core consisting of mixed MOX and UO_2 fuel assemblies, accurate prediction of pin power distribution would be more difficult. The Monte Carlo method would be a powerful tool in such a case.

References

- 1) Nakagawa M., Mori T.: Joint Int. Conf. on Mathematical Methods and Supercomputing in Nuclear Applications, 702-713(1993)
- 2) *idem* : Nucl. Sci. Eng., 107, 58(1991)
- 3) Mori T., Nakagawa M., Sasaki M.: J. Nucl. Sci. Technol., 29, 325(1992)
- 4) Tsuchihashi K. et al.: "Revised SRAC Code System", JAERI-1302(1986)

Table 2.4.1 k_{eff} and Reactivity Worth of PWR

	BOC Reference	Critical core 2000 ppm boron	12 C.R. clusters inserted
4 group model			
k_{eff}	1.2165	0.9930	0.9780
1σ	± 0.00029	± 0.00027	± 0.00034
$\delta k/kk'$		0.185	0.0154
$1\sigma(\%)$		0.20	2.9
Continuous energy model			
k_{eff}	1.2233	1.0008	0.9852
1σ	± 0.00040	± 0.00051	± 0.00047
$\delta k/kk'$		0.182	0.0158
$1\sigma(\%)$		0.33	4.4

Table 2.4.2 Radial Power Distribution of Fuel Assembly and Pin in PWR (10^{-5})^a

Assembly	F21	F26	F21	F26	F21	F26	F21	F31
Assembly power								
4 group model	260	290	250	272	224	237	181	135
Continuous energy model	263	302	260	283	237	241	179	131
Differences (%)	-1.1	-4	-4	-4	-5.5	-1.7	1.1	3.1
Pin power								
4 group model	1.06	1.18	1.04	1.10	0.883	0.992	0.703	0.553
Continuous energy model	0.962	1.24	1.08	1.09	0.951	0.908	0.790	0.502
Differences (%)	10	-5	-4	1	-7	9	-11	10

^a F21, F26 and F31 show the assemblies with 2.1%, 2.6% and 3.1% enriched fuel, respectively. These are located in the order from the center to the outer of core.

2.5 Development of Intelligent Reactor Design System IRDS (4)

- Integration of Design Process on Engineering Workstation -

T. Kugo, K. Tsuchihashi, M. Nakagawa and T. Mori

The development of Intelligent Reactor Design System(IRDS) has been continued following to the system design¹⁾ done in the FY 1989. The objective of the system is to support conceptual design of a reactor core which covers neutronics and thermal-hydraulics fields. In the FY 1992, IRDS integrates the design steps of pre- and post-processing, and execution of analysis on the Sun workstation using Sun View window system. The progress of the development of IRDS is described below.

Design Information Management

One of the goals of IRDS is to be an integrated system to cover the technological fields including neutronics and thermal-hydraulics. For this purpose, information is unified in *design model* and the information transfer between fields is carried out through *design model*. The structure of *design model* was designed using frame representation for the neutronics field²⁾. In the FY 1992, to cover the thermal-hydraulics field, frame items for information on plenum gas and grid spacer were added.

To reduce the effort to construct user's design concept, design information on 17 reactors in operation and under planning, are compiled in Design Data Base(DDB) to provide reference data. An interactive man-machine interface was developed to construct new design concepts by modifying the reference data. As a role of the man-machine interface, it is important to reflect directly user's design concepts imaged in his mind as much as possible. For this purpose, Graphical User Interface(GUI) are used. And a material database was implemented to provides the nuclides composition depending on temperature and pressure of constituent materials. The use of GUI allows a user to easily specify the arrangement information of core components. An example of GUI is shown in Fig. 2.5.1 where a prototype FBR core arrangement is displayed. A user can specify a position of an interesting assembly by clicking a mouse on the display.

System Drive

Design task is driven by selecting window menu with a mouse. Selection of simulation module and geometrical modelling is automatized by IF THEN rules in taking account of task requirement and reactor type.

All input data for simulation is automatically prepared by taking numerical data from *design model* and filling defaulted values in remaining data. The input data prepared automatically can be changed through menu windows or a text editor, if necessary.

Output data is processed for graphic display to show the results of parametric survey calculations under the optimization process. A user can selectively display the results of two interesting parameters by selecting them among important one.

Implementation using X-Windows System

IRDS has been developed based on Sun View windows. However, considering the trend which X-Windows is adopted as a standard platform for UNIX system, we decided to change a platform from Sun View windows to X-windows. In the FY 1992, the subsystem developed for the thermal-hydraulics analysis³⁾ which is implemented in IRDS, was rewritten using X-Windows. In the FY 1993, IRDS will be totally rewritten using X-Windows. This subsystem supports execution of analysis and pre- and post-processing using interactive man-machine interface with menu windows and GUI. In the X-windows version, sub-channel analysis module, COBRA/HCLWR, becomes available in addition to unit channel analysis modules. The system is useful for parametric survey calculation and an automatic search of design window in which design is feasible⁴⁾. An example of GUI of X-windows version is shown in Fig.2.5.2 where a subchannel model is specified for a PWR assembly.

References

- 1) Tsuchihashi K., et al.: "Development of Intellectual Reactor Design System :IRDS," JAERI-M 90-177(1990)(in Japanese).
- 2) Kugo T. and Tsuchihashi K.: Reactor Eng. Dep. Annual Report, 19, JAERI-M 92-125.
- 3) Nakagawa M., et al.: Reactor Eng. Dep. Annual Report, 29, JAERI-M 91-138.
- 4) Nakagawa M., et al.: J. Nucl. Sci. Technol., **29**[11], 1116, (1992).

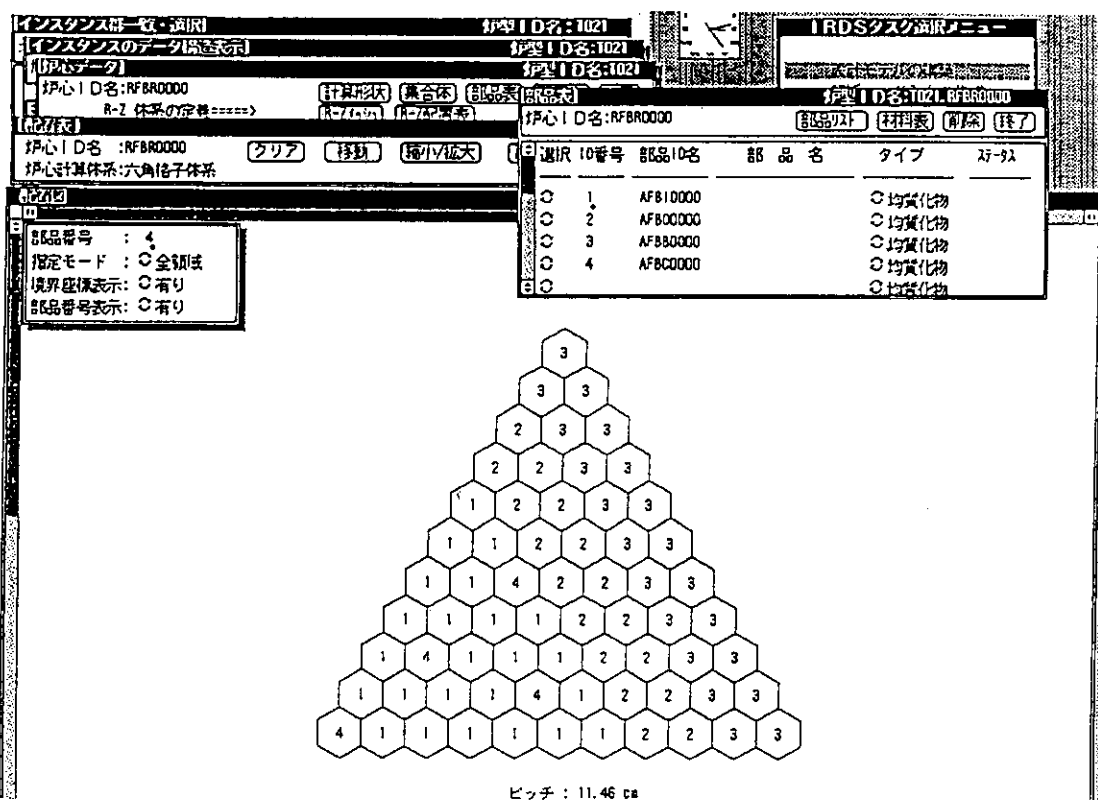


Fig. 2.5.1 A graphic display used to specify core arrangement of a FBR core

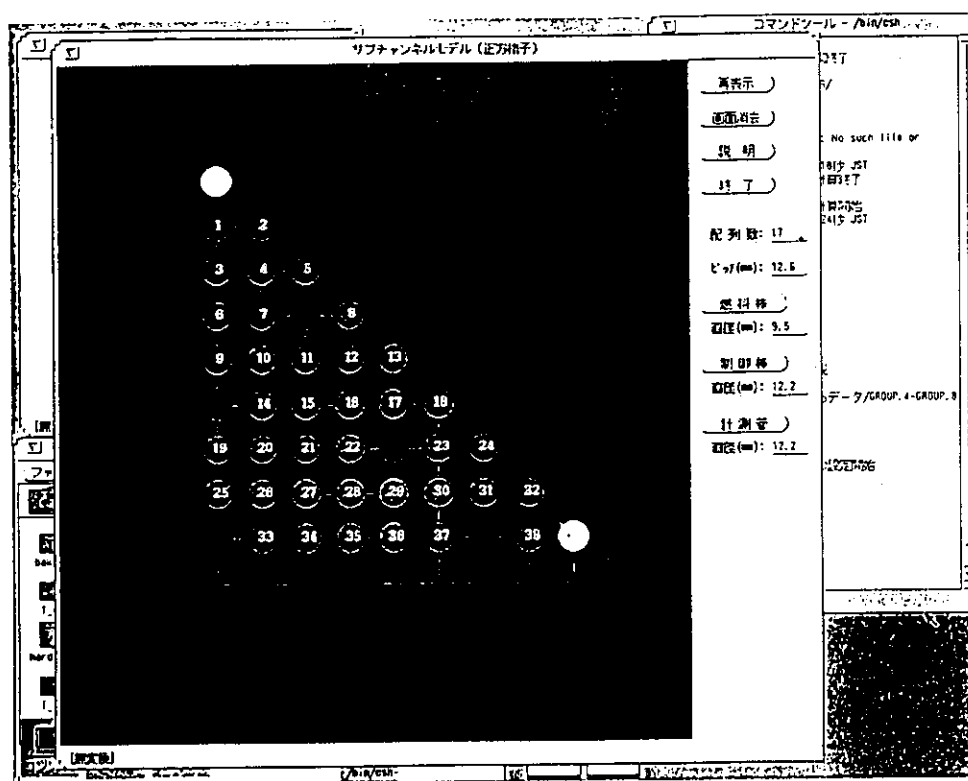


Fig. 2.5.2 A graphic display used to specify subchannel model under X-Windows

3. Reactor Physics Experiment and Analysis

The Fast Critical Facility (FCA) and the Very High Temperature Reactor Critical Assembly (VHTRC) were used to perform several fast reactor physics and high temperature gas cooled reactor physics experiments.

Experimental measurements were performed on metallic fueled LMFBR mockup assemblies FCA XVI-1 and -2. The calculation based JENDL-2 data agreed well with the criticality, sodium void worth and reaction rate ratio measurements. The calculated Doppler reactivity worth, however, tends to underestimate the measured worth. The effective delayed neutron fraction was measured using Cf-252 source technique. The calculated fraction was found to overestimate the experimental value by about 8%.

Experimental measurements performed on mixed oxide fueled LMFBR mockup assemblies FCA XII-1 and -2 included the direct measurement of U-238 capture to fission ratio by gamma ray spectroscopy of the fuel plate itself, which was shown to provide a very clean way to obtain cell average capture to fission ratios. Comparison of measured and calculated Mn-55 capture rate distributions showed that a well defined cell averaged cross section treatment is required even for structural material such as Mn-55. The high temperature U-238 Doppler effect was measured by sample reactivity method up to 1500 C and by foil activation method up to 2000 C.

An improved analysis method for treating the Doppler reactivity contribution of the resonance interactions between the hot sample and cold core was demonstrated using the collision probability code PEACO-X for the Doppler effect of the various FCA assemblies

Experimental measurements performed on VHTRC-4 core for the High Temperature Engineering Test Reactor (HTTR) included the reactivity worth of multiple burnable poison rods and ten simulated water ingress configurations. The more detailed HTTR mockup assembly VHTRC-6 was used to demonstrate the measurement of axial power distributions and U-238 capture to Pu-239 fission reaction rates by direct gamma ray spectroscopy of fuel pins. The good agreement between measurements and calculations for all of these experiments support the fundamental design of the HTTR.

Changing from sodium to lead coolant in LMFBRs is attractive because of a negative void reactivity, an almost zero burnup reactivity swing, additional shielding, and a coolant that is not chemically active with water. Various analysis methods were compared for the BFS-61 critical assembly, which was a Russian mockup of a lead cooled 700 MW thermal reactor concept. Using the JENDL-3 data library, the effective multiplication factor was underestimated by about 2% using homogeneous SRAC models, while MVP, CITATION, and SRAC calculations using a more detailed model showed generally good agreement with experiment and with Russian calculations using RECOL and MCNP-4. Comparison of the elastic scattering cross section for lead in different cross section libraries showed some differences in the important energy range around 100 eV.

Studies on the utilization of Th/U-233 fuel in thermal reactors were extended from conventional light water reactors to graphite and heavy water moderated reactors because of the potential for better neutron economy. This study indicated that the graphite moderated Th/U-233 reactor with very high burnup and small U-233 inventory should be coupled with a heavy water moderated U-233 production reactor with a conversion ratio greater than 1.0.

(Takehiko Mukaiyama)

3.1 Mock-up Experiments of Metallic-fueled LMFBR in FCA Assembly XVI-2

S. Iijima, H. Oigawa, and M. Bando*

An availability of data and method for a design of metallic-fueled LMFBR was examined in the mock-up experiments at FCA. Two kind of mock-up cores were constructed in the experimental program. The first core named FCA assembly XVI-1^{(1),(2)} was a full-scale mock-up core referred to 150 MWe metallic-fueled LMFBR. Nuclear characteristics related to fuel expansion and fuel shifting reactivities were measured at the boundary between the core and the radial blanket as a significant reactivity feed back parameter in a core design of metallic-fueled core. In addition to these characteristics, typical nuclear characteristics such as sodium void, Doppler and control rod worth and power distribution were measured. Because of shortage of plutonium inventory, fuel with a combination of plutonium and enriched uranium was used at the whole core. Since there was some difference of adjoint flux between the combination core and a plutonium core, the experiments of assembly XVI-2 were made to focus on the effects caused by the difference of fissile materials.

XVI-2 was a zone-type partial mock-up core and consist of a test region fueled by plutonium and a driver region fueled by a combination of enriched uranium and plutonium. A cross-sectional view of assembly XVI-2 is shown in Fig. 3.1.1 and its rz model is presented in Fig. 3.1.2. A cylindrical test region (IC in Fig. 3.1.1) is surrounded radially by a driver region (OC1 and OC2 in Fig. 3.1.1). The diameter of the test region is ~ 69 cm, and the core height is ~ 91 cm. The IC drawer consists of the core cells and the natural uranium block. The plate arrangements of the core cell are shown in Fig. 3.1.3. Plutonium enrichment of the core cell is 10.5wt%.

Beside the typical measurements of criticality, reaction rate ratios, reaction rate distributions, material sample worth and control rod worth, reactivity feed back parameters such as sodium void, Doppler and axial fuel expansion were measured at the test region. The ^{238}U -capture-to- ^{239}Pu -fission ratios was measured with the foil irradiation method at the core center. Doppler reactivity was measured with a natural uranium metallic sample (25mm diameter and 150mm length). Sodium void worths for a step and channel void were measured at central 3×3 drawers (9.32cm in equivalent radius) of the test region.

The experiments were analyzed with JENDL-2 cross section library and the JAERI's standard calculation system for fast reactor neutronics. The availability of data and method was examined systematically by using the results of assembly XVI-1 and XVI-2.

* HITACHI Ltd.

References

- 1) Iijima S. et al.: " Benchmark Physics Experiment of Metallic-Fueled LMFBR at FCA", Proc. of ANS Topical Meeting on Advances in Reactor Physics, 2-92. March 8-11, 1992, Charleston, S.C. (1992).
- 2) Iijima S. et al.: " Benchmark Physics Experiment of Metallic-Fueled LMFBR at FCA - Core Design of FCA Assembly XVI-1 and Criticality -. JAERI-M 92-196 (1992). (in Japanese).

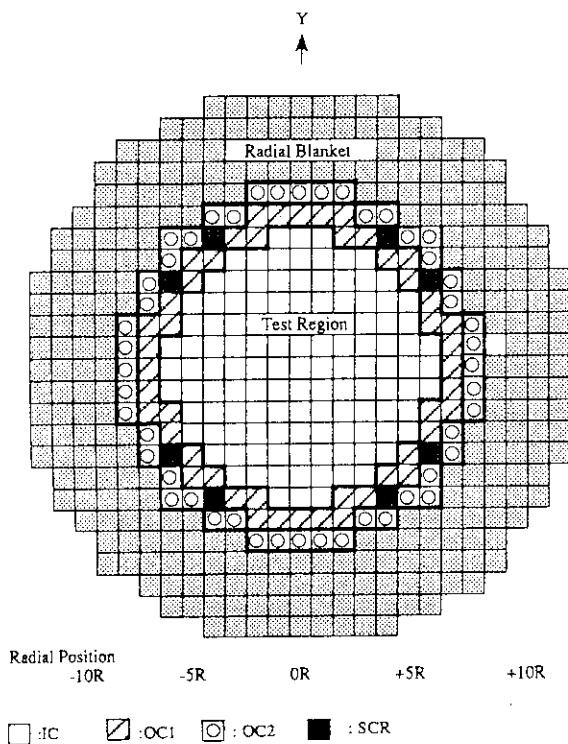


Fig. 3.1.1 Cross-sectional view of FCA assembly XVI-2

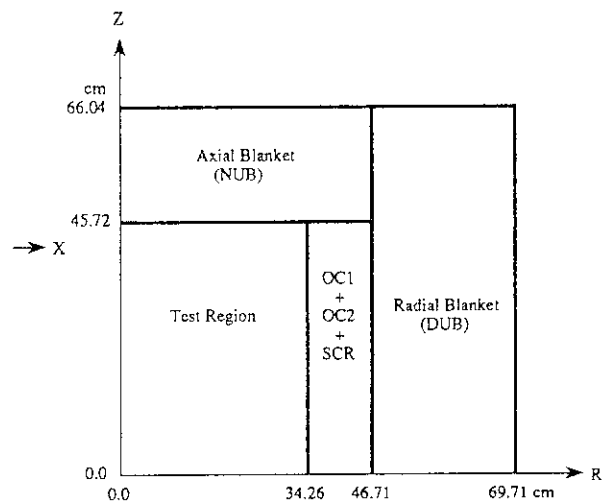


Fig. 3.1.2 RZ model of FCA assembly XVI-2

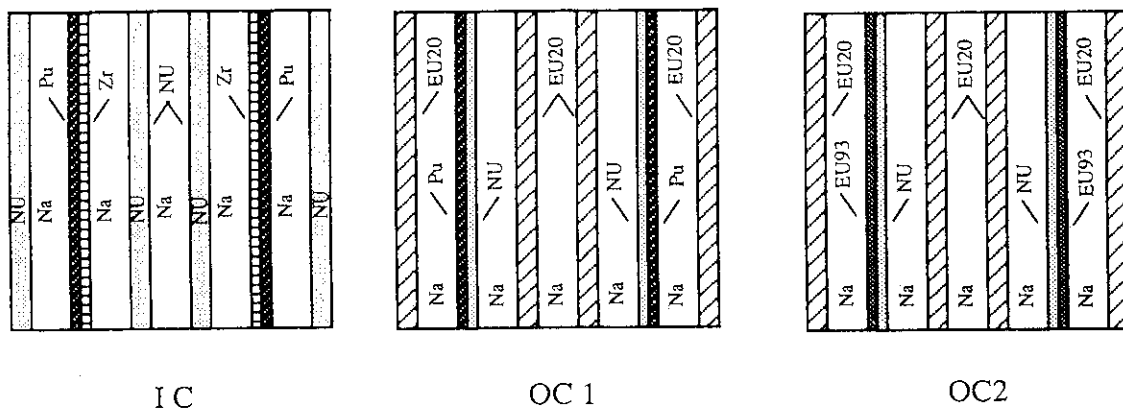


Fig. 3.1.3 Typical unit cell used in FCA assembly XVI-2

3.2 Measurement of Capture to Fission Ratio (C8/F) by γ -ray Spectroscopy of Fuel Plate in FCA Assembly XVII-1

A. Ohno, K. Hayasaka, K. Satoh, H. Sodeyama and T. Osugi

U-238 capture to fission ratio(C8/F) is an important physical parameter for evaluation of the calculation method and data on breeding ratio of a FBR core.

To obtain cell averaged C8/F, γ -ray from a fuel plate was directly measured. This method is more favorable than the measurements using foils or counters because these foreign materials in a core disturb a neutron field. On the other hand, it is necessary to make a large correction for self absorption of γ -ray in a fuel plate, because a plate is much thicker than foils. This becomes major contribution for corrections. Therefore, we selected similar energy γ -ray, namely 278keV γ -ray of Np-239 and 293keV γ -ray of Ce-143, for capture and for fission reactions, respectively, since the correction for similar energy γ -ray is almost cancelled when the ratio is taken.

Prior to irradiation, a background spectrum was measured on each fuel plate in the drawer. Irradiation amount is 240 watt-hours (80 Wx3 h). Count rates of peak areas of interest was obtained by analyzing γ -ray spectrum. In addition to γ -rays mentioned above, γ -rays of 210keV from Np-239 and of 538 keV from Ba-140 were also analyzed to check how accurate is the correction of self-absorption of γ -ray in the fuel plate.

C8/F is obtained as follows;

$$\frac{C8}{F} = \left(\frac{A_c}{A_f} \right) \cdot f_a \cdot f_c \cdot f_b \cdot f_c \cdot Y \cdot B \cdot f_r$$

where

A_c/A_f : ratio of count rates of 278 keV to 293keV γ -ray,

f_a : ratio of correction factors for self-absorption of 278 keV to that of 293 keV γ -ray in fuel plate,

f_c : ratio of correction factors for detection efficiency of 278 keV to that of 293 keV γ -ray inclusive of geometrical arrangement,

f_b : ratio of branching ratios of γ -rays of interest,

f_c : ratio of decay corrections of activity of Np-239 to that of Ce-143 in irradiation,

Y : fission yield of neclide of interest,

B : ratio of decay corrections of activity of Np-239 to that of Ce-143 after irradiation,

f_r : ratio of disintegration constants of Np-239 to that of Ce-143.

Figure 3.2.1 shows measured ratios of capture rate in DUO_2 fuel plate to fission rate in 92%Pu fuel plate, together with the calculated values obtained by the conventional method used in FCA. The calculation agrees with the measurement within experimental errors at the core center, but overestimates by about 8% at the core boundary. The experimental error is evaluated from statistical error of count rate and difference in fission rates obtained using γ -rays of Ce-143 and Ba-140.

For fission reaction rate, the correction factor α was derived using a simple plate model in which gamma source is distributed uniformly. For capture reaction rate, the factor α was derived using a concaved γ -ray source distribution of which center value is smaller by 10% than that at the surface of the DUO_2 fuel plate. Even if this distribution changes by 50%, the factor changes by only about 0.6%. Credibility of the factor α was checked using γ -rays of 210keV from Np-239. Table 3.2.1 shows capture reaction rates obtained from γ -rays of both 210 keV and 278keV and they agree within 1%. For fission reaction, γ -rays of 537 keV from Ba-140 were used in addition to γ -rays of 293 keV from Ce-143. Those values are also shown in Table 3.2.1 and agree within 2.5% for both DUO_2 and 92%Pu fuel plate.

Table 3.2.1 γ -ray self absorption correction factor α and detection efficiency ϵ and reaction rate for each fuel plate.

Fuel plate	γ ray energy	α	ϵ ($\times 10^{-3}$)	Reaction rate
DUO ₂	210keV(Np-239)	$0.1614 \pm 1.2\%$	1.485	$7.000 \times 10^{11} \pm 3.1\%$
	278keV(Np-239)	$0.2890 \pm 0.6\%$	1.262	$1.035 \times 10^{11} \pm 1.6\%$
	293keV(Ce-143)	0.3164	1.204	$1.368 \times 10^{11} \pm 1.8\%$
	537keV(Ba-140)	0.6297	0.716	$1.335 \times 10^{11} \pm 3.5\%$
Pu	293keV(Ce-143)	0.6808	1.204	$1.122 \times 10^{12} \pm 1.4\%$
	537keV(Ba-140)	0.8721	0.716	$1.104 \times 10^{12} \pm 2.6\%$

α : Correction factor of γ -ray self absorption.

ϵ : γ -ray detection efficiency.

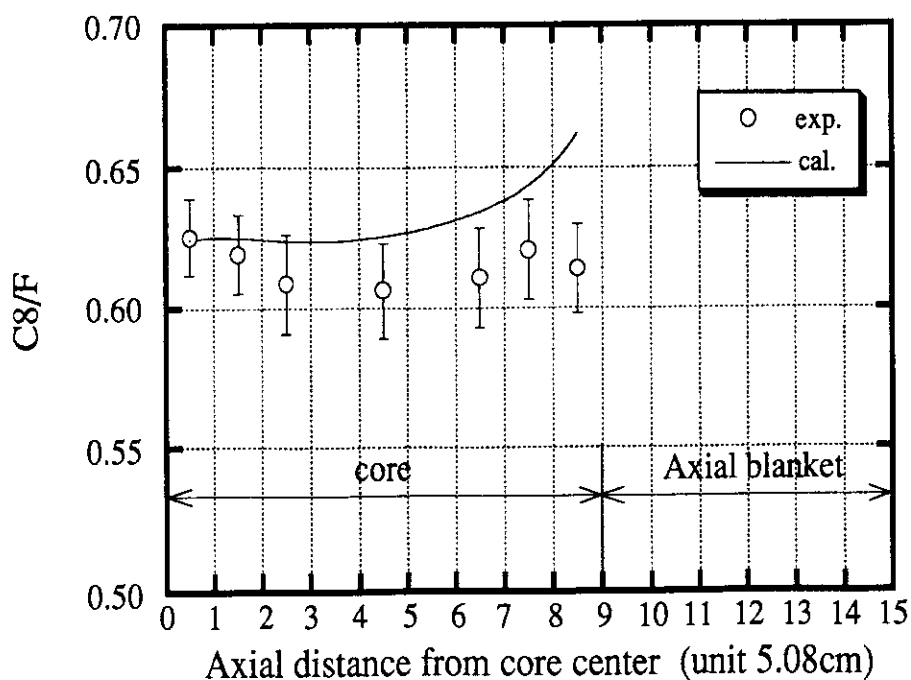


Fig.3.2.1 Measured and calculated C8/F

3.3 Measurement and Analysis of Mn-55 Capture Rate Distribution in FCA Assembly XVII-1

T. Osugi, T. Nemoto, T. Sakurai, A. Ohno and S. Usami*

Capture rate of Mn-55, which has sharp resonance cross-sections around energies of 1.0keV and 100eV, has been measured in FCA assembly XVII-1. The effect of resonance shielding to the reaction rates was examined by comparing the activations of the Mn-55 foils put into the standard and stainless steel(SS) cells. In the SS cell, the central depleted uranium oxide plate of the standard cell was replaced with the SS plate, which has Mn-55 as impurity. The background cross-section of 1.0keV resonance reaction of Mn-55 for the stainless steel plate was estimated to be about 1,800 barn, while that for depleted uranium oxide plate was infinity. The effect of neutron spectrum to the reaction rate was also examined by comparing the reaction rates between the core and blanket cells. Plate configuration and foil position in cells are shown in Fig.3.3.1.

Cell calculations were made by use of the collision probability code SLAROM¹⁾ and 70 group cross-section set JFS-3-J2²⁾ based on evaluated data library JENDL-2³⁾. Figure 3.3.2 shows the relative distribution of Mn-55 capture rate in core cell calculated by one dimensional infinite slab model. The effective microscopic cross-sections of Mn-55 were generated for each plate in cell by use of the background cross-section under isolated lump approximation. The calculated distributions well agree with the measured ones.

Figure 3.3.3 shows the normalized axial distribution of Mn-55 capture rate. The cell averaged cross-sections of the Mn-55 capture rate are calculated taking account of the neutron flux distribution in the cell. The difference in the reaction rates between core and blanket cells is well predicted by the present calculation.

Table 3.3.1 summarizes the SS effect of the Mn-55 capture rate in the core and blanket regions. Here, the SS effect is defined by the ratio of the reaction rate in SS plate to that in depleted uranium oxide plate. For core cell, the SS effect based on the infinite background cross-section approximation instead of the isolated lump approximation for the Mn-55 capture reaction is also shown in the table. It is concluded that the plate-wise microscopic cross-section and well-defined cell averaged cross-section are necessary even in the capture rate calculation of the structural material such as Mn-55.

* Power Reactor and Nuclear Fuel Development Corporation

References

- 1) Nakagawa M. et al. : "SLAROM: A Code for Cell Homogenization Calculation of Fast Reactor", JAERI 1294(1984)
- 2) Takano H. and Ishiguro Y. : "Production and Benchmark Tests of Fast Reactor Group Constant Set JFS-3-J2", JAERI-M 82-135(1982)
- 3) Nakagawa T. (Ed.) : "Summary of JENDL-2 General Purpose File", JAERI-M 84-103(1984)

Table 3.3.1 Comparison between measured and calculated results of the SS effect in the Mn-55 capture rate

	<u>CORE</u>	<u>BLANKET</u>
EXPERIMENT	$0.928 \pm 3\%$	$0.923 \pm 4\%$
CALCULATION(C/E value)		
(a) $\sigma_0 = \text{infinite}$	1.010 (1.097)	-----
(b) $\sigma_0 = \text{isolated lump approximation}$	0.883 (0.952)	0.863 (0.935)

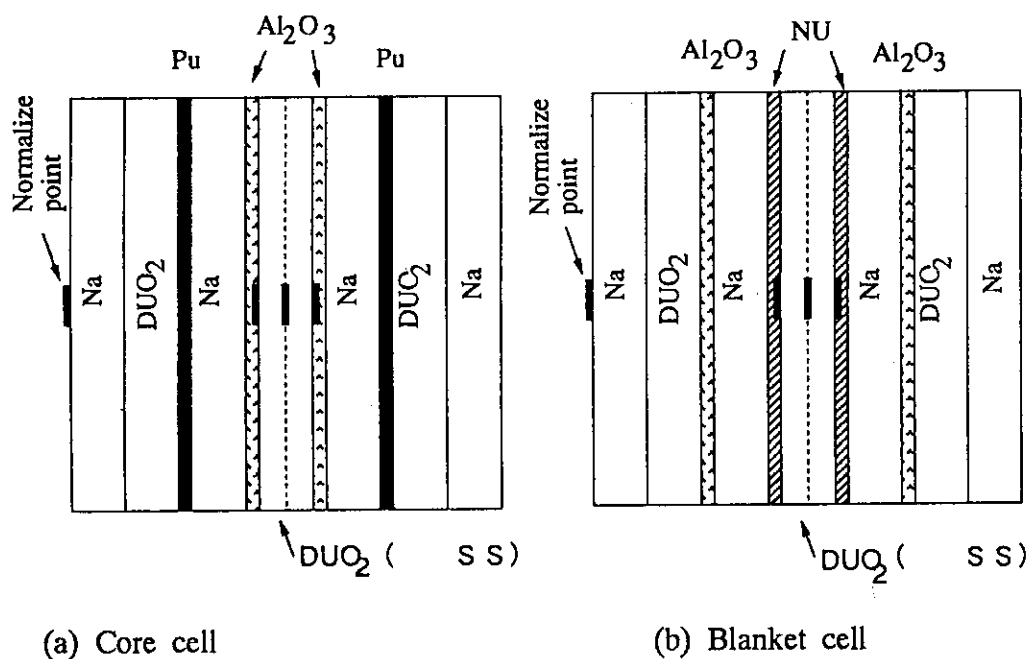


Fig.3.3.1 Position of activation foil in cells

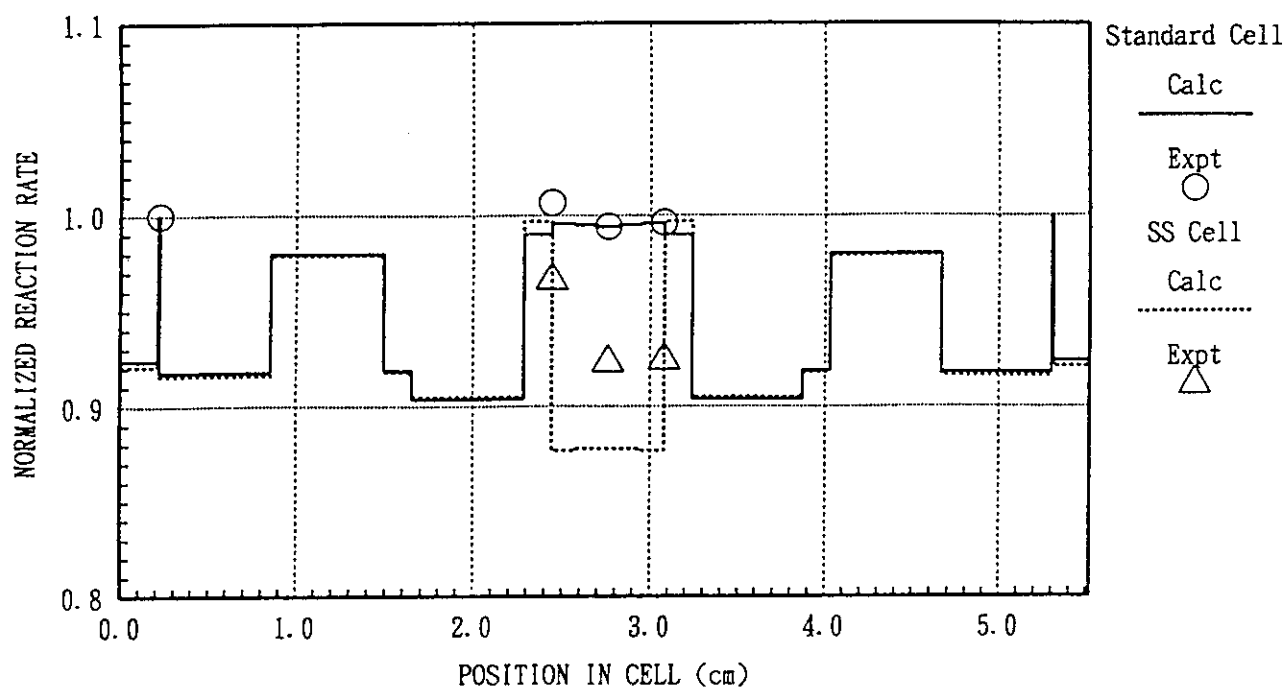


Fig.3.3.2 Mn-55 capture rate distribution in core cell

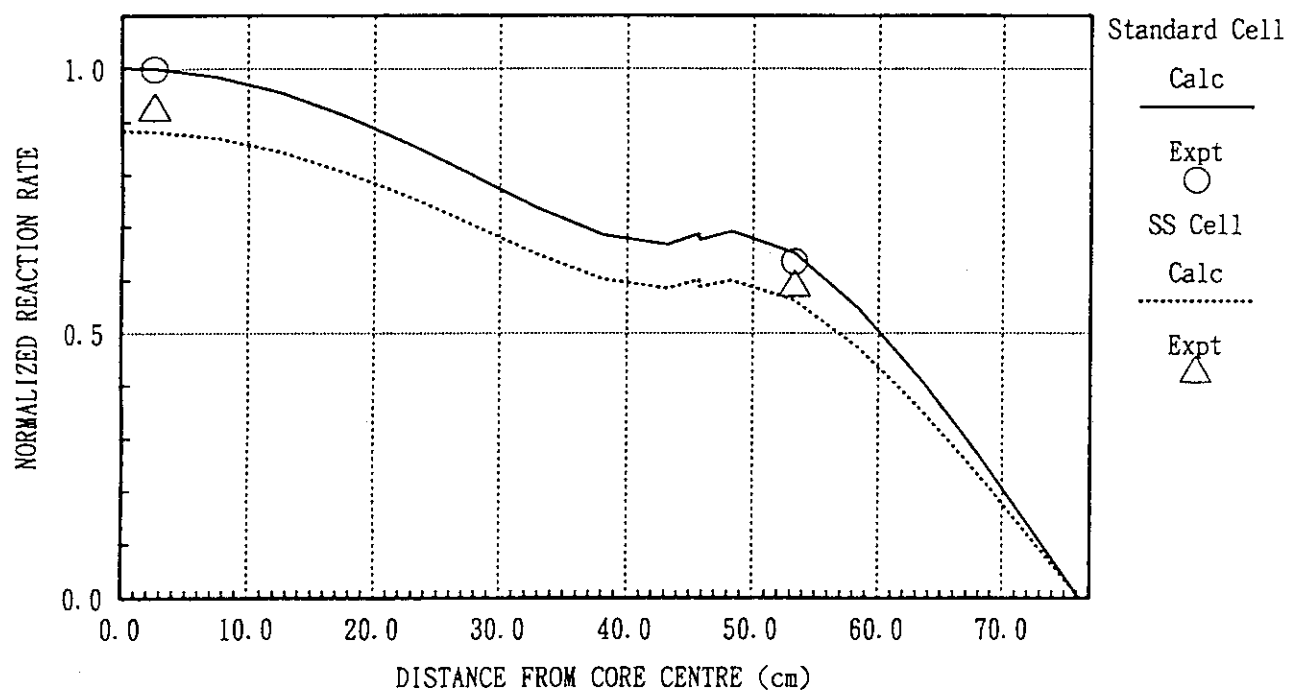


Fig. 3.3.3 Axial reaction rate distribution of Mn-55 capture

3.4 Measurement of Doppler Effect up to 2000°C in MOX-LMFBR Mockup Core FCA Assembly XVII-1

H. Oigawa, S. Okajima, M. Andoh, and T. Mukaiyama

In order to improve the calculation method of the Doppler effect in fast reactors, high temperature Doppler effect of ^{238}U was measured for temperature range up to 2000°C in FCA assembly XVII-1 which was built to measure reactor physics parameters of a prototype MOX-LMFBR. Two different methods were adopted in the Doppler effect measurements, namely, the sample reactivity measurement⁽¹⁾ up to 1500°C and the foil activation measurement⁽²⁾ up to 2000°C.

Sample Reactivity Measurement

A $^{238}\text{UO}_2$ sample (20mm^φ x 150mm^L, 390gU) contained in a high temperature resistant container was placed and heated at the center of the core. The net reactivity worth caused by the Doppler effect of the sample was measured by the critical method using a fine control rod which maintains the reactor power at a constant level. The experimental error was about $\pm 3 \times 10^{-7}$ Dk/k, which was derived from the standard deviation of critical rod positions measured at a given temperature.

In the analysis, Doppler reactivity worths were calculated by first order perturbation theory with using JENDL-3.1. An ultra-fine group collision probability code "PEACO-X"⁽³⁾ was used to obtain the effective cross section change caused by the temperature change of the sample.

In Fig 3.4.1, the measured Doppler reactivity worths are compared with the calculated ones. As shown in the figure, the calculation underestimates the measured worths. The ratio of the calculated value to the experimental one (C/E value) was 0.89 for the temperature rise from 20°C to 1500°C. The same tendency of the calculation was observed also in the measurement in FCA assembly XVI-2⁽⁴⁾ which is a mockup core of a metallic-fueled LMFBR and whose neutron spectrum is harder than that of the present assembly XVII-1. The discrepancy between the experiment and the calculation may be caused by the poor calculation of real and adjoint fluxes near the sample which play an important role in the reactivity worth calculation and which are considered to be perturbed largely by the experimental device made of tungsten and stainless steel. The improvement of the calculation is under way.

Foil Activation Measurement

A $^{238}\text{UO}_2$ foil (12.7mm^φ x 0.5mm^L, 570mgU) wrapped with a tungsten cover was suspended in a high temperature resistant container⁽²⁾ and heated at the center of the core by exposure of Nd:YAG laser beam. The foil was then irradiated for 3 hours at the reactor power of 80W. Doppler effect of the foil was expressed as "Doppler ratio":

$$\text{Doppler ratio} = \frac{R(T) - R(T_0)}{R(T_0)}$$

where $R(T)$: capture rate of the foil irradiated at temperature T ,
 T_0 : room temperature.

The capture rate of the foil was measured by counting γ -rays of ^{239}Np which is the product of the capture reaction of ^{238}U .

In the analysis, JENDL-3.1 and PEACO-X were used to obtain Doppler ratio. The 70-group collision probability code, SLAROM, was also used to calculate the reaction rate of ^{238}U above 100keV where PEACO-X cannot solve the neutron slowing down equation.

In Fig. 3.4.1, the measured Doppler ratios are also compared with the calculated ones. As shown in the figure, the calculation agrees with the measurement within the experimental error. The C/E value was 1.06 for the Doppler ratio at 2000°C.

References

- 1) Oigawa H., Okajima S. and Mukaiyama T. : "Reactor Engineering Department Annual Report (April 1, 1989-March 31, 1990)", JAERI-M 90-145, p33, (1990).
- 2) Oigawa H., Okajima S. and Mukaiyama T. : "Reactor Engineering Department Annual Report (April 1, 1991-March 31, 1992)", JAERI-M 92-125, p46, (1992).
- 3) Okajima S., Oigawa H. and Mukaiyama T. : "Measurement of Doppler Effect up to 2000°C at FCA (3) - Development of a Cell Code, PEACO-X, with Ultra-fine Group Structure - ", JAERI-M 92-185, (1992).
- 4) Okajima S., Oigawa H. and Mukaiyama T. "Reactor Engineering Department Annual Report (April 1, 1991-March 31, 1992)", JAERI-M 92-125, p50, (1992).

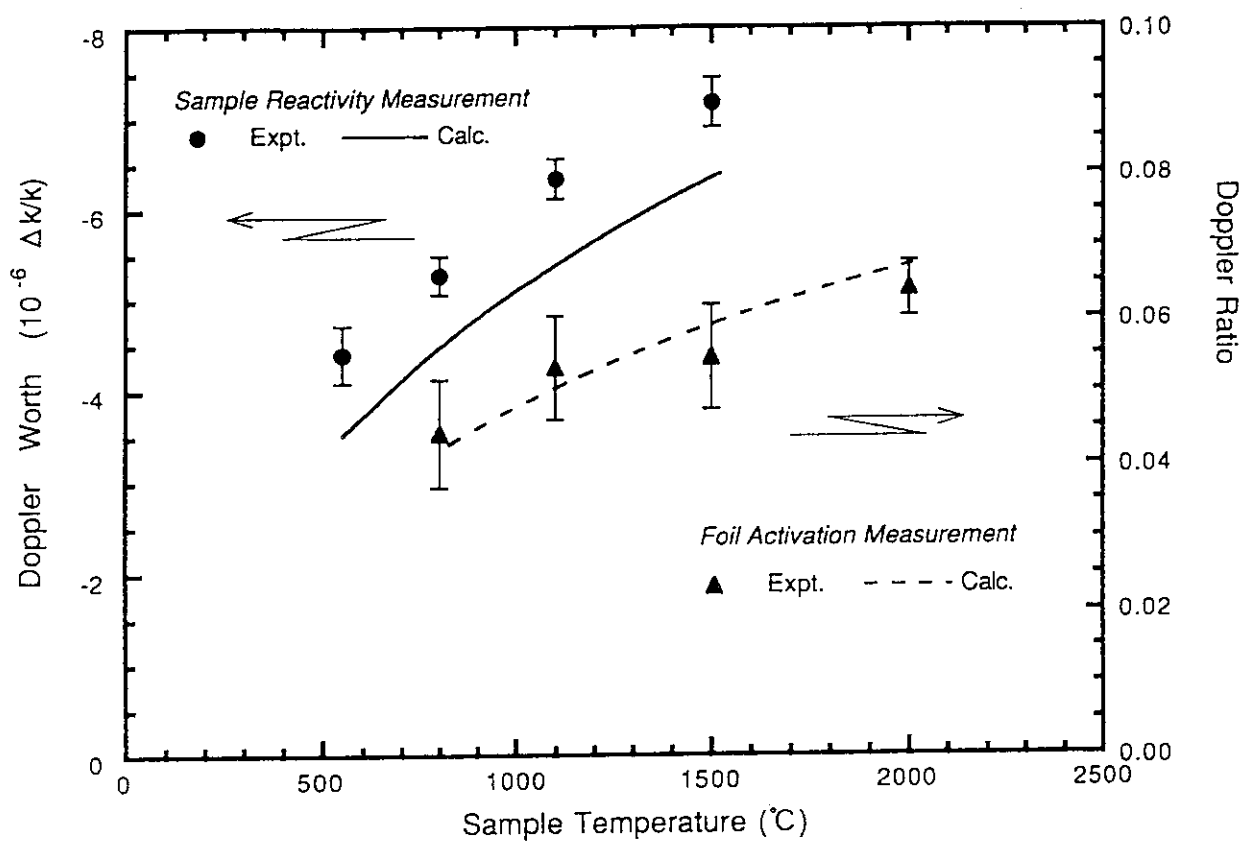


Fig. 3.4.1 Doppler effect measured in FCA assembly XVII-1

3.5 Analysis of Doppler Effect Measurement by PEACO-X Code

S. Okajima, H. Oigawa and T. Mukaiyama

The previous ^{238}U Doppler effect measurements at FCA were systematically analyzed using the collision probability code, PEACO-X¹⁾, in order to evaluate the contribution of the resonance interaction effect between the hot sample and the adjacent cold core. Data used in this analysis were obtained from the measurements in ten different Pu-fueled fast reactor mockup assemblies. In the analysis of Doppler experiments, most calculation methods cannot properly treat resonance shielding effects in a heterogeneous cell, such as the resonance interaction effect between hot sample and cold core, the resonance overlapping effect between different resonant isotopes *etc.* The former effect arises from the Dancoff effect between resonances of a given isotope in a core and those of the same isotope in a heated sample. Calculations that take this effect into account give larger Doppler reactivity worths than conventional methods.

A perturbation formulation was used to calculate the Doppler reactivity effect of the change in temperature of the Doppler sample. This formulation is based on the assumption that the Doppler effect arises solely from the change of ^{238}U capture, that is,

$$\Delta\rho = \frac{N^{28}}{D} \int \delta\sigma_c^{28} \phi \phi^\dagger dE dV$$

where D is the perturbation denominator and ϕ and ϕ^\dagger are the unperturbed real and adjoint fluxes. The resonance interaction effect between hot sample and cold core should be included in the term of $\delta\sigma_c^{28}$, which is the effective Doppler change in the capture cross section of ^{238}U . The PEACO-X code can treat the resonance interaction effect between hot sample and cold core because it precisely calculates the neutron balance between the sample and the adjacent materials with an ultra-fine energy structure.

The calculations were made using the JENDL-3.1 library²⁾. The unperturbed real and adjoint fluxes with a 70 group structure were obtained from a two-dimensional R-Z diffusion calculation. To determine the magnitude of this resonance interaction effect, the Doppler reactivity worth was calculated with two different cell calculation codes for $\delta\sigma_c^{28}$, the conventional code, SLAROM³⁾, and the PEACO-X code.

Figure 3.5.1 shows the ratio of the calculated Doppler reactivity worth with PEACO-X derived cross sections to that with SLAROM derived cross sections, as a function of the background cross section for ^{238}U in the core. The calculated Doppler reactivity worths increase by 6 - 11% when this resonance interaction effect is taken into account. It can be

seen from Fig. 3.5.1 that the ratio becomes smaller as the background cross section for ^{238}U in the core becomes larger. A comparison between the calculated and measured Doppler reactivity worths is shown in Table 3.5.1. By comparing the C/E values between SLAROM and PEACO-X calculations, it is clear that the PEACO-X calculation better predicts the measured Doppler reactivity worths. The C/E values for PEACO-X range from 0.95 to 1.07 except for those in Assemblies XII-1(Na voided), XVI-1 and XVI-2. The C/E values in Assemblies XII-1(Na voided), XVI-1 and XVI-2 are 0.79, 0.80 and 0.72, respectively. In these cores the neutron spectrum is rather hard and the contribution to the ^{238}U Doppler effect in the higher energy range is significant. When JENDL-3.1 is used, there is no contribution above 50 keV to the ^{238}U Doppler effect because there are no resonance parameters above 50 keV in the JENDL-3.1 library.⁴⁾

In conclusion, the impact of the resonance interaction effect between hot sample and cold core on ^{238}U Doppler effect measurements was evaluated using the PEACO-X code. When this resonance interaction effect is taken into account in $\delta\sigma_c^{28}$, the calculated Doppler reactivity worths become 6 - 11 % larger than those with the conventional method and show good agreement with measurements.

References

- 1) Okajima, S., Oigawa, H., Mukaiyama, T. : "Measurement of Doppler Effect up to 2000 °C at FCA (3) -Development of a Cell Code, PEACO-X, with Ultra-fine Group Structure-", JAERI-M 92-185, (in Japanese), (1992).
- 2) Nakagawa, M., Tsuchihashi, K. : "SLAROM: A code for cell Homogenization Calculation of Fast Reactor", JAERI 1294, (1984).
- 3) Shibata, K., et al. : "Japan Evaluated Nuclear Data Library, Version -3 -JENDL-3-", JAERI 1319, (1990).
- 4) Oigawa, H. : J. Nucl. Sci. Technol., 28[11], 1058 (1991).

Table 3.5.1 Calculated and measured Doppler reactivity worth^{*)} for NUO2-25 sample^{**)}

Assembly No.	Experiment ($10^{-6} \Delta k/k$)	C/E		(2) / (1)
		(1) SLAROM	(2) PEACO-X	
V-1 ^{a)}	-9.04 \pm 0.19	0.906	0.980	1.082
V-1(Na voided) ^{a)}	-6.71 \pm 0.20	0.979	1.070	1.093
VI-1 ^{b)}	-9.39 \pm 0.19	0.892	0.965	1.082
VI-2 ^{b)}	-8.78 \pm 0.08	0.891	0.959	1.076
X-3 ^{c)}	-8.57 \pm 0.13	0.967	1.029	1.064
XII-1 ^{d)}	-4.40 \pm 0.05	0.886	0.970	1.095
XII-1(Na voided) ^{d)}	-3.83 \pm 0.07	0.789	0.875	1.109
XVI-1 ^{e)}	-4.35 \pm 0.18	0.798	0.871	1.091
XVI-2 ^{e)}	-3.86 \pm 0.26	0.715	0.785	1.098
XVII-1 ^{f)}	-8.29 \pm 0.18	0.877	0.945	1.078

*) Reactivity change caused by the temperature change in the sample from room temperature to 800 °C

**) Doppler sample is a natural UO₂ pellet of 25mm ϕ x 150 mm L, ²³⁸U weight of 604.8 g.

a) Mock-ups of Experimental Fast Reactor "JOYO"

b) Mock-ups of the outer and the inner core, respectively, of the Prototype Fast Reactor "MONJU"

c) Mock-up of JOYO Mark II Core

d) Mock-up of an axially heterogeneous LMFBR

e) Mock-ups of a metal-fueled Fast Reactor

f) Mock-up of a Prototype MOX-fueled Fast Reactor

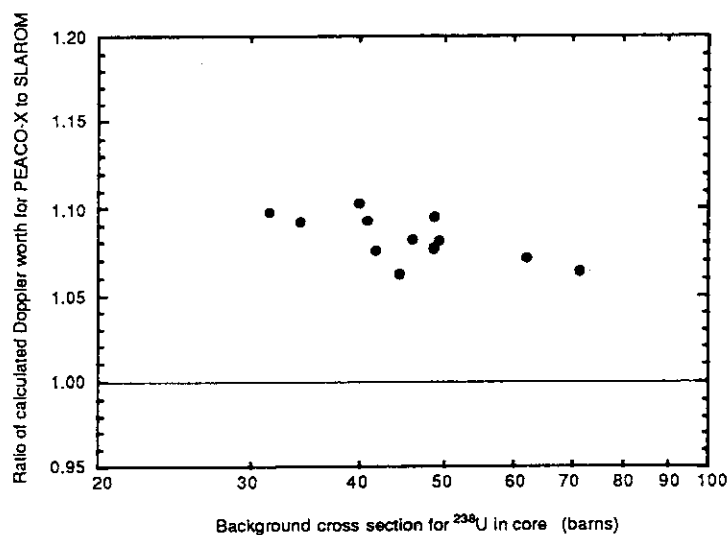


Fig. 3.5.1 Ratio of the calculated Doppler reactivity worth for PEACO-X derived cross sections to that for SLAROM derived cross sections as a function of the background cross section for ²³⁸U in core

3.6 Measurement of Effective Delayed Neutron Fraction at FCA

T. Sakurai, M. Nakano*, T. Nemoto, H. Oigawa and M. Bando**

An effective delayed neutron fraction (β_{eff}) was measured by the ^{252}Cf technique¹⁾ in FCA assembly XVI-1²⁾ which is a metallic-fueled LMFBR mockup. The purpose of the measurement was to check the accuracy of calculated β_{eff} used in the interpretation of reactivity experiments.

^{252}Cf technique

In the ^{252}Cf technique, β_{eff} is determined by :

$$\beta_{\text{eff}} = \frac{S_{\text{Cf}}}{\rho_{\text{Cf}} \bar{v} R_f F} \left(\frac{\phi_{\text{Cf}}^+}{\phi_f^+} \right), \quad (3.6.1)$$

where ρ_{Cf} is the apparent reactivity due to emission of spontaneous fission neutrons from a ^{252}Cf source (dollars), S_{Cf} is the source strength (n/s), R_f is the fission rate of core material at the core center (/s cm³), \bar{v} is the neutron emission rate averaged in the reactor, F is the normalization integral (cm³) and $\left(\frac{\phi_{\text{Cf}}^+}{\phi_f^+} \right)$, which usually becomes close to unity, is the importance ratio of source neutrons to reactor fission neutrons. An experimental correction is applied to the calculated value of F , the accuracy of which depends on that of calculated distributions of fission rates and fission importance.

Measurement

The apparent reactivity of the ^{252}Cf source was measured by introducing the source into the core center through a radial penetration hole. The reactivity was determined by position change of a fine control rod (F/R) which keeps the reactor power at constant level. Calibration of F/R in dollar unit was done by the positive period method. The measured reactivity was normalized by a count rate (M) of a neutron flux level monitor.

The source strength was calibrated by the manganese bath method at National Physical Laboratory in Great Britain, prior to the shipment.

The fission rate at the core center was measured by the foil activation technique with use of a high resolution Ge detector which was calibrated against fission chamber³⁾ standards. The measured fission rate was also normalized by a count rate of the common neutron flux

* Takasaki Research Establishment

** Energy Research Lab., Hitachi Ltd.,

monitor.

In order to obtain an experimental correction factor to the calculated normalization integral, measurement of fission rate distributions of ^{239}Pu , ^{235}U and ^{238}U along principal axes of the reactor were performed by the foil activation technique. Axial distribution of the ^{252}Cf source worth was also measured as the fission importance distribution.

Calculation

Calculation of β_{eff} was performed by 70 group diffusion theory based on two dimensional r-z model, while F , $\bar{\nu}$ and $\left(\frac{\phi_{\text{Cf}}^+}{\phi_f^+}\right)$ was calculated by 25 group diffusion theory based on three dimensional x-y-z model. JFS-3-J2 group constants set and delayed neutron yields evaluated by Tomlinson ⁴⁾ were used.

Experimental correction to the calculated normalization integral

The calculated and experimental distributions are compared in Fig.3.6.1 for ^{239}Pu fission rates and ^{252}Cf source worth. Good agreements were achieved for the radial distributions, while some discrepancies were observed for the axial distribution near the boundary of core and blanket. The same discrepancies were observed for the axial fission rate distributions of ^{235}U and ^{238}U . The correction factor was deduced to be 1.038 by taking account of these discrepancies.

Results and conclusion

Experimental β_{eff} was deduced by combining measured parameters and calculated ones shown in Table 3.6.1. Calculated β_{eff} is also shown in the table. The calculation overestimates the experiment by about 8%. Further investigation is necessary to explain the present significant discrepancy between calculation and experiment.

References

- 1) Fisher E. A. : Nucl. Sci. Eng., Vol.62, P 105, (1977)
- 2) Iijima S., et al.: "Benchmark Physics Experiment of Metallic-fueled LMFBR at FCA (I)", JAERI-M 92-196(1992) (in Japanese)
- 3) Ōbu M.: "Preparation and Characteristics of Fission Chambers with Actinide Nuclides", JAERI-M 9757(1981) (in Japanese)
- 4) Tomlinson L. : "Delayed Neutrons from Fission: A Compilation and Evaluation of Experimental Data," AERE-R-6993, U.K. Atomic Energy Research Establishment, Harwell (1972)

Table 3.6.1 Comparison of β_{eff} between experiment and calculation

$\rho_{\text{Cr}} \cdot M$	6.69	$\pm 1.3\%$	(dollars cps)
S_{Cr}	4.94×10^7	$\pm 1.2\%$	(n/s)
R_f / M	2.09×10^3 *	$\pm 1.8\%$	(/s cm ³ cps)
\bar{v}	2.74		
F	2.68×10^3 **	$\pm 3.8\%$ ***	(cm ³)
$\left(\frac{\phi_{\text{Cr}}^+}{\phi_f^+}\right)$	1.001		
$\beta_{\text{eff}} (\text{expt.})$	482	$\pm 5\%$	(pcm)
$\beta_{\text{eff}} (\text{calc.})$	523		(pcm)

* A small calculated correction ($\sim 1.5\%$) for fission rates of ^{240}Pu and ^{241}Pu was applied.

** The calculated normalization integral multiplied by the experimental correction factor

*** The error of the experimental correction factor

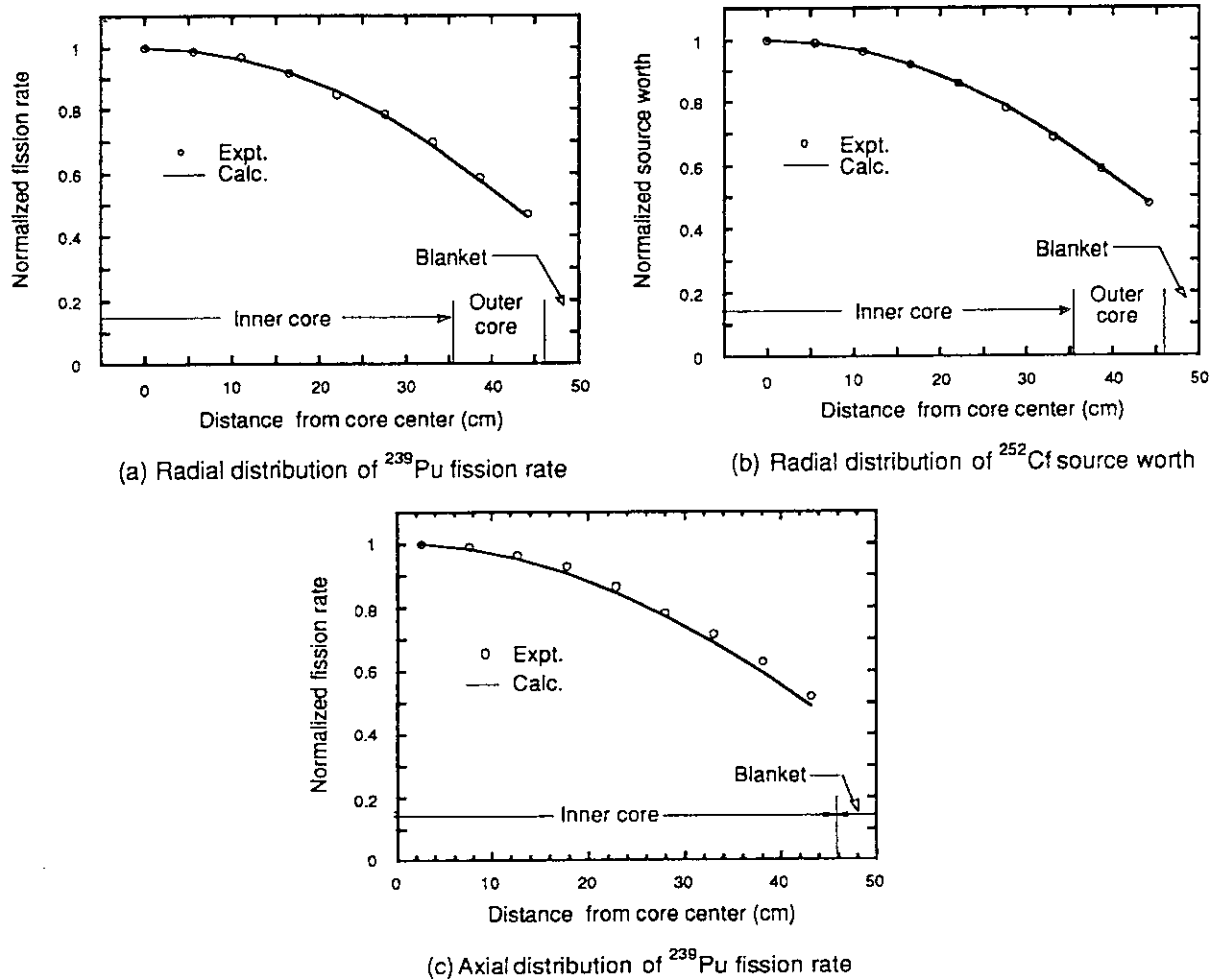


Fig.3.6.1 Comparison of distributions between experiment and calculation

3.7 Measurement of Reactivity Worth of the Multiple Burnable Poison Rods in the VHTRC-4 Core

F. Akino, M. Takeuchi and T. Ono

In order to verify the calculation accuracy related to the neutronic design of HTTR (High Temperature Engineering Test Reactor)¹⁾, the critical experiments have been conducted using the critical assembly VHTRC (Very High Temperature Reactor Critical Assembly)²⁾. The HTTR is designed to accommodate burnable poison rods for the reactivity compensation. Accordingly, the experimental burnable poison rods (BP rods) equivalent to those designed for the HTTR were prepared for the mock-up experiment at VHTRC. They were made by inserting 40 absorbing pellets (diameter: 12mm, stack length of the absorber: 723mm) in a hollow graphite rod. The absorbing pellets were made of B_4C particles dispersed in graphite powder. The boron content of the BP rod for the fixed side of VHTRC contained the 0.97wt% boron. On the other hand, the boron content of the BP rod for the movable side of VHTRC contained the 1.9wt% boron in the absorbing pellet.

The reactivity worths of the multiple BP rods were measured in the VHTRC-4 core by pulsed neutron method. This core loaded with 2-4-6wt% enriched fuel in an axially zoning pattern. The fuel rod of fixed side contained with 2wt% and 4wt% enriched uranium, each 10 fuel compacts. On the other hand, the fuel rod of movable side contained with 4wt% and 6wt% enriched uranium, each 10 fuel compacts. The core sustained criticality with about 12 fuel columns at the room temperature.

The reference core for the PNS experiment was loaded with 276 fuel rods and four BF_3 counters. After the measurement of the prompt neutron decay constant, α , of the reference core, the reactivity worths of the multiple BP rods were measured for following four core patterns:

6BP1: The 6BP1 core was constructed from the reference core by inserting 6 BP rods in the fuel columns. A BP rod was loaded in each of the 6 fuel columns.

12BP1: The 12BP1 core was constructed from the reference core by inserting 12 BP rods in the fuel columns. A BP rod was loaded in each of the 12 fuel columns. The arrangement of BP rods is shown in Fig.3.7.1.

12BP2: The 12BP2 core was constructed from the reference core by inserting 12 BP rods in the fuel columns. Two BP rods were loaded in each of the 6 fuel columns.

18BP3: The 18BP3 core was constructed from the reference core by inserting 18 BP rods in the fuel columns. Three BP rods were loaded in each of the 6 fuel columns.

The BP rods were inserted into the corner of hexagonal fuel blocks. To determine the prompt neutron decay constant, the raw data were fitted by the least-squares method to a single exponential type formula using the ALPHA-D code³⁾. The reactivity worth was determined by measuring the prompt neutron decay constant with the revised King-Simmon's pulsed neutron method (ρ_{RKS})⁴⁾. The measured values of the reactivity worth of the BP rods are listed in Table 3.7.1.

The analysis was made by using the SRAC code system⁵⁾ with ENDF/B-IV nuclear data library. The double heterogeneity of the fuel compact and the coated particle was taken into account in the cell calculation by the collision probability method. The thermal neutron in the energy region from 0.0 eV to 1.1254 eV were divided into 39 groups and the fast neutron in the energy region from 1.1254 eV to 10 MeV were divided into 22 groups. Using the neutron spectra obtained by the cell calculation, the cross sections of 61 groups were condensed into the 24 groups (thermal: 13 groups, fast: 11 groups) for the core calculation. The group constants for the reflector were calculated by means of the asymptotic spectrum consisting of fission, 1/E and Maxwellian spectra. The core calculation was performed using the 3-dimensional diffusion code CITATION. A cross section of the hexagonal fuel block was expressed by 24 meshes in a triangular model. In the axial direction, the assembly of the 240 cm length was divided into 30 meshes.

The calculated values of the reactivity worth of BP rods, together with measured ones, are shown in Table 3.7.1. The measured and calculated values are found to agree with each other within 10%. This result indicates that the reactivity worth of the multiple BP rods can be obtained satisfy the accuracy requirement within 10% for the fundamental nuclear design of HTTR.

References

- 1) JAERI: "Present Status of HTGR Research and Development"(1992).
- 2) Yasuda H., et al.: JAERI-1305(1987).
- 3) Kaneko Y., et al.: Nucl. Sci. Eng., 50, 173(1973).
- 4) Akino F., et al.: J. Nucl. Sci. Technol., 17, 593(1980).
- 5) Tsuchihashi K., et al.: JAERI-1302(1987).

Table 3.7.1 Reactivity worth of the multiple burnable poison rods in the VHTRC-4 Core

Core pattern	Number of BP rods	BP rod/column	Reactivity worth(\$)	
			Measured	Calculated
6BP1	6	1	9.68 ± 0.12	8.57(10.51)
12BP1	12	1	14.1 ± 0.2	14.41
12BP2	12	2	18.3 ± 0.3	16.77
18BP3	18	3	25.0 ± 0.4	24.72

The value with parenthesis indicates the reactivity worth using the core calculation with two region model in the fuel block.

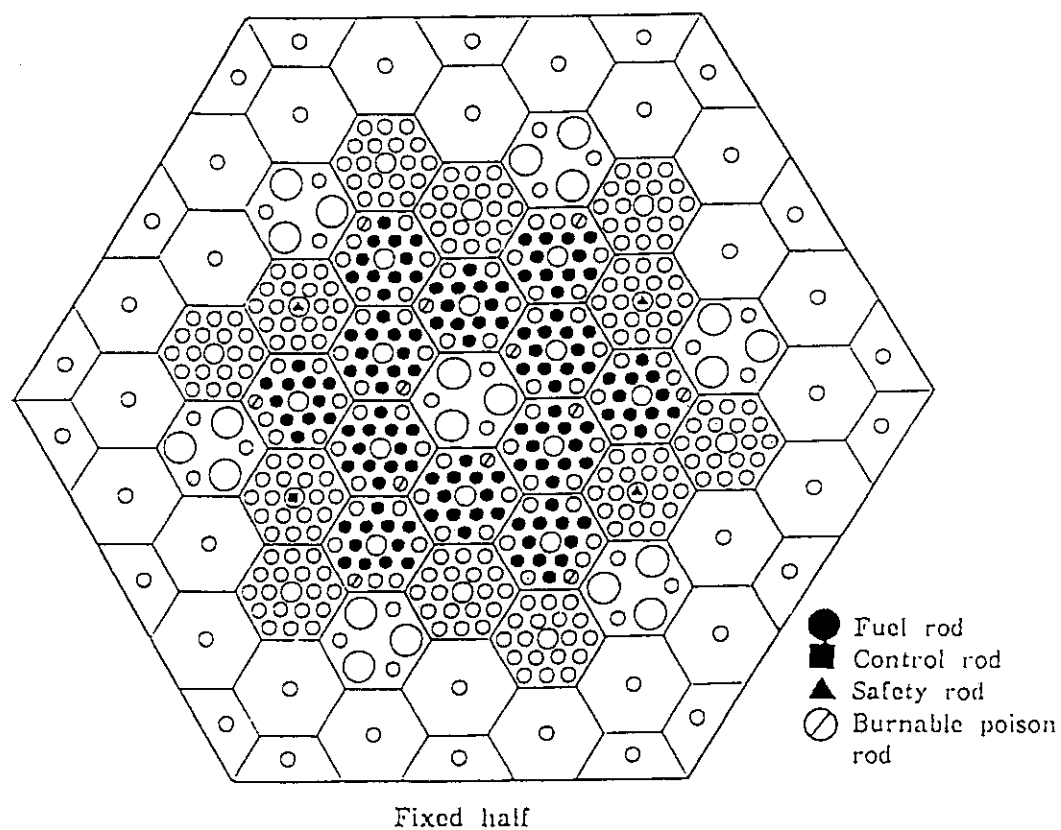


Fig. 3.7.1. Arrangement of the multiple burnable poison rods in the VHTRC-4 core (12 BP1 core pattern)

3.8 HTGR Water Ingress Simulation Experiment at VHTRC-4 Core

T. Yamane, M. Takeuchi, T. Ono, M. Seki, S. Fujisaki and H. Yasuda

The effect of water ingress on reactivity balance in an HTGR core was studied through simulation experiments at a VHTRC-4 core.

The core of a critical assembly VHTRC consists of pin-in-block type fuel using coated particles of low-enriched uranium(LEU). The VHTRC-4 core is loaded radially in the fixed pattern of 12 fuel rods per fuel block and axially in the zoning pattern of 2, 4 and 6 wt%-enriched fuels. Expanded plastics of polyethylene with nominal densities of 0.024 and 0.064 g/cm³ were used to simulate two different density conditions in water ingress accidents. For each density, two types in geometrical shape were prepared; FC and CR types. The FC type plastics were inserted into an inner 18mm diameter hole of fuel compacts in fuel rods. The CR type plastics were inserted into large holes(ϕ 102 holes) of 102mm diameter in graphite columns which were normally filled with graphite rods: in this series of experiments, three ϕ 102 holes in the central graphite column and twelve ϕ 102 holes of 6 graphite columns in the radial reflector were utilized and we will refer to them as 3C and 12R respectively.

Total 10 variants of loading configuration of plastics were constructed and the reactivity effect of water ingress was determined from the change of critical mass. Measured minimum critical mass(in the unit of number of fuel rods) for each core configuration is shown in Fig.3.8.1. The decrease of critical mass with increasing amount of polyethylene is observed in the cases having the same polyethylene loading pattern, and this fact indicates that the reactivity effect is positive in the simulated range of the present experiments. It is found that the reactivity effect of water ingress into the void region in the core and the central graphite column is positive, when the effect is discussed as the change from void state. However, no significant change was observed in critical mass in the case of the loading of CR type in 12R ("Core(FC)&12R(CR)") compared with the void state in 12R ("Core(FC)&12R(Void)").

Analysis was performed with the SRAC code system using nuclear data based on the ENDF/B-IV. The cross sections for hydrogen taking account of molecular binding effect in polyethylene were adopted in the SRAC nuclear data library. Sixteen group constants were obtained from a cell calculation by the collision probability method and eigenvalue

calculations were carried out with a diffusion code CITATION using a three-dimensional T-Z model. Among SRAC's options for processing diffusion constants, the isotropic component of the Behrens' term by Benoist's model was chosen to expect more accurate treatment of voided regions of 3C and 12R. The calculated critical mass for each experimental case is shown in Fig.3.8.2. General trend of the dependence of critical mass on loading amount of polyethylene is similar with the experimental results, except that the calculated reactivity effect of polyethylene inserted into the void region in the radial reflector is always positive in the contrast with no significant reactivity effect observed in the experiments. Figure 3.8.3 shows the ratio of calculated to measured critical mass. Although the C/E values in the cases of "Core(FC)&12R(Void)" and "Core(FC)&12R(CR)" seem to settle down around unity, these values are apparently not consistent with those in the case of "Clean core" and others. This result suggests that the reactivity effect of large voids in the radial reflector is not accurately estimated in the present calculation.

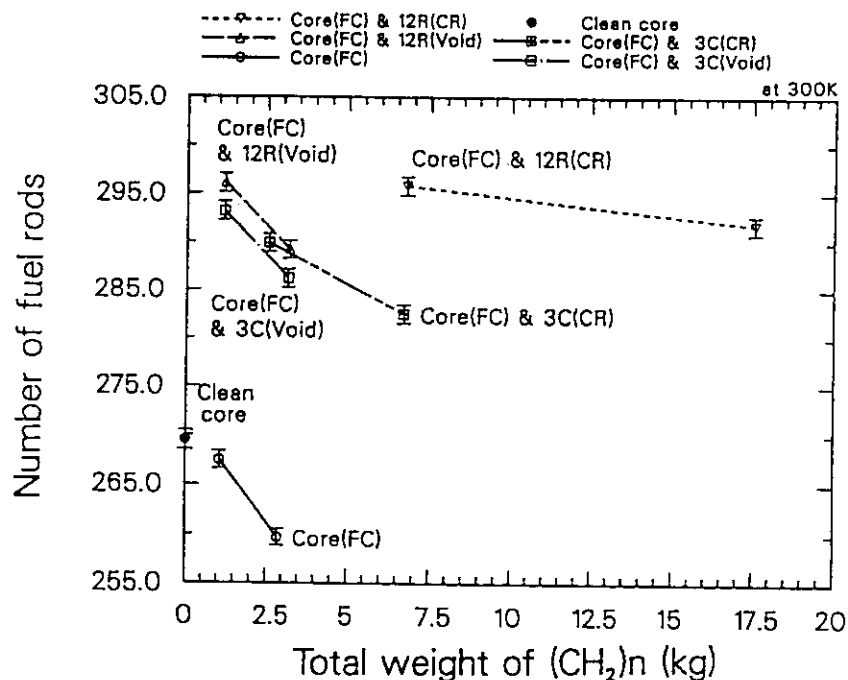


Fig.3.8.1 Measured critical mass versus amount of polyethylene loading

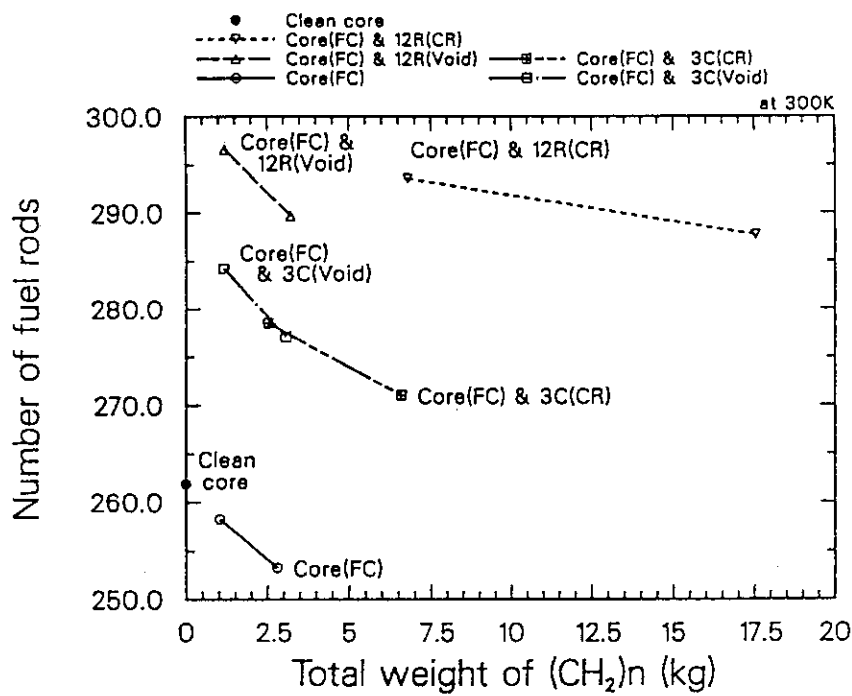


Fig.3.8.2 Calculated critical mass versus amount of polyethylene loading

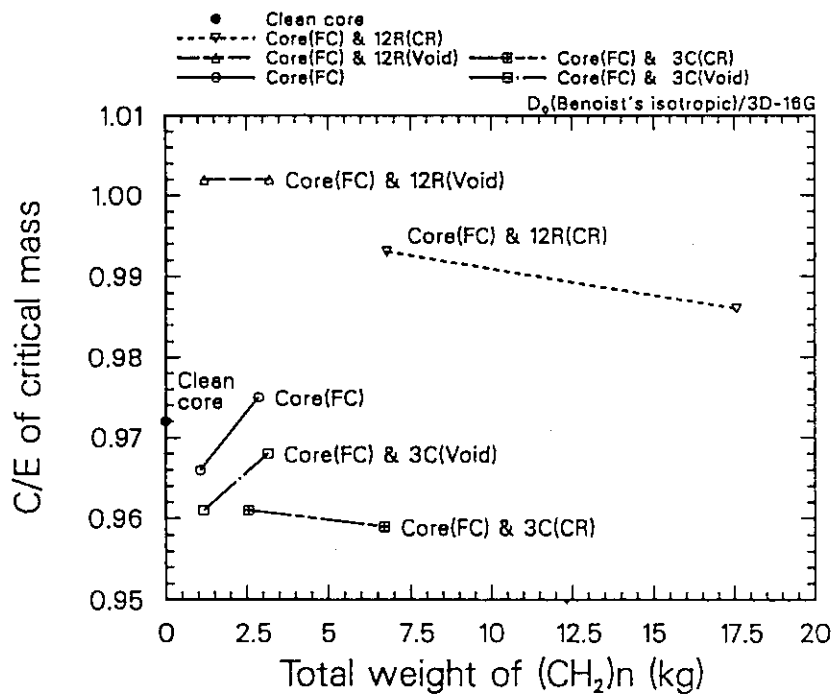


Fig.3.8.3 Ratio of calculated to measured critical mass

3.9 Measurement of Axial Power Distribution in the VHTRC-6 Core

T. Ono, M. Seki, T. Sasa, T. Takeuchi and A. Ohno

In the core design of HTTR, optimization of power distribution is made by changing enrichment of uranium in axial and radial direction of the core. In VHTRC, measurements of neutron flux distribution have been conducted in order to estimate the accuracy of core calculation related to the power distribution. From view points of measuring power distribution, directly fission rates in fuel compacts were measured in VHTRC-6 core. So, the power distribution was carried out analyzing γ -spectra of fuel compacts measured with a Ge detector.

The VHTRC-6 core is loaded with 2, 4, and 6wt%-enriched fuel rods in axially zoning patterns. The fuel rods of fixed side contained with 2wt% and 4wt%-enriched uranium, each 10 fuel compacts. On the other hand, the fuel rods of movable side contained with 4wt% and 6wt%-enriched uranium, each 10 fuel compacts. And, two kinds of burnable poison rods(BP rods) which have different boron concentrations are inserted in each side of VHTRC-6 core. Fuel rods loading pattern and measurement positions in VHTRC-6 core are shown in Fig. 3.9.1. In the experiment, all fuel compacts of each fuel rods in fixed and movable side were measured at three positions of which radial distances were different from core center. γ -rays from $^{143}\text{Ce}(293\text{keV})$ and $^{133}\text{I}(530\text{keV})$ were selected in spectral analyses by taking account of fission yield, half-life, intensity and energy of γ -ray. Relative power distribution were obtained from count rates of γ -peak area of interest by applying time decay correction. The statistic error of count rate and uncertainty in weight of fuel compact were considered as experimental error.

The analysis of experimental result was made by use of the SRAC code system. The experimental and calculated relative power distributions are shown in Fig. 3.9.2. The difference between measured and calculated values was 1.6% in average and 5.4% at most. This result indicates that calculated values agreed with the measured value within experiment errors(about 4%) in this measurement.

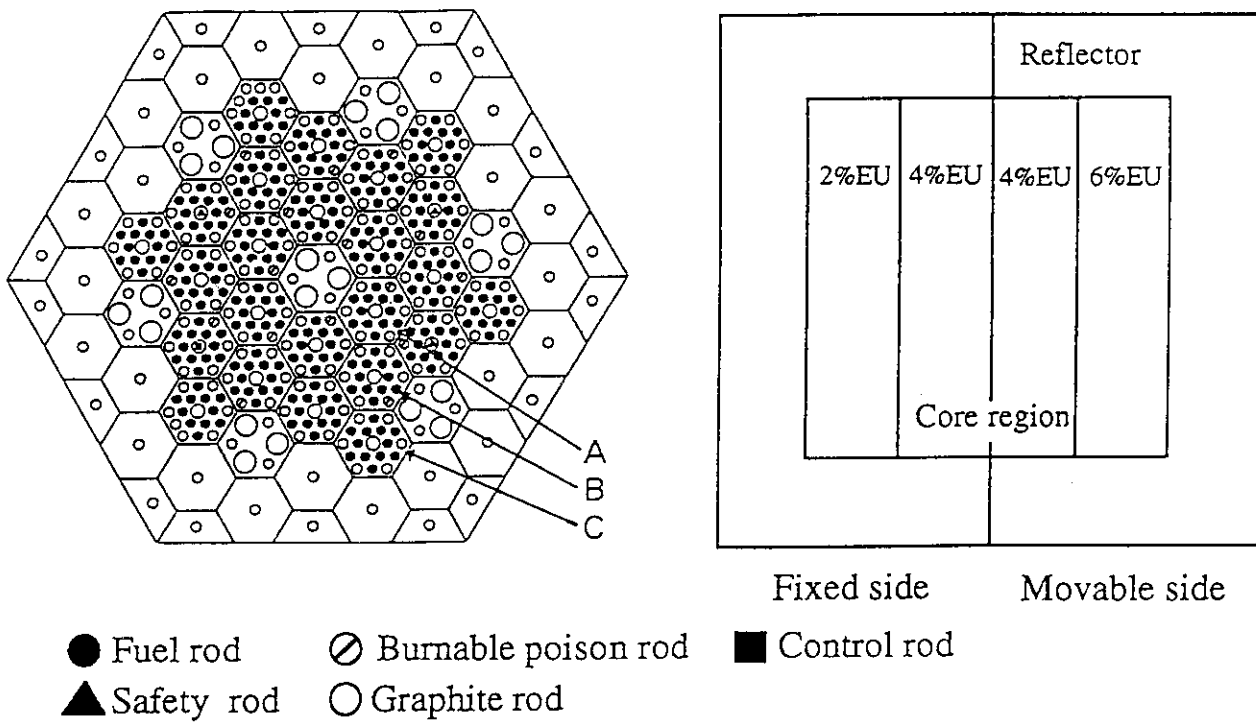
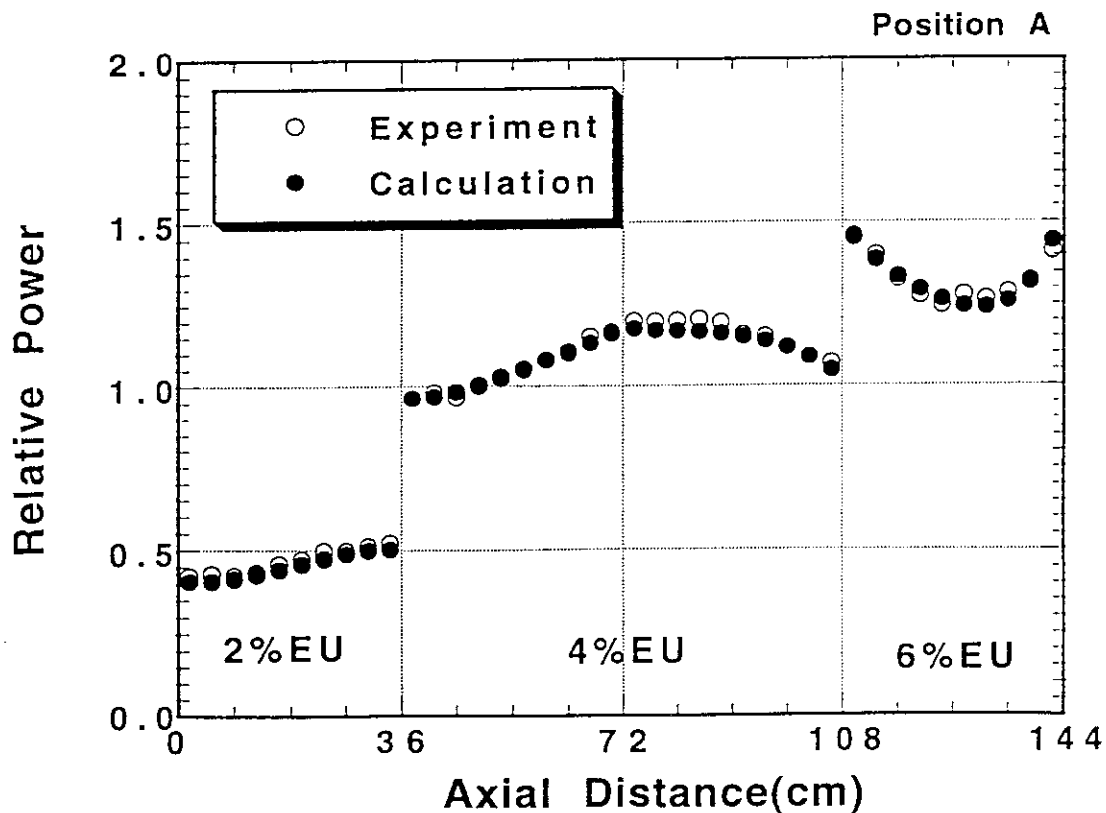


Fig.3.9.1 Fuel loading pattern and measurement positions in VHTRC-6core

Fig.3.9.2 Axial Power Distribution of ^{143}Ce

3.10 Measurement of Reaction Rate Ratio (C8/F) in Fuel Compact at VHTRC-6 Core

M.Seki, T.Ono, T.Sasa, M.Takeuchi and A.Ohno

Reaction rate ratio of capture to fission (C8/F) is an important physical parameter for evaluation of conversion ratio. This is measured usually by using foil and/or counters. Introduction of foils and/or counters into the core gives rise to unpreferable perturbation in neutron flux around them. Precise evaluation of this perturbation effect is so complicated and time consuming. In this experiment, direct measurement of this reaction was evaluated directly by measuring γ -spectroscopy of fuel compact.

The reaction rate ratios (C8/F) were measured at specific positions in the VHTRC-6 core, shown in Fig.3.10.1. The VHTRC-6 core is loaded with the 2,4 and 6 wt%-enriched fuels in the axially-zoning patterns shown in Figure 3.10.1. And two kinds of burnable poison rods which have different boron concentrations are inserted in each side of VHTRC assembly. Size of hollow fuel compact is 36mm in outer diameter, 18mm in inner diameter and 36mm high. Prior to the irradiation, background spectrum of each fuel compact was measured. Irradiation amount was 10Wh (10W \times 1h).

Capture reaction rates were obtained by analyzing 279keV γ ray peak mainly coming from ^{239}Np and fission reaction rates were obtained by 293keV γ ray peak coming from ^{143}Ce . Reaction rate ratios (C8/F) of each fuel compacts were obtained using count rates by making several corrections such as detector efficiency, time decay, self absorption of γ ray in fuel compacts and fission yields. The experimental errors were evaluated from statistic error of count rate and uncertainty in detection efficiency curve.

Analysis was carried out using the SRAC code system. Twenty four group constants were obtained from cell calculation by the collision probability method and core calculation was performed by the three dimensional diffusion theory.

The measured C8/F was shown in Fig.3.10.2, together with calculated values. The calculation results agreed well within the experimental errors.

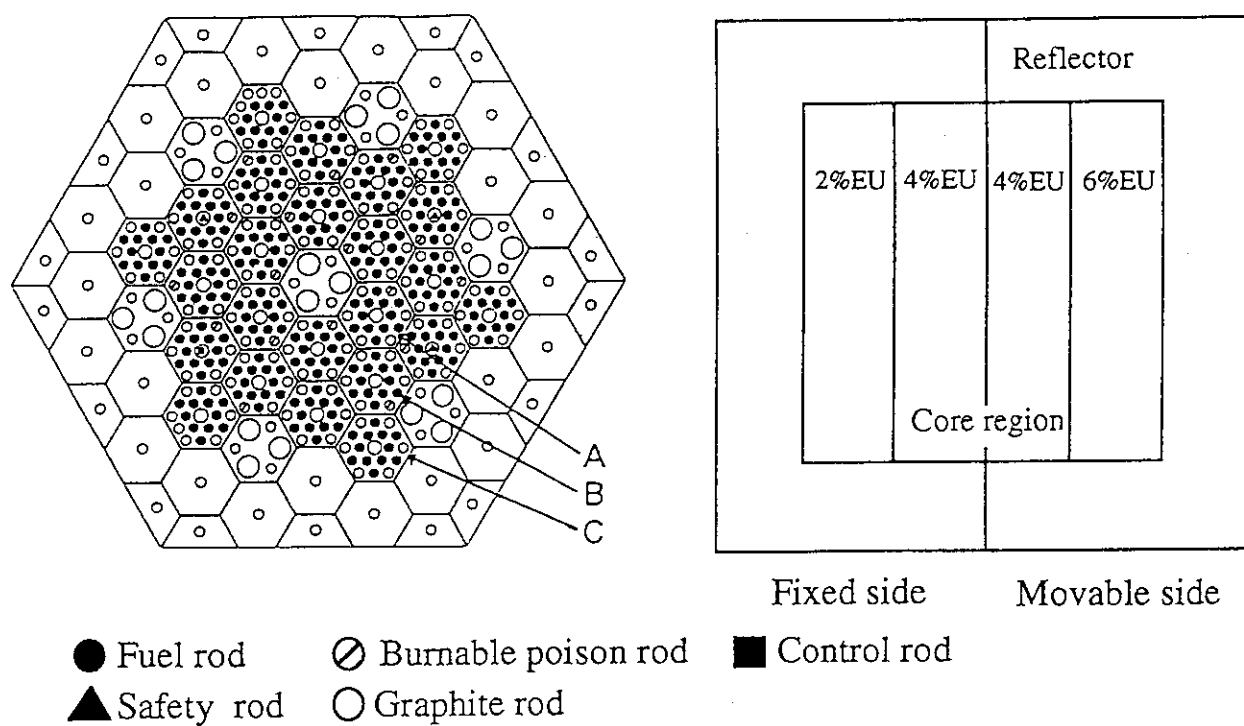


Fig.3.10.1 Fuel loading pattern and measurement positions in VHTRC-6core

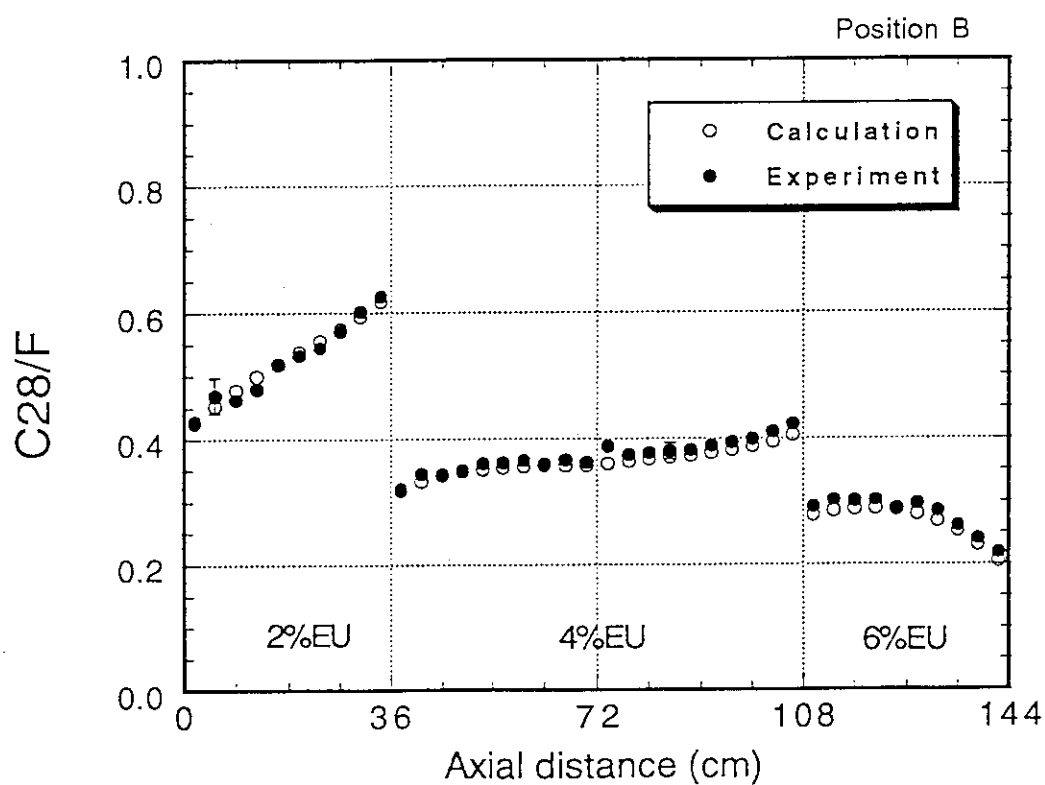


Fig3.10.2 Axial Distribution of Reaction Rate Ratio (C28/F)

3.11 Benchmark Calculation of the Lead Cooled Fast Reactor Critical Assembly BFS-61

H.Akie, H.Takano and K.Kaneko*

Lead cooled fast reactors have, from the viewpoint of safety, favorable characteristics such that :

- 1) Lead is not chemically active with water,
- 2) Negative void reactivity can be obtained,
- 3) Burnup reactivity swing is almost zero because of high fuel breeding,
- 4) Shielding capability of lead is very good.

From these reasons design studies are now made, especially in Russia, to realize a highly safe fast reactor concept with lead coolant¹⁾.

To develop lead cooled fast reactors, some critical experiments have been performed in Russia to validate the reactor physical data and methods used for the design calculations. One of these critical assemblies is BFS-61, which is composed based on a 700 MW thermal reactor conceptual design¹⁾. The active core region of the critical assembly consists of Pu metal, depleted U metal, lead, etc., and surrounded by reflectors of lead, steel and depleted UO₂.

The BFS-61 critical experiment was analysed according to the geometry models specified by Russia²⁾. A continuous energy Monte Carlo code MVP, the SLAROM/CITATION-FBR system and the SRAC system were used. In SLAROM and the SRAC calculations, the in-core heterogeneity of BFS-61 was treated with the collision probability method on the doubly heterogeneous cell model, and the whole core calculation was made with the diffusion calculation. The evaluated nuclear data library JENDL-3.1 was used in all the calculations.

Firstly, the geometry models were compared by using the SRAC system, because there are three models specified with and without in-core heterogeneity. The MHET model almost exactly represents the geometry of the critical assembly. The models MRZ-1 and MRZ-2 are the two-dimensional R-Z cores composed of the homogeneous mixtures for the core and the

*The Japan Research Institute, Ltd., Tokyo

reflector regions. The SRAC results showed that the homogeneous models give the underestimated effective multiplication factors by about 2%.

The effective multiplication factors of BFS-61 calculated with the MHET model are shown in Table 3.11.1. Here, the RECOL and MCNP-4 calculations were performed in Russia²⁾, also with the JENDL-3.1 data library. The MVP result slightly underestimates the multiplication factor, and is in good agreement with the MCNP-4 result. The underestimations of about 0.3% may be due to the JENDL-3 library.

Table 3.11.1
Effective multiplication factors(k_{eff} s)
calculated for BFS-61

MVP	0.9964±0.0009
CITATION-FBR	1.0000
SRAC	1.0035
RECOL*	1.000±0.003
MCNP-4	0.9967±0.0020

* : Continuous energy Monte Carlo
code(Kurchatov Institute)

The central reaction rate ratios were also calculated. The result by MVP underestimated C8/F5(U-238 capture/U-235 fission) value and overestimated F9/F5(Pu-239 fission/U-235 fission) value compared with the experimental data and the MCNP-4 result. Furthermore, the reactivity effects of lead voidage and hydrogen introduction in the active core region were evaluated.

In addition to these analyses, the effect of cross section data substitution was studied for the lead cross section, which is considered to be one of the most important data in lead cooled fast reactors. The two calculations were made with the SRAC system by replacing lead cross sections of JENDL-3 by those of JENDL-2 and ENDF/B-IV. The effective multiplication factor obtained with the JENDL-2 lead cross sections is 0.3% larger than that with JENDL-3 cross sections, and 1.4% larger for the case of ENDF/B-IV data. The differences in the multiplication factor are mostly caused from the differences in elastic

scattering cross section. As shown in Fig.3.11.1, the cross section differences are found especially in the energy range around 100keV, that is the most important energy range in fast reactors. The elastic scattering cross section of lead plays a very important role in the void reactivity changes of lead cooled fast reactors. It is concluded that the ENDF/B-IV data for lead do not have a sufficient accuracy for the calculations of these reactors.

References

- 1) E.O.Adamov et al.: "Progress in Lead-cooled Fast Reactor Design", Proc. Int. Conf. on Design and Safety of Advanced Nuclear Power Plants (ANP'92), 25-29 Oct., 1992, Tokyo, Japan, 16.6-1 (1992).
- 2) A.G.Morozov : private communication (1993).

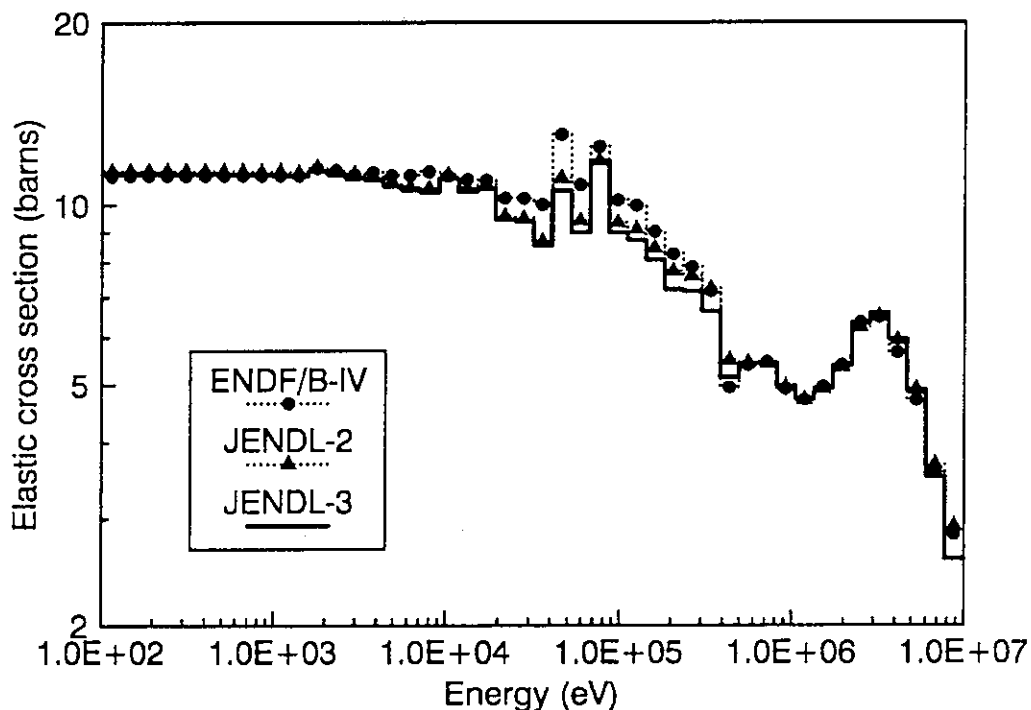


Fig. 3.11.1 Elastic scattering group cross sections of Pb natural in the SRAC library

3.12 Studies on Production and Utilization of U-233 Fuel in Thermal Reactors

H.Akie, Y.Ishiguro, K.Kuroki* and T.Yano**

The utilization of Th/U-233 fuel in the widely used light water moderated reactors has been studied. The conversion ratio greater than 1.0 was shown to be feasible in an axially heterogeneous BWR core with effective volume ratio of moderator to fuel (V_m/V_f) of 0.25, while the large amount of U-233 inventory is needed.¹⁾

The parametric survey calculations were made for Th/U-233 reactors with graphite or heavy water moderator, because these moderators seem suitable for a Th/U-233 reactor from the viewpoint of neutron economy. Furthermore, study was done on the potential of U-233 production by using light water reactors to supply initial loading U-233 of Th/U-233 reactors.

Parametric survey for graphite and heavy water moderated Th/U-233 reactors

Parametric survey calculations were made by the cell burnup calculations with the SRAC code system. The cell model of pebble bed type fuel is supposed for a graphite reactor. In the cell model, the double heterogeneity of fuel particle and fuel pebble is taken into account. For the heavy water reactor, the CANDU type reactor was selected. The single pin cell model was used, which is equivalent to the CANDU type fuel cluster with pressure tube, calandria tube, D_2O coolant and moderator. In both reactors, the fuel is $(Th/U-233)O_2$. Surveyed parameters are the U-233 enrichment and the atom ratio of carbon to heavy metal (C/HM) for the graphite reactor and the moderator/fuel volume ratio (V_m/V_f) for the heavy water reactor. The parameter C/HM for the graphite reactor is varied from 60 to 1000, and V_m/V_f for the heavy water reactor from 0.9 to 300. The design values of a pebble bed reactor THTR and a typical CANDU reactor are C/HM=280 and $V_m/V_f=15$, respectively. Conversion ratio, U-233 inventory and burnup rate of the fuel are evaluated.

The results of the survey calculations can be summarized as follows :

- a) The high conversion ratio is achieved in the cell with small C/HM or V_m/V_f value. The U-233 enrichment in such cells is higher, under a fixed burnup rate, than the cells with larger C/HM or V_m/V_f .

*Faculty of Engineering, Kyushu Univ.,

**Faculty of Engineering, Hokkaido Univ.

- b) In graphite reactors, the conversion ratio is less than 0.9 even for $C/HM=60$, while extremely high burnup can be achieved with small U-233 inventory.
- c) The conversion ratio larger than 1.0 is feasible in the heavy water reactor. In the high conversion or the high burnup cores, however, the U-233 inventory is also large.

Characteristics of Pu - U-233 converter LWR

Cell burnup calculations were made with the SRAC system. A single pin cell model with the fuel of PuO_2 and ThO_2 mixture was used. The moderator/fuel volume ratios (V_m/V_f) of the cell models range from 0.25 to 3.0, including the value for conventional PWR(1.9). The Pu enrichment is adjusted for each cell to achieve the burnup rate of 60 GWd/t. In Table 3.12.1, the U-233 production rates are summarized in terms of tonne per GW electric. The tighter a fuel lattice is, and therefore the harder a neutron spectrum is, the more U-233 is produced. In the cell of $V_m/V_f=0.25$, 0.5 tonne/GWe of U-233 is produced per year, where the Pu inventory is about 20 tonne/GWe.

Table 3.12.1 Pu - U-233 production in PuO_2/ThO_2 fueled LWRs

V_m/V_f	0.25	0.8	1.4	1.9	3.0
Pin diameter (cm)	1.23	0.95	0.95	0.95	0.95
Fissile Pu enrichment [†] (wt.%)	9.6	9.7	8.1	7.0	6.5
Linear power (kW/m)	15.0	15.0	15.0	15.0	15.0
Discharge burnup (GWd/t)	60.0	60.0	60.0	60.0	60.0
Discharged U-233 amount (tonne/GWe)	5.40	2.04	1.51	1.36	1.17
U-233 production rate (tonne/GWe/300 FPD)	0.50	0.33	0.26	0.23	0.20

[†] : Pu from LWR spent fuels

Summary

A concept of the graphite moderated Th/U-233 reactor is attractive to achieve very high burnup with small U-233 inventory. On the other hand, the heavy water moderated reactor is suitable to achieve the conversion ratio greater than 1.0. The characteristics of the cores selected from these viewpoints for each type of reactor are summarized in Table 3.12.2, and compared with the LWR that has already been studied. The high burnup and low inventory graphite reactor is considered to be highly feasible. It needs, however, to be combined with U-233 production reactors. The heavy water reactor has the large U-233 inventory, as the LWR does. But the inventory of the heavy water reactor can be no more than 70% of that of the LWR. Furthermore, the V_m/V_f value of the heavy water reactor is far more feasible than that of the LWR.

Table 3.12.2 Characteristics of Th/U-233 fueled thermal reactors

Moderator	Graphite	D ₂ O	H ₂ O
Moderator/fuel	C/HM=1000	$V_m/V_f=1.0$	$V_m/V_f=0.25$
U-233 enrichment (wt.%)	12.0	6.0	8.5 [†]
Burnup (GWd/t)	190 [‡]	63 [‡]	45 [†]
Average conversion ratio	0.41	1.05	1.02
U-233 inventory (tonne/GWe)	1.0	10.5	15.0

[†] : in the fuel region of the axially heterogeneous core

[‡] : achievable maximum value

Reference

- 1) H.Akie, et al.: Proc. Int. Specialists' Mtg. on Potential of Small Nuclear Reactors, Tokyo Japan, Oct.1991, p.197 (1992).

4. Advanced Reactor System Design Studies

It is a preferable world topic to propose a reactor fueled with plutonium from nuclear warheads to produce electricity. For burning of the plutonium, a concept of once-through type nuclear fuels is studied from phase relations of ceramic materials, their chemical properties and burnup characteristics. As new fuel forms for the once-through plutonium burning, fluorite-type phases of thorium (ThO_2) and gadolinia-stabilized-zirconia are accepted due to their solid solubility of Pu and some fission products, irradiation and chemical stabilities. The existing PWR can transmute almost 99 % of Pu-239, and the spent fuel becomes completely poor plutonium-composition. The spent fuels would be buried under deep geological formations, as they are without any chemical and heat treatments.

In a feasibility study of lead-cooled fast breeder reactor with nitride fuel assemblies, the inherent safety core with considerable negative coolant void reactivity and very small burnup reactivity swing are achieved on the basis of parametric survey for the effect of nitride-15 concentration on important core characteristics. Furthermore, the plant technology is studied for system configuration, heat balance, steam generator concept, reactor system concept, core design safety, decay heat removal system and aseismicity.

Continuous effort is being devoted on the design studies of system integrated pressurized light-water reactor with passive safety (SPWR) since 1986. As a result, the most rational plant concept of 600 MWe power is proposed in which the containment vessel is filled with water and reactor vessel is placed in it.

A concept of passive safety light water reactor system is proposed on a standpoint for reducing manpower and human-errors in operation and maintenance. In order to simplify reactor control, chemical and auxiliary systems, in-vessel control-rod-drive-mechanism units are employed. The plant concept of 600 MWe power is imaged and the conceptual flow diagram of primary system with passive engineered safety feature system is designed. Furthermore, a feasibility of high-load following capability system is shown from studying parametrically load changes without any actuation of control systems.

(Hideki Takano)

4.1 A Design Study of Lead-cooled Fast Breeder Reactor with Nitride-fuel Assembly

H. Takano, H. Akie and K. Kaneko*

One of the most essential features for prolongation of nuclear power generation is effective utilization of uranium resources, and furthermore high-level radioactive wastes (HLW) would be transmuted in a fuel cycle system. However, a prolongation of LWRs main-stream era is presumed before a practicability of FBRs which have the most attractive feature. Because, the construction cost of an FBR with sodium-cooled MOX-fuel assemblies is nearly two times that of a corresponding LWR. From the view point of safety, a prime design is required to reduce positive void-reactivity as low as possible. Furthermore, a high cost for the MOX-fuel cycle will lose an attractiveness for FBR development. To solve these problems, some advanced fast reactors were studied¹⁻⁴⁾, and the concept with use of lead in place of sodium coolant proposed in Russia¹⁾ is one of the most feasible safety and economic fast reactors.

A neutronic study has been performed for the use of the lead coolant and nitride fuel in place of sodium and MOX ones. In the comparison of macroscopic cross sections between Pb and Na, the elastic and inelastic scattering cross sections of Pb are much larger than those of Na, and the capture resonance integral of Pb is smaller than that of Na. Thus, the voiding of lead coolant enhances neutron leakage and reduces the positive void reactivity. The slowing down power of Pb is much smaller than that of Na, and this causes harder neutron spectrum and higher breeding gain.

The effects of the concentration from N-14 to N-15, the lead coolant and the ratio of fuel pin pitch to rod diameter on the core performance such as coolant void reactivity, burnup reactivity swing, breeding ratio and Pu-inventory were parametrically investigated and the characteristics of nitride fuel assembly with lead-coolant were shown. The effect of the N-15 concentration on the void reactivity is positive in a sodium cooled core and is negligibly small in a lead-cooled core whose neutron leakage is dominant at the coolant voidage. The concentration of N-15 contributes to reduce plutonium inventory and

*The Japan Research Institute, Ltd., Tokyo

increase breeding gain.

A design study of lead-cooled fast reactor with nitride fuel assemblies has been performed to improve the safety, plant cost, uranium resource utilization, transmutation of HLW nuclides and fuel cycle cost for the sodium-cooled MOX-fuel FBR. A plant power size limited by aseismic capability and a compact helical-coil steam generator integrated reactor system were studied.

The main reactor core characteristics are shown in Table 4.1.1. It should be emphasized that the whole core coolant void reactivity becomes considerably large negative value. And small burnup reactivity swing of 0.14 %dk/k and breeding ratio of 1.26 are achievable.

A feasibility for the reactor plant technology has been studied for system configuration, heat balance, steam generator concept, reactor system concept, core design safety, decay heat removal system and aseismicity. The following conclusions were obtained:

- (1) System configuration of compact pool type is fit to the lead-cooled reactor with a helical-coil SG integrated concept.
- (2) Parameter study for heat balance design shows the transfer area 15 % larger than that of sodium-cooled reactor. The SG inlet/outlet lead temperatures are 470/570 C. The assembly structure with pin pitch to diameter ratio more than 1.5 is selected under consideration for fuel cladding damage, cladding allowable maximum temperature and bundle pressure drop.
- (3) The lead-cooled reactor has larger margin to conventional ATWS events, because of large margin to coolant boiling, negative void reactivity and lower burnup reactivity swing.
- (4) Maximum plant power size is limited by aseismic capability for S-2 earthquake of response acceleration smaller than 2G. The reactor vessel diameter is 13 m and the reactor power is 600 MWe. The construction site is on tertiary or quaternary period's soft soil.

References

- 1) Velikhov E.P., et al.:" The High Safety and Economy NPP with Liquid Lead Cooled Reactor," Nuclear Power and Industry Ministry, USSR, Moscow (1990).
- 2) Takano H. et al.:" A Concept of Advanced Fast Breeder Reactor with Instantaneous

Negative Temperature Coefficient," Proc. Int. Conf. on Fast Reactors and Related Fuel Cycles, Vol.II,P.16.1, Oct.28-Nov.1, 1991, Kyoto.

- 3) Matveev V. et al.:" The Concept of BN-1600 Reactor Core with Zero Sodium Void Reactivity Effect and Minimum Burnup Reactivity Margin," *ibid*, Vol.II, P.16.3, (1991).
- 4) Bergeonneau Rh.,et al.:" Advanced Fast Reactor Core Design Studies Improving Economy and Safety," *ibid*, Vol.II, p14.6, (1991).

Table 4.1.1 Main core performance

reactor thermal power (MWt)	1500
reactor core	
height (cm)	100
diameter (cm)	355
blanket thickness (cm)	30
ratio of pin-pitch to -diameter	1.51
fuel type	(U,Pu)N
initial Pu inventory (ton)	4.0
burnup cycle length (EFPD)	2000
burnup rate (GWd/tHM)	92
breeding ratio	1.26
burnup swing (%dk/k)	0.14
whole core void reactivity (%dk/k)	-1.5
Doppler reactivity(10^{-3} Tdk/dT)	-3.7

4.2 Concept of Passive Safe Reactor SPWR (System-integrated PWR)

K.Sako, T.Oikawa, J.Oda*

SPWR Design Outline

SPWR is a passive safe reactor concept proposed by JAERI. This reactor is being designed since 1986 as a next generation power plant employing a new concept which can provide high passive safety, easy operation/maintenance and economic compatibility simultaneously as well as effective use of experience and technology already obtained in the course of light water reactor development. At present, the first design study has been completed.

Figure 4.2.1 shows the basic concept of SPWR. It is an integrated PWR with poison tank filled with borated water in place of control rod for reactor shutdown.

Table 4.2.1 shows the major parameters of SPWR plant. Figure 4.2.2 shows the concept of the reactor which is selected as the most rational one as the result of design study for few years. A containment vessel is filled with water and a reactor vessel is covered with water-tight shell is placed in it.

Engineered safety systems can be simplified as shown in Fig.4.2.3.

Reactor Shutdown System

The shutdown systems are redundant as follows;

- 1) Passive shutdown system: poison injection system by natural convection with hydraulic pressure valves. The valve will be opened passively in the case of main coolant pump failure due to loss of pump delivery pressure.
- 2) Active shutdown system: active poison injection by closing a valve on the pump delivery pressure transmission line.
- 3) Scheduled shutdown system: active poison injection from outside of the containment vessel.

Passive Safety Features

High passive safety characteristics can be assured by the following:

- 1) Large rapid reactivity insertion is not possible because of absence of control rod.
- 2) Highly reliable passive reactor shutdown system is employed as explained above.
- 3) Grace period before core dry-out in the case of LOCA is very long by the virtue of absence of large size piping and large inventory of primary coolant.
- 4) Core flooding can be always kept by pressure balanced injection system which is passively actuated when water level in the reactor vessel comes down to certain level.
- 5) Passive system (heat pipe type cooler) is employed also for containment water cooling.

* Ishikawajima-Harima Heavy Industries Co. Ltd.

Controllability of Reactor

Excellent operational characteristics of SPWR is achieved by the followings;

- 1) Reactivity change due to fuel burn-up is slow and periodical control of boron concentration is enough for its compensation.
- 2) Rapid load change can be followed-up automatically by negative power coefficient.
- 3) Daily load change will be also followed-up without changing boron concentration in primary coolant.

References

- 1) Sako, K et al. "Passive Safe Reactor SPWR", ANP'92 (Oct. 1992, Tokyo), P5-2.
- 2) Araya, F et al. "Safety Analysis of Highly Passive Safe Reactor SPWR", ibid. P17-2.
- 3) Oikawa, T et al. "Design Review of SPWR with PSA Methodology, ICONE-2 (Mar. 1993, San Francisco).

Table 4.2.1 Major Parameters of SPWR Plant

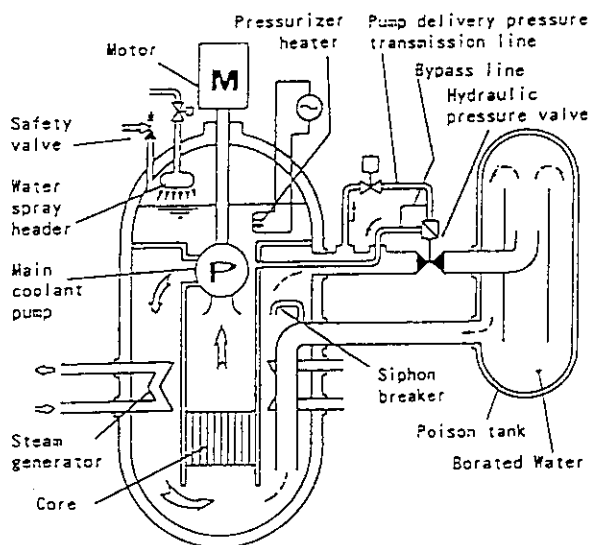


Fig.4.2.1 Basic Concept of SPWR

NET ELECTRIC POWER	600MWe
REACTOR POWER	1,800MWt
REACTOR COOLANT	
Operating pressure	13.8MPa
Core inlet/outlet temp.	290/320°C
Coolant Flow rate	44,400t/h
Core pressure drop	0.05MPa
SG pressure drop (1ry)	0.11MPa
Total pressure drop	0.19MPa
CORE	
Equivalent core dia./height	3.83/2.40m
Core average power density	65MWt/m ³
No. of fuel assemblies	199
Total Uranium inventory	71t
235U enrichment	4.5%
Core average fuel burn-up	48GWd/t
FUEL ASSEMBLY	
Lattice pitch (triangle)	259mm
No. of fuel rods	325
Rod dia./pitch(triangle)	9.5/14.0mm
MAIN COOLANT PUMP(Involute type)	
No. of pump	1 unit
Rotating speed	600rpm
NPSH	24m
Motor power	4.6MWe
STEAM GENERATOR	
(Once-through helical coil type)	
No. of headers	2 sets
Steam temp./pressure	295°C/5.5MPa
Feed water temp./pressure	210°C/6.5MPa
Steam flow rate	3,260ton/h
No. of heat transfer tubes	5,384
Material of tube	Incolloy 800
Tube outer/inner dia	19/15mm
Heat trans. area (inner, total)	17,000m ²

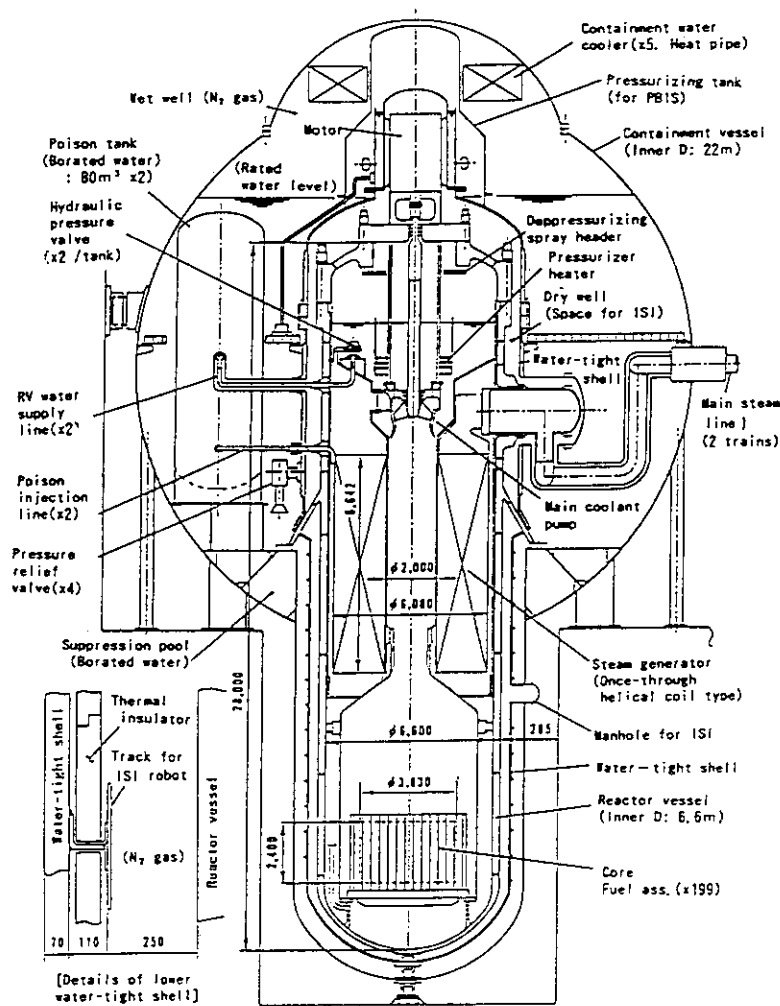


Fig.4.2.2 Concept of SPWR Plant (1800MWt)

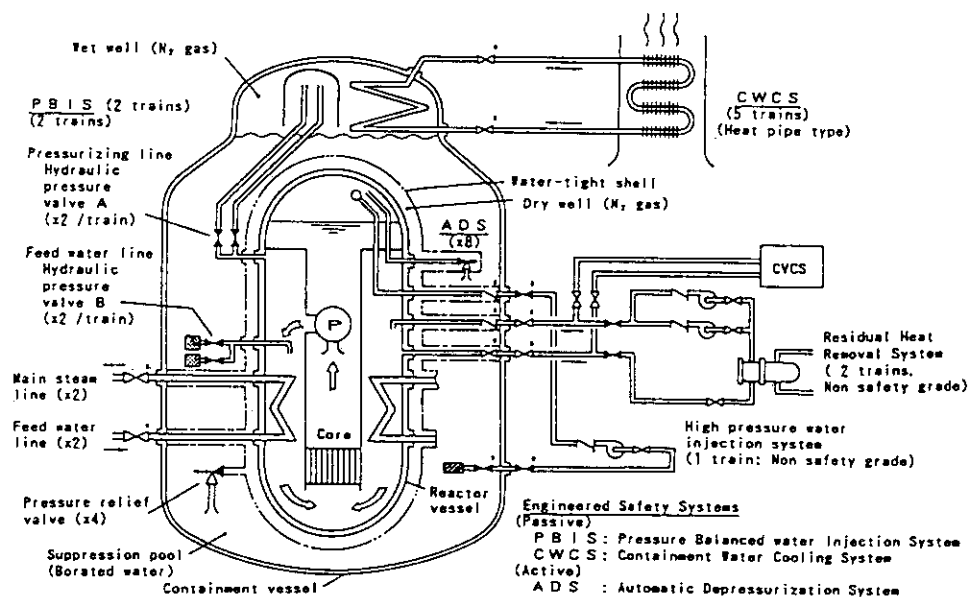


Fig.4.2.3 Engineered Safety Systems

4.3 A New Concept of Once-through Type Plutonium Burning

H.Akie, T.Muromura and H.Takano

For the burning of excess plutonium by the nuclear weapons reduction, a new concept of once-through type nuclear fuels was studied from the viewpoint of phase relations of ceramic materials, their thermodynamic properties, and their burnup characteristics.

As a once-through type fuel of Pu burning, it is likely that a two-phase mixture of fluorite-type phase and alumina has favorable characters. The fluorite-type phases, thorium (ThO_2) and Gd_2O_3 -stabilized zirconia ($\text{ZrO}_2(\text{Gd})$) seem to be acceptable due to their solid solubilities of Pu and some fission products, irradiation stability and chemical stability. The magnetoplumbite-type phase will be produced by the reaction between alumina and alkali and alkaline earth elements in the fission products during irradiation in LWR or FBR. The spent fuels finally obtained will become a stable waste form without any chemical and heat treatments, which would be able to bury under deep geological formations, as they are.

The burnup characteristics of these fluorite-type fuels (thorium and zirconia-gadolinia) were investigated for several LWRs in the range of the volume ratio of moderator to fuel (V_m/V_f) from 0.25 to 3.0, and for a typical sodium cooled fast reactor. Cell burnup calculations were made for the pin cell models of these reactors. The cell calculations were performed with the SRAC system based on the JENDL-3 nuclear data. The Pu composition with Pu-239 content of about 94% was assumed to be that from nuclear warheads.

The burnup dependence of total Pu amount calculated for ThO_2 type fueled LWRs are shown in Fig.4.3.1. In this figure, the Pu amount is normalized to the 1GW electric power. It can be observed from the figure that the amount of Pu survival increases with smaller V_m/V_f values. This is because of the larger initial Pu inventory in LWR of the smaller V_m/V_f value to obtain the same burnup rate as the cases of larger V_m/V_f . Figure 4.3.2 describes the burnup change of the Pu isotope composition in LWR of $V_m/V_f=1.9$. More than 95% of Pu-239 can be transmuted in this reactor, and the amount of Pu-242 increases. In the spent fuels, the Pu quality becomes completely poor. The burnup characteristics of Pu in LWRs with the $\text{ZrO}_2(\text{Gd})$ type fuel have a similar tendency to the ThO_2 fuel case. It was calculated that 98% of Pu-239 can be transmuted in LWR of $V_m/V_f=1.9$.

The total Pu amounts in ThO_2 - PuO_2 fueled FBRs of the different enrichments are compared in Fig.4.3.3. Though the initial Pu inventory is not so large as compared with the LWRs of the same fuel, a large amount of Pu survives even at the burnup rate of 100GWd/t. In fast reactors, the fission cross section of Pu-239 is smaller than that in LWRs. In order to achieve a high burnup rate, much higher Pu enrichment is needed than the cases in LWRs. As a result, Pu surviving rate is also higher than in LWRs. On the other hand in fast reactors, the fission/absorption ratio of Pu is high, and the production rate of higher Pu isotopes, Am and Cm is much smaller than in LWRs. From these reasons, fast reactors are suitable not for once-through Pu burning, but for Pu recycling.

From the burnup characteristics of the fuels, LWRs with the larger V_m/V_f value than 1.4, such as conventional LWRs($V_m/V_f=1.9$), are considered to be suitable for the once-through Pu burning. The PuO_2 - $\text{ZrO}_2(\text{Gd})$ - Al_2O_3 fuel has, however, the problem of positive void reactivity. The Doppler reactivity and the delayed neutron fraction are to be studied, and the small delayed neutron fractions can be deduced for both fuel types. Because of these problems, the heterogeneous reactors will be studied, where the ThO_2 - PuO_2 - Al_2O_3 or PuO_2 - $\text{ZrO}_2(\text{Gd})$ - Al_2O_3 fuels are partially charged in the core region.

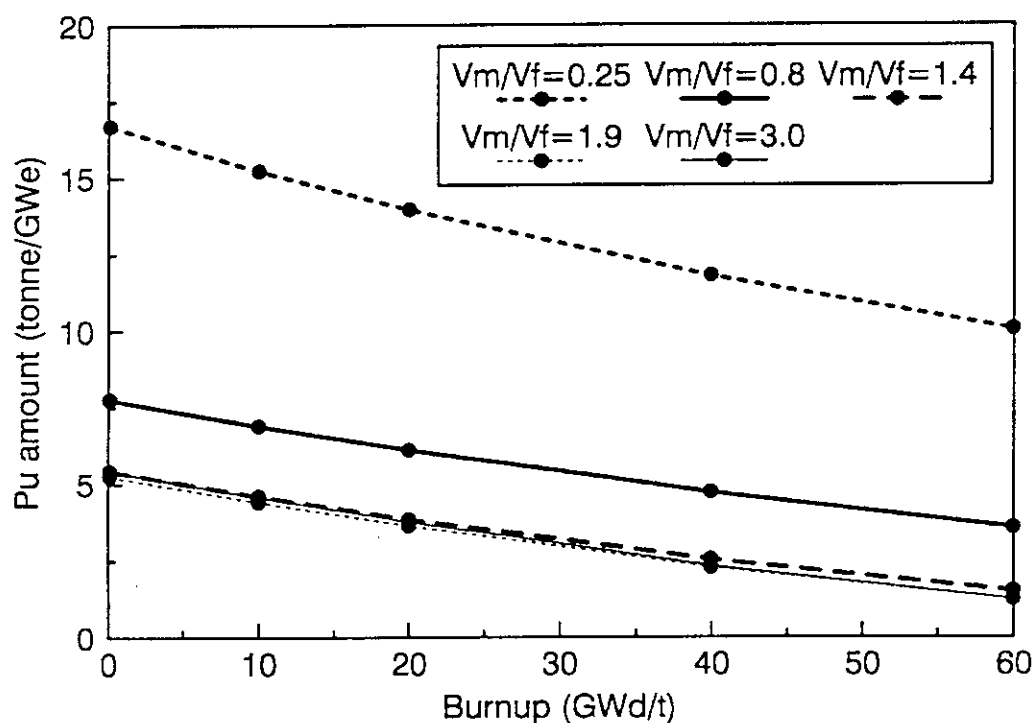


Fig. 4.3.1 Burnup dependence of total Pu amount in ThO_2 - PuO_2 fueled LWRs

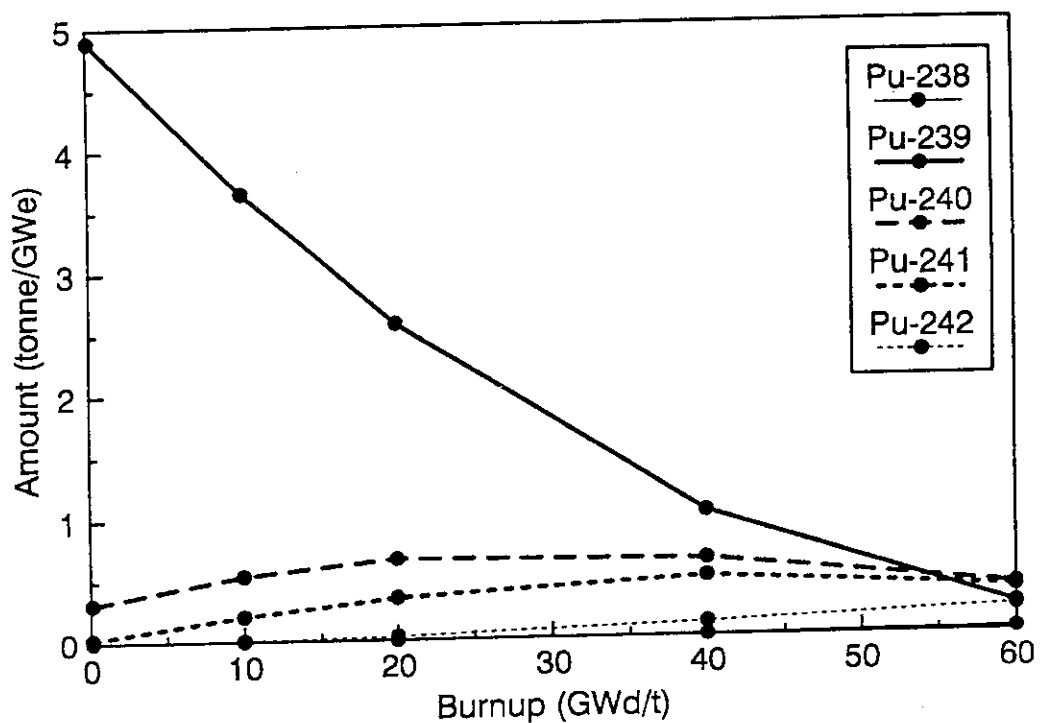


Fig. 4.3.2 Burnup change of Pu composition in $\text{ThO}_2\text{-PuO}_2$ fueled LWR of $V_m/V_f=1.9$

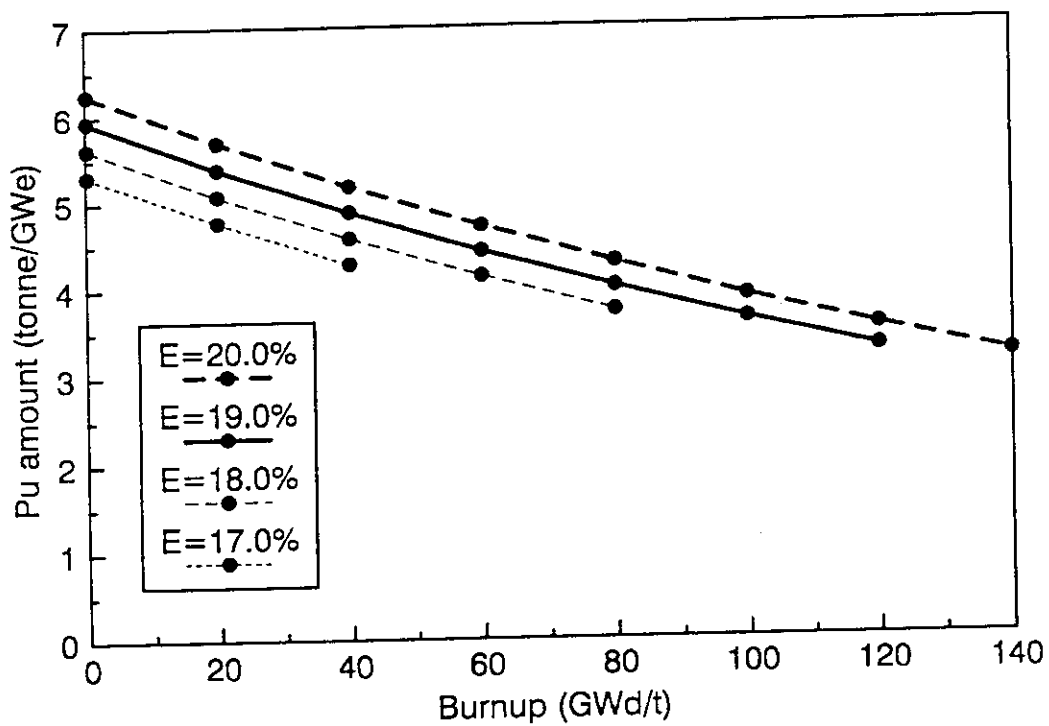


Fig. 4.3.3 Burnup dependence of total Pu amount in FBR of $\text{ThO}_2\text{-PuO}_2$ fuel

4.4 A Concept of Passive Safety Light Water Reactor System Requiring Reduced Operational and Maintenance Efforts

Y. Murao, F. Araya, T. Iwamura, K. Kunii and H. Watanabe

The reduction of manpower in operation and maintenance and influence of human errors on reactor safety are essential to improve the safety of future light water reactors. For this purpose a concept of a passive safety reactor requiring reduced maintenance efforts is proposed.

In the concept, the Nuclear Steam Supply System (NSSS) has a inherent matching nature of core heat generation and heat removal (inherent load following capability). Accordingly the reactor power can be naturally reduced by reducing feedwater flow rate or steam flow rate within an allowable steam temperature change. This enable to simplify a reactor control system and auxiliary system like a chemical and volume control system. In-vessel Control Rod Drive Mechanism (CRDM) units are adopted to eliminate chemical shim which makes the negative reactivity effect on moderator density weaker and low power density core and once-through steam generators are adopted to reduce the Doppler effect to minimize the change of steam generator exit temperature, respectively. The CRDM is developing at the Japan Atomic Energy Research Institute for a new nuclear marine ship concept¹⁾. In consideration of containing radioactive materials in the primary coolant system, a large volume pressurizer and passive residual heat removal systems are also adopted to realize the closed primary coolant system.

Figure 4.4.1 shows an image of the 600 MWe plant in this concept. The core size is fixed to be the same as the Westinghouse type PWR with three loops. The dynamic response of the NSSS was estimated with the RETRAN code by assuming that the reactivity coefficient is those for the end of cycle core of the SPWR²⁾. The results show that the core power generation rate is quickly follow the change of the heat removal rate without having significant pressure overshoot or undershoot and no inventory change in the primary coolant. This indicates that transients are considered to be roughly determined by quasi-steady state characteristics. From the estimated quasi-steady state response characteristics of primary loop on the change of heat removal rate in the NSSS of the reactor, a similar design of the B&W once-through steam generator³⁾(total heating tube length: 15.9 meters) with an extension of heating tube in 3.4 meters gives satisfaction of the criteria for temperature change of 8K in

the normal operation as shown in Fig.4.4.2. The control for reactor power, the volume in the primary coolant system, boron concentration becomes principally not necessary in the inherent power-cooling matching system. And some systems like the chemical and volume control system (CVCS) can be simplified and some systems can be eliminated.

A passive engineered safety feature system is adopted. In the system, the water from core makeup tanks is designed to be physically injected into the reactor pressure vessel as well as that from accumulator tanks. Only depressurization valves, main steam isolation valves, actuating valves for the containment spray systems, borated water injection valves for the back-up reactor shutdown system and back-up gravity water injection valves for severe core damage accidents are actively operated. The emergency diesel generator can be eliminated. And the engineered safety feature system does not require any systems or components of "safety class". Figure 4.4.3 shows the conceptual flow diagram of the primary system with passive engineered safety feature system. The most important points of this concept are: (1) By closing main steam line the core heat generation is physically interrupted in a short time. (2) Without considering the heat removal from the main steam line residual heat from the core can be removed by the residual heat exchanger systems and/or the in-containment air cooler. (3) The radioactive material can be contained in the NSSS in the tube failure event in the SGs.

By applying the inherent matching system and passive safety systems, the other systems like the CVCS can be simplified and some systems and components of "safety class" can be eliminated. Accordingly the present concept can be required reduced operational and maintenance efforts.

References

- 1) Ishizaka, Y., et al., Development of a Built-in Type Control Rod Drive Mechanism (CRDM) for Advanced Marine Reactor X (MRX), Proceedings of ANP'92, Vol. I, P4.6, Tokyo, Japan, Oct. 25-29, 1992.
- 2) Araya F., Sako K., Kim Y. and Kaneko K., Concept of Highly Passive Safe Reactor SPWR -2. Dynamic Analysis-, presented at International Specialists' Meeting on Potential of Small Nuclear Reactors for Future Clean and Safe Energy Source, TIT, Tokyo, Japan, Oct. 23-25, 1991.
- 3) Metropolitan Edison Co., Three Mile Island Nuclear Station-Unit 2, License Application, FSAR, DOCKET NO.50-320-73, April 1974.

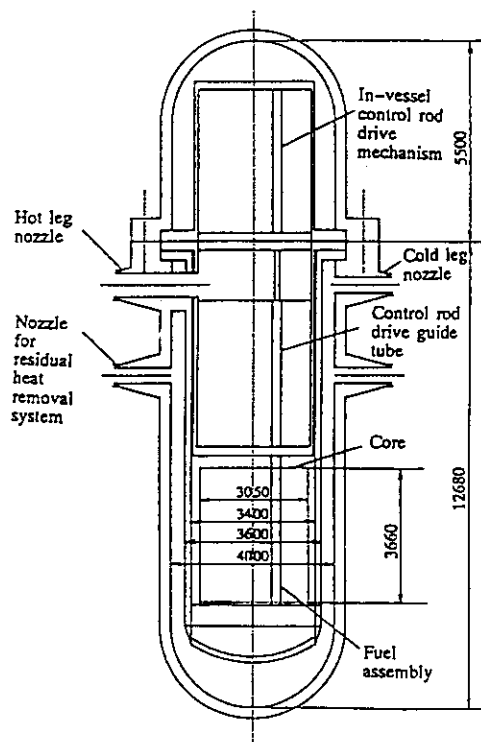


Fig. 4.4.1 Pressure vessel and internals

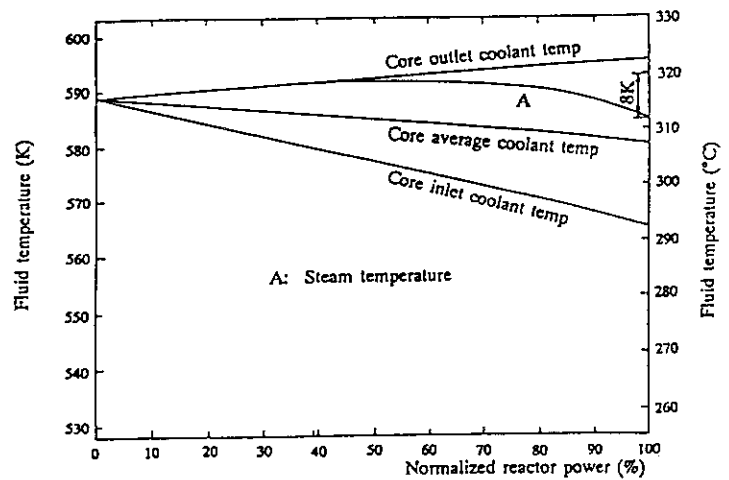


Fig. 4.4.2 Evaluated relation between reactor power and fluid temperatures

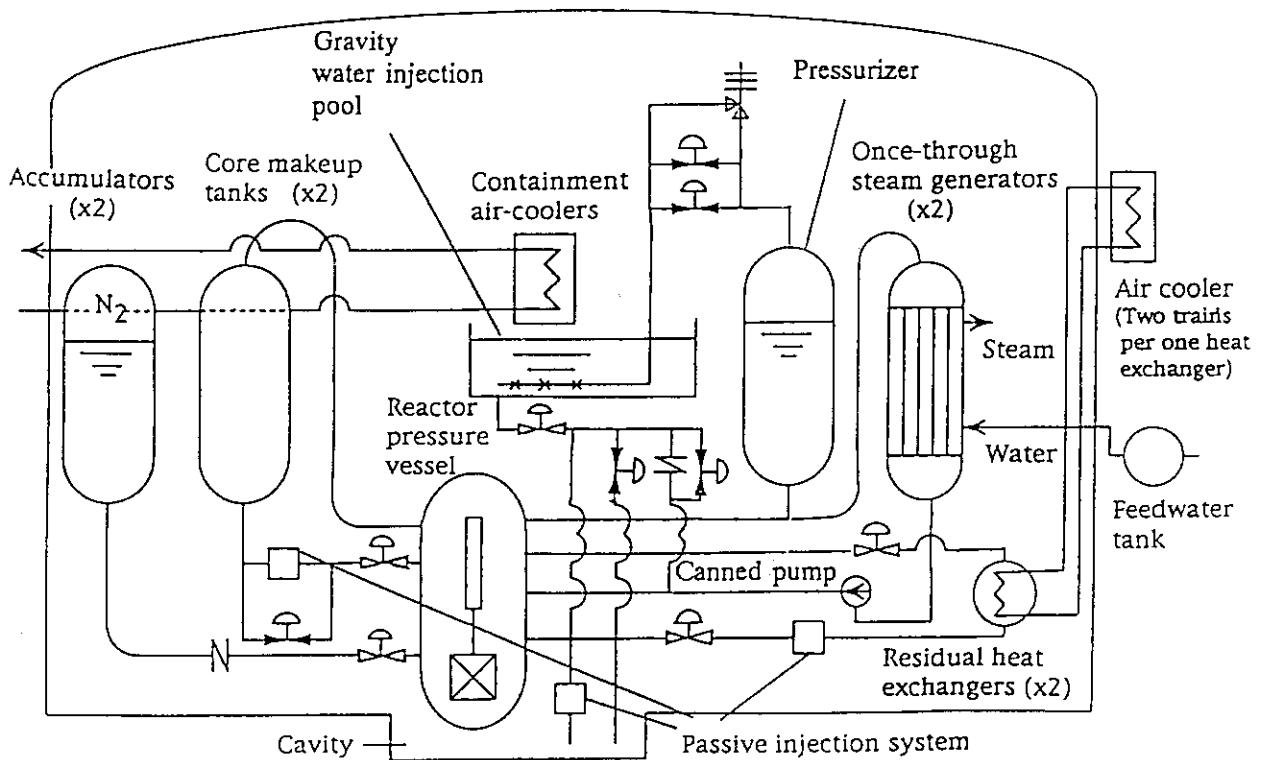


Fig. 4.4.3 Conceptual flow diagram of primary system with passive safety system

4.5 A Study on Possibility of a Reactor with Highly-load Following Capability

F. Araya and Y. Murao

A concept is being developed at Japan Atomic Energy Research Institute (JAERI) for realizing a passive safety reactor which requires less operational and maintenance works than ordinary light water reactors. In the concept, as well as a passive emergency core cooling system without actuating the pressure relief valves, it is sought to have an inherent matching nature of core heat generation and heat removal, that is, an inherent load following capability in the Nuclear Steam Supply System (NSSS) for the physical stability in operation and suppression of the core heat generation in emergency. In order to know the necessary conditions to establish such a capability, as the first step, possibility of a highly-load following reactor was investigated and the necessary conditions for not actuating pressure relief valves were identified.

Analyses are performed in the following steps; (1) a base case calculation is executed and the results are detailedly analyzed for understanding the load follow transients. And calculational conditions will be determined for further parametric calculations. (2) The parametric calculations are performed and the effects of the parameters are investigated. (3) Based on the analysis of calculated results, for base case calculation necessary conditions for a reactor concept with highly-load following capability were proposed and discussed.

The RETRAN-02 code¹⁾ was used for the calculations. The input data used in this study is based on that developed for the analysis of steam generator tube rupture event at the Mihama unit 2²⁾. The input data models only primary coolant system neglecting secondary coolant system in the present study. The heat removal from primary system to secondary system is modelled by the non-conducting heat exchanger model incorporated in the RETRAN-02, in which removed heat is directly removed from the primary coolant in the U-tube and is given by input data. Using this model, the load change is given by changing the heat removal rate. The load change rate is set to 100%/min, and the magnitude of the load change of 50% of full load is arbitrary determined.

As shown in Fig. 4.5.1, the core power follows the load change with some delay and undershoot. In a time delay A (about 4 seconds) after the initiation of load reduction, the power initiates to decrease, and in a time delay B (about 20 seconds) after the termination of load reduction, the power roughly approaches to the final value. The time delay A is

explained by the delay time t_1 due to the transportation of the fluid from the SG to the core which is estimated to be about 4 seconds. The time delay B is explained by the sum of time delays t_2 and t_3 . The time delay t_2 caused by the heat capacity of the primary coolant system is estimated to be 14 seconds for temperature rise of 17.3 K based on the mass inventory in primary system. Time delay t_3 necessary for the temperature rise of the fuel rods is about 5 seconds. As shown in Fig. 4.5.1, although the Power Operated Relief Valves (PORVs) are opened, the pressurizer pressure increases to the maximum pressure of 18.59 MPa (pressure rise of 2.56 MPa) at around 104 seconds. During this time period, the pressurizer experiences complete water filling.

Based on the analysis of base case results, the following parameter studies were performed and the effects of the parameters on load following capability were evaluated.

- (1) In the case of decreasing primary coolant volume, since the coolant temperature changes faster than the base case, the power transient is improved and also the pressure response is obviously improved.
- (2) The load following capability is improved by increasing absolute value of density reactivity coefficient. In the case of 1.4 times large reactivity coefficient than that of the base case, the improvement is best in the parameter study cases presented in this paper.
- (3) Decrease in linear heat generation rate has effect to improve load following capability.
- (4) In the case of increasing pressurizer volume, the pressure transient is improved, namely greatly stabilized due to increase in compressibility of the system. This pressure stabilization effect has also effect to improve load following capability during transient.
- (5) A reactor with better load following capability is realized by elimination of chemical shim for increasing absolute value of density reactivity and decreasing linear heat generation rate.

Based on the results of parameter studies, possibility of a reactor which can follow the load change without any actuation of components such as pressure control systems was investigated by performing the load following transient calculation with setting parameters so as to improve load following capability. The linear heat generation rate was set by the relatively lower value 17.9kW/m which was the same as the base case. The coolant density reactivity coefficient was set by that of SPWR³⁾ at EOC which was relatively large within the presently available data. Since the boron concentration at this time is, about 50ppm, relatively small, this reactivity coefficient was considered to be nearly equal to that for the pure water. The doppler reactivity coefficient was also set by using the SPWR data. The pressurizer volume was set as follows by a manner of try and error. The height of pressurizer was set to

1.5 times higher than that of original height, and the water level and cross sectional area in the horizontal plane were set to the original ones. It is namely that the steam volume was set to 2.2 times of original steam volume. As for the primary coolant volume, optimization of volume was not applied because this strongly depends on the reactor design. The calculated results are shown in Fig. 4.5.2 in which the base case results are also shown for comparison. Figure 4.5.2 shows that a reactor which can follow 50% load change without any actuation of control system would be realized by increasing pressurizer volume by 1.5 times of original design, and setting the reactivity to that of SPWR at EOC. Although the calculated results were not shown here, it was also found that the reactor can follow the overcooling transient up to 120% of full load without any safety problem such as DNB occurrence.

References

- 1) Peterson C. E., McFadden J. H., Paulsen M. P. and Gose G. C., RETRAN-02 - A Program for Transient Thermal-Hydraulic Analysis of Complex Fluid Flow Systems, EPRI NP-1850-CCM, (May 1981).
- 2) Hirano M. and Sun J., Analysis of Mihama-2 Steam Generator Tube Rupture (SGTR) Event (Preliminary Analysis), JAERI-M 92-060, (April 1992) (in Japanese).
- 3) Sako K, Oikawa T., Iida H., Oda J., et al., Concept of Highly Passive Safe Reactor SPWR, Presented at the SR/TIT International specialists' Meeting on the Potential of small Nuclear Reactors for Future clean and Safe Energy Sources, Tokyo, Japan, Oct. 23-25, (1991).

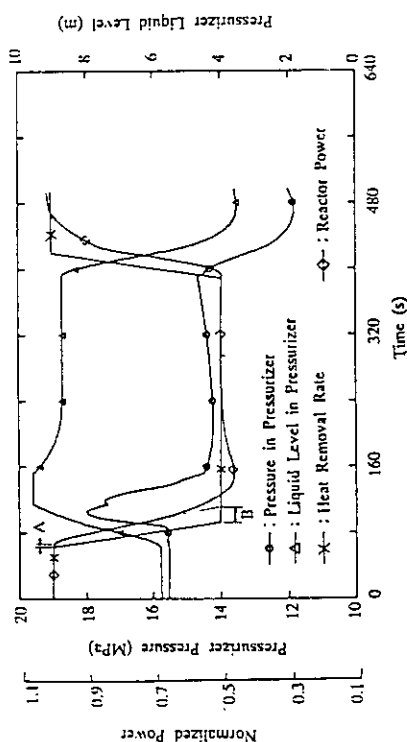


Fig. 4.5.1 Histories of heat removal, core power, pressurizer pressure and liquid level in base case.

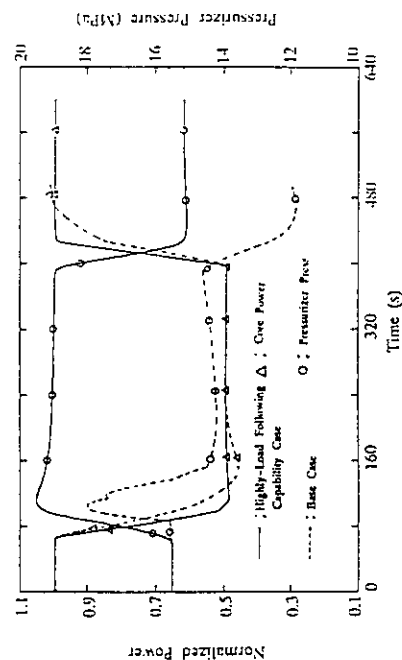


Fig. 4.5.2 Comparison of optimized parameter case and base case.

5. Fusion Neutronics

The year of 1992 seemed to be a turning point for the fusion neutronics activities at JAERI. After the first D-T neutrons were generated by the Fusion Neutronics Source facility (FNS) in August, 1981, many and excellent results have been produced by FNS. The FNS facility is entering into the second 10-year period. At the same time, the agreement of International Thermonuclear Experimental Reactor/Engineering Design Activity (ITER/EDA) was signed by the four parties, Japan, US, EC and Russia in July, 1992. The second international comparison on measurement techniques of tritium production rate was completed under the frame work of NEA/NSC activity and the final report has been published.

Some supplemental experiments for Phase-IIIA, -IIIB and nuclear heating of the JAERI/USDOE Collaborative Program on Fusion Blanket Neutronics were performed in April and July, 1992, and all of experiments relevant to the Collaboration have been completed. Since this JAERI/USDOE Collaboration will be completed in October, 1993, the Program entered into the final stage, namely, our main efforts payed to summarizing, evaluating and reporting of results. For example, influence of calculation parameters in the experimental analysis was examined using the results of the Collaborative Program. It is pointed out that the high energy flux calculation is affected by the group structure for whole region of experimental assemblies, while the low energy flux calculation is locally oscillated in the heterogeneous region depending on the P_L expansion and spatial mesh. Integral tests of the JENDL Activation file and the REAC*3 libraries were also carried out using the results of a series of experiments on induced activities. As this type experiment is unique and only one in the world, the data are expected very much for applying to the integral tests of the other activation files.

To obtain the benchmark data on copper, an integral experiment was performed on a copper cylindrical slab assembly. The measured parameters were similar to those of previous experiments. Two types of measurement techniques have been developed. One is the technique for the neutron spectrum in the energy region of eV using a BF_3 proportional counter. This technique is based on the relation between slowing down time and mean neutron energy. The other is the improvement of neutron measurement technique for DD plasma diagnostics. As the result of applying the fast digital signal processing to the pulse shape analysis of a ^3He gas proportional counter, a better data processing was obtained such as pulse pile-up correction, dynamic and optimum noise reduction and so on.

As a new international collaboration, the Subtask of "Neutronics" will be started soon in 1993 under the IEA Co-Operative Program on Nuclear Technology of Fusion Reactors. For this purpose, we have began the discussion about the collaboration.

(Hiroshi Maekawa)

5.1 Benchmark Experiment on Copper Slab Assembly Irradiated by D-T Neutrons

F. Maekawa, Y. Oyama, C. Konno, Y. Ikeda, J. Pulpan and H. Maekawa

Copper is a main element widely used for material of fusion devices, e.g., for superconductive magnets and various electrical instruments. Benchmark experiments under a D-T neutron environment were performed and they were analyzed. Nuclear data libraries and transport codes used in the analyses were verified by comparing the analyses to the experiments.

A copper slab assembly in cylindrical shape, 630 mm in diameter and 608 mm in thickness, was placed at 200 mm from the tritium target of the 80° beam line of Fusion Neutronics Source (FNS). Hitting the target with d^+ beam of 350 keV, D-T neutrons of 14.8 MeV at peak energy were generated. The assembly was bombarded with the D-T neutrons to obtain the following benchmark data; i) neutron spectra above 1 MeV by a liquid organic scintillation detector NE213 and those between 3 keV and 1 MeV by proton recoil gas proportional counters, ii) reaction rates such as the $^{27}\text{Al}(n,\alpha)^{24}\text{Na}$, $\text{Cu}(n,x)^{64}\text{Cu}$, $^{93}\text{Nb}(n,2n)^{92m}\text{Nb}$, $^{115}\text{In}(n,n')^{115m}\text{In}$ and $^{197}\text{Au}(n,\gamma)^{198}\text{Au}$ reactions, by the foil activation method, iii) gamma-ray spectra by the NE213 and iv) gamma-ray heating rates by TLD. They were measured at positions of 0, 76, 228, 380 and 532 mm from the target side surface of the assembly.

The continuous energy Monte Carlo code MCNP-4 and the two-dimensional SN code DOT-3.5 were employed for the analyses. The FSXLIB-J3 cross section library was used for MCNP. For DOT analyses, the JSSTD and FUSION-J3 libraries were used. Both libraries for DOT had the same group structure of neutron 125 and gamma-ray 40 groups, but the self shielding correction factors were considered only in the former. All the three libraries were based on JENDL-3 revision 1. In addition, the FENDL library¹⁾ which was compiled by IAEA was used for DOT analysis. The number of groups of it was 175 for neutron. Because of some troubles in nuclear data processing codes, the self shielding correction factors could not be taken and gamma-rays could not be calculated in the FENDL analysis. JENDL-3 Dosimetry File was commonly used to calculate reaction rates through out the analyses.

Calculated to experimental values, C/Es, of $^{93}\text{Nb}(n,2n)^{92m}\text{Nb}$ reaction are shown in Fig. 5.1.1. Since all the C/Es range between 0.97 and 1.15, all the calculations predict adequately penetration of 14 MeV neutrons up to 532 mm in depth. When the C/Es are examined in detail, FENDL is in better agreement with the experiment than JENDL-3.

Figure 5.1.2 shows the measured and calculated neutron spectra. At 76 mm in depth, all the calculated spectra below 1 MeV are larger than the experiment; all C/Es for integrated flux between 3 keV and 1 MeV are 1.3 ~ 1.4. At 532 mm in depth, all the calculated spectra

between 0.1 MeV and 1 MeV are 30 % smaller than the experiment. As for the spectrum between 3 keV and 10 keV, MCNP calculation is 50 % larger than the experiment, and peaks and valleys in the spectrum calculated by DOT with JSSTD L are overemphasized. In summary for neutron data in JENDL-3 and FENDL, penetration of 14 MeV neutrons is almost satisfactory, but as for low energy region below 1 MeV, there are still some needs to make an improvement for cross sections.

Gamma-ray spectra at 228 mm are shown in Fig. 5.1.3. Agreements between two calculations and experiment are good in the energy range lower than 6 MeV. A peak around 8 MeV observed in the experiment, which corresponds to direct transitions from the capture state to the ground state after radiative neutron capture reactions, however, is not expressed in both calculations. This fact implies that energy distributions of secondary gamma-rays from the capture reaction are not appropriate for natural copper in JENDL-3.

Reference

- 1) Ganesan S. and Muir D. W.: "FENDL Multigroup Libraries", IAEA-NDS-129 (1992).

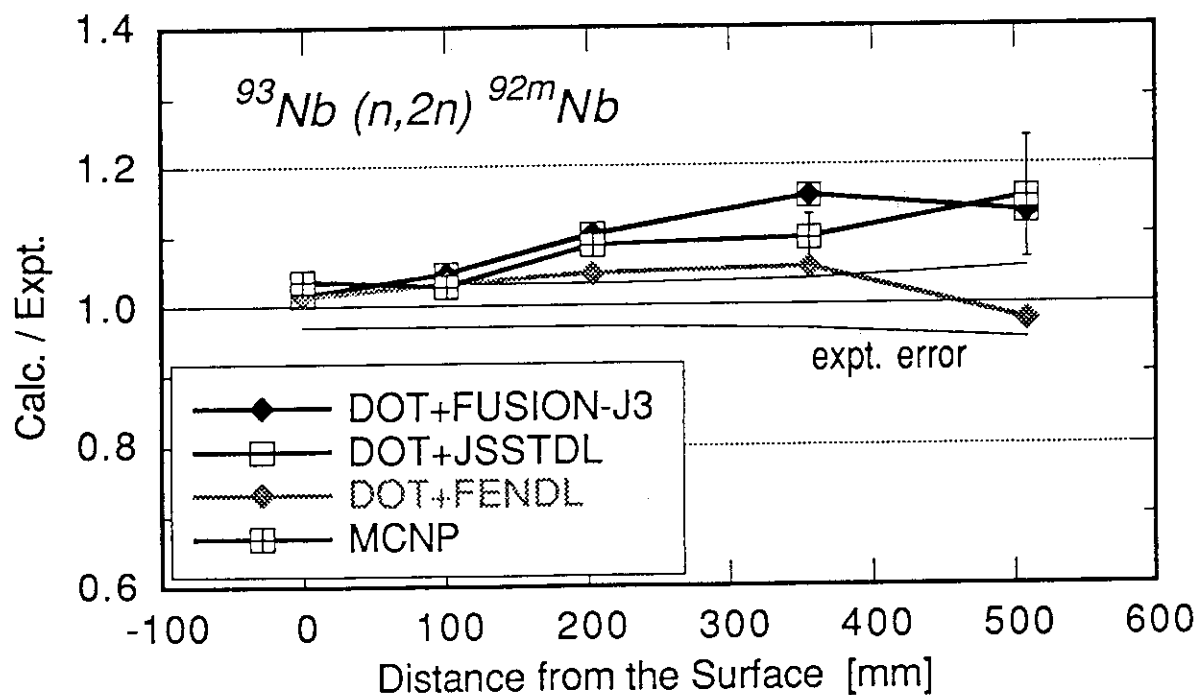


Fig. 5.1.1 Calculated to experimental values of $^{93}\text{Nb}(n,2n)^{92m}\text{Nb}$ reaction rate

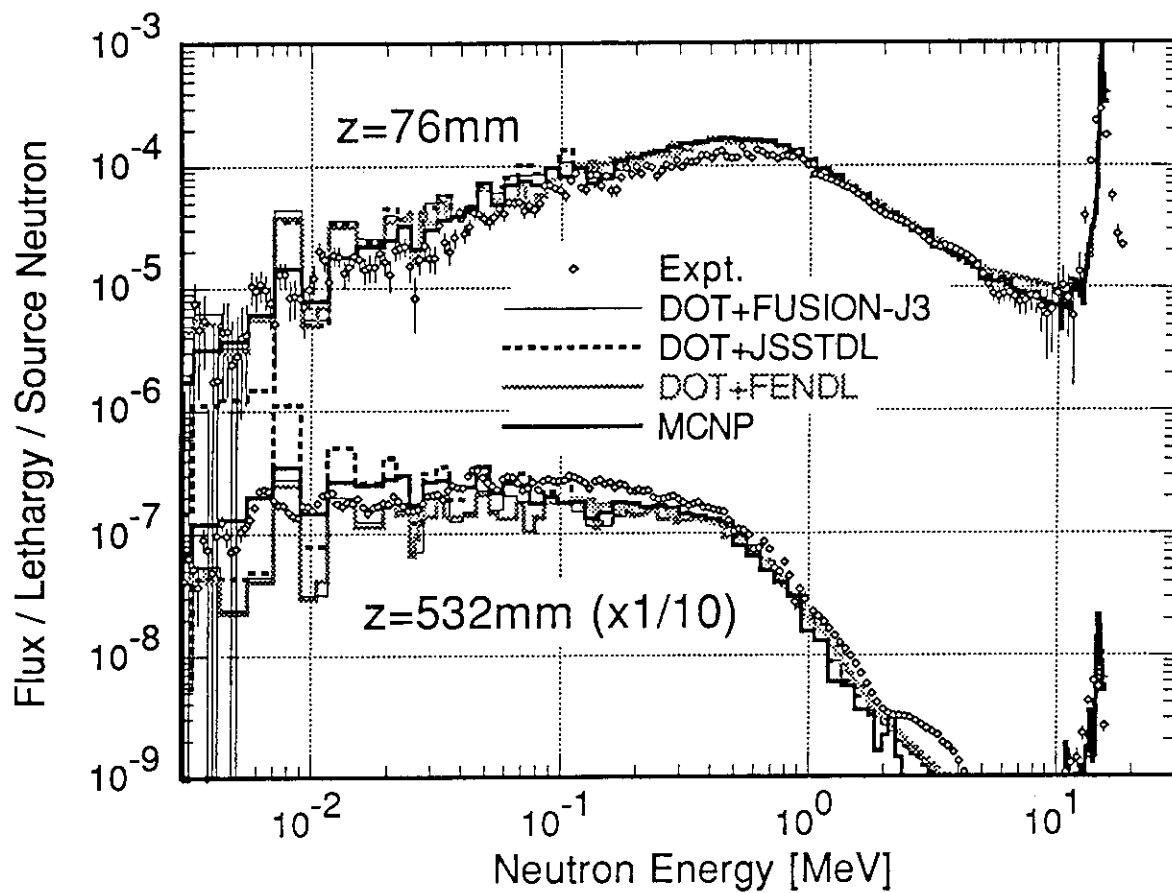


Fig. 5.1.2 Measured and calculated neutron spectra at 76 mm and 532 mm from the front surface of the assembly

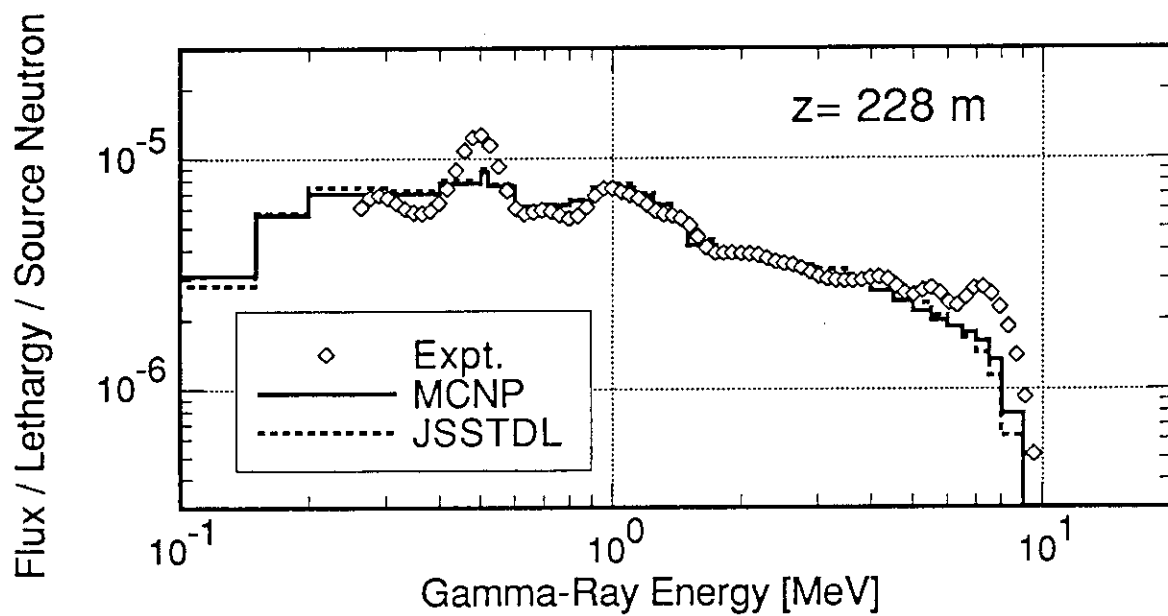


Fig. 5.1.3 Measured and calculated gamma-ray spectra at 228 mm from the front surface of the assembly

5.2 Influence of Calculation Parameters in Analyses for Blanket Neutronics Experiments of JAERI/USDOE Collaborative Program

Y. Oyama, K. Kosako*, C. Konno, Y. Ikeda, F. Maekawa, H. Maekawa

All experiments of the JAERI/USDOE collaborative program of fusion blanket neutronics have been completed by the series of Phase III experiments with the line source and the annular blankets. This collaborative program aimed at evaluating prediction accuracy of nuclear parameter calculation for a fusion reactor design. For these experiments, analyses by transport calculation codes progressed in this period of FY1992. A discrete ordinate S_N code such as DOT3.5 has been most frequently used in these calculations. Usually, it is necessary to optimize the calculation parameters in the analyses in terms of the mesh size, the number of groups and so on. Since the experimental systems have a variety of configurations by materials with completely different cross sections, a parametric study of these calculation parameters through the analyses of the experiments can provide very useful information for application of the calculation code to problems in the design.

Parametric calculations were carried out with the DOT3.5 code for four experimental assemblies with a closed geometry selected from the Phase II experiments,^{1,2)} i.e., the homogeneous assembly (Phase-IIA reference), the beryllium sandwiched assembly (Phase-IIA BES), the beryllium lined assembly (Phase-IIB BEF) and the water cooling channel assembly (Phase-IIC WCC). The DOT3.5 was vectorized (version-3) for speed-up and proved to give consistent results within 1-2% with the original one. The standard calculation parameters applied through the collaboration were determined by practical consideration of computer resources at the early stage of the experiment. However, a computer ability has progressed during the collaboration period, so the parametric survey became paractical. These parameters subjected were FUSION-J3 (P5-125 groups) cross section set, S-10 angular quadrature set and average mesh size of 5 mm. These parameters were changed to compare the calculated results with the standard calculations. Table 5.2.1 summarizes the examined parameters and their variations.

Influence of group structure (number of group) is shown in Fig. 5.2.1 for reaction rates with different energy responses. The figure shows the results for the reference assembly; the high threshold reaction rates calculated by FUSION-40 (42 groups) tend to decrease with the depth, while the capture reaction sensitive to lower energy overestimates the reaction rates at the front region and decreases with the depth. The influence of the order of Legendre expansion in the BES assembly is shown in Fig. 5.2.2 for the same group structure of 125 groups. There are large differences of reaction rates for the $Au(n,\gamma)$ and ${}^6Li(n,\alpha)$ reactions in the beryllium and lithium carbonate regions between calculations with the P-5 and the P-7 expansions. Selection from angular quadrature sets of S-10 and S-16 has a small impact on

* NEDAC, Nuclear Energy Data Center

the calculated results as shown in Fig. 5.2.3. The effect less than 5% was found especially on the low energy reactions at the material boundary. The influence of the spatial mesh sizes is conspicuous at the heterogeneous region such as coolant channels. Figure 5.2.4 shows the effects of various mesh size selections. The mesh size of about 5 mm was chosen for the standard calculation. Since the mean free path of thermal neutron is about 2.5 mm in the lithium oxide, the 2.5 mm mesh calculation is expected to be the best result. The mesh size larger than 10 mm shows an enhancement of ${}^6\text{Li}(n,\alpha)$ reaction rate at the moderated region of coolant, because the flux gradient are too large inside the mesh. This influence spreads to a range of 2-3 meshes.

In conclusion, the high energy flux calculation is influenced by the group structure for the whole region of experimental assembly, while the low energy flux calculation is locally oscillated in the heterogeneous region largely depending on the P_L expansion and the spatial mesh. These general guides can be applied to design calculations, but the further study is necessary to obtain the best sets of parameters from wider parameter space, including the other optimizing parameters such as weighting function and self-shielding correction factor for group cross sections. Also a similar study of optimization guide is desired for a Monte Carlo code.

References

- 1) Oyama Y., et al.: "Phase IIA and IIB Experiments of JAERI/USDOE Collaborative Program on Fusion Blanket Neutronics --- Neutronics Experiments on Beryllium Configuration in a Full-Coverage Blanket Geometry ---," JAERI-M 89-215 (1989).
- 2) Oyama Y., et al.: "Phase IIC Experiments of the JAERI/USDOE Collaborative Program on Fusion Blanket Neutronics --- Experiments and Analysis of the Heterogeneous Fusion Blanket ---," JAERI-M 92-182 (1992).

Table 5.2.1 Calculation parameters for the DOT3.5 code

	Standard	Variation
Group structure	FUSION-J3 (125 groups)	FUSION-40 (42 groups)
P_L order	P-5	P-7
Quadrature set S_N	S-10	S-16
Spatial mesh size	5 mm	2.5, 10, 20 mm

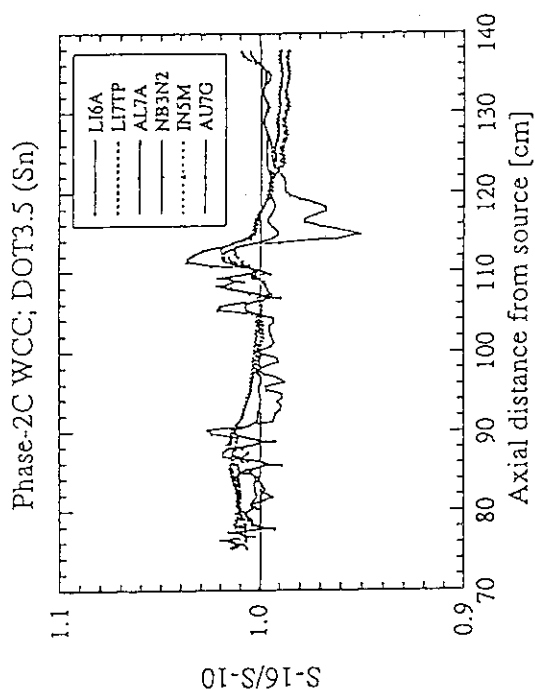


Fig. 5.2.3 Ratio of the S-16 calculations to the S-10.

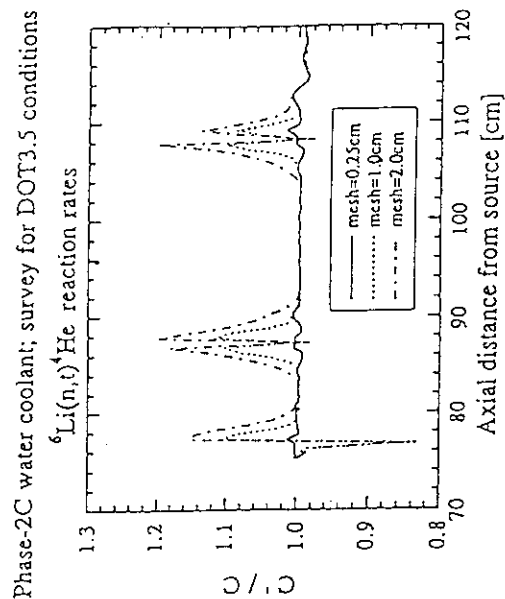


Fig. 5.2.4 Ratios of the calculations with various mesh sizes to the standard calculation.

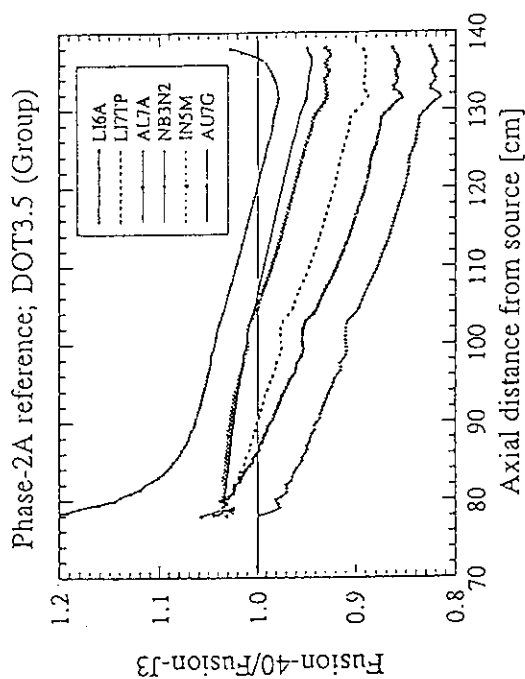


Fig. 5.2.1 Influence of group structure of FUSION-40 to FUSION-J3.

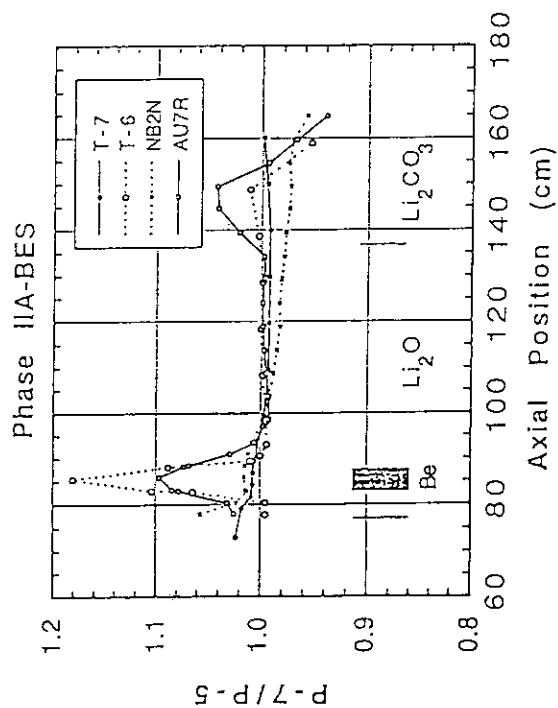


Fig. 5.2.2 Effect of higher order of Legendre expansion. Ratio of the P-7 calculations are plotted to the P-5.

5.3 Integral Tests of the JENDL Activation File and the REAC*3 Libraries for Fusion Applications

Y. Ikeda, A. Kumar*, C. Konno, K. Kosako**, Y. Oyama, H. Maekawa,
M. Z. Youssef* and M. A. Abdou*

Induced radioactivity due to D-T fusion neutron is an important factor in terms of reactor safety consideration and radioactive waste management. A series of experiments on the induced radioactivity¹⁾ has been conducted in the framework of JAERI/USDOE collaborative program on fusion neutronics in order to offer the data base for the verification of currently available calculation code as well as relevant nuclear data. Meanwhile, an extensive effort has been devoted to evaluate the JENDL Activation File²⁾ in order to meet urgent requirement for more reliable activation calculation. The activation cross section file of REAC*3³⁾, also has been recently updated. It is strongly requested that the activation files should be validated from the fusion reactor development point of view. For the validation purpose, both JENDL and REAC*3 activation files along with the CROSSLIB library of THIDA code system⁴⁾ and the old version of REAC*3 library have been tested by using the integral experimental values obtained in the JAERI/USDOE collaboration.

In the present study, candidate structural materials for fusion reactor were focused on. Aluminum and Silicon are the major compositions for the Al alloy and SiC, pursuing low activation concept. Titanium, vanadium and chromium are the compositions of vanadium alloy (V-5Cr-5Ti) addressed in a comprehensive ITER design. Iron, nickel, again chromium, manganese are the elements common in austenite steels, e.g. SS-316. Importance of cobalt is recognized as impurity in almost all material, which brings long-live ⁶⁰Co. Copper is also major materials used in many parts of device. Figure 5.3.1 shows the two neutron spectra, namely A and B, calculated by MORSE-DD with JENDL nuclear data library. Emission rates of γ -rays which associated with specific radioactivities of interest are used as the experimental values to be compared with calculations.

The libraries and calculation code, presently examined are (a) multigroup activation cross sections with 125 energy bins based on the JENDL activation file[JENDL], (b) CROSSLIB90 with 42 energy groups[LIB90], (c) cross section data file with 63 multigroup in REAC*3 code system [Reac*63] and (d) updated cross section library with 175 multigroup (VITAMIN-J format) for REAC*3 code system [Reac175]. Calculations were carried out for all materials at two neutron spectrum fields with different irradiation time, short and long. Adequacy of cross sections pertinent to production of each radioactivity are examined through C/E analyses for all cases. The results of experimental analyses are given as

* Fusion Reactor Engineering Laboratory, UCLA

** Nuclear Energy Data Center

material wise and isotopic radioactivity products wise. As the limited space of this report, a demonstrative example of analysis is given only for ^{24}Na in Al.

The reaction of $^{27}\text{Al}(n,\alpha)^{24}\text{Na}$ is one of most accurately studied and cross section has been evaluated precisely. The JENDL gives most preferable results with C/Es around 1.0. **Reac*63** shows comparably good results. **LIB90** is slightly larger than 1.0 by 10 %. The cross section of **Reac*175** is very close to those of JENDL and **Reac*63**. However, C/E with **Reac*175** is 1.3 to 1.4 for all cases. This overestimations are due to contribution of $^{27}\text{Al}(n,\alpha)^{24m}\text{Na}$. The ^{24m}Na is the isomeric state of ^{24}Na and deexcites to the ground state of ^{24}Na with 2 ms half-life. In the **Reac*175**, both reactions are separately treated. However, in general, the cross section of $^{27}\text{Al}(n,\alpha)^{24}\text{Na}$ is given as a sum of both the metastable and ground state productions. In this view, the cross section of $^{27}\text{Al}(n,\alpha)^{24m}\text{Na}$ is doubly counted in the **Reac*175** library. Although different reaction passes should be treated independently as in the **Reac*175** from the completeness, the cross section for the metastable state production should be subtracted from the ground stated production cross section.

All C/E values studied here are plotted in Fig. 5.3.2 to give uncertainty ranges of radioactivity calculations. Almost all C/Es fall in between 0.5 and 1.5, though some of them exhibit extremely high values exceeding a factor of 5 and low values less than 0.1. From the dedicated analysis of each radioactivity, it was concluded that some cross sections are physically unreasonably installed in the library. Especially, several orders of magnitudes difference was found in the cross sections for rare exotic reactions, e.g., $(n,2p)$, $(n,n'\alpha)$. On the other hand, small C/E indicates that there is no corresponding cross sections in spite of importance of the reactions. These two aspects are caused from the completeness rather than quality. The present study demonstrates the importance of both sides, completeness and quality. In order to explain the disagreement, sometimes it is required to look into all possible reaction channels, even though these reactions are most unlikely to take place. To meet the requirement from completeness, we have to rely on model calculations base on some theoretical approach or reaction systematics. In general, these prediction method are reliable when sufficient experimental data are available. It is demonstrated that it is very dangerous to fully rely on the numbers derive from the calculation.

References

- 1) Ikeda, Y., et al. : "Joint Report of JAERI/USDOE Collaborative Program on Fusion Neutronics --Induced Radioactivity Measurements in Fusion Neutron Environment--," JAERI-M 93-018 (1993).
- 2) Nakajima, Y. : "JENDL Activation Cross Section File," JAERI-M 91-032 (1991) pp43-57.
- 3) Mann, F. : "REAC*3 Nuclear Data Libraries," Proc. Intl. Conf. on Nucl. Data for Sci. and Technol., Jülich, Germany, 12-17 May 1991, pp936-938.
- 4) Seki, Y., et al. : "THIDA-2: An Advanced Code System for Calculation of Transmutation, Activation, Decay Heat and Dose Rate," RSIC computer code collection, CCC-410(1987).

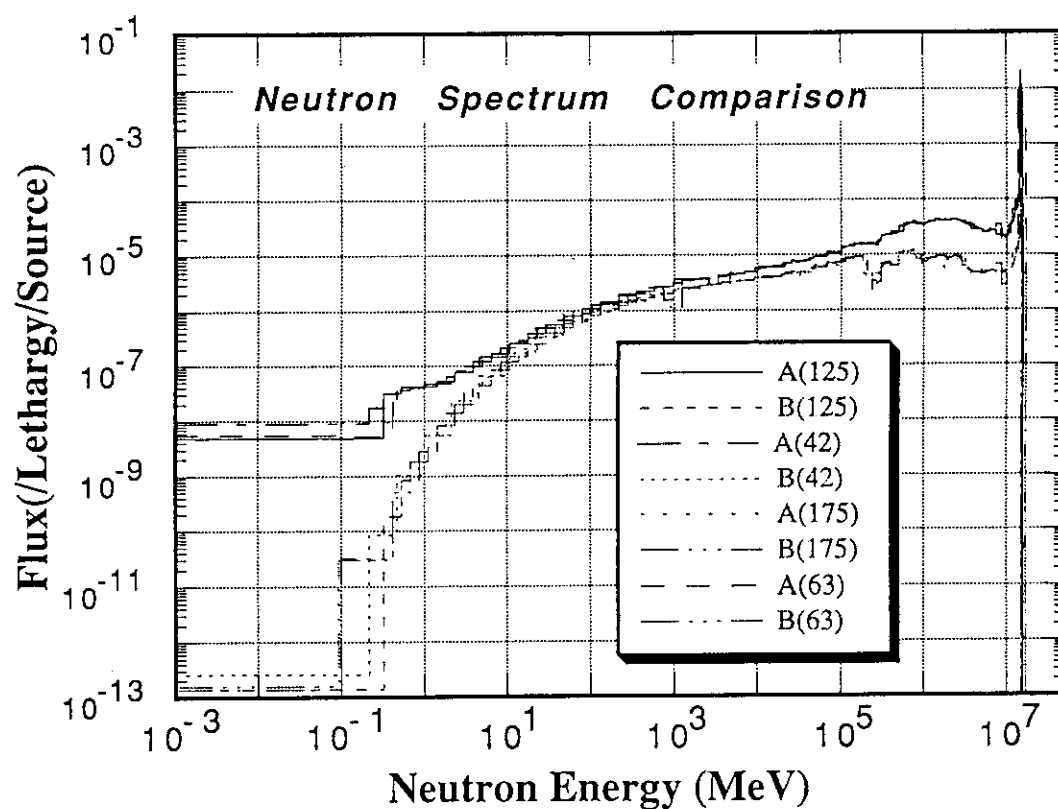


Fig. 5.3.1 Neutron spectra used for the present test of the radioactivity calculation.

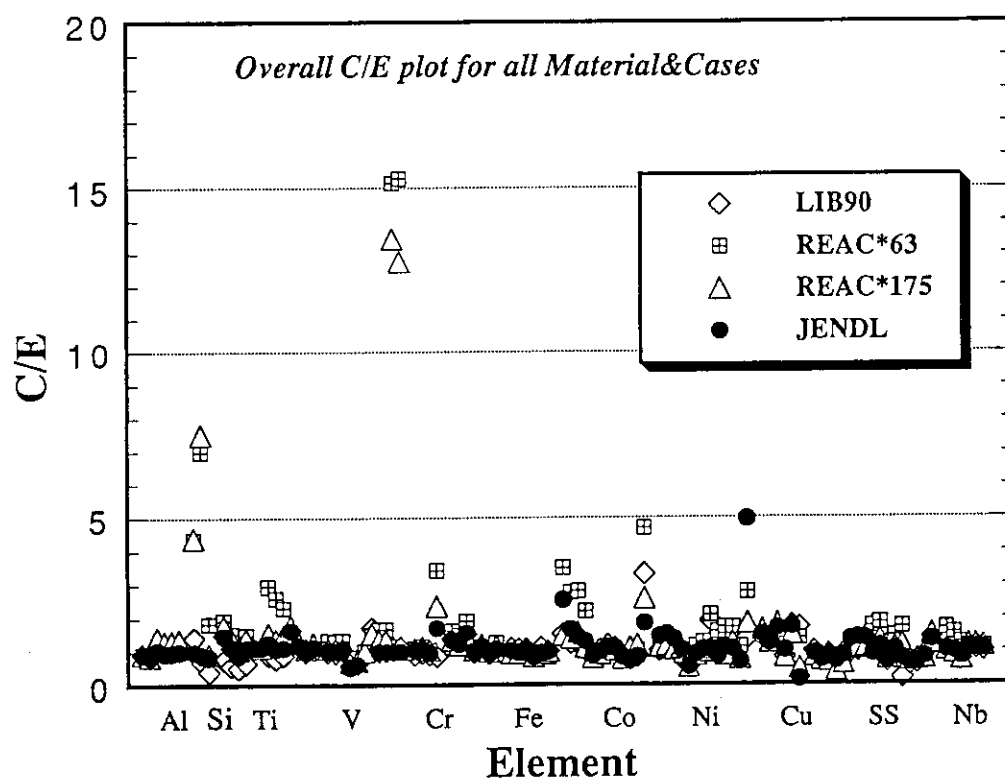


Fig. 5.3.2 Overall C/E plots for all radioactivities in each material cases with four libraries.

5.4 Development of Measurement Technique for Neutron Spectrum in Energy Region of eV in Large Assemblies

F. Maekawa and Y. Oyama

Spectra of eV energy are quite important to examine low energy neutron transport as well as gamma-ray production by radiative capture reactions. In the integral experiment for fusion neutronics, neutron spectra above about 1 keV are measured with the recoil proton method. Spectra below 1 keV, however, has been scarcely measured so far.

When pulsed mono-energy neutrons are injected into a large experimental assembly and we observe the neutron energy spectrum at a certain position in the assembly with passage of time, the initial source spectrum changes into thermal neutron spectrum keeping almost the Gaussian shape with finite energy resolutions. The mean energy of the spectrum at each instant can be related to a slowing down time from the time of neutron generation. Utilizing the relation between slowing down time to the mean energy, namely t-E relation, measurement of neutron spectra of eV energy was attempted.

A cylindrical assembly made of type 316 stainless steel¹⁾ was placed at 300 mm distance from the tritium target of Fusion Neutronics Source, FNS. D-T neutron pulses of 0.5 μ s width and 200 μ s repetition rate were injected to the assembly, and time-dependent $^{10}\text{B}(n,\alpha)$ reaction rate was measured at positions of 356, 508, 711 and 914 mm from the surface of assembly. A BF_3 gas proportional counter of 14 mm in outer diameter, 99 mm in effective length and 0.39 MPa (900 mmHg) in pressure was used. The counter was calibrated under a standard thermal neutron field to estimate a number of effective ^{10}B atoms contained.

Time-dependent neutron energy spectra were calculated by the Monte Carlo transport code MCNP-4. The t-E relation for the assembly was obtained from the calculated spectra. The relation was experimentally checked between 1.4 eV and 336 eV applying the resonance filter technique. Fig. 5.4.1 shows calculated and measured relations. It is found that an agreement between them is suitable. Energy resolution which corresponded to energy width of a spectrum at each instant and was inherent to the material of the assembly were also derived from the calculated spectra as shown in Fig. 5.4.2. Below 100 eV, they are about 50 % in FWHM which almost equal to the theoretical value, while they are worse above 100 eV because of distortion of neutron spectrum caused by large resonance peaks of cross section.

The calculated t-E relations were used to convert the measured time-dependent $^{10}\text{B}(n,\alpha)$ reaction rates into the energy-dependent reaction rates, and then neutron energy spectra were obtained dividing them by the cross section of $^{10}\text{B}(n,\alpha)$ reaction. The cross section at each energy was corrected by 10 ~ 30 % for broadening of neutron spectrum at corresponding time. The spectra were normalized to the absolute values considering the number of effective

^{10}B atoms and numbers of neutrons generated at the target.

A neutron spectrum obtained in the present measurement is shown in Fig. 5.4.3 with calculated one by MCNP. In the measured spectrum, detailed structures due to large resonance cross sections, i.e., small dips around 45 eV by Molybdenum and 336 eV by Manganese, are observed as they are seen in the calculated spectrum. As for absolute value of the spectra, agreement between both spectra is good; energy-integrated spectra by MCNP are about 10 ~ 30 % larger than those by the experiment for four energy intervals of each decade between 1 eV to 10 keV.

The first attempt to measure neutron spectrum of eV energy region as benchmark data of fusion neutronics experiments was successfully performed. By applying the present technique, energy range on neutron spectrum measurements was largely expanded up to thermal energy and neutron spectrum in the whole energy range came to be measurable with reasonable accuracy.

Reference

- 1) Konno C., et al.: Fusion Technol., 21 [3] part 2A, (1992) pp 2169-2173.

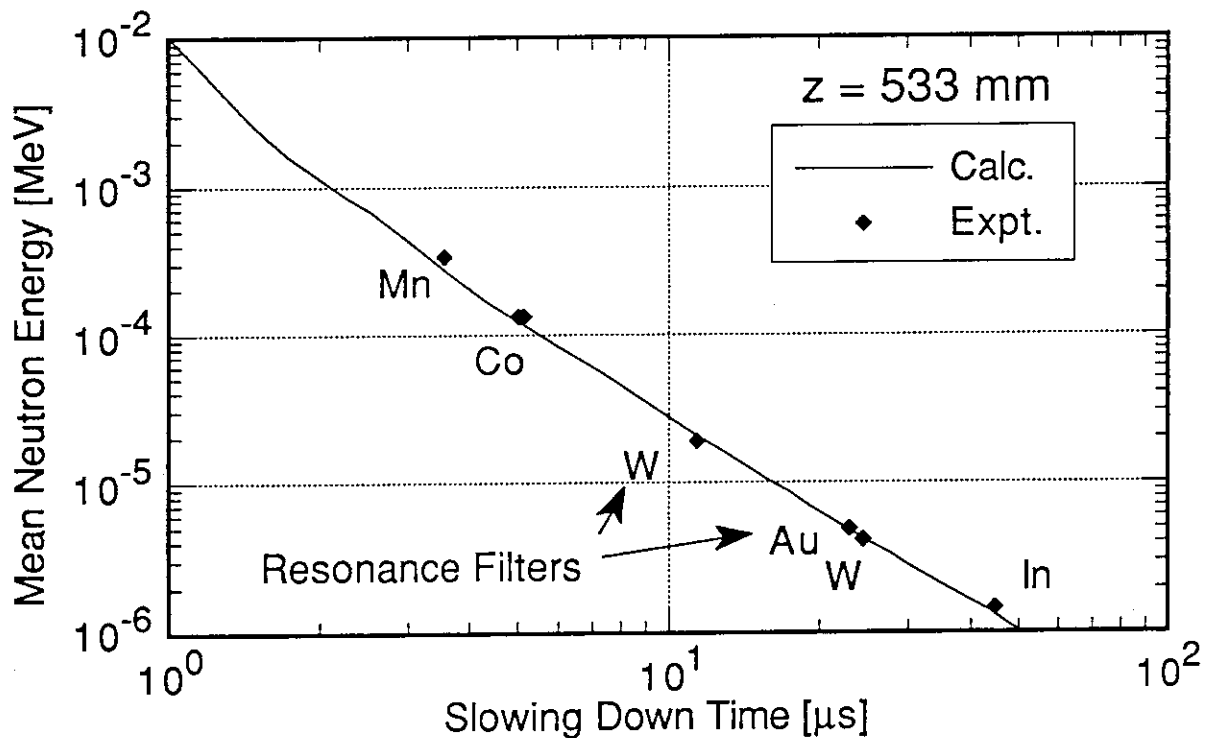


Fig. 5.4.1 Relation between slowing down time and mean energy at 533 mm in the SS316 assembly

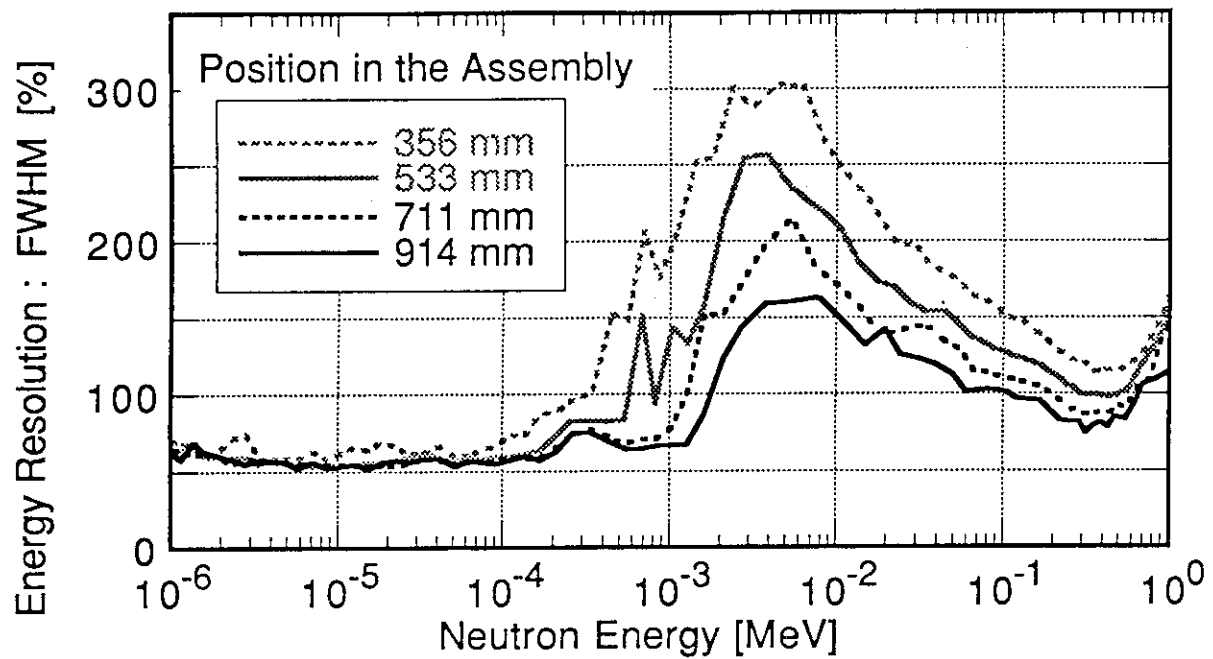


Fig. 5.4.2 Energy resolution for the SS316 assembly estimated from time-dependent neutron spectra calculated by MCNP

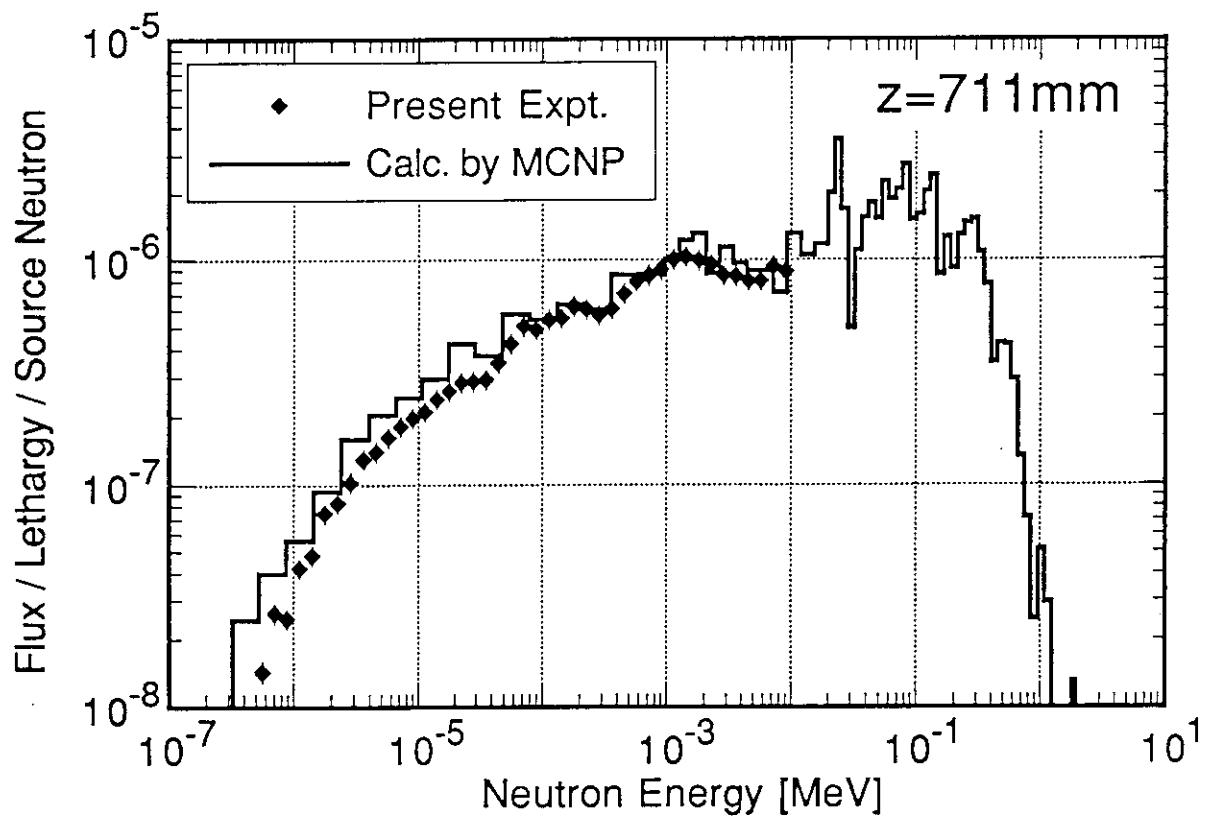


Fig. 5.4.3 Measured neutron spectrum at 711 mm in the SS316 assembly with calculated one by MCNP

5.5 Second International Comparison on Measurement Techniques of Tritium Production Rate for Fusion Neutronics Experiments

F. Maekawa and H. Maekawa

The second international comparison on measurement techniques of tritium production rate (TPR) for fusion neutronics experiments¹⁾ (ICMT-2) was performed under the framework of NEA/NSC activity, following the first comparison (ICMT-1) and the additional measurement of tritium concentration^{2), 3)}. The procedure of ICMT-2 was almost the same as ICMT-1. Simulated fusion blanket assemblies were constructed at two D-T neutron source facilities, FNS/JAERI and LOTUS/EPFL-Switzerland. Nine organizations from seven countries sent Li-containing samples to the two facilities. These samples were irradiated in the assembly under a condition of uniform neutron field. A primary difference between two irradiations at both facilities were amounts of produced tritiums; approximate TPRs were 4×10^{-13} and 1.6×10^{-12} T-atoms/Li-atom for FNS and LOTUS, respectively. The difference enable us to study a relation between S/N ratio and accuracy of measurement. The irradiated samples were sent back to each participant and tritium production rates were measured applying their own techniques based on the liquid scintillation counting method. Tritium water samples of an unknown concentration, "blind sample", were also distributed from JAERI and the concentration was measured to make a common reference.

Figure 5.5.1 shows measured TPRs in ICMT-1 and ICMT-2. Comparing ICMT-2 with ICMT-1, standard deviation of measured TPRs among the organizations for the FNS irradiation, relatively low TPR, are largely improved up to about 10 %. While for the LOTUS irradiation, relatively high TPR, the standard deviations of ICMT-1, 10 %, do not improve in ICMT-2. As a result, it is found that present accuracy of TPR measurement is about 10 % in one standard deviation and the TPRs scatter ± 20 % at maximum among the

Contributors (including ICMT-1) :

Argonne National Laboratory	U. S. A.
Atomic Energy of Canada Limited/ Chalk River Laboratories	Canada
Commissariat a l'Energie Atomique/ Cadarache	France
Energieonderzoek Centrum Nederland	Netherlands
Institut de Genie Atomique/ École Polytechnique Fédérale de Lausanne	Switzerland
delle'Energia Nucleare e delle Energie Alternaive	Italy
Moscow Engineering Physics Institute	Russia
Osaka University	Japan
The University of Tokyo	Japan
Japan Atomic Energy Research Institute	Japan

organizations. This present status is far from the expected accuracy of this international comparison program, 5 %.

Through examinations of the measured data, some problems in TPR measurement are clarified. Even in a measurement process of a tritium concentration for less than a few tens Bq/g, it is difficult to achieve 5 % accuracy in a standard deviation of measured concentration. In fact, in the present measurement of blind HTO sample of which concentration is about 30 Bq/g, the standard deviations are larger than 5 %. But the concentration of 30 Bq/g is higher than any concentrations obtained from irradiated pellets in ICMT-2, 1 ~ 20 Bq/g, and they are not low but highest class of concentrations as those extracted from pellets irradiated by existing D-T neutron sources. To achieve the accuracy of 5 % for TPR measurement, it is necessary to improve the measurement accuracy for tritium concentration of less than a few tens of Bq/g, or to extract tritium water which concentration is higher than a few tens of Bq/g.

Considering ratios of FNS/LOTUS or inner/outer for ICMT-2, the accuracy of the relative TPRs measured by most of the organizations are less than 5 %. But the standard deviation among organizations exceeds 10 % and it is larger than the required accuracy of 5 %. It is found that the most of causes of deviations among organizations are systematic and attributed to the extraction processes of tritium water from irradiated pellets. Since these systematic errors are inherent in each organization and experimenters are not conscious of all the error sources, all the organizations should reexamine their techniques and make an effort to find out the unknown error sources to achieve 5 % accuracy.

References

- 1) Maekawa F. and Maekawa H.: "Second International Comparison on Measuring Techniques of Tritium Production Rate for Fusion Neutronics Experiments (ICMT-2)," NEACRP-L-340; NEA/NSC/DOC(92)6; JAERI-M 93-017, (1993).
- 2) Maekawa H., Nakamura T. and Haldy P.-A.: "International Comparison on Measuring Techniques of Tritium Production Rate for Fusion Neutronics Experiments (Interim Report)," NEACRP-A-1021, Session B.3.6; JAERI-memo 01-442, (1989).
- 3) Maekawa H.: "International Comparison on Measuring Techniques of Tritium Production Rate for Fusion Neutronics Experiments -Summary of Additional Questionnaire and Result for ANL Samples-," NEACRP-A-1080, Session B.3.6; JAERI-memo 03-069, (1991).

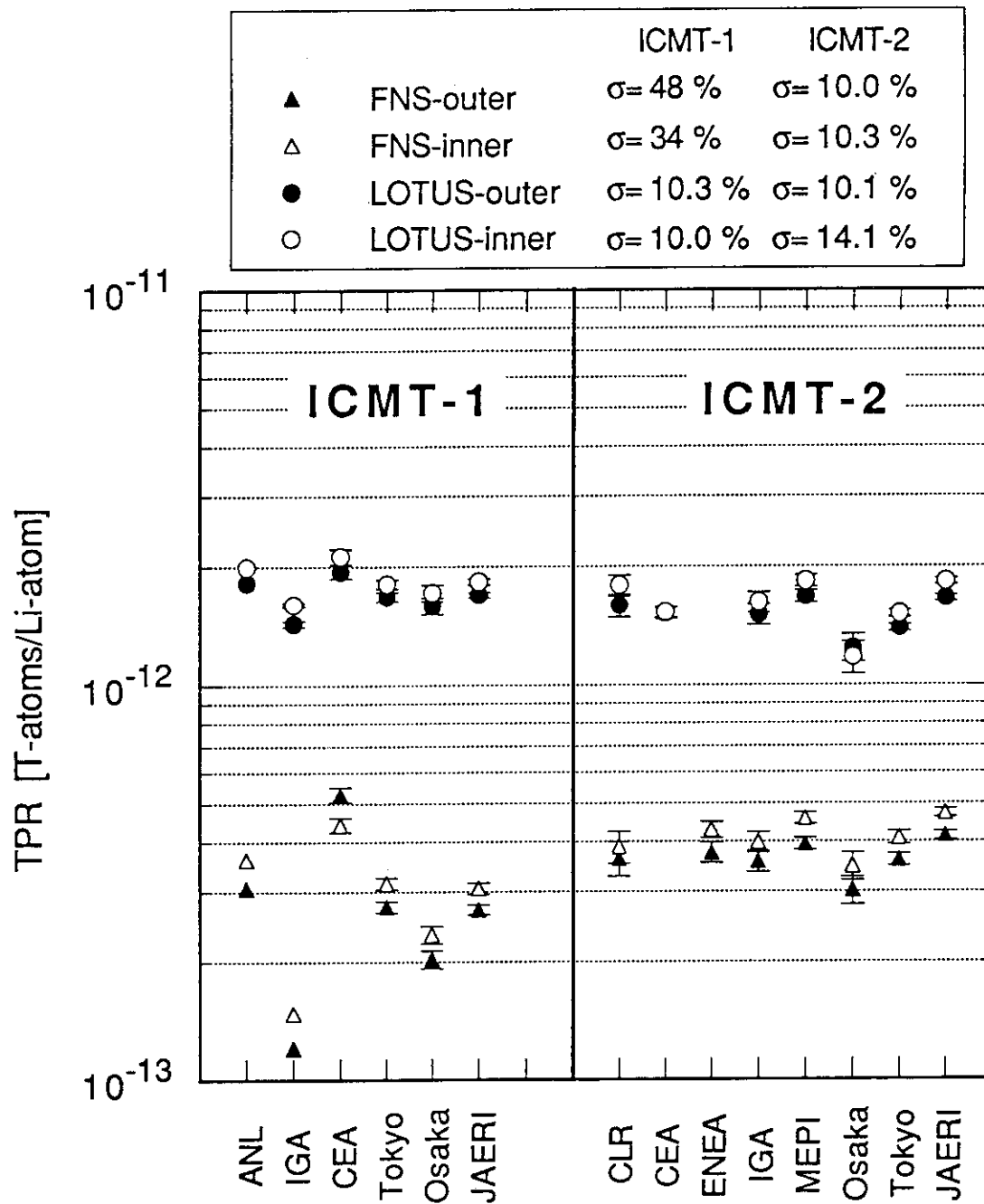


Fig. 5.5.1 Measured TPRs for the ICMT-1 and ICMT-2 programs

5.6 Improvement of Neutron Measurement Technique for DD Plasma Diagnostics in Magnetic Confinement Fusion Device (2)

T. Iguchi*, N. Nakayamada*, J. Kwarabayashi*, H. Takahashi*, M. Nakazawa*, Y. Ikeda and H. Maekawa

To improve techniques of DD neutron measurement in magnetic confinement fusion (MCF) devices, a series of mock-up experiments have been made on neutron yield monitoring and neutron spectrometry using the experimental assembly consisting of the accelerator DD neutron source and the cylindrical SS-316 stainless steel assembly, which simulates the neutron field near the MCF vacuum vessel and structures.

In the last year, the calibration accuracy of neutron yield monitoring was checked with a ^3He long counter used in JT-60U and 'NEUTRAK', a commercial solid state track detector. The results showed the systematic differences between the measurements and MCNP calculations depending on the ^{252}Cf and DD neutron transmission spectrum through the SS-316 assembly of three different kinds of thickness. These transmitted neutron spectra were also measured with a ^3He gas ionization chamber and a ^3He gas proportional counter for the purpose of DD plasma ion temperature diagnostics based on neutron spectrometry. However, some discrepancies between unfolded spectra and calculated ones were found in the lower energy region mainly due to inadequacies of the detector response function.¹⁾

In this year, the following two complementary experiments have been done to make clear source of experimental errors and improve the present accuracy of neutron measurement in the same experimental assembly;

(1) Neutron yield measurement using activation foils, (2) Re-measurement and analysis of neutron spectrum using a ^3He gas ionization chamber and a ^3He gas proportional counter. Activation measurements in the DD neutron source and transmitted neutron spectrum through a 50 mm thick SS-316 wall were carried out by adopting the $^{58}\text{Ni}(n,p)$, $^{115}\text{In}(n,n')$ and $^{197}\text{Au}(n,\gamma)$ reactions, which were already applied to neutron yield measurement at JT-60U. Table 5.6.1 summarizes the comparison results of activation rates obtained from the experiment and the corresponding MCNP calculation, where activation cross sections were adopted from JENDL-3 dosimetry file and anisotropy of DD neutron source spectrum was considered. Good agreement between experiment and calculation is found for neutron flux in the higher energy region than about 0.5 MeV. However, the C/E ratio on the lower energy neutron flux including thermal neutrons shows overestimation of a factor of 4, of which trends are very similar to the previous results.

As for the neutron spectrum measurement using a ^3He gas ionization chamber, the response functions in the energy range between 0.5 MeV and 6.0 MeV have been evaluated in

* The University of Tokyo

advance by adjusting the results of Monte Carlo calculation to the measured data for accelerator monoenergetic neutron sources. Re-analysis of transmitted neutron spectrum using the evaluated response functions gives better agreement between experiment and calculation than those in the last year, as shown in Fig. 5.6.1.²⁾

In addition, the fast digital signal processing has been introduced to the pulse shape analysis of a ^3He gas proportional counter to distinguish nuclear reactions, mainly $^3\text{He}(n,p)t$ and $^3\text{He}(n,n)^3\text{He}$ reactions, produced in the detector gas. This technique enables us to do more advanced data processing through digital sampling of pulse signals than the ordinary analog ones, such as pulse pile-up correction, dynamic and optimum noise reduction, signal discrimination of specific reactions, etc. This technique is expected to be suitable for the measurement per one shot MCF experiment in a short time (a few sec.). In the present study, the time distribution of primary electrons reaching the anode wire $f(\tau)$, which are first produced along the ion track from nuclear reactions, has been inversely estimated from the digital output of pulse shapes. The output pulse shape $V(t)$ is given by the convolution integral; $\int f(\tau) \cdot V_r(t-\tau) d\tau$, where $V_r(t-\tau)$ is an impulse response, that is, the pulse shape of unit charge drifting in the radial direction of the detector. Figure 5.6.2 shows an example of $f(\tau)$ obtained from least squares unfolding of the measured data. In Fig. 5.6.2, there is found a single peak corresponding to $^3\text{He}(n,n)^3\text{He}$ reactions (one charged particle of ^3He recoil) and double peaks corresponding to $^3\text{He}(n,p)t$ reactions (two charged particles of p and t). Figure 5.6.3 gives the pulse height distribution from signals showing double peaks in $f(\tau)$, where the reduction of the ^3He recoil edge and the enhancement of the $^3\text{He}(n,p)t$ peak are successfully demonstrated.

References

- 1) Nakayamada, N., Iguchi, T., et al. : Proc. Annual Meet. of AESJ in Tokai Univ. (1992).
- 2) Nakayamada, N., Iguchi, T., et al. : Proc. Annual Meet. of AESJ in Kyoto Univ. (1993).

Table 5.6.1. Comparison of activation rates between experiment and calculation

Reaction type	Threshold Energy	DD n. Source			SUS Assembly(5cmt)		
		Cal.	Exp.	C/E	Cal.	Exp.	C/E
$^{58}\text{Ni}(n, p)$	1.0MeV	1.05E-29	1.06E-30	0.99	9.21E-30	9.66E-30	0.95
$^{115}\text{In}(n, n')$	0.5MeV	1.76E-29	1.68E-29	1.05	2.10E-29	2.18E-29	0.96
$^{197}\text{Au}(n, \gamma)$	none	1.51E-30	2.58E-29	0.06	4.86E-29	1.18E-29	4.12

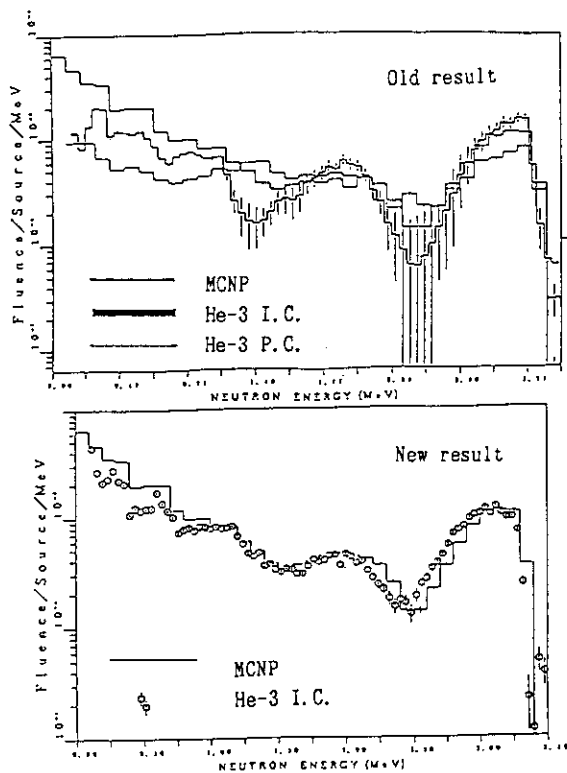


Fig. 5.6.1 Old and new results of neutron spectra after transmission of DD source neutrons through a 5 cm thick SS-316 assembly.

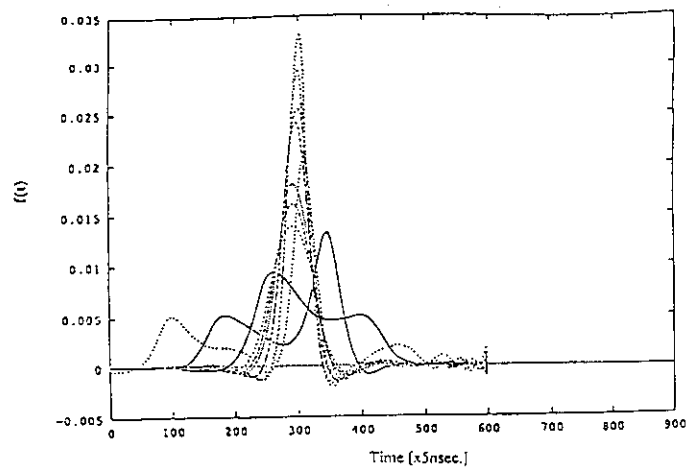


Fig. 5.6.2 Estimated time distribution of primary electrons reaching the anode wire $f(\tau)$ from the digital output of pulse shapes.

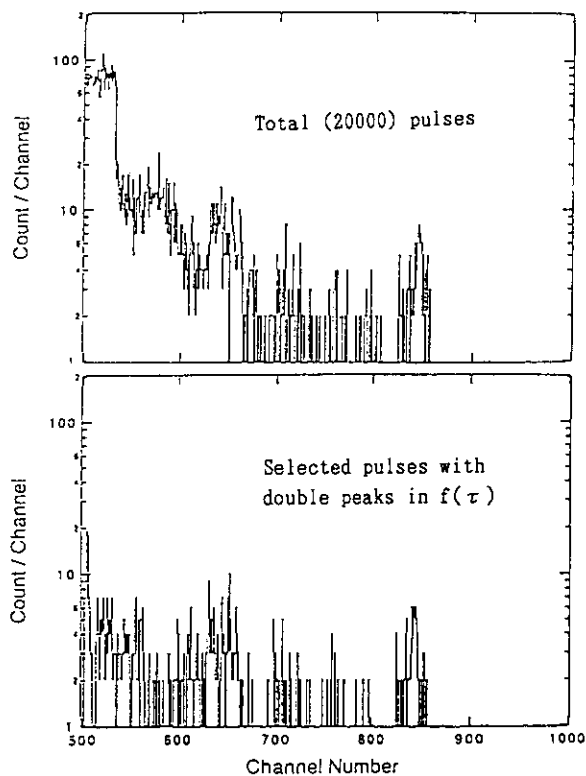


Fig. 5.6.3 Pulse height distributions distinguished on $f(\tau)$.

5.7 Measurement of Recoiled Activities from Al, Fe, Ni, Zr, Nb, Mo and SS-304 due to Neutron Sputtering at 14.9 MeV and Their Systematics

Y. Ikeda, C. Chikara and H. Maekawa

A systematic measurement of the neutron sputtering yield (S_n) for 14 MeV neutrons has been continued with particular attention on the partial reaction process associated with radioactivity emissions. The S_n of recoiled radioactivities due to (n,2n), (n,p) and (n, α) reactions in Fe, Ni, Zr, Mo and SS-304 stainless steel were studied in this fiscal year.

The D-T neutrons were generated using FNS by bombarding tritium target with deuterium beam (d^+) with 20 mA and 350 keV. Measurements for Al, Fe and Nb were carried out by using a collector in air. A configuration of target in vacuum was employed for measurements of another Al, Ni, Zr, Mo and SS-304. The collector materials of plastic tape were placed in both front and back sides of the target foils using rather thick plastic holder at the distance of 0.2, 0.5, 1.0 and 2.0 mm (3.0 mm Nb) in the air, and 1.0 mm in the vacuum. The diameter of target materials was 10 mm. The samples were placed at distances of 10 to 20 mm from the neutron source in the direction of 0° with respect to d^+ beam and were irradiated with D-T neutrons of 14.9 MeV. The D-T neutron fluences at Al, Fe, Ni, Zr, Nb, Mo and SS-304 foils were determined from the activation rates for $^{27}\text{Al}(n,\alpha)^{24}\text{Na}$, $^{56}\text{Fe}(n,p)^{56}\text{Mn}$, $^{58}\text{Ni}(n,2n)^{57}\text{Ni}$, $^{90}\text{Zr}(n,2n)^{89}\text{Zr}$, $^{93}\text{Nb}(n,2n)^{92m}\text{Nb}$, $^{100}\text{Mo}(n,2n)^{99}\text{Mo}$ and also $^{58}\text{Ni}(n,2n)^{57}\text{Ni}$ dosimetry reactions, respectively. After irradiation, the activities in the collectors were measured with a Ge detector. The numbers of radioactive recoil atoms deposited were determined from their activation rates assuming 100 % collection efficiency. Background activity due to impurity or unexpected contamination was examined by irradiating the samples by inserting a mask with different materials between the target material and collector. As a result, no corresponding activity of concerned was observed in the collector. The S_n , defined as the number of recoil atoms emitted from the target per incident neutron was derived from the measured activity and neutron flux determined.

Recoiled radioactivities and their forward sputtering yields are tabulated in Table 5.7.1. At present, experimental errors are estimated to be within $\pm 30\%$. The S_n for ^{90m}Y is 20 times smaller than that of ^{92m}Nb . This is simply due to the small reaction cross section of 5 mb for $^{93}\text{Nb}(n,\alpha)^{90m}\text{Y}$ around 14 MeV energy region¹⁾, while the cross section for $^{93}\text{Nb}(n,2n)^{92m}\text{Nb}$ is 459 mb. The S_n of ^{24}Na is 6 times higher than that of ^{92m}Nb . The cross section of 113 mb at 14.6 MeV for $^{27}\text{Al}(n,\alpha)^{24}\text{Na}$ is, however, 4 times lower than that for $^{93}\text{Nb}(n,2n)^{92m}\text{Nb}$. The enhanced S_n for ^{24}Na to this order of magnitude is explained by the large momentum transfer and low stopping power for ^{24}Na in Al. In general, S_n for SS-304 seems less than those observed in Fe and Ni, even though the radioactivity measured is same.

This is attributable to the difference in abundance of the target nuclide.

In order to give an overall guide line for S_n from a nuclear reaction point of view, S_n s were reduced by using corresponding cross section values as well as abundance of target nuclide. The reduced S_n s, are plotted in Fig. 5.7.1 with respect to the proton number (Z) of target material. Hereafter, we denote the reduced S_n as RS. Some of experimental data are referred in the literature. In Fig. 5.7.1, it was found that RS present a strong correlation with Z though the number of data is not so sufficient. In general, RS decrease with increase of Z. This is understandable by taking into account the large momentum transfer in light element and the higher stopping power in the higher Z material. For (n,p) and (n,2n), RSs are identical, while RSs for (n, α) show slightly higher value than that for (n,2n). The RS for the total S_n gives much higher than those for other non-elastic reactions and the curve for the systematic trend shows slower decrease. The difference between the curves for (n,2n) and (n, α) could be explained by the difference in the momentum transfer in the recoil process; kinematic energy of recoil atom associated with alpha particle is expected two to four times larger than that associated with two neutron or one proton emission.

There is large uncertainty to finalize this approach to formulate the systematic trends of RSs for the specific reactions, because experimental data are still deficient. Even though, it is worthwhile to investigate any systematics for the S_n and the present approach encourages us to do further experiment on different elements.

Reference

- 1) Ikeda, Y., Konno, C., Oishi, K., Nakamura, T., Miyade, H., Kawade, K., Yamamoto, H. and Katoh, T. : "Activation Cross Section Measurements for Fusion Reactor Structural Materials at Neutron Energy from 13.3 to 15.0 MeV Using FNS Facility," JAERI-1312 (1988).

Table 5.7.1 Measured forward neutron sputtering yield at 14.9 MeV

Target Material	Reaction	Recoiled Activity	Sputtering Yield (/ neutron)
Al	(n, α)	^{24}Na	6.33×10^{-7}
Fe	(n,p)	^{56}Mn	4.98×10^{-8}
Ni	(n,p)	^{58}Co	9.71×10^{-8}
	(n,np)	^{57}Co	1.96×10^{-7}
	(n,2n)	^{57}Ni	1.05×10^{-8}
Zr	(n,p)	$^{90\text{m}}\text{Y}$	2.21×10^{-9}
	(n, α)	$^{87\text{m}}\text{Sr}$	7.63×10^{-10}
	(n,2n)	^{89}Zr	1.11×10^{-7}
Nb	(n, α)	$^{90\text{m}}\text{Y}$	1.82×10^{-9}
	(n,2n)	$^{92\text{m}}\text{Nb}$	7.06×10^{-8}
Mo	(n,p)	$^{92\text{m}}\text{Nb}$	1.03×10^{-9}
	(n,p)	^{96}Nb	1.44×10^{-10}
	(n,p)	^{97}Nb	1.21×10^{-9}
	(n, α)	^{89}Zr	2.18×10^{-9}
	(n,2n)	^{99}Mo	5.53×10^{-9}
SS-304	(n,p)	^{54}Mn	1.83×10^{-8}
	(n,p)	^{56}Mn	1.73×10^{-8}
	(n,p)	^{58}Co	1.39×10^{-8}
	(n,np)	^{57}Co	2.27×10^{-8}
	(n,2n)	^{51}Cr	5.46×10^{-8}
	(n,2n)	^{57}Ni	1.37×10^{-9}

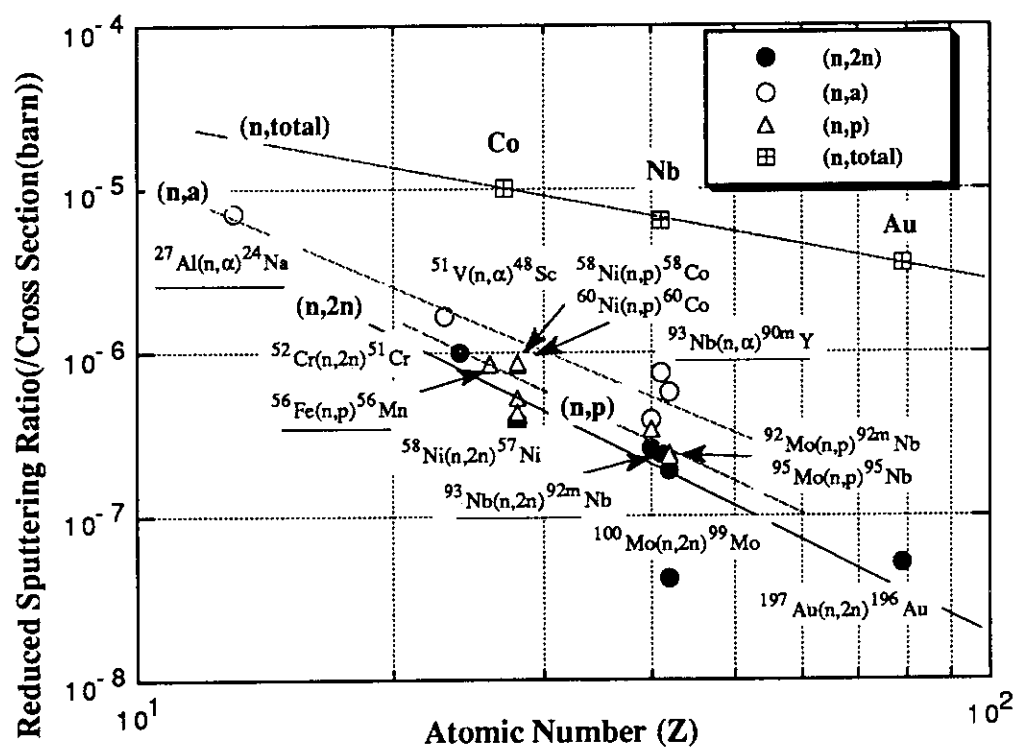


Fig. 5.7.1 Systematic trend of sputtering yields for specific reactions as a function of Z of target material

5.8 14 MeV Neutron Generation Characteristics of FNS Tritium Target

—Measurement of Tritium Depth Profile—

C. Kutsukake, J. Kusano, S. Tanaka, Y. Abe and M. Seki

The upgrade of FNS accelerator has been proposed. The major items for the upgrade is increasing beam current to achieve higher neutron yield for the next fusion neutronics experiments. For this purpose, it is important to provide basic data of the target performance such as the dependency of neutron generation rate on total incident beam current, incident beam energy and the tritium behavior in the titanium. We reported the neutron generation characteristics of FNS target.¹⁾ In this fiscal year, we have investigated of the depth profile of tritium reduction ratio versus initial tritium distribution in the titanium. The depth profile of tritium reduction ratio were measured by using change of depth for D-T reaction with incident deuteron (d^+) energy. Figure 5.8.1 shows incident d^+ energy loss in titanium along with the D-T reaction cross section.

The depth profile of tritium reduction ratio was measured by the following steps ; ① The energy spectrum of α particles via the $T(d,n)\alpha$ reaction was measured changing d^+ beam energy from 200 keV to 380 keV. ② The target was irradiated with d^+ beam of 250 keV energy. ③ After the irradiation, the α particle energy spectra were measured again with each d^+ beam energies same as before. ④ The counting rate of each channel of the α particle spectrum in initial condition were compared with that after irradiation. ⑤ The calibration of depth profile for the tritium reduction rate was done by comparing of the calculated value of the α particle energy spectrum to the measured value. ⑥ The α particle energy corresponding to the depth were calculated by the D-T reaction kinematics considering the incident d^+ energy and α particle energy loss in the titanium layer. Figure 5.8.2 shows the calculated α particle energy corresponded to each incident d^+ energy.

We investigated a dependency of the tritium reduction ratio on the d^+ beam irradiation and the change of the tritium reduction ratio by the target heating. The d^+ beam energy was 250 keV and the integrated beam current was nearly 9 mAh for the irradiation. The target heating was carried out under the condition of no cooling water flow and 350 keV 60 μ A d^+ beam irradiation. The amount of tritium in the small target disk is about 0.37 TBq ; the tritiated titanium layer on a copper alloy is 20 mm in diameter; and deposited titanium depth is about 3 mg/cm². The SSD used for the α particle spectrum measurement is located 1.4 meter from the target at an angle of 179° to the d^+ beam direction.

Figure 5.8.3 shows α particle energy spectra at initial, after 250 keV irradiation, and after target heating in the condition of 370 keV incident d^+ beam energy. The α particle

energy corresponding to 150 channel is equivalent to 1.2 μm depth from the titanium surface. Figure 5.8.3 shows a decrease of count rate at around 150 channel. The α particle energy spectrum after heating became nearly same as the initial α particle spectrum.

Figure 5.8.4 shows the depth profile of the tritium reduction ratio as a function of integrated incident beam current. The change by target heating is also plotted. The largest depression of tritium density is found at 1.2 μm depth in the titanium layer. It is concluded that the tritium depression range of d^+ beam with 250 keV is around 0.5-1.5 μm .

References

- 1) Reactor Engineering Department Annual Report,; JAERI-M 91-138 (1991)
- 2) Reactor Engineering Department Annual Report,; JAERI-M 92-125 (1992)

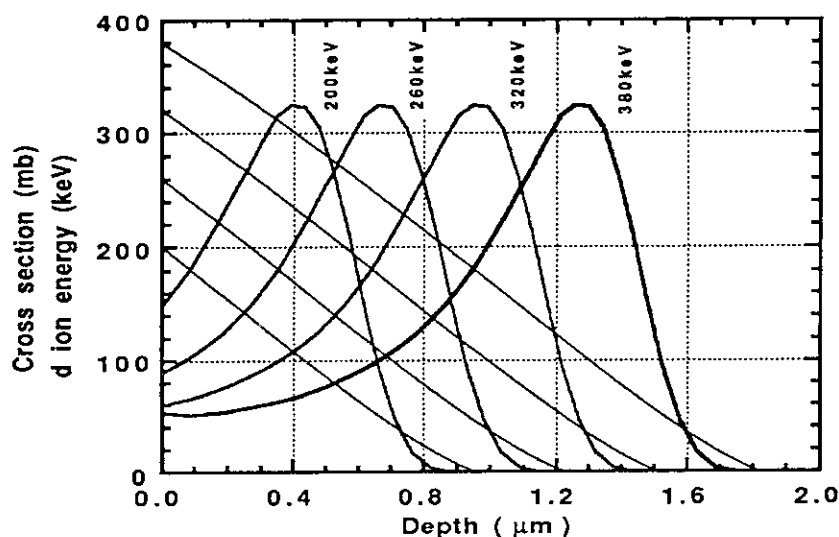


Fig. 5.8.1 Deuteron energy and D-T cross section in titanium

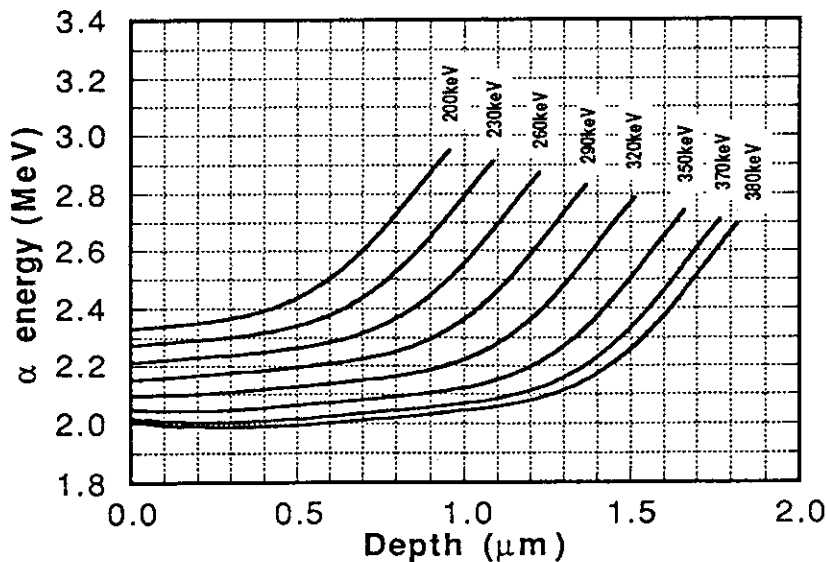


Fig. 5.8.2 Alpha particle energy by the D-T reaction in the titanium

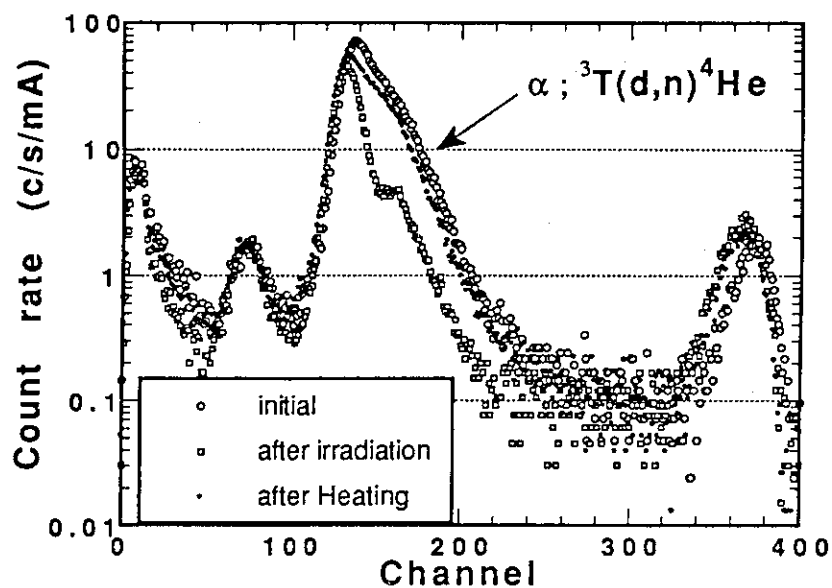


Fig. 5.8.3 The alpha particle spectrum transition by the irradiation and heating

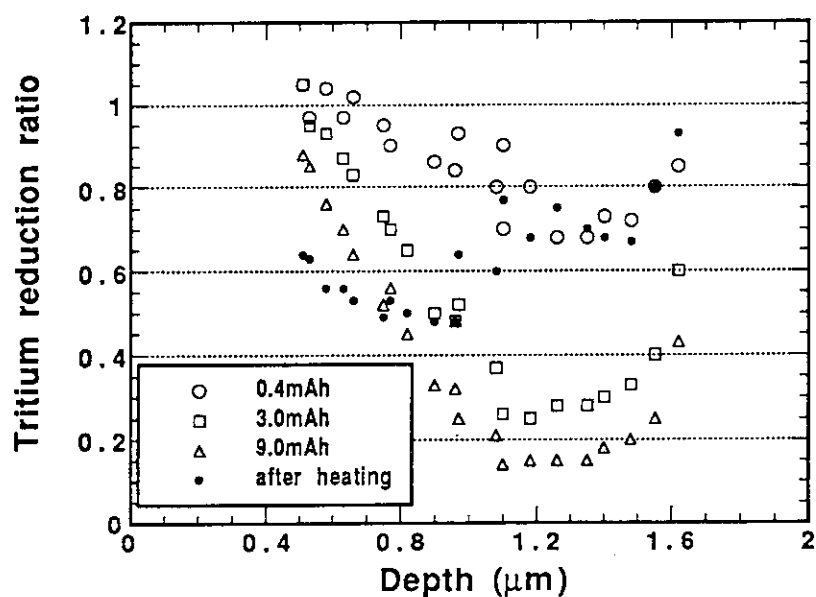


Fig. 5.8.4 Depth profile of tritium reduction ratio at 250keV deuterium irradiation

6. Radiation Shielding

As for accelerator shielding, a few remarkable progresses have been realized. The accelerator shielding programme using a 90 MV AVF cyclotron TIARA has started as a project of JAERI and several universities after the warming-up for about 4-years. The production of quasi-monoenergetic neutrons having energies of about 40 MeV and 65 MeV were confirmed by a proton recoil telescope detector, which were produced through ${}^7\text{Li}(p,n)$ reaction with a thin ${}^7\text{Li}$ target and monoenergetic protons of 43 and 67 MeV. With the neutrons, transmission experiments have been made for ordinary concrete and iron shields, where neutron energy spectra using a 5" ϕ x 5" NE213 scintillator and Bonner spheres, reaction rates of for ${}^{238}\text{U}(n,f)$ and ${}^{232}\text{Th}(n,f)$, and dose rates using a rem counter and solid state track detectors were measured. The experiments have been analyzed by the MORSE and DOT3.5 codes with a coupled group cross section library HILO86.

The HILO86 library was revised as the HILO86R considering the self-shielding factors of the cross sections less than 19.6 MeV for 10 kinds of materials. Significant difference for dose attenuation was observed in iron shield even for 400 MeV neutrons among the HILO, HILO86 and HILO86R data. The difference should be evaluated with the experiments at TIARA. The development of a code system has been continued to evaluate the fluence to dose equivalent conversion factors for photons from 10 MeV to 10 GeV and for neutrons 15 MeV to 10 GeV. The calculations for high energy photons have suggested that the ambient dose equivalent (1-cm depth dose) in a sphere ICRU phantom underestimates the effective dose based on the ICRP-recommendation 60.

The energy and dose responses of LiF TLDs were measured to apply for synchrotron radiation dosimetry, and discussed with the cavity ionization theory.

Survey calculations were carried out to estimate the effects of voids and additional shields of $\text{B}_4\text{C}/\text{Pb}$, W and $\text{B}_4\text{C}/\text{W}$ in a bulk shield, and to design benchmark experiments in FNS for ITER.

(Shun-ichi Tanaka)

6.1 Neutron Shielding Experiments at TIARA

Y.Sakamoto, H.Nakashima, Y.Nakane, S.Tanaka* and S.Tanaka

The accelerator shielding programme has started as a project of JAERI and several universities using a 90 MV AVF cyclotron TIARA (Takasaki Ion Accelerators for Advanced Radiation Application). The programme is consisted of measurements of shielding data for neutron, neutron cross sections and production cross sections of secondary radiation bombarded by ion beams.

Figure 6.1.1 shows the layout of the neutron shielding experiments. Quasi-monoenergetic neutrons were generated via ${}^7\text{Li}(p,n)$ reaction of a thin lithium target bombarded by monoenergetic protons. Proton beam current and source neutron intensity were monitored by a Faraday cup and fission counters. Quasi-monoenergetic neutron beams passed through the iron shield collimator with 10-cm-diameter.

Source neutron spectra per unit beam current at the position of 5.5 m apart from the target^{1,2)} are shown in Fig.6.1.2. The spectra for neutrons above 15 MeV were measured by a proton recoil telescope (PRT) detector which detected recoil protons emitted from polyethylene radiator by neutron bombardment using of ΔE detector for particle discrimination and E detector for energy measurement. The spectra below 15 MeV were evaluated by a phase-space model. For 43 MeV and 67 MeV protons the peak components and continuous components by break-up reaction were measured clearly.

Neutron transmission experiments were executed for concrete and iron shields which were multiple layers of 1.2 m wide x 1.2 m high with thickness of 10 cm or 25 cm respectively. Figures 6.1.3 and 6.1.4 show the ${}^{232}\text{Th}$ fission reaction rates per source neutron behind concrete and iron shields on the beam axis. The reaction rates calculated by the DOT3.5 code using the DLC-119/HILO86 neutron cross section library³⁾ are also plotted in these figures. The agreement with measured and calculated values is very good.

*Takasaki Establishment

References

- 1) Yoshioka M. et al, Proc. Annual Meet. of AESJ in Nagoya Univ., G24(1992).
- 2) Baba M. et al, Proc. Annual Meet. of AESJ in Kyoto Univ., C35(1993).
- 3) Radiation Shielding Information Center Data Package DLC-119/HILO86.

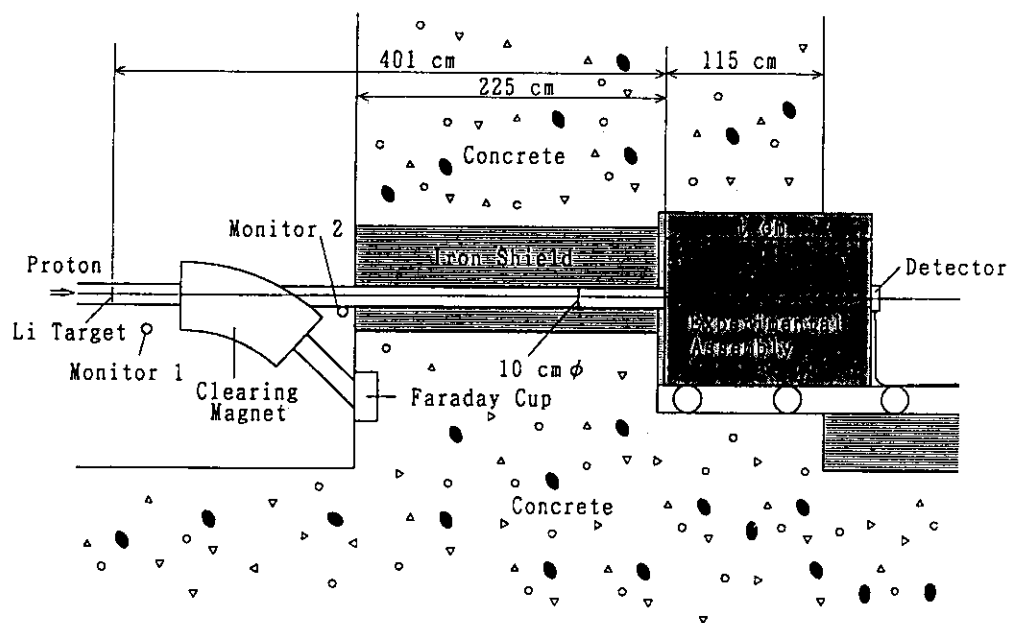
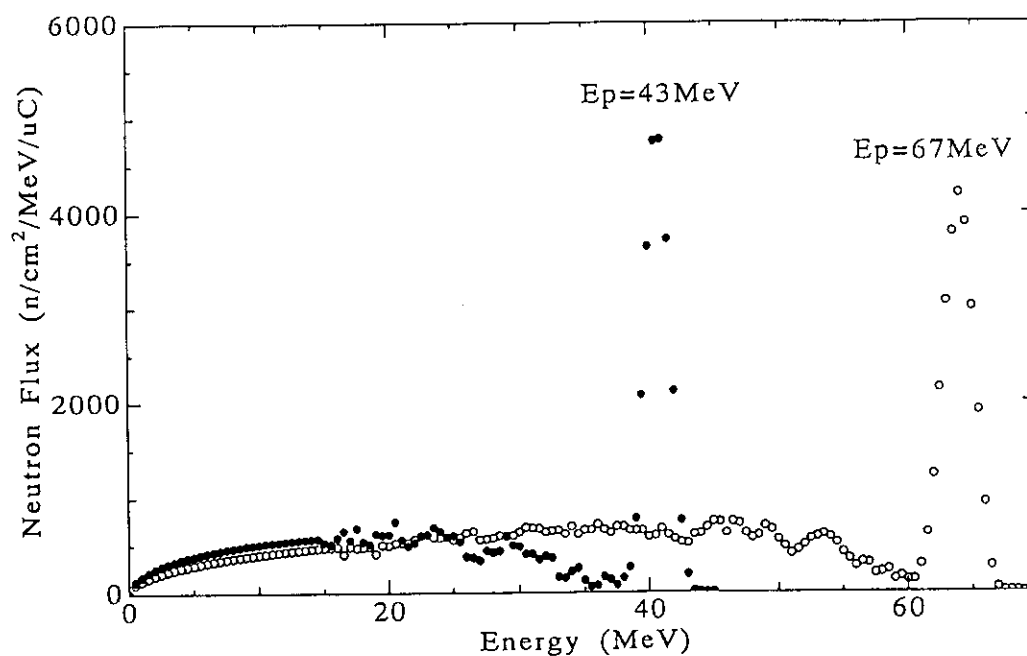


Fig.6.1.1 Layout of neutron shielding experiments.

Fig.6.1.2 Source neutron spectra via ${}^7\text{Li}(p,n)$.

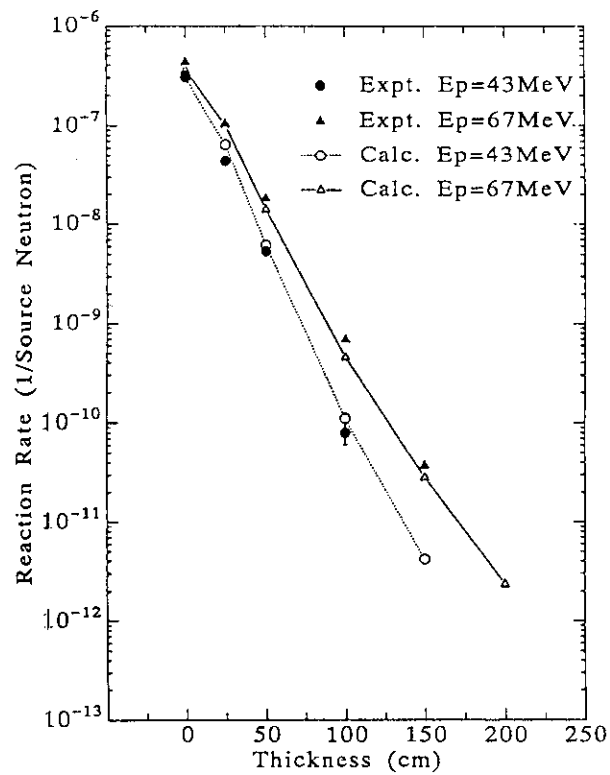


Fig.6.1.3 ^{232}Th fission reaction rates behind concrete by 43 and 67 MeVp.

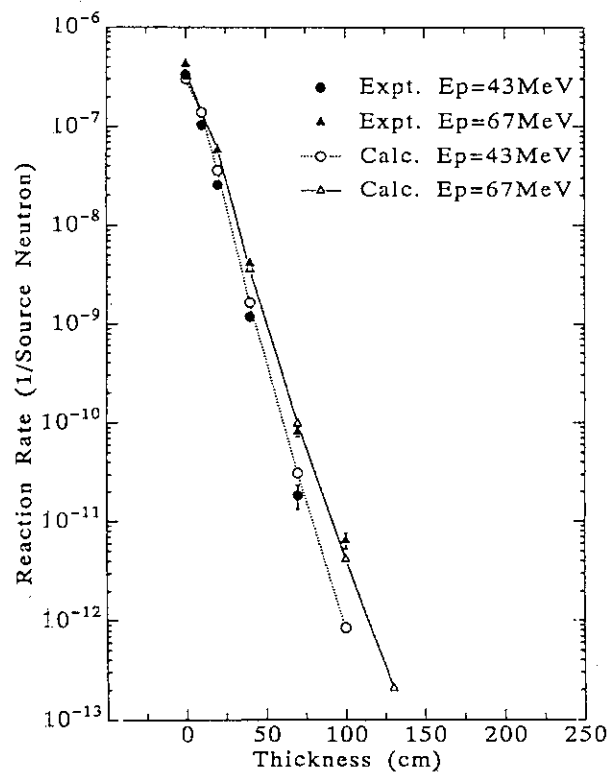


Fig.6.1.4 ^{232}Th fission reaction rates behind iron by 43 and 67 MeVp.

6.2 HIL086R: Revised Version of Neutron-photon Multigroup Cross Section Library HIL086 for Neutron Energies up to 400MeV

H.Kotegawa, Y.Nakane, A.Hasegawa and S.Tanaka

Multigroup cross sections have been widely used for shielding calculations of nuclear facilities with discrete ordinates codes and Monte Carlo codes such as ANISN, DOT, MORSE and so forth. Few of group cross section libraries, however, are available for neutron energies higher than 20 MeV, except HIL0 and its revised version HIL086¹⁾. We have made several test calculations using these libraries with the ANISN code, and noticed serious discrepancy, especially in the neutron dose attenuation in iron for a ^{252}Cf neutron source from the calculated results using macroscopic effective cross sections(JSD100^{*}) of neutron 100 groups and gamma-ray 44 groups which were produced from infinite dilution cross sections JSD100 taking self-shielding factors JFT100 into account, although the results with the JSD100^{*} have already been verified in comparing with measurements. This is the incentive of the present work to revise the HIL086 data and to prepare the revised library HIL086R²⁾.

Neutron cross sections of 37 energy groups less than 19.6MeV and gamma-ray cross sections of 22 energy groups less than 20MeV have been collapsed from 295-neutron and 104-photon JSSTD L library³⁾ based on JENDL-3 cross section library taking self-shielding factors into account. The JSSTD L data library is composed of infinite dilution cross sections produced with the weighting spectra of $1/E$ above thermal neutrons and Maxwell distribution for thermal neutrons, and of Bondarenko type self-shielding factors with the same group structure with that of HIL086, and the JSSTD L cross sections have been condensed using the CONDENS-MACRO-JG code in the JSSTD L system³⁾. The cross sections above 19.6 MeV are the same as those of HIL086. Finally, macroscopic effective cross sections for the HIL086R library were prepared for 10 typical shielding materials.

Figure 6.2.1 shows comparison of macroscopic total cross sections of iron in HIL086R, HIL086 and HIL0 libraries. As seen from this figure, the peak cross section around 26 keV in HIL0 and HIL086

becomes a large concave in the HIL086R because of the large self-shielding factor.

Energy spectra in iron and ordinary concrete for ^{252}Cf neutron and several monoenergetic neutron sources have been calculated using HIL086R, HIL086 and HIL0 libraries. Figure 6.2.2 shows comparison of energy spectra at thickness of 100 and 200 cm in iron for point isotropic ^{252}Cf neutron source, which were calculated with ANISN-JR code in spherical geometry. The results with the JSD100* and the HIL086R are in reasonable agreement, while the discrepancy with the HIL086 is very serious at thickness of 200 cm.

Like the energy spectra, dose equivalent attenuations in ordinary concrete and iron were also examined for ^{252}Cf neutron, and 10, 50, 200, 400 MeV monoenergetic neutron sources using HIL086R, HIL086 and HIL0 libraries.

Consequently, comprehensive comparisons of calculational results using the HIL086R with those obtained by other libraries HIL086, HIL0 and JSD100* made clear the significant effect of self-shielding factors in resonance energy region. Furthermore, it was verified that the influence of the different cross sections less than 19.6 MeV is significant on the neutron and secondary gamma ray dose equivalents even for 400 MeV neutron source.

References

- 1) Alsmiller R.G., Jr Barnes J.M. and Drishler J.D.: "Neutron-Photon Multigroup Cross Sections for Energies $\leq 400\text{MeV}$ (Revision 1)", ORNL/TM-9801(1986).
- 2) Kotegawa H. et.al: "Neutron-Photon Multigroup Cross Sections for Neutron Energies Up to 400MeV: HIL086R -Revision of HIL086 Library-", JAERI-M 93-020(1993).
- 3) Hasegawa A.: "Development of a Common Nuclear Group Constants Library System: JSSTD-295n-104 γ ...", Nuclear Data Science and Technology, pp.232, Springer Verlag(1991).

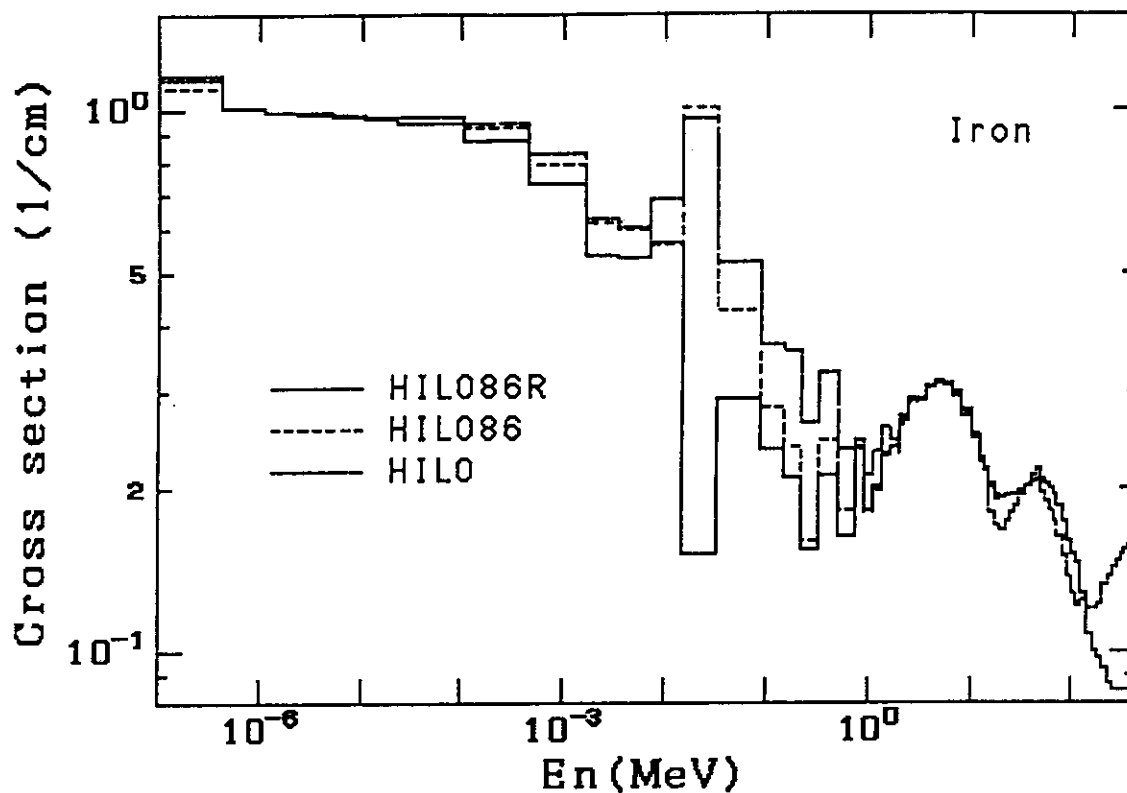


Fig.6.2.1 Comparison of total cross sections of iron in HIL086R, HIL086 and HIL0 libraries.

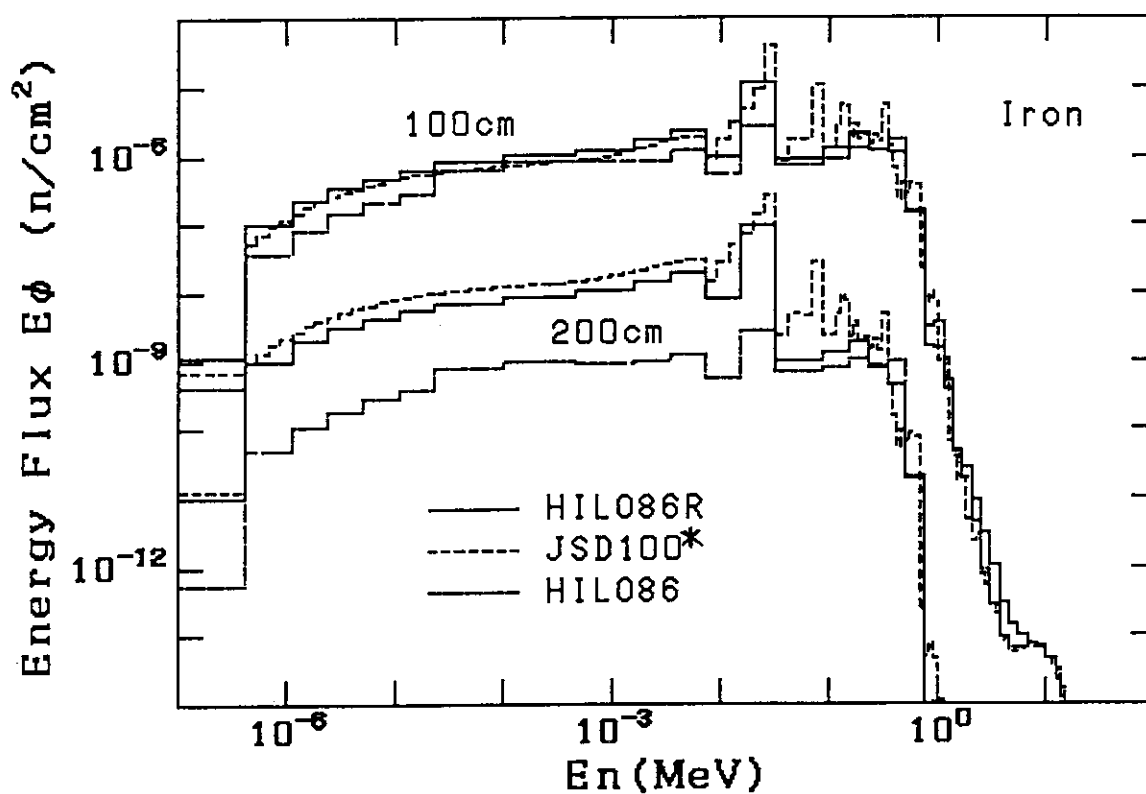


Fig.6.2.2 Energy spectra at thickness of 100 and 200 cm in iron for ^{252}Cf neutron source.

6.3 Evaluation of Fluence to Dose Equivalent Conversion Factors for High Energy Radiations

S.Tanaka, O.Sato*, S.Furihata*, S.Uehara**, N.Yosizawa*, S.Iwai** and Y.Sakamoto

It has never been presented the fluence to dose conversion factors to estimate the effective dose in the ICRP publication-60 and the dose equivalent in the ICRP publication-27 for photons and neutrons greater than about 10 MeV, although the factors are essential for shielding design of high energy accelerators. Thus, a computer code system and basic data have been developed for evaluating the fluence to dose conversion factors for photons above 10 MeV and for neutrons above 15 MeV up to 10 GeV.¹⁾ The present code system is composed of the HERMES (High Energy Radiation Monte Carlo Elaborate System) code system, the mathematical phantom description and the related data such as quality factors.

In the ICRP publication-60, the radiation weighting factor for photons, neutrons and electrons has been introduced to estimate the effective dose of radiations instead of the quality factors, but the values were not given for higher energy radiations. Energetic radiations, specially neutrons, interact with human body elements to produce many kinds of charged particles, therefore the quality factors are needed to estimate the effective dose for the charged particles. In the present work, the quality factors for charged particles up to 10 GeV were calculated on the base of the Q-L relationship specified in the ICRP publication-60, and further the effective quality factors were obtained to facilitate the code system as shown in Fig.6.3.1. With the effective quality factor \bar{Q} , the equivalent dose H_T for each organ is given from the absorbed dose D_T due to charged particles by

$$H_T = \bar{Q}(E_0) D_T ,$$

where E_0 and D_T are calculated using MORSE code with a kerma code for neutrons below

* Mitsubishi Research Institute, Inc.

** Mitsubishi Atomic Power Industries, Inc.

15 MeV, while using the HETC code for ones above 15 MeV.

As for photons, effective dose can be obtained from the absorbed dose calculated with the EGS4 code, since the quality factor for electrons(photons) independent upon the energy.

The calculated results are shown for photons from 10 MeV to 10 GeV in Fig.6.3.2, where the effective doses for AP(anterior posterior) and PA(posterior anterior) conditions are compared with the maximum dose equivalent in the ICRU sphere and plane phantoms and the 1 cm depth dose in the ICRU sphere one. The results in Fig.6.3.1 imply the following important features;

- (1) The effective dose for PA incidence is larger than that for AP one in the energy region above 10 MeV, which is opposite to the feature less than 10.
- (2) Every effective dose is fairly larger than that of 1 cm depth dose. This indicates that the 1 cm depth dose is unavailable for an index instead of the effective dose.
- (3) The maximum dose equivalent is always greater than effective doses, therefore it is useful as an index of the effective dose instead of 1 cm dose equivalent.
- (4) As there is no remarkable difference for the maximum dose equivalent between sphere and plane phantoms, the data of plane phantom is also useful.

Reference

- 1) Sato O., et al.: "Evaluation of Fluence to Dose Equivalent Conversion Factors for High Energy Radiations(II)", to be published as JAERI-M(1993).

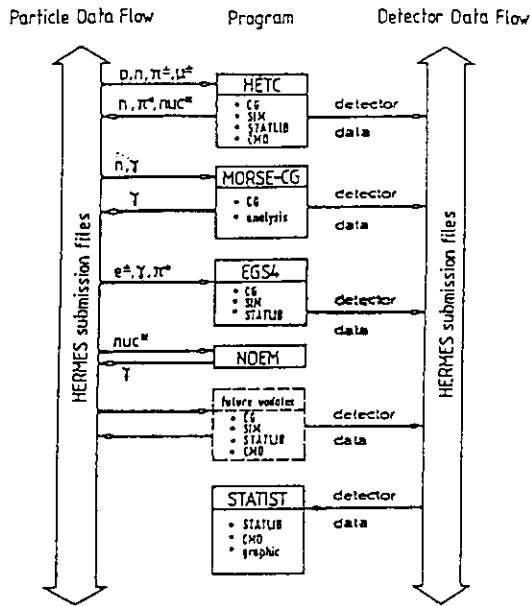


Fig.6.3.1 Organization of the HERMES code system.

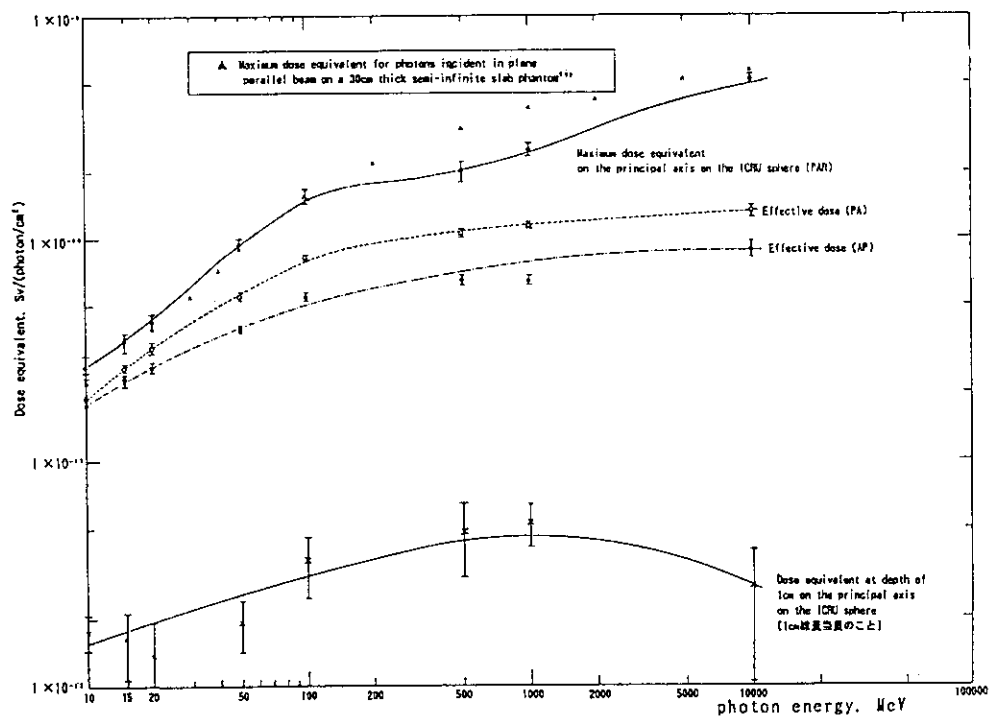


Fig.6.3.2 Comparison of effective doses with dose equivalents in ICRU sphere and semi-infinite slab phantom of 30 cm thickness irradiated by 10 MeV to 10 GeV parallel photon beam.

6.4 Response of LiF TLDs to 10-40 keV Monoenergetic Photons from Synchrotron

S.Tanaka, N.Nariyama*, M.Yoshizawa, H.Hirayama**, S.Ban**, Y.Namito** and Y.Nakane

Energy and dose responses of LiF TLD(TLD-100) of $3.2 \text{ mm}^2 \times 0.38 \text{ mm}$ thick were studied to apply it for dosimetry of synchrotron radiations.¹⁾ Glow curves of the TLD were measured at 5 keV intervals for 10 to 40 keV monoenergetic photons from synchrotron radiations, and the energy and dose responses were evaluated based on the glow curve data. A typical glow curve measured is demonstrated in Fig.6.4.1, where the highest peak 3 is designated as the main peak. Energy responses were evaluated for the integrated area including the main peak and one above that. In Fig.6.4.2, the measured responses are compared with the calculated one from the cavity ionization theory. The measurement agreed with the calculation for lower temperature region of the glow curve including the main peak, while was about 2 times higher.

Dose responses up to 10^3 Gy in air were measured for 10 keV, 30 keV photons and ^{60}Co gamma rays by integrating total area of glow curve as shown in Fig.6.4.3. Supralinearity was observed above a few Gy and became maximum around several hundreds Gy, but the maximum values were strongly dependent upon the photon energy. The values are about 4.3 for ^{60}Co gamma rays, while 2 for 10 keV and 2.8 for 30 keV X-rays, respectively. The dependence of supralinearity on incident photons was elucidated using the linear energy transfer. For electrons from each photons, the restricted absorbed dose average LET L_{AD} are 9.3, 8.1 and 4.2 keV/ μm . The values suggest that the supralinearity has a close relationship with the linear energy transfer of incident particles.

Reference

- 1) Nariyama N., et al.:to be published on Radiation Protection Dosimetry.

* Ship Research Institute

** National Laboratory for High Energy Physics

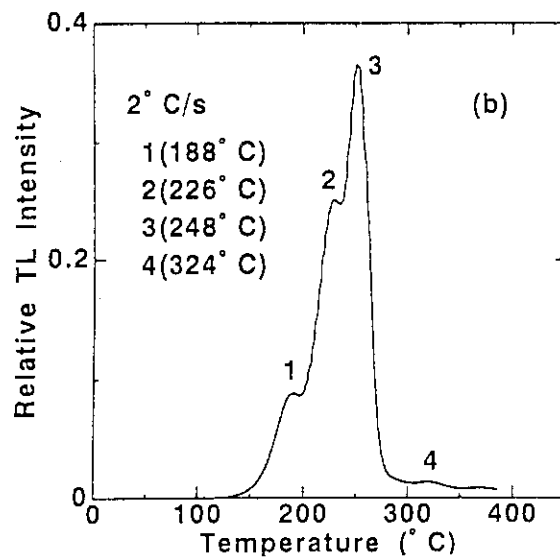


Fig.6.4.1 Glow curve of LiF TLD.

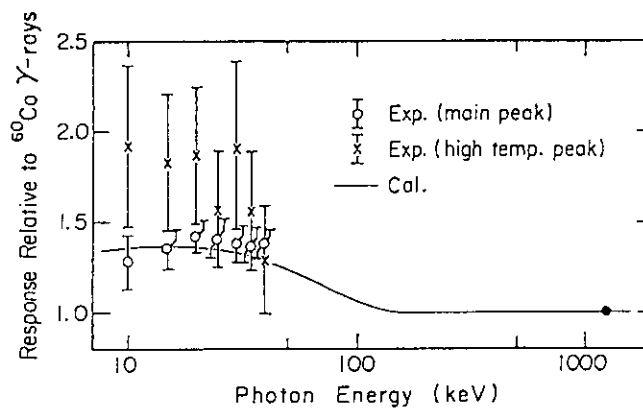


Fig.6.4.2 Energy responses of LiF TLD.

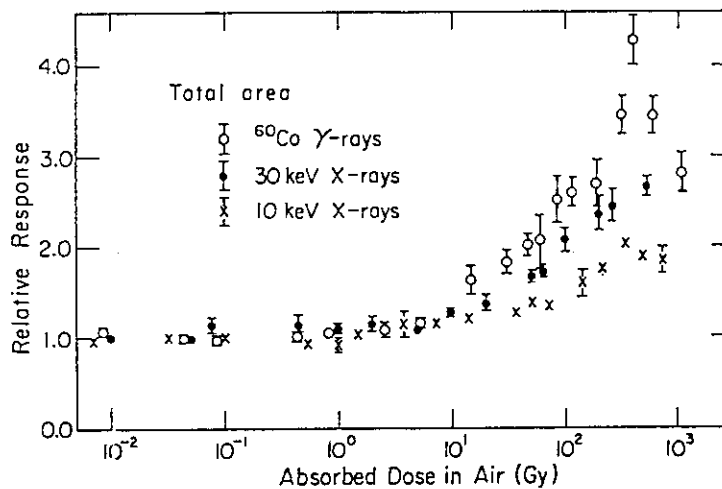


Fig.6.4.3 Dose responses of LiF TLD.

6.5 Survey Calculation for Bulk Shielding Experiments

—Effects of Void and Special Material—

C. Konno, A. Iwai, K. Yamada^{*1}, T. Abe^{*1}, K. Hayashi^{*2}, K. Maki^{*3},
F. Maekawa and H. Maekawa

In shielding design of next fusion reactors such as ITER, there are key problems, e.g., the deep penetration of neutrons in shielding materials and the effects of cooling water, special material, void and gap streaming on shielding performance. Benchmark experiments have been performed in JAERI-FNS in order to examine the validity of calculation codes and nuclear data for these problems. The preliminary analysis is essential to obtain the guideline for benchmark experiments, such as experimental assemblies (shape and material configuration) and measuring points. The effects of void and special material were examined for the next benchmark experiments.

The preliminary analysis was performed using the two-dimensional Sn transport code DOT3.5 with P5-S16 approximation. The GRTUNCL code was used to obtain the first collision sources. FUSION-40¹⁾ with 42 groups for neutron and 21 groups for gamma-ray was adopted as the group constant. The reference assembly was the same as in the SS316 bulk shielding experiments²⁾ shown in Fig. 6.5.1. The test region was a cylindrical assembly of SS316 (1.2m in diameter and 1.12 m in thickness).

Three voids with different sizes (100, 150 and 200 mm in diam. x 102 mm in thickness) were considered. One void was made at the central position of 559 mm from the front surface of the test region. The effects of void were estimated by the ratio of the calculated values with void to that without void. Figure 6.5.2 shows the obtained ratios for gamma-heating rate in the central axis. The voids give 20 % larger heating rate at 200 mm from the void, where the measurement is to be performed, than the reference. Heating rate for the smallest void (100 mm in diam. x 102 in thickness), however, is only 10 % higher than that in the reference. Considering experimental error of ± 15 % for gamma-heating rate, the effects of void more than 20 % are needed. Thus, the 100 mm in diam. x 102 mm void is not good for the benchmark experiment. Next the position of void (150 mm in diam. x 102 mm) was changed at the depths of 152, 254 and 356 mm. Though the void effects tended to decrease as the position of void is shallower, the difference in the effect was not so large. This indicates that it is possible to set a void at the front position in order to make S/N better.

*¹ Business Automation Company

*² Hitachi Engineering Company

*³ Energy Research Lab., Hitachi Ltd.

The effect of a ring void (outer diameter 300 mm, inner diameter 160 mm and width 102 mm), at the depth of 254 mm was also studied since the void problem is attractive in testing calculation codes. The results for neutron flux and gamma heating rate along the central axis are shown in Fig. 6.5.3. Since there is no void in the central axis, the void effects appear at the deeper position than that in the case of the void in the central axis.

As for special materials, three material configurations, 10 mm B_4C + 40 mm Pb (B_4C/Pb), 50 mm W (W) and 10 mm B_4C + 40 mm W (B_4C/W), were examined. The special material with a common area of 600 mm in diameter was set at the depth of 610 mm in the test region. The effects of these materials were estimated by the ratio of the calculated values with special materials to with SS316. Table 6.5.1 shows the obtained ratio of gamma heating rate at the depths of 711 and 914 mm. Since all the effects are larger than 20 %, it is possible to examine experimentally the effects of special shielding materials in all configurations. The B_4C/Pb and B_4C/W largely reduce the gamma heating at 711 mm. The effect of B_4C/Pb , however, dose not continue to the deeper position. On the other hand, reduction of the gamma heating by W is only 35 % at 711 mm, but the effect continues to deeper position. According to this preliminary analysis, B_4C/W is the most desirable shielding material.

References

- 1) Maki K., et al. : " Nuclear Group Constant set FUSION-J3 for Fusion Reactor Nuclear Calculations Based on JENDL-3," JAERI-M91072 (1991) (in Japanese).
- 2) Konno C., et al. : " Bulk Shielding Experiments on Large SS316 Assemblies", Fusion Technol. Vol. 21 [3] Part B, 2169 (1992).

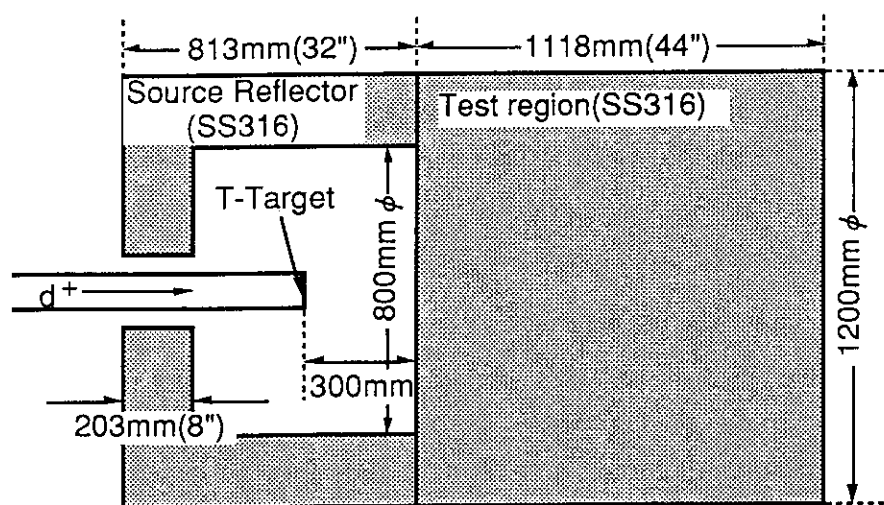


Fig. 6.5.1 Base Assembly for pre-analysis

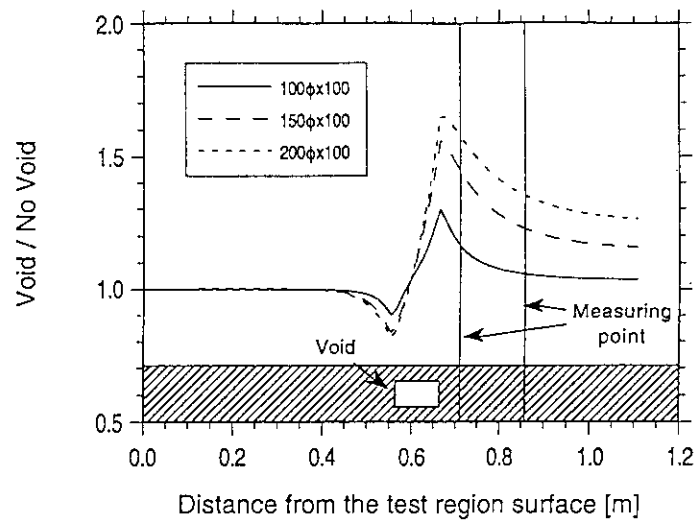


Fig. 6.5.2 The ratio of gamma-heating rate with the void to that without the void

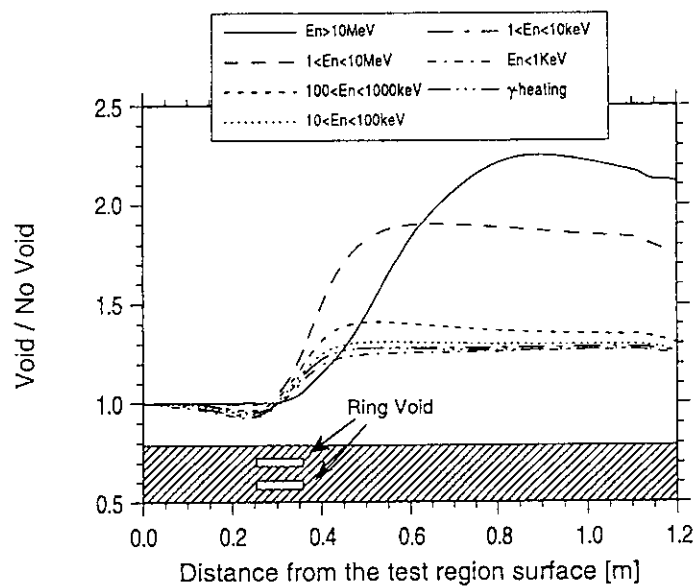


Fig. 6.5.3 The ratio of neutron flux and gamma-heating rate with a ring void to those without a ring void

Table 6.5.1 The effect of special shielding materials for gamma-ray heating

Material	Ratio (Material/Reference)	
	711 mm*	914 mm*
B ₄ C/Pb	0.45	0.80
W	0.65	0.74
B ₄ C/W	0.43	0.57

* : Distance from the front surface of the test region

7. Reactor and Nuclear Instrumentation

In the field of reactor instrumentation, R & D works being relevant to the development of High Temperature Engineering Test Reactor (HTTR) were almost finished. Some remaining works have been performed. Post-irradiation examinations for N-type thermocouples that were tested in the JMTR were carried out, and running tests of the developed fuel failure detection system have been continued.

In the field of nuclear instrumentation, R & D of a non-destructive measuring technique for inspection of TRU elements in drum-sized wastes has been carried out actively. In the work, a matter of recent concern and interest is the behavior of neutrons from (α, n) reactions. Thus, a computer program was developed for calculation of neutron emission rate in (α, n) reactions in arbitrary chemical compounds and mixtures. The program is very useful for estimation of alpha activity in wastes. Also, the possibility of detecting spontaneous fission neutrons, separated from (α, n) neutrons in high-level radioactive wastes, was studied in connection with the measurement technique of time interval distributions of all successive detection pulses in the passive neutron method.

As activities in the R & D works for HTTR instrumentation reduced, some fundamental researches have newly started. In connection with development of beam diagnosis in large ion accelerators, gamma-ray irradiation tests for opto-electronic materials such as LiNbO_3 , etc., were carried out with observing the absorption spectra in the thermal relaxation process. Also, the feasibility of beam profile monitoring was studied based on the inverse estimation of current distribution from measurements of magnetic fields. The inverse estimation utilized a genetic algorithm with promising results. The feasibility study for directional detection of sources of magnetic fields, i.e., electric currents or magnetic dipoles, have proceeded. Experiments with a hybrid system of high-Tc superconductor and magnetic-flux sensor presented promising results. In relation to this work, a highly sensitive magnetometer for very low temperature use was developed with utilizing a ferromagnetic amorphous wire. A study of magnetic-flux penetration behaviors in disk-type sintered $\text{Bi}_2\text{Sr}_2\text{CaCu}_2\text{O}_x$ revealed interesting nonlinear characteristics that might be feasible in new applications.

(Katsuyuki Ara)

7.1 Computer Program for Emission Rate Calculation of Neutrons from (α , n) Reactions in Arbitrary Compounds and Mixtures

H. Gotoh, M. Haruyama, M. Takase and T. Las*

Most passive neutron methods seem to make more effort on the estimation of the emission rate of spontaneous fission neutrons than on that of (α ,n) neutrons. This convention is originated from the fact that the former emission rate is determined only by the kinds and their abundances of transuranic nuclides contained in testing items whereas the latter emission rate depends not only on those of the transuranic nuclides but on the chemical composition of the transuranic elements. In using passive neutron methods for the estimation of alpha radioactivity contained in radioactive waste packages there will be another approach which places stress on the evaluation of (α ,n) neutron emission rate rather than on that of spontaneous fission rate, because the main interest is placed on the total alpha radioactivity contained in waste packages at the treatment and the disposal of radioactive wastes.

In order to promote this approach the authors made a computer program for the calculation of the conversion probability from alpha particles to neutrons by (α ,n) reactions in arbitrary compounds and mixtures. The program is written in BASIC and executable on personal computers. In the calculation we need data of the thick target neutron yields and the helium stopping powers in simple substances; and we need not any additional informations. We used the data of R. Heaton et al.¹⁾ for the thick target yield and the data of J. F. Ziegler in his book²⁾ for the stopping power.

It is conceivable that sometimes we encounter simple chemical compounds such as PuO_2 whereas we encounter some mixtures of several

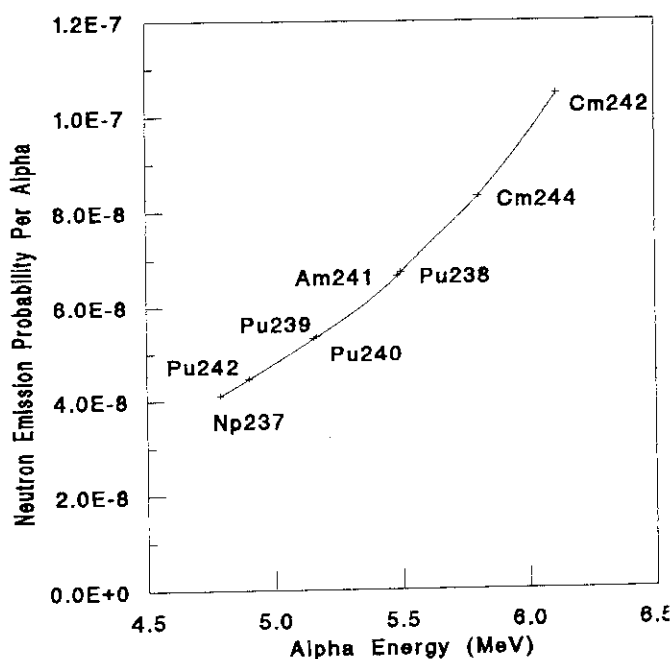


Fig.7.1.1 Neutron Emission probability per alpha particle for several long life transuranic nuclides in dioxide. The alpha particle energy corresponds to the strongest alpha line of each nuclide.

* Radioactive Waste Management and Technology Center, Tangerang, Indonesia

number of compounds or even some mixtures of mixtures of different compounds. To manage such occasions, we adopted a material registration system of recursive definition of items.

Figure 7.1.1 is a result of the calculation. The neutron emission probability per alpha particle through (α, n) reactions is plotted as a function of alpha particle energy for several transuranic nuclides in dioxide state such as PuO_2 . The alpha particle energies are correspond to the strongest alpha lines of long life alpha radioactive transuranic nuclides ^{237}Np , ^{238}Pu , ^{239}Pu , ^{240}Pu , ^{242}Pu , ^{241}Am , ^{242}Cm and ^{244}Cm important for radioactive waste treatment and disposal. Curium-242 emits (α, n) neutrons about 2.5 times more than ^{237}Np does. Among Np, Pu and Am except Cm the emission probabilities change at most within $\pm 30\%$.

Figure 7.1.2 shows (α, n) reaction neutron yield per alpha particle as a function of MgO weight percentage in homogeneous PuO_2 -MgO mixture. Neutron emission probability (neutron yield per alpha) grows as MgO weight percentage grows.

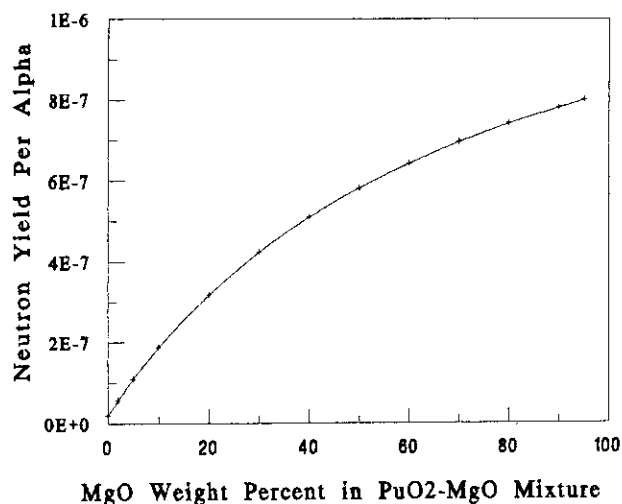


Fig.7.1.2 (α, n) reaction neutron yield per alpha particle as a function of MgO weight percentage in PuO_2 -MgO mixture.

References

- 1) Heaton R. et al. : Nucl. Instr. Meth. A276(1989)529.
- 2) Ziegler J. F. : Helium, Stopping Powers and Ranges in All Elements, Pergamon (1977).

7.2 Detection Possibility of ^{244}Cm in High Level Radioactive Wastes from Reprocessing Process

H. Gotoh, M. Haruyama and M. Takase

The alpha radioactivity of high level radioactive wastes generated in reprocessing process is mainly supplied by ^{244}Cm and ^{241}Am after several years cooling. The half-life of the former is about 18.1 years and that of the latter is so long as 433 years. If we can measure the intensities of both neutron generating processes separately, the obtained information will be useful for making a plan of disposal of high level radioactive waste packages.

Curium-244 emits neutrons mainly via spontaneous fission process and ^{241}Am purely via (α, n) reaction process. Although the former can be related to the time-correlated count and the latter to the time-uncorrelated count in passive neutron method, the vastly intense neutron emission

intensities of high level waste packages seem to have been making anyone hesitate to use the passive neutron method in measuring them separately.

The present authors have derived a theoretical expression for the distribution of time intervals between all successive detection pulses in the passive neutron method.¹⁾ This expression can be used to predict what sort of equipment should be prepared if we want to measure separately spontaneous fissions and (α, n) reactions of high level radioactive waste packages.

Figure 7.2.1 shows the predicted time interval distribution

to be taken by a passive neutron detection system with a dieaway time of $0.1\mu\text{s}$ and with a

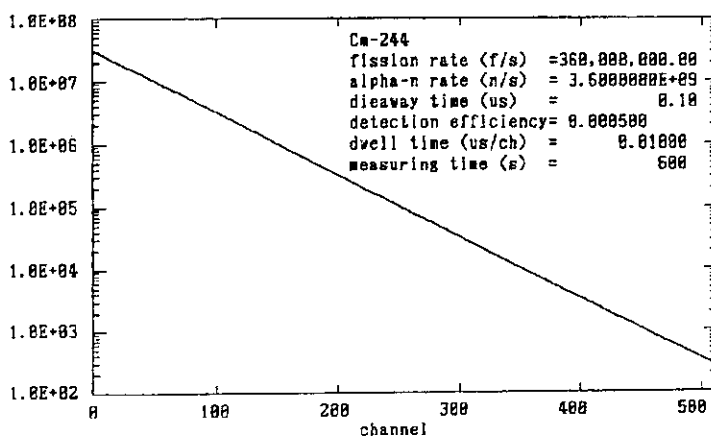


Fig.7.2.1 Predicted time interval distribution for a high level waste package by a detection system with detection efficiency 0.05% and with dieaway time $0.1\mu\text{s}$

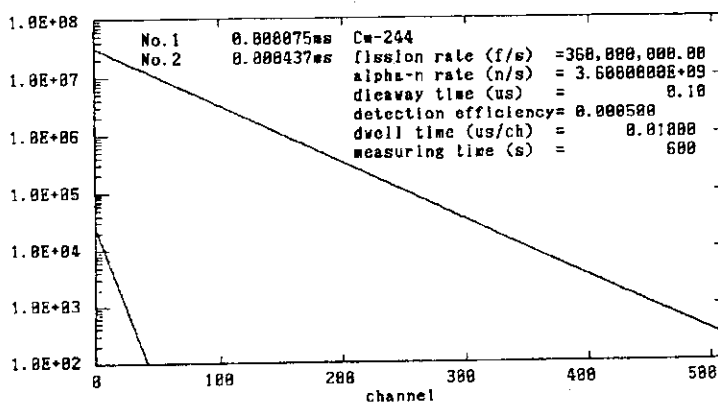


Fig.7.2.2 Decomposition of the time interval distribution shown in Fig.7.2.1 into a sum of two exponential functions

detection efficiency of 0.05% for a waste package containing ^{244}Cm with a spontaneous fission rate of $3.6 \times 10^8 \text{ s}^{-1}$ and (α, n) neutron source with a neutron emission rate of $3.6 \times 10^9 \text{ s}^{-1}$ from ^{241}Am in a measuring time of 600s. The data is supposed to be taken by a time interval analyzer with a dwell time of 10 ns/channel and with a channel size of 512. Although the distribution curve looks like a straight line at a glance in semi-logarithmic presentation, it can not be fitted with a straight line in a statistical criterion.

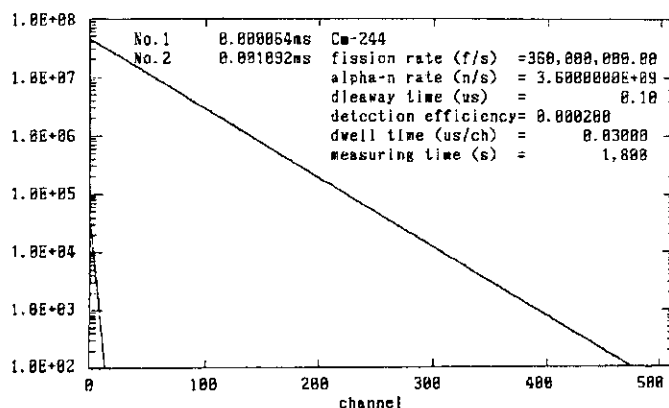


Fig.7.2.3 Predicted time interval distribution to be taken with a detection system with detection efficiency 0.02% and dieaway time $0.1 \mu\text{s}$

Figure 7.2.2 shows the result of fitting the same data with a sum of two exponential functions. The time constants of the two exponential functions were about $0.075 \mu\text{s}$ and about $437 \mu\text{s}$. The total count of the faster component was $186,104 \pm 56,665$ (30%) and that of the slower component was $1,373,594 \pm 67,698$ (4.9%). The uncertainty of the former count corresponds to that of the spontaneous fission rate. We conceive that we can attain a precision of 30% in a 10 min measurement with a small detection efficiency of 0.05% if we measure with a small dieaway time of $0.1 \mu\text{s}$.

Figure 7.2.3 shows that we can attain the same precision of 30% with a lower detection efficiency of 0.02% at the sacrifice of measuring time of 20 min. The small dieaway time of $0.1 \mu\text{s}$ is important in this condition.

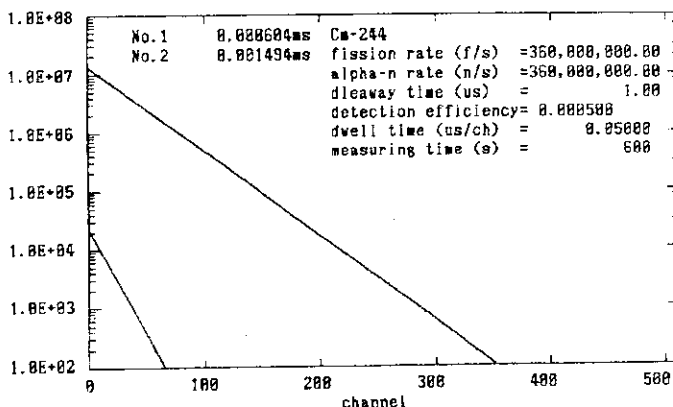


Fig.7.2.4 Predicted time interval distribution to be taken by a detection system with detection efficiency 0.05% and with dieaway time $1 \mu\text{s}$

Figure 7.2.4 shows that a larger dieaway time of $1 \mu\text{s}$ induces a larger uncertainty of 50% in a 10 min counting.

The small dieaway time of $0.1 \mu\text{s}$ will not be realized if we insist on using thermal neutron detection, because any slowing down process will take a time longer than $0.1 \mu\text{s}$. So

we will be obliged to use fast neutron detection mechanism such as helium recoil proportional counting.

Reference

- 1) Gotoh H. et al. : JAERI-M 91-138(1991)130.

7.3 Radiation Effects of Opto-electronic Materials

H. Yagi, H. Itoh and M. Yamada

An investigation of the radiation effects has been made for some kinds of opto-electronic materials in the low temperature region up to 500K. Tested specimens are LiNbO_3 , $\text{Bi}_{12}\text{SiO}_{20}$ (BSO), the Faraday rotator glass and others. The LiNbO_3 has a first-order electrooptic effect (i.e. the Pockels effect). The BSO shows the Faraday effect and is applied to the sensing of the magnetic field or the electric current. The absorption spectra and the thermo-luminescence were measured in the thermal relaxation.

An irradiation chamber was constructed with a helium refrigerator build in a heater and the specimens were controlled in the temperature range 20K to 500K. The specimen was irradiated by the Cobalt-60 source at the temperature of 20K. After the irradiation, the chamber including the specimen was setting into a double beam spectrophotometer and the absorption spectra were measured in the wave length range from 200nm to 900nm. The apparatus of this experiment includes the irradiation chamber is shown in Fig. 7.3.1. After the irradiation at the 20K the absorption spectra of the LiNbO_3 and the BSO were measured at optional temperatures under the thermal relaxation speed of 0.05K/s. The results of the measurements were shown in Fig. 7.3.2 (a) and (b). Figure 7.3.3 (a) and (b) show the absorbance as a function of temperature based on the results of the absorption spectra in the thermal relaxation. To estimate the depth of the trap levels, the Glow Curves were observed for the same specimens. The thermo-luminescence of the LiNbO_3 and the BSO was confirmed. The Glow Curves are shown in Fig. 7.3.4 (a) and (b).

For comparison with glass, the same measurements were performed for the Faraday rotator glass (FR-5), the tellurite glass (AOT-44B) and the lead glass, respectively. The measurements of absorption spectra showed the different characteristics between the single crystal (e.g., LiNbO_3 and BSO) and the glass. The absorption wave lengths of defects that were made by the gamma-ray irradiation and the depth of their trap levels were determined.

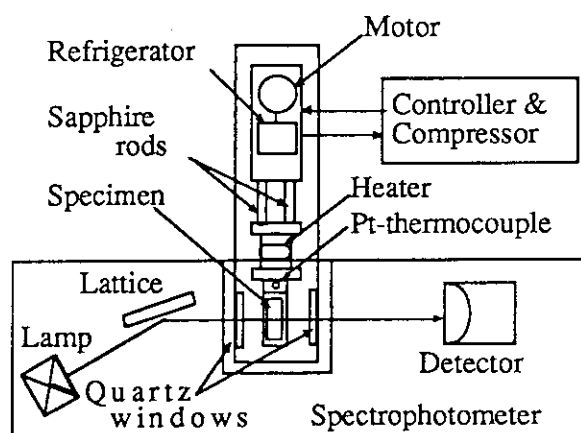
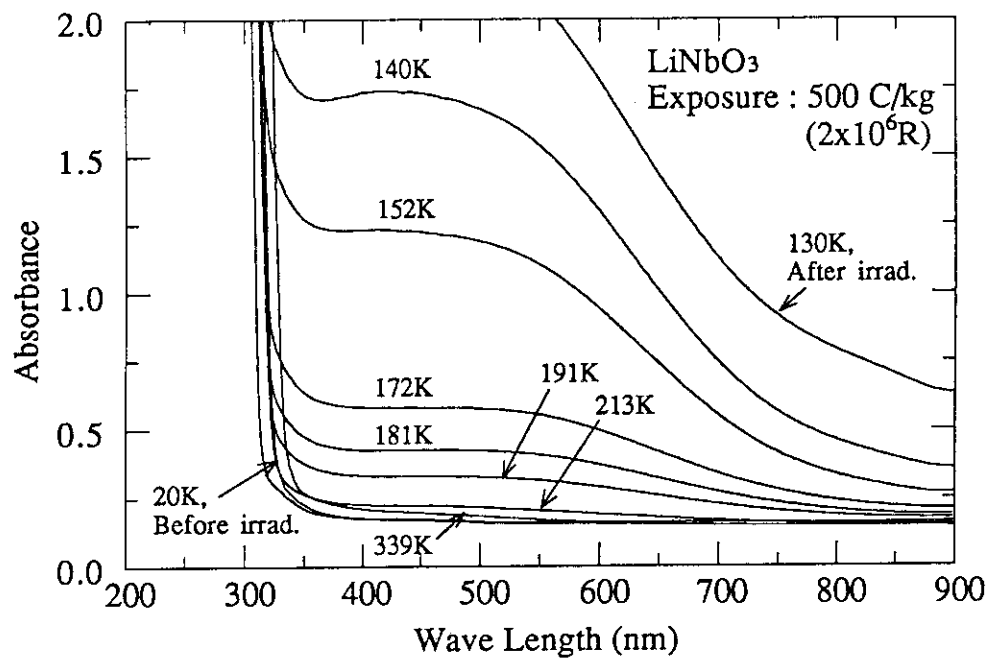
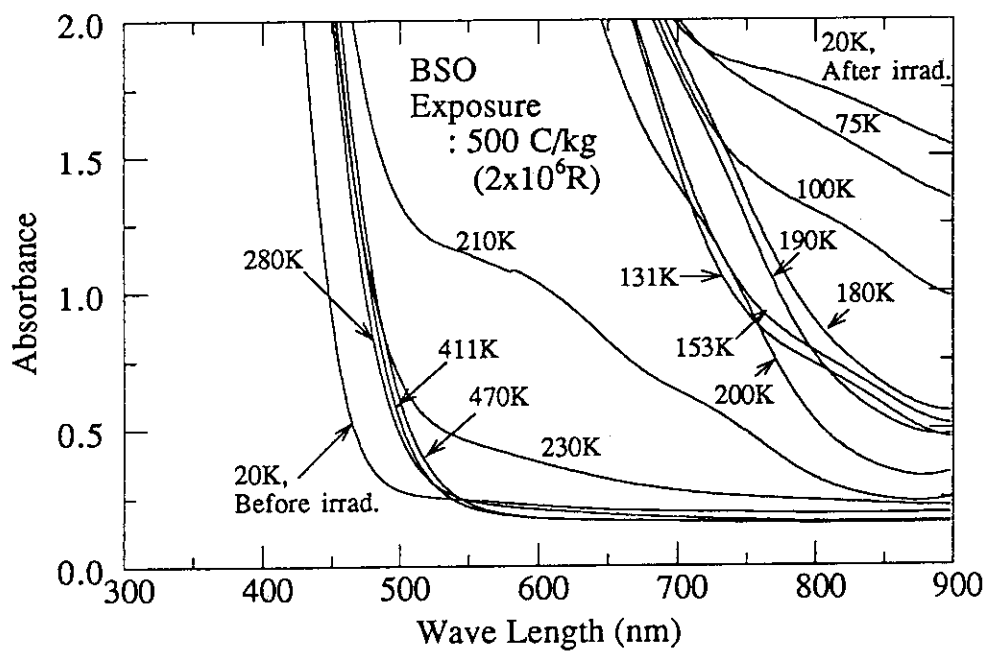


Fig.7.3.1 Configuration of the absorption spectra measurements in the thermal relaxation

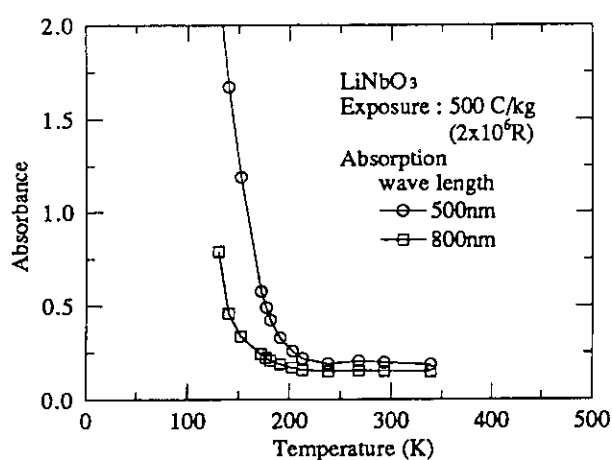


(a)

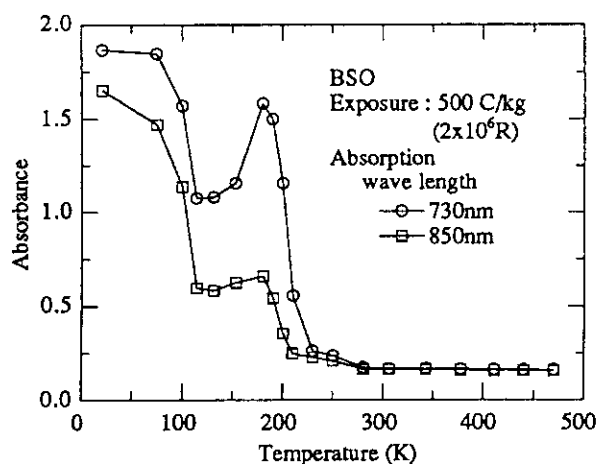


(b)

Fig.7.3.2 Absorption spectra of the LiNbO_3 (a) and the BSO (b) under the thermal relaxation speed of 0.05K/s after the irradiation of 500C/kg at the 20K

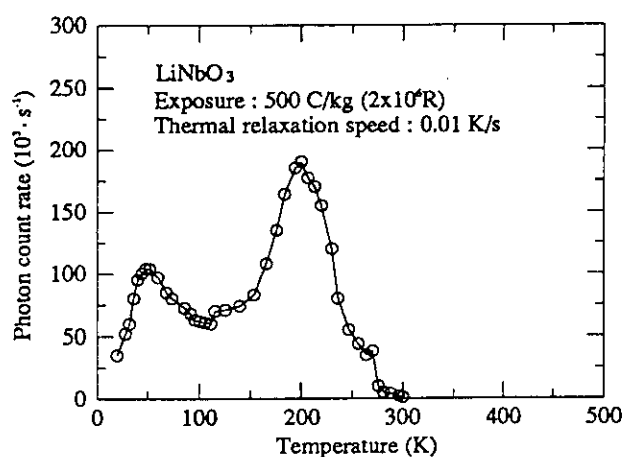


(a)

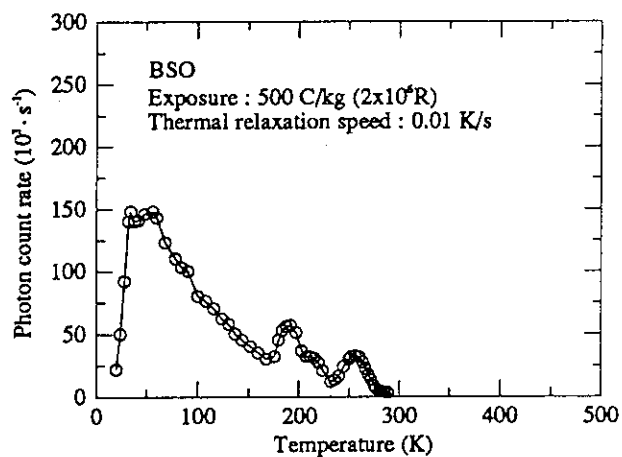


(b)

Fig. 7.3.3 Absorbance as a function of temperature for the LiNbO₃ (a) and the BSO (b) based on the results of the absorption spectra under the thermal relaxation



(a)



(b)

Fig. 7.3.4 Grow Curves of the LiNbO₃ (a) and the BSO (b) under the thermal relaxation speed of 0.01K/s after the irradiation of 500C/kg at the 20K

7.4 Beam Profile Monitor Using Inverse Estimation Method of Current Distribution from Magnetic Fields by Genetic Algorithm

M. Kishimoto

Beam Profile Monitor for Intense Proton Accelerators

In the Japan Atomic Energy Research Institute, the development of the intense proton accelerator (1.5GeV, 10mA) for the OMEGA project (Options Making Extra Gains of Actinides and Fission Products) has been continued. But, for intense proton beam, the conventional invasive measuring methods can not be adopted and the new beam measuring instruments need to be developed.

The authors have been studying about the selective magnetic field detection with high-temperature superconductor¹⁾ and applied it to the new type of non-invasive beam profile monitor. The schematic diagram of the beam profile monitor is shown in Fig.7.4.1. This beam monitor consists of two high-temperature superconductor disks, which are separated with a gap of very short distance. The magnetic sensors are settled in that gap so as to surround the beam vacuum pipe. By the magnetic shield effect of these disks due to perfect diamagnetism of superconductor, the magnetic field induced from proton beam in the vicinity of the superconductor disks can be detected selectively and in high sensitivity. Then, the current distribution of proton beam is estimated from the magnetic fields by genetic algorithm (GA)²⁾.

Genetic Algorithm

GA is a new type of algorithm on the basis of the mechanism of evolution of living organisms³⁾. Normally, most organisms adjust themselves to the environment through the process of selection, reproduction and mutation. GA is search and optimization algorithm that utilizes these mechanisms of organisms and has wider application than do the conventional ones. The feature of GA is easy to avoid local minimum problem because GA searches from a population of points simultaneously.

Application of Genetic Algorithm to Inverse Estimation of Current Distribution

We consider the estimation problem of the current distribution as the optimum allocation problem of the currents in the cross-section of beam vacuum pipe. So, we divide the current distribution area into $M \times N$ segments and define the coordinate system as shown in Fig.7.4.2. The current I_{ij} which flows through the segment (i, j) is represented as :

$$I_{ij} = n_{ij} J_u dx dy$$

where, J_u is unit current density and n_{ij} is an integer from 0 to 255, which represents the

strength of the current flowing through the segment (i, j) ($i=1\sim M, j=1\sim N$). Then, the state of the current distribution area is represented by the $M\times N$ state matrix which element is the current strength (Fig.7.4.3).

As fitness, which is index of evaluation of gene in genetic algorithm, we consider the error evaluation function. In Fig.7.4.2, the magnetic field that the currents induce at the measuring point is given by

$$\mathbf{B}^\alpha = \frac{\mu_0}{4\pi} \sum_{i=1}^M \sum_{j=1}^N \frac{\mathbf{I}_{ij} \times (\mathbf{r}_{ij} - \mathbf{r}_\alpha)}{|\mathbf{r}_{ij} - \mathbf{r}_\alpha|^3}$$

where \mathbf{r}_{ij} and \mathbf{r}_α are the position vectors of the segment (i, j) and the measuring point respectively. When the magnetic field measured at point α is \mathbf{B}_m^α , we define the error evaluation function to evaluate the fitness of the gene as :

$$\frac{1}{2} \sum_{\alpha} |\mathbf{B}_m^\alpha - \mathbf{B}^\alpha|^2$$

We try to find out the current distribution of proton beam to make this error evaluation function equal to zero by means of GA.

Computer Simulation

To verify the effectiveness of the estimation method of current distribution by GA, computer simulations were carried out. The parameters of simulation are shown in Table.7.4.1 and the simulation results are shown in Fig.7.4.4. From simulation results, we find that GA has the very good effectiveness for the inverse estimation of beam current distribution.

References

- 1) K.Ara, K.Sakasai, M.Kishimoto, Nonlinear Phenomena in Electromagnetic Fields, Elsevier Science Publishers B.V., 1992, 193-196
- 2) M.Kishimoto, K.Sakasai, K.Ara, W-42, ISEM-Sapporo, 1993
- 3) John.H.Holland, Scientific American, July 1992, 44-55

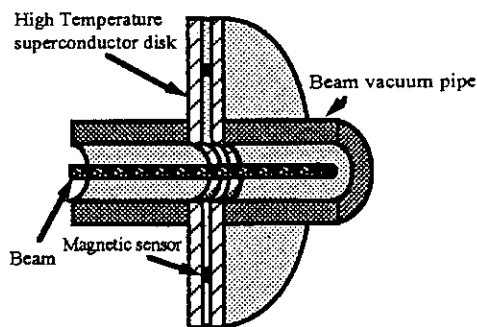


Fig.7.4.1 Schematic diagram of beam profile monitor

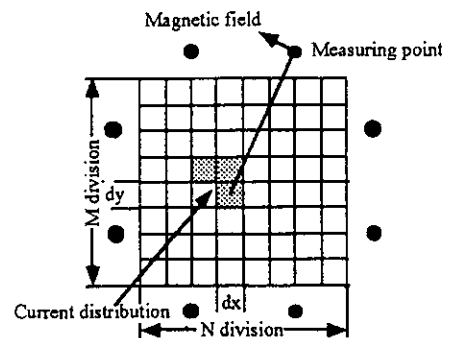


Fig.7.4.2 System of measurement

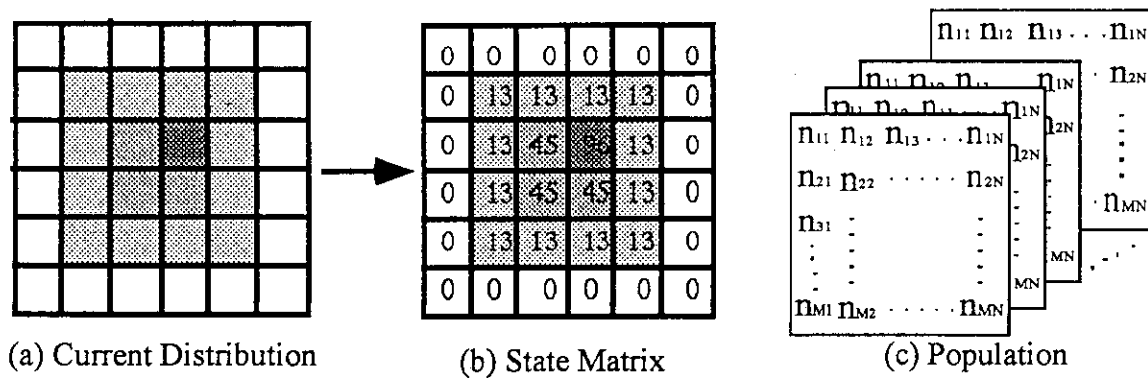


Fig.7.4.3 State Matrix and Gene

Table.7.4.1 Simulation Parameters

Segments	256 (16 × 16)
Measuring points	24 points
Current area	9 segments
Population	100

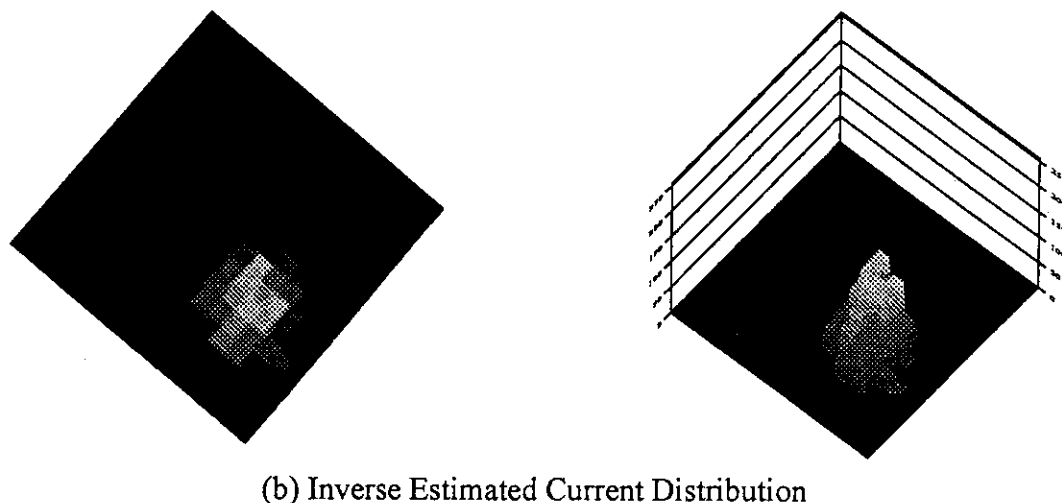
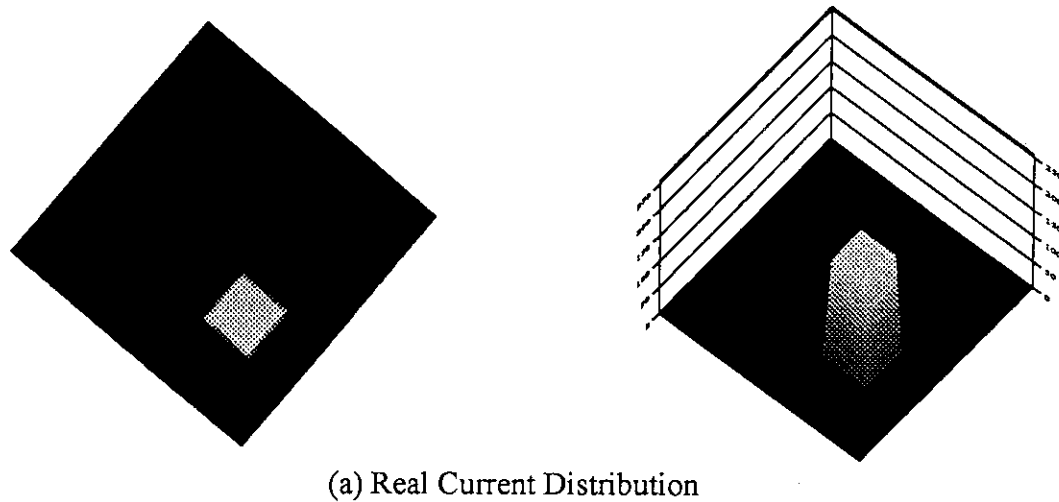


Fig.7.4.4 Simulation Result

7.5 AC Magnetic-flux Penetration in a Sample Disk-type Sintered $\text{Bi}_2\text{Sr}_2\text{CaCu}_2\text{O}_x$ under Low Magnetic Fields Applied by a Planar Coil

K. Ara, M. Katagiri, H. Itoh and K. Sakasai

Mohri et al. studied the characteristics of nonlinear ac magnetic-flux penetration in disk-type high T_c superconductors, and applied the results to fast-response magnetometers^{1,2)}. In these studies, attempts were made to magnetize the disk samples by an ac current through coils wound on the circumference of their outer edges. In these cases, the flux penetration first nucleated at the edge of sample and then propagated inward. This condition presented remarkable so-called nonlinear BH minor loops. The authors investigated ac magnetic-flux penetration characteristics in a sample disk-type sintered $\text{Bi}_2\text{Sr}_2\text{CaCu}_2\text{O}_x$ under relatively low magnetic fields, applying with a planar coil. The results obtained were both different and interesting.

Figure 7.5.1 schematically shows the preparation of the sample used in the measurements. The sample sintered $\text{Bi}_2\text{Sr}_2\text{CaCu}_2\text{O}_x$ disk has an outer diameter of 30 mm and a thickness of 0.5 mm. The critical current density (J_c) of the sample was found to be about 1200 A/cm^2 at 90 K. The excitation coil used for the application of the magnetic fields and the pickup coil for detecting the degree of magnetic-flux penetration are constructed of aluminum, deposited on respective 0.3 mm thick sapphire plates.

The sample was cooled to 72 K with no application of magnetic fields. An ac current of 10 kHz was then applied, increasing its amplitude gradually under condition of a zero dc bias current. The magnetic-flux penetration was measured in terms of peak-to-peak values of the ac voltage induced in the pickup coil. The results of the measurements are shown in Fig. 7.5.2. In the figure, the scales of the ac flux penetration are also given in terms of the average ac magnetic flux density, estimated from the induced ac voltage, and that of the average magnetic field produced by the ac excitation current when the coil was placed in free space. It can be seen that the flux penetration was zero for ac excitation currents of less than 0.35 A[peak-to-peak]. Flux penetration occurred at 0.35 A and strongly developed with slight increases in the current. After the flux penetration reached about 3.6 Gauss at 0.4 A, the values increased in proportion to the excitation current. When the current

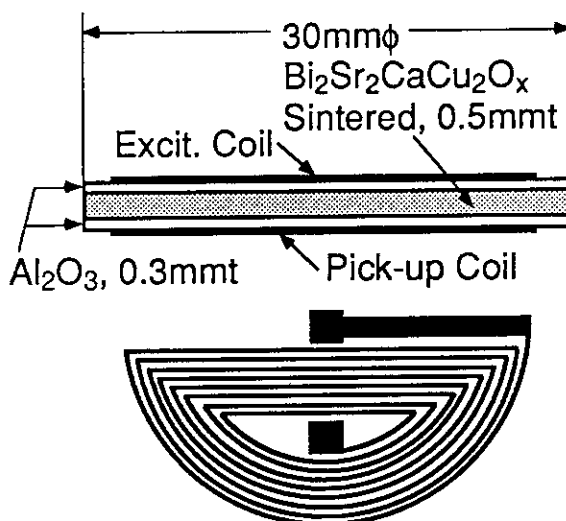


Fig. 7.5.1 Schematic representation of the preparation of the measurement sample.

was decreased, a steep decline in the flux penetration occurred at about 0.3 A and reached zero at about 0.26 A, thus obtaining the characteristic hysteresis flux penetration shown in Fig. 7.5.2.

The excitation current of 0.35 A, where the flux penetration nucleates, might be related to the $2H_{c1}$ content of the sample, which is effective for ac excitation. Since an ac current of 0.35 A [peak-to-peak] can produce a magnetic field of 4.7 Oersteds [peak-to-peak] with the excitation coil placed in free space, it is possible that, $H_{c1} = (4.7/2)/(1-n)$, where n is the demagnetizing coefficient. However, the estimation of n for the system shown in Fig. 7.5.1 is somewhat difficult to obtain. In the excitation current region of

0.35A→0.4A, the flux-penetration appears to be unstable. Namely, the growth of a stable flux penetration was not completed. The results also show that the penetration was stable in the current region greater than 0.4 A. These explanations are supported by the observed waveforms of the induced voltages compared with those of the excitation currents.

The observed waveforms were determined at Points (a) and (b) shown in Fig. 7.5.2, making use of an oscilloscope and a computer. At Point (b), the phase difference between the magnetic-flux penetration and the excitation current is close to zero. This means that the ac flux penetration at Point (b) consumes very little or no energy. Namely, the ac susceptibility of the sample is for the real component, consuming very little or no energy. At Point (a), however, the waveform of the ac magnetic-flux penetration is distorted with a phase difference of about 90°.

The former phenomenon means that the relationship between the flux penetration and the applied magnetic field is not linear. That is, the normal growth of the flux penetration is slowed by the consumption of energy at Point (a), and probably over the current region of 0.35A→0.4A. The latter results mean that the ac susceptibility of the sample is for the imaginary component. This is also evidence of energy consumption by the ac flux penetration at Point (a).

The ac excitation current was then fixed at a value of 0.34 A [peak-to-peak] where the flux penetration did not yet occur, and a dc bias current was superposed on it. While increasing the value of the dc bias current from zero, the occurrence and change of the flux penetration were measured by means of the induced voltages in the pickup coil. The results are shown in

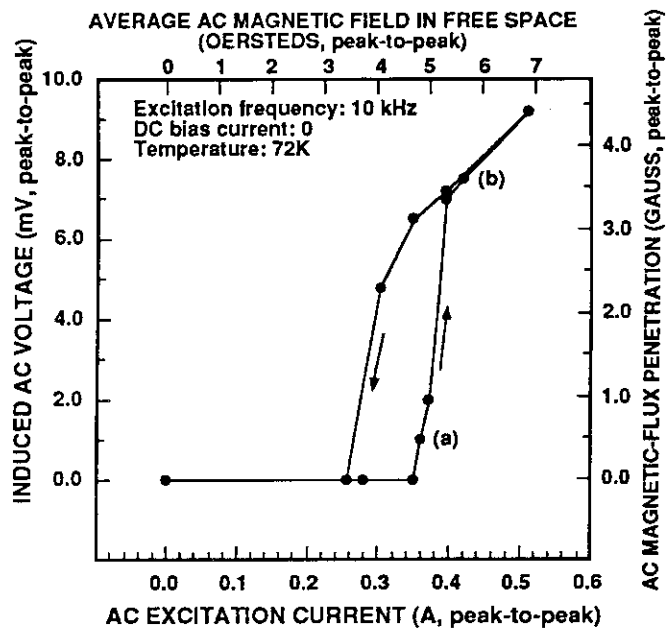


Fig. 7.5.2 The characteristics of the ac magnetic-flux penetration under conditions of zero dc bias current.

Fig. 7.5.3. The ac flux penetration began at a dc bias current of 0.017 A, and became saturated at about 0.058 A. The penetration of the ac magnetic flux remained at a fixed value of approximately 3.3 Gauss, even though a dc bias current was decreased to zero. This means that dc magnetic flux, produced by the dc bias field and once it obtained a stable state, became remanent. When the ac excitation current of 0.34 A was repeatedly turned off and on at Point C in Fig. 7.5.3, the penetration of ac magnetic flux took the path of C→A→C→A. We had to wait more than 10 seconds without applying any excitation and bias current before resuming the development of ac flux penetration along the path [A→B→C].

The above mentioned experiments and measurements appear to be very effective in the understanding of the magnetization and demagnetization process of high-Tc superconductors. Also, the characteristics of the nonlinear flux penetration introduced in this note might be feasible in new applications.

References

- 1) Mohri K., Uchiyama T., and Ozeki A.: Tech. Digest 8th Sensor Symposium. 235(1989).
- 2) Uchiyama T., Mohri K., Ozeki A. and Shibata T.: IEEE Trans. Mag. 26, 1442(1990).

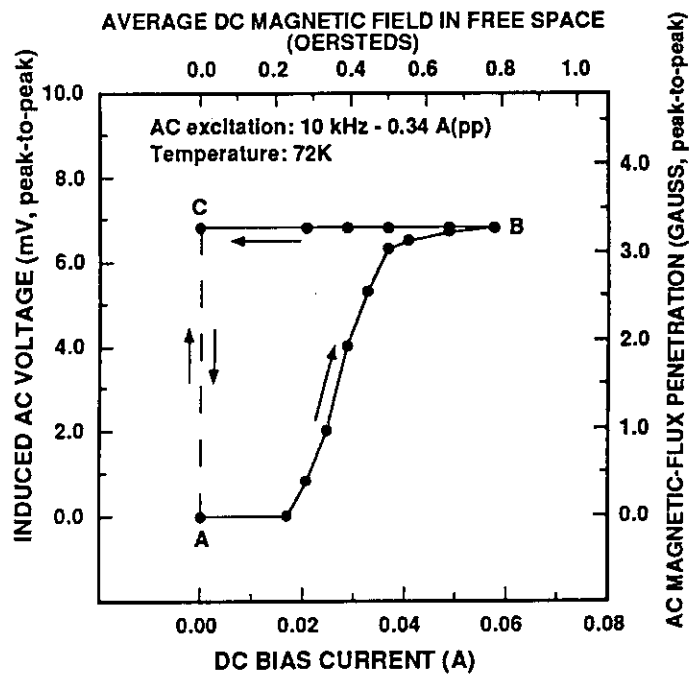


Fig. 7.5.3 The development of the ac magnetic-flux penetration as a function of the increase in a dc bias current, following path [A→B], and the maintenance of the flux penetration as a function of decreasing the dc bias current following path [B→A].

7.6 Electric and Magnetic Characteristics of Co-Fe-Si-B Based Amorphous Wire and its Application to a Multivibrator-type Magnetometer at Low Temperature

K. Sakasai, K. Ara, H. Itoh, M. Kishimoto and M. Katagiri

In experimental studies of solid state physics, sometimes a magnetic field sensor being able to work at very low temperature is needed. Semiconductor Hall devices are most common ones but their sensitivity to the magnetic field is relatively low at low temperature: the application of them is limited to relatively high magnetic fields. SQUIDs are, on the other hands, excellent devices for the measurement of very weak magnetic fields; but they are costly devices and too much expensive to measure the fields of mG order.

Mohri and Sasada recently succeeded at 77K in operation of multivibrator-type magnetometers,^{1),2)} where Co-Fe-Si-B based amorphous wires were adopted as core materials. Their successes motivated the authors to try out to develop the magnetometer being able to work at the temperature below 77K to about 4.2K. Thus the electric and magnetic characteristics of a Co-Fe-Si-B based amorphous wire were investigated at low temperature below to about 4.2K.

The sample amorphous wire of $(\text{Co}_{94}\text{Fe}_6)_{72.5}\text{Si}_{12.5}\text{B}_{15}$ with a diameter of $120\mu\text{m}$ was manufactured by UNICHIKA Ltd. and provided to JAERI: its intrinsic electrical and magnetic characteristics are shown in Table 7.6.1. In the table, B_s is the saturation and H_c the coercive force and μ_m the maximum permeability. The resistance of the specimen was measured with varying the ambient temperature and a minimum resistivity point appears at 30K, but the value retain still 97.6% of that at 300K.

Composition	: $(\text{Co}_{94}\text{Fe}_6)_{72.5}\text{Si}_{12.5}\text{B}_{15}$
Diameter	: $120\mu\text{m}$
Electrical resistivity	: $125\mu\Omega\cdot\text{cm}$
Magnetic Characteristics	
B_s	: 8 kG (DC)
H_c	: 0.06 Oe (DC)
μ_m	: 14,480 at 1kHz
	: 1,640 at 100kHz
	: 290 at 1MHz
Other feature	: zero magnetostriction

Table 7.6.1 The typical properties of the manufactured amorphous wire.

Since the wire is used under ac excitation in the multivibrator-type magnetometer, the magnetic properties of the wire at low temperatures were examined through measurements of ac hysteresis magnetization curves under an excitation of 25.4 kHz. Figure 7.6.1 shows schematically the electronic setup for measurements of the hysteresis magnetization curves. The curves all obtained were compared with those at room temperature and temperature-dependent magnetic characteristics in term

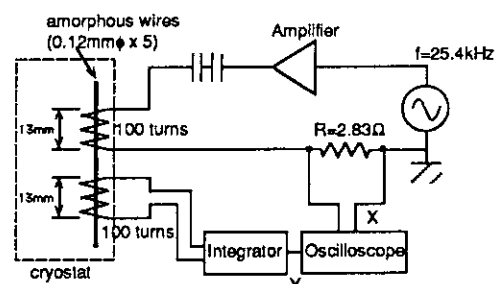


Fig.7.6.1 Schematic diagram of an electronic setup for measurements of ac magnetization hysteresis curves.

of B_s , H_c and μ_m were obtained in normalized forms as shown in Fig.7.6.2. One see that all B_s , H_c and μ_m increase as the temperature decreases. Those degrees of characteristics change are not of order to deny the possibility of applying this amorphous wire at low temperature below 77K.

Based on the obtained data, a multivibrator-type magnetometer was fabricated and tested at low temperature. The negative feedback circuit was incorporated also for examining its effectiveness for sensitivity stabilization. The magnetometer probe circuit fundamentally consists of a single core multivibrator and a filter amplifier. The sigle core multivibrator is made of a core, an excitation coil, N , a gate coil, N_g , a feedback coil, N_f , and complementary MOSFETs.

In order to examine the performance of the magnetometer at low temperaturers, the probe was installed in a metallic capsule of a cryostat and the magnetic fields were applied to the magnetometer by letting currents flow through the calibration coil, N_c , wound together with other magnetometer coils, N , N_g and N_f . The tests were carried out at a room temperature, 77K and 6K. Figure 7.6.3 shows calibration curves of the magnetometer without the negative feedback. So the curves represent the intrinsic characteristics of the magnetometer probe itself. Because it is difficult to distinguish the differences of the curves in the figure, the calibration data were treated to fit them to a linear function with a least-square method. The results are:

$$\begin{aligned} M(\text{R.T.}) &= 0.0029989 + 2.2855H \\ M(77\text{K}) &= 0.0022672 + 2.3245H \\ M(6\text{K}) &= 0.0015345 + 2.3319H \end{aligned}$$

where H represents input magnetic fields and M output voltage of the sensor. One see that the sensitivity increased 1.7% at 77K and 2.0% at 6K, respectively, as compared with that at the room temperature.

Although we expected that the decreases of the sensitivity were due to the increases of iron loss (eddy current loss and hysteresis loss) in the core material of the magnetometer at low temperatures, the realities are different. This might come from the remarkable decreases of the

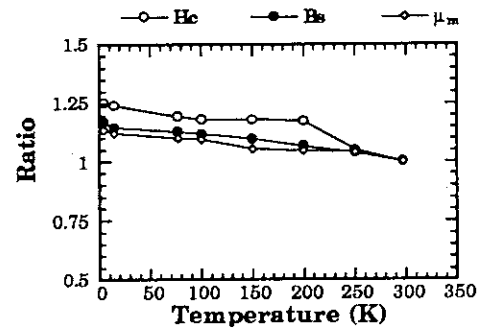


Fig.7.6.2 Temperature dependency of obtained B_s , H_c and μ_m .

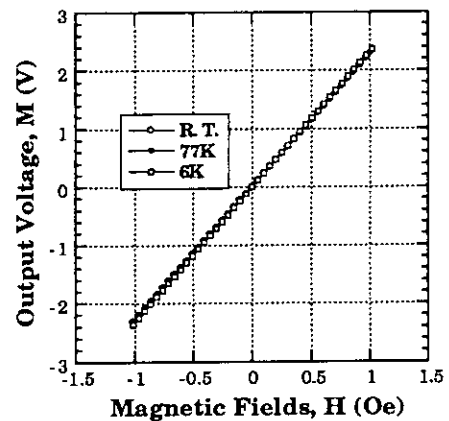


Fig.7.6.3 The calibration curves of the magnetometer without the negative feedback

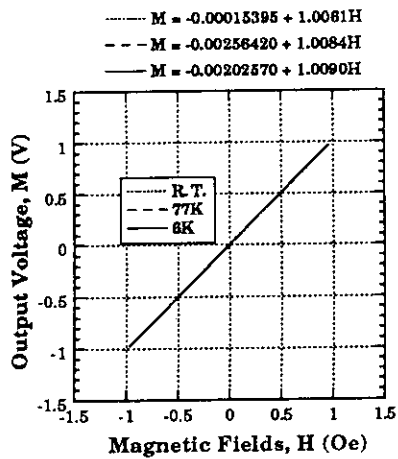


Fig.7.6.4 The calibration curves of the magnetometer with the negative feedback

Since the magnetometer probe of multivibrator type is magnetically excited with self-oscillation of high frequency, the high frequency magnetic fields usually leak to the outside environment from the probe. The electrical and magnetic environments surrounding the probe seem, therefore, to have an influence on the sensitivity of the probe. This was examined by removing the probe from the metallic capsule of cryostat into a liquid nitrogen bath and carrying out a calibration test without applying the negative feedback. The result is shown in Fig.7.6.5a) together with that at a room temperature. One sees that the sensitivity increase at 77K is 6.7% as compared with that at the room temperature and it is larger than 1.7% that was obtained at the test in the metallic capsule of cryostat. This relatively large change of the sensitivity was, however, stabilized also by applying the negative feedback as shown in Fig.7.6.5b).

References

- 1) Mohri K. : IEEE Trans. Mag. MAG-20, 5, 942(1984)
- 2) Sasada I. : J. Appl. Phys., 73, 5635(1993)

electric resistance of the coil, N , in the magnetometer probe at low temperatures because the ohmic loss (i.e., the voltage drop) in the coil, N , decreases the sensitivity of magnetometer. The final result may be that the sensitivity increase due to the decrease of ohmic loss in the coil, N , has made slight overcompensation for the decrease of the sensitivity due to the increase of iron loss in the core material.

Figure 7.6.4 shows the calibration curves with the negative feedback. One sees in the figure that the magnetometer could have a good linearity and a constant sensitivity with the negative feedback even at a different low temperature.

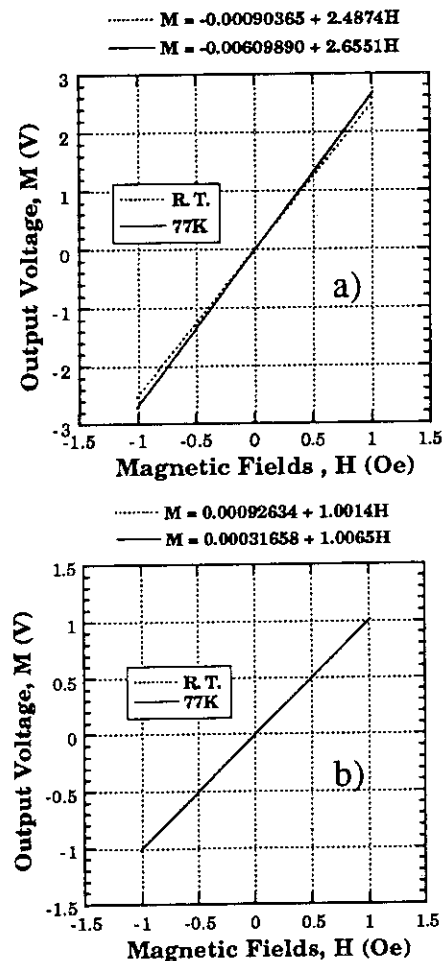


Fig.7.6.5 The calibration results in a liquid nitrogen bath a) without the negative feedback and b) with one.

7.7 Directional Detection of Current Dipoles by a Hybrid System of Superconducting Plates and a Magnetic Sensor

K. Sakasai, M. Kishimoto and K. Ara

It is important to reconstruct a source distribution of the magnetic fields from the results of magnetic field measurement outside the human body¹⁻³⁾. However, localization of the source, so called the inverse problem in magnetic field measurement, is known as a problem which has no unique solution⁴⁾. Therefore many attempt have been made to localize current sources or magnetic sources in a human body introducing a simple source model such as a single dipole model or a two-dimensional current source model⁵⁻⁶⁾. The authors have introduced a new method for directional detection of current dipoles or magnetic dipoles by utilizing a diamagnetic substance⁷⁾.

The proposed method to detect current dipoles in a limited area is shown in Fig.7.7.1. The sensor is installed between two superconducting parallel plates. The detectable region is that being cut out by two extension planes of the two plates. In the system the sensor can detect selectively magnetic fields produced by current dipoles perpendicular to or magnetic dipoles parallel to the planes. A good electric conductor such as copper behaves as a diamagnetic substance in high frequency alternative magnetic fields in consequence of eddy currents induced on its surface. For confirmation of effectiveness of the system, simulation experiments were carried out with high frequency source dipoles and copper devices. It was proved that the method is very useful for selective and directional detection of the sources⁸⁾.

For detection of static current dipoles, fundamental experiments were carried out by utilizing high T_c Bi-Sr-Ca-Cu-O superconducting parallel plates. The experimental scheme is illustrated in Fig.7.7.2. The plate has a thickness of 2mm and a side of 100mm. The distance be-

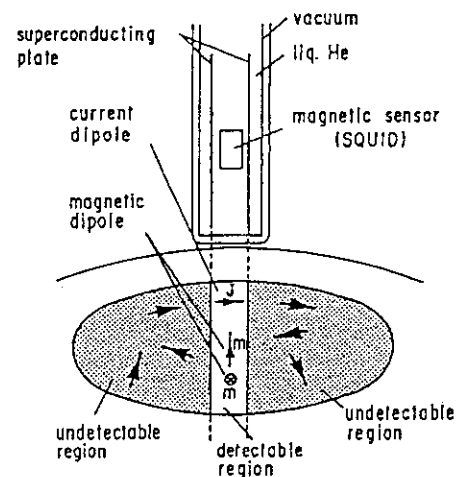


Fig.7.7.1 Detection of Current Dipoles in a limited area.

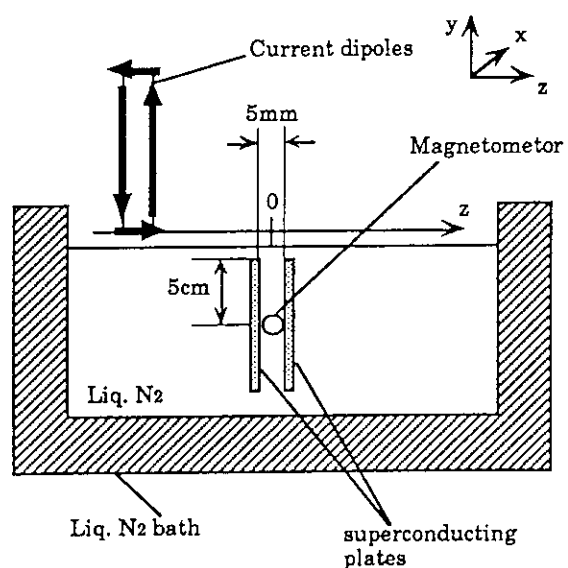


Fig.7.7.2 Experimental Scheme

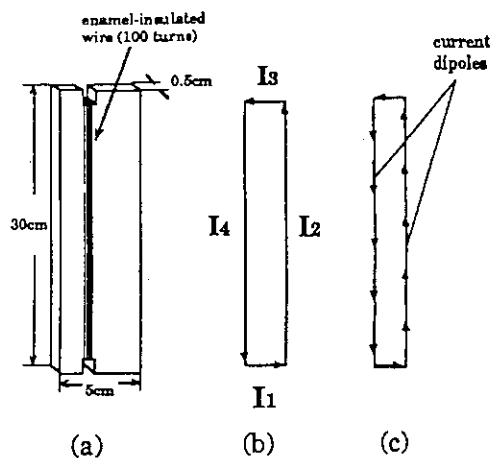


Fig.7.7.3 Preparation of Current Dipoles

tween two plates is 5mm. The critical temperature and critical current density of the sample plate are about 90K and 800A/cm², respectively.

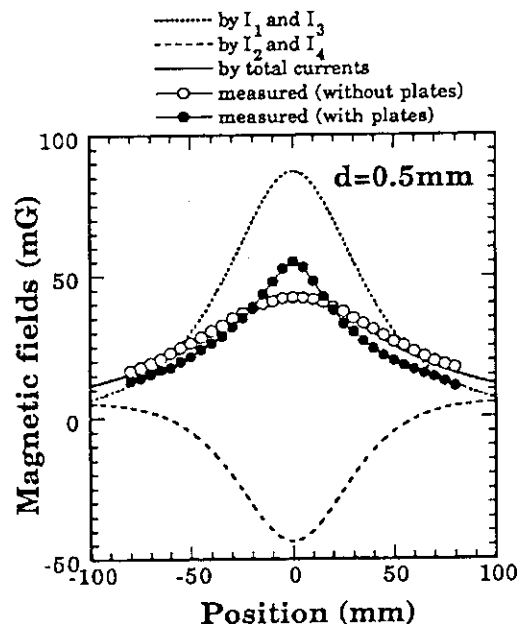
The current dipoles are simulated by letting currents of 0.3A flow in a coil as shown in Fig.7.7.3a). The currents flowing in the coil can be divided into 4 components; I_1 which flows in the bottom side of the coil, I_3 in the top side, I_2 and I_4 in the both sides. They are schematically shown in Fig.7.7.3b). The magnetic fields by I_1 or I_3 can be replaced by those by single current dipole at the center of the each side, but not those by I_2 or I_4 . I_2

or I_4 must be considered as a set of current dipoles, which are visually shown in Fig.7.7.3c).

Thus the currents flowing in the coil have both current dipoles perpendicular to and those parallel to the superconducting plate. The magnetic fields measured with the sensor are greatly influenced by the current current dipoles parallel to the plate. In the experiments the sensor was installed at a center of the two plates in a liquid nitrogen bath and output voltage from the sensor was measured as a function of the position of the simulated current dipoles. The experiments were carried out in cases of $d=0.5\text{mm}$, $d=5.5\text{mm}$ and $d=10.5\text{mm}$, where d is a distance between the top side of the plate and the bottom side of simulated current dipoles at a position $z=0$.

As an example of the experiments, the x-component of the fields measured with the sensor in case of $z=0.5\text{mm}$ are shown in Fig.7.7.4 as compared with that of the case without the plates. In the figures, a dotted line, a dashed line and a solid line indicate calculated magnetic fields by I_1 and I_3 , by I_2 and I_4 , and by total currents, respectively.

In the figure magnetic fields with plates are higher than those without plates in a range $|z|<20\text{mm}$. That is because the magnetic fields by the currents parallel to the plate (I_2 and I_4) are greatly shielded by the superconducting plates. In a range $|z|>20\text{mm}$, the fields with plates are lower because the currents perpendicular to the plate (I_1 and I_3) are also shielded. In other words, the magnetic fields are increased when the dipoles are in a region being cut out by two exten-

Fig.7.7.4 Experimental Results of $d=0.5\text{mm}$

sion planes of the two plates and the fields are decreased when the dipoles are outside the region. When spatial resolution is defined as a full width at half maximum (FWHM) of the peak, the spatial resolution is improved by introducing the two superconducting parallel plates, as shown in Fig.7.7.5, where the results in Fig.7.7.4 are normalized with the peak values. As seen in the figure, spatial resolution in case with plates is almost the same as that of magnetic fields by the currents perpendicular to the plates (I_1 and I_3), although the peak values are smaller. Other results in cases of $z=5.5\text{mm}$ or $z=10.5\text{mm}$ are similar with those of $z=0.5\text{mm}$.

As a result of the above experiments, it is concluded that the sensor with superconducting parallel plates can measure only the current component perpendicular to the plates spatially and selectively even if the current component parallel to the plates exists. In actual it is important to increase the peak values, but the degree of the effectiveness of the system depends on the system configuration. So extensive experiments are under planning together with computer simulation.

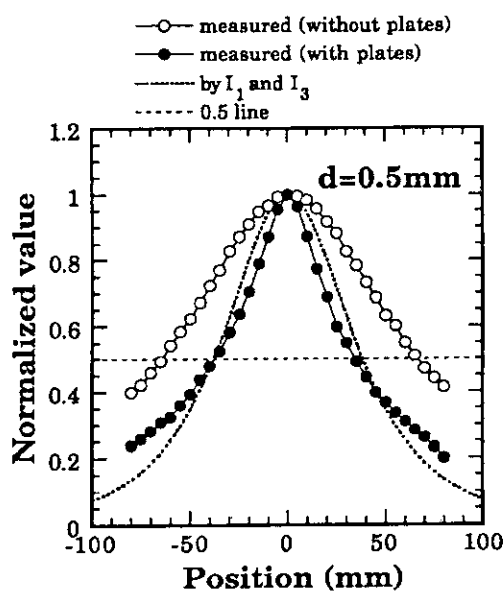


Fig.7.7.5 Experimental results of $d=0.5\text{mm}$ (normalized with peak values)

References

- 1) Uchikawa Y. and Kotani M. : J. Mag. Soc. Jpn., 15, 759(1991)
- 2) Ueno S. : Trans. Inst. Electr. Eng. Jpn., A, 111, 773(1991)
- 3) Saotome H. et al. : Trans. Inst. Electr. Eng. Jpn., A, 112, 279(1992)
- 4) Williamson S.J. and Kaufman L. : J. Magn. Magn. Mat., 22, 129(1981)
- 5) Kullman W. and Dallas W. J. : IEEE Trans. Biomed. Eng., BME-34, 837(1987)
- 6) Roth B.J., Sepulveda N. G. and Wiskvo J. P. Jr., : J. Appl. Phys., 65, 361(1988)
- 7) Ara K. and Sakasai K. : Proc. Tech. Magnetism, Paper Mag-91-100(1991)
- 8) Sakasai K. and Ara K. : J. Mag. Soc. Jpn., 16, 337(1992)

8. Reactor Control, Diagnosis and Robotics

As a new development in the study of advanced methods of reactor control, a robust control system has been designed by applying the Hardy-infinity control theory to a nonlinear model of the BWR core dynamics. The result of computer simulation shows that the control system is sufficiently stable and gives satisfactory performances.

New developments have been made in the studies on nonlinear reactor dynamics problems. In the study on nonlinear reactor dynamics, a simplified three dimensional model has been derived from a higher order model of a BWR to obtain an explicit analytical expression for reactor instability criterion. The derived criterion is useful for qualitative analysis of the BWR instability problems.

The reactor noise analysis methods have been applied to various problems. The method of multivariate autoregressive modelling (MAR) was applied to investigate the cause of power oscillation observed in the Nuclear Safety Research Reactor (NSRR). Through the spectral, coherence and noise power contribution analyses as well as the analysis of closed loop frequency response functions, it has been concluded that the power oscillation may be due to poor characteristics of the feedback control loop.

The analysis of the reactor noise data of the nuclear-powered ship "Mutsu" obtained in the experiments of dynamics identification using pseudo-random input signals conducted during her experimental navigation is being continued. The excellent load following characteristics of the Mutsu plant has been confirmed by the spectrum and coherence analyses. The interaction among two steam generators and a pressurizer was studied in detail using the signal transmission path (STP) analysis based on the MAR modelling.

The benchmark analysis of acoustic noise signals for detection of sodium/water reaction due to sodium leak was continued. By applying the twice squaring and band-pass filtering method, the sodium/water reaction was successfully detected for the test data having a noise-to-signal ratio of -16 dB. A neuro-fuzzy methodology for detecting the sodium leak is also under development to improve the detection reliability.

New developments have been made also in the robotics research. A method for improving the resolution of the ultrasonic synthetic aperture method to determine the position of objects has been developed by using an inverse filtering technique which takes into account of the sensor dynamics. An accurate and yet practical method of solving inverse kinematics of multi-link manipulators has been developed on the basis of formal separation of joint variables and nonlinear optimization techniques.

(Yoshikuni Shinohara)

8.1 Application of H_∞ Control Theory to Power Control of a Nonlinear Reactor Model

K. Suzuki, J. Shimazaki and Y. Shinohara

This paper represents a study to control the dynamic reactivity instability in BWR systems, with a special emphasis on the use of H_∞ control theory.

BWR Core Model In this work we used March-Leuba BWR model¹⁾ suited for analytical studies performed in conjunction with numerical calculations. In the model the nonlinearity term appears in the neutronic equation through the parametric feedback introduced by reactivity. The parameter ϵ , which is proportional to the void reactivity coefficient, controls the gain of the feedback and, thus, defines the linear stability of this reactor model. There exists a critical value ϵ_0 above which the model becomes unstable and can be used to study BWR dynamic behavior in the nonlinear regime.

Augmented Model and Controlled Object Figure 8.1.1 shows a unity feedback system as the basic control system configuration considered in this study. The control object $G(s)$ consists of an actuator-sensor augmented model $G_a(s)$ and a modeling error $\Delta(s)$. $\Delta(s)$ indicates a multiplicative modeling error between the augmented model and the real controlled object. $G_a(s)$ denotes the nominal linear transfer function of the augmented model which consists of the linear reactor core model ($G_0(s)$), a neutronic power measurement system (NPMS) and a control rod drive system (CRDS). There is only one control input to the reactor core, and therefore only one actuator is considered. Let us consider the CRDS system provided with compensation of the rod position feedback. For simplicity, the servomotor of CRDS is modeled by an integral element

$$G_m(s) := \frac{g_m}{s}, \quad (8.1.1)$$

where g_m is the gain factor and its value is assumed to be 0.4[−]. We assign a value of 2.5[−] to the position feedback gain factor k_f in Fig. 8.1.1. In addition, it is appropriate to include in the augmented model the dynamics of the neutronic power measurement system, i.e., the dynamics of fission chamber and instrumentation electronic circuit. A simple first-order lag model is usually applied to model the dynamics of a neutronic power measurement system.

The transfer function is given as follows:

$$G_n(s) = \frac{k_n}{\tau_n s + 1}, \quad (8.1.2)$$

where the values of k_n and τ_n are assumed to be 1.0 [-] and 0.1 [s], respectively.

$K(s)$ in Fig. 8.1.1 indicates the compensator's transfer function to be determined so as to establish the design specifications described later for both robust stability and disturbance attenuation characteristics. In H_∞ control theory, such a compensator can be realized by obtaining a proper transfer function.

Control Theory In the past decade there has been much progress in the area of H_∞ control theory in order to achieve robust, uncertainty-tolerant multivariable feedback design. The real problem in the robust multivariable feedback control system design is to synthesize a control law which maintains system response and error signals to within prespecified tolerance despite the effects of uncertainty on the system. Uncertainty may take many forms but among the most significant are noise/disturbance signals and transfer function modeling errors. Another source of uncertainty is nonlinear distortion which is not represented in the model. This is dealt as a mixed sensitivity problem in the H_∞ control theory.

Design Specifications and Design Procedure Design specifications adopted in the paper are 1) to achieve robust internal stability(robustness specification) and 2) to minimize the sensitivity function as much as possible(performance specification). These design specifications are realized with frequency weighting functions. Design procedures are 1) to construct the generalized plant $G(s)$ with weighting functions corresponding to the design specifications and find a state-space realization of $G(s)$, and 2) to find a stabilizing controller $K(s)$ such that the infinity norm of transfer function $T_{wz}(s)$ is minimized and is less than or equal to one.

Results The final H_∞ controller is stable proper and has 8 states which is the same as the augmented plant. Fig. 8.1.2 shows the responses of the neutronic power and the controlled reactivity determined by the H_∞ compensator when the reactivity disturbance of 5 cents is added in step function.

References

- 1) March-Leuba J., Cacuti D. G. and Perez R. B. : Nucl. Sci. Eng., **93**, 111(1986).
- 2) Suzuki K., Shimazaki J. and Shinohara Y. : to appear in Nucl. Sci. Eng..

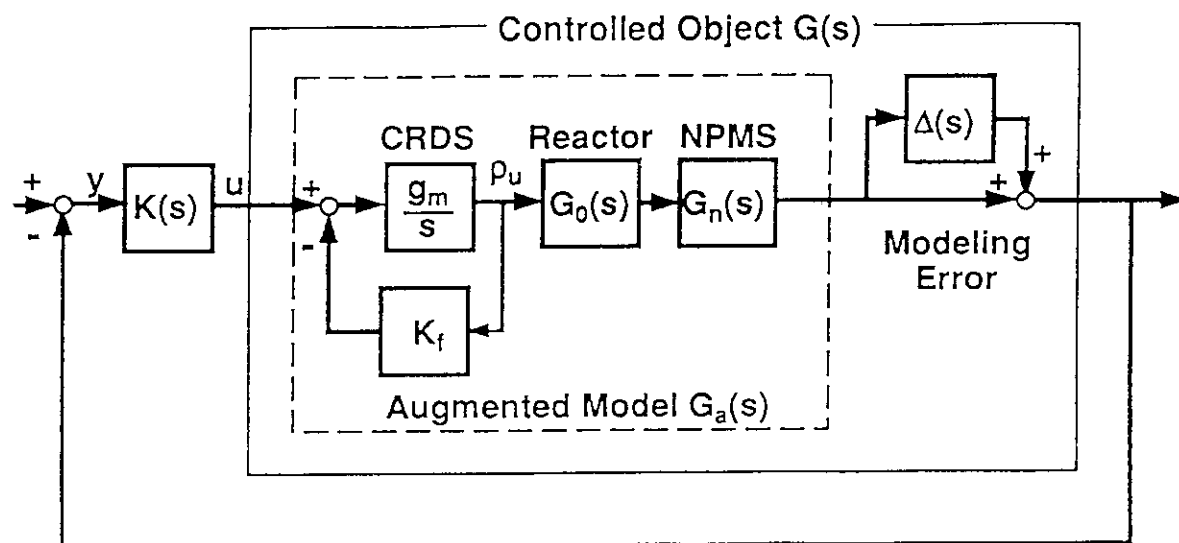
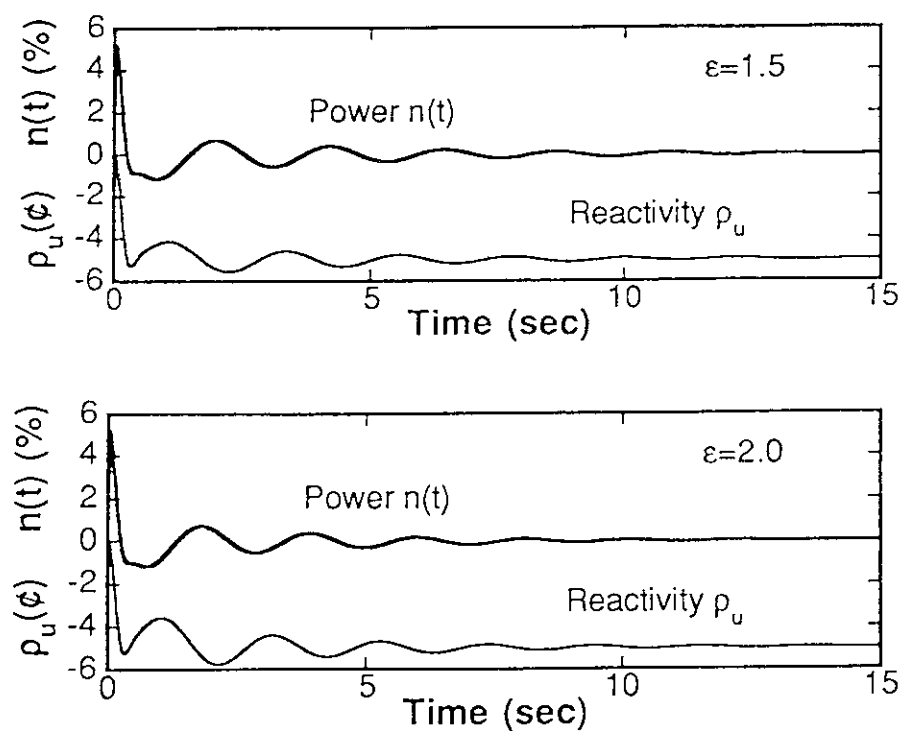


Fig. 8.1.1 Actuator-sensor augmented model and feedback control system.

Fig. 8.1.2 Disturbance attenuation responses by H_∞ robust compensator.

8.2 An Analytical Study of Nonlinear Reactor Dynamics Based on Bifurcation Theory

T. Suzudo and Y. Shinohara

Some experiments and events in actual nuclear reactors have indicated that boiling water reactors (BWRs) tend to lose stability under low-flow and high-power conditions causing power oscillations. Since the structures of nuclear reactors are very complicated, complicated computer codes have been developed to perform detailed dynamics analyses; for which cumbersome simulation procedures are necessary. Such a research is useful for design and operation planning and has become effective because of the rapid advance of the computer technology. However, these simulation studies do not give the general and comprehensive view of the dynamics.

We know many simple nonlinear differential equations are known to have limit-cycle regimes, and the essential dynamics of the reactor power oscillation have no complicated structure in a mathematical sense. Therefore the dynamics could be represented by a much simpler model, especially in the onset of the instability. For this study we have derived a simplified third-order nonlinear model

$$\ddot{\rho}(t) + c_1\dot{\rho}(t) + c_2\dot{\rho}(t) + c_3\rho(t) + \frac{k\rho(t)}{\beta - \rho(t)} = 0, \quad (1)$$

amenable to analytical study, where $\rho(t)$ is a reactivity; β is a delayed neutron fraction; c_1 – c_3 and k are empirically determined constant parameters.

The analytical study of the model yields an explicit expression of the linear stability condition

$$c_1c_2 - c_3 > \frac{k}{\beta}, \quad (2)$$

which directly indicates the relation between each model parameter and the stability.

Generally nonlinear terms in the model equation play an important role in stabilizing the system into a nearby periodic orbit beyond linear stability condition. Subsequent analytical study leads the model equation at the bifurcation point to the combination of a harmonic oscillator and nonlinear terms such as

$$\dot{u} = -\omega v \quad (3)$$

$$\dot{v} = \omega u + g(u, v), \quad (4)$$

where ω is a oscillation frequency; g is a group of nonlinear terms. This is a canonical form of a nonlinear oscillation problem, which yields the explicit expression of weak stability condition

$$\begin{aligned} \phi(c_1, c_2, c_3) = & c_1 c_2 (c_1^2 + c_2^2) (3c_1^4 + 13c_1^2 c_2^2 + 4c_2^4) \\ & - (c_1 c_2 - c_3) (2c_1^6 + 20c_1^4 c_2^2 + 14c_1^2 c_2^4 + 8c_2^6) < 0. \end{aligned} \quad (5)$$

As long as the weak stability condition is satisfied, the periodic motion does not become divergent even though the linear stability condition is not satisfied.

All these results from the analytical studies provide a clear mathematical view of the BWR stability, which is not given by numerical approach. The explicit forms of the stability conditions can easily be applied to the qualitative analyses of BWR dynamics.

8.3 Multivariate Autoregressive Analysis of Power Oscillation in NSRR

K. Hayashi and Y. Shinohara

In the Nuclear Safety Research Reactor (NSRR), which is a TRIGA type pulsed reactor, unexpected power oscillation has been observed before its recent modification. To diagnose the cause of the power oscillation, three experiments were conducted to perform reactor noise analysis¹⁾⁻³⁾. It was concluded from the results of these experiments that the power oscillation was due dominantly to the automatic control system which showed poor dynamic performance when a relatively large disturbance was induced by operating the ¹⁶N diffuser. On the other hand, a dynamic model was studied to explain theoretically a possible mechanism of power oscillation⁴⁾. However, the detailed mechanism of the oscillation has not been identified yet.

Since a power oscillation may occur in a feedback system, an analysis of the multivariate feedback system consisting of the reactor and automatic control system was performed by using a multivariate autoregressive (MAR) modelling method, and the characteristics of each noise source, transfer function and their contribution to the oscillation were investigated.

The analysis based on the MAR model was performed for eight variables of the reactor noise data, i.e., a reactor power, a bank position and six control rod positions, which were measured at the third (Phase-III) experiment.

From the results of spectral and coherence analyses, it is found that the main frequency component of the power oscillation appears at a frequency of 0.25 Hz. This component is accompanied by its lower and higher harmonics, which indicates the nonlinearity of the phenomenon. The results of noise power contribution ratio analysis show that three signal components coming from the noise sources of the reactor power, the bank position and the control rod-1 position are dominant in all the variables at this oscillation frequency. However, the results of the analysis of their open loop frequency response functions and noise source power spectra show that they do not have a peak at this frequency. Therefore, the cause of the oscillation cannot be ascribed to any particular noise source or any particular transfer function.

Next, the closed loop frequency response function of the whole system was estimated and a peak at 0.25 Hz was found. Then, the total gain function of the feedback loop consisting of the reactor power, the bank and one of the six rods was calculated for six combinations. It was found that only the rod-1's loop has a positive gain in the frequency range below the oscillation frequency.

It is concluded from above mentioned analyses that the power oscillation in the NSRR was not due to an independent abnormality in the noise sources or transfer function but due to a combination of these transfer functions forming a nonlinear feedback loop.

References

- 1) Hayashi K. et al.: "Diagnosis of NSRR Based on Reactor Noise Analysis (I)", JAERI-M 84-056 (1984) (In Japanese).
- 2) Hayashi K. et al.: "Diagnosis of NSRR Based on Reactor Noise Analysis (II)", JAERI-M 84-137 (1984) (In Japanese).
- 3) Hayashi K.: "Study on Statistical Analysis of Nonlinear and Nonstationary Reactor Noises", JAERI-M 93-041, 82-101 (1993) (In Japanese).
- 4) Konno H., Hayashi K. and Shinohara Y.: "Nonlinear Dynamics of Reactor with Time Delay in Automatic Control System and Temperature Effect", J. Nucl. Sci. Technol., 29, 530-546(1992).

8.4 Noise Analysis for Plant Dynamics Identification of Nuclear Ship Mutsu

K. Hayashi, J. Shimazaki, K. Nabeshima and Y. Shinohara

To identify the plant dynamics of the nuclear ship Mutsu, dynamics experiments using pseudo random binary sequence (PRBS) signal have been conducted at her experimental navigation. Experiments using reactivity or load disturbance were performed by manual operation of the control rod or the main steam valve under the following operational conditions of the plant; (1) at 70 % of nominal reactor power and quiet sea, (2) 50 % and quiet sea, and (3) 70 % and normal sea. The reactor plant signals and ship motion signals measured under the above mentioned conditions have been analyzed by using statistical methods.

To begin with, spectral and coherence analyses were performed to evaluate the characteristics of the whole plant. The results show that the reactivity disturbance was transferred strongly to the process variables in the primary circuit around the reactor but not to the secondary system variables. The load disturbance was transferred not only to the secondary system variables but also to the primary system variables through the automatic control system. The latter result confirmed the fact that the load following characteristics of the Mutsu plant is quite good.

In the above mentioned analyses, it was found that the power spectral densities (PSDs) of the steam pressure signals in both steam generator (SG) 1 and 2 have different patterns in a frequency range of 0.08-0.2 Hz. The reason of this difference has been investigated using a multivariate autoregressive (MAR) model from the viewpoint of interactions caused by feedback effects among the two steam generators and one pressurizer.

First, a MAR model with respect to four signals, i.e. the steam pressure signals and the steam flow signals in both SG-1 and SG-2, was determined and analyzed. The results of analysis of the noise power contribution ratio (NPCR) and noise source PSD show that, for a peak at a frequency of 0.18 Hz, the noise source of the SG-2 steam pressure signal has a large magnitude. This signal component is found to be dominant in both SG-1 and SG-2 steam pressure signals. Furthermore, it was concluded from the results of signal transmission path (STP) analysis that the spectral peak component of the SG-1 steam pressure signal comes from the SG-2 steam pressure noise source through the direct path between both steam pressure signals.

Next, to investigate the characteristics of the SG-2 steam pressure noise source, a total of ten variables including not only the above mentioned four signals but also the signals of reactor power, pressurizer pressure, SG-1 and SG-2 water levels, SG-1 and SG-2 feed water flows were analyzed using the MAR modelling method. The results show that three noise

source components, i.e., the SG-2 steam pressure, SG-2 water level and pressurizer pressure were dominant in the SG-1 steam pressure signal at the peak frequency but the PSDs of these noise sources have no peaks. This means that the signal component of the SG-1 steam pressure signal at the peak frequency was made by the feedback loops among these three variables. The result of the STP analysis shows that the signal component at 0.18 Hz in the SG-1 steam pressure signal is due to the SG-2 steam pressure noise source; it is first transferred to the SG-2 water level and the pressurizer pressure by direct paths, then they are amplified by the strong feedback loop existing between the SG-2 water level and the pressurizer pressure, and finally it is transferred from the SG-2 water level to the SG-1 steam pressure.

The reason why the signal transmission is in one direction only may be related to the fact that the connections of the spray and the surge lines of the pressurizer to the primary system is not symmetrical and that the effect is transferred through the pressurizer control system.

8.5 Benchmark Analysis of Acoustic Noise Signals for Sodium/Water Reaction Detection

Y. Shinohara, K. Watanabe and K. Hayashi

Within the framework of the Coordinated Research Program on Acoustic Signal Processing for the Detection of Sodium Boiling or Sodium/Water Reaction in LMFBR organized by the International Atomic Energy Agency, a benchmark test has been performed using the test data supplied through the Agency.

Two kinds of test data were recorded on a magnetic tape supplied. The first one uses the background noise from a PFR Steam Generator Unit and the leak noise from a Russian leak test facility. The second one contains a leak noise example from the UK and the background noise from a Steam Generator Unit of SPX1 in France.

The method of signal processing used is essentially the same as that already used in the previous benchmark analyses.¹⁾ It is a relatively simple nonlinear signal processing with band-pass filtering and squaring of the original noise signal in two times to enhance the signal-to-noise ratio.

The original signal is first filtered by a band-pass filter having a band-pass frequencies between f_{c1} and f_{c2} and then squared. The squared signal is again filtered by another band-pass filter having a band-pass frequencies between f_{c3} and f_{c4} and then squared again. The resultant signal is integrated over a time interval dT to obtain what we call here the feature signal. The cut-off frequencies of the band-pass filters were chosen based on the frequency characteristics of the PSD functions.

The sample mean value M and sample mean standard deviation D of the feature signal are calculated over a selected time interval T to determine a threshold value $L = M + F \times D$, where F is a factor to be adjusted.

The problem of the test was to determine the start time of inserted leak signal and the detection margin for the Record 4 through 8 and Record 11 in the test data supplied. The start time of the leak signal is determined as the time when the feature signal exceeds the threshold value L . The results are summarized in Table 8.5.1.

As far as the test data in Records 4 through 8 are concerned, it is concluded from the results of analysis that the leak signals with the signal-to-noise ratio down to -16 dB can be detected reliably by the method of twice squaring with band-pass filtering with a decision time of 0.5 second and a detection margin of 3.

Reference

- 1) Shinohara Y. et al.: The result of sodium boiling noise detection benchmark test. Report prepared for Research Coordination Meeting on Acoustic Signal Processing for the Detection of Sodium Boiling or Sodium/Water Reaction in LMFBR. Vienna, November, 1990.

Table 8.5.1 The start time of the leak noise signal

Record No.	Start Time	Detection Margin
4	11:58	3.0
5	22:47	*
6	32:28	*
7	40:35	3.0
8	51:29	3.0
—	—	—
11	1:17:50	*

* The detection margin was reduced to estimate the start of leak noise.

Note:

The parameters used for the present signal processing are:

$$dT = 0.5 \text{ sec}, T = 10 \text{ to } 20 \text{ sec}, F = 3$$

For Records 4 through 8:

$$f_{c1} = 8.0 \text{ kHz}, f_{c2} = 18.0 \text{ kHz}, f_{c3} = 12.0 \text{ kHz}, f_{c4} = 36.0 \text{ kHz}$$

For Record 11:

$$f_{c1} = 2.4 \text{ kHz}, f_{c2} = 13.6 \text{ kHz}, f_{c3} = 12.0 \text{ kHz}, f_{c4} = 30.4 \text{ kHz}$$

8.6 Neutron-fuzzy Methodology for Sodium Leak Detection in LMFBRs

L. H. Tsoukalas, Y. Shinohara, Y. Fujii and K. Watanabe

A neuro-fuzzy methodology for sodium leak detection in LMFBRs is under development. The overall objective of simultaneously minimizing the likelihood of spurious indication P_s and the likelihood of missing a valid event P_m while taking into account process or plant-specific knowledge, results in the fuzzification of the decision boundary. Acoustic sodium/water reaction data provided by IAEA is used to train via neural networks a set of fuzzy *if/then* rules for decision-making. These rules can be further refined and extended to include user-defined criteria and expert knowledge about the process.

In order to develop a reliable on-line sodium/water noise detection system, it is necessary to distinguish the noise due to sodium/water reaction from the background noise in the reactor. The problem is similar to that of reliably detecting sodium boiling in fast reactors for which several techniques have been proposed.¹⁾ It involves an appropriate signal processing technique for extracting a feature signal such as the mean square or power within a defined frequency band and a decision-making methodology for establishing the reaction's occurrence. The output of the decision making algorithm may be used to trip the reactor or, as an indication to the operator who may take appropriate action, often after considering other valid inputs. In the former case the probability of a spurious indication is constrained by an annual integrated spurious trip rate, e.g., less than 0.1 per year. The signal processing unit provides an estimate of the feature at equal intervals of time T apart. In general the statistics of the estimate of the feature are described by a probability density function $f_1(x)$, in the case there is no reaction. Once the reaction has started the statistics associated with the monitored feature change to $f_2(x)$. Action would normally be initiated if the estimated boundary of the feature exceeded some preset threshold level or *decision boundary*. P_s and P_m are conjointly dependent on the position of the decision boundary with the possibility that either may be made as small as desired, but at the expense of the other.

In the present work we consider the decision boundary to be a fuzzy region defined by specifying a fuzzy threshold value \bar{x}_1 , when only one feature is monitored, as well as membership functions encoding knowledge about the specifics of an actual system. Hence P_s the probability of a spurious indication and P_m the probability of missing a valid event are defined to be probabilities of fuzzy events²⁾ as follows

$$P_s = \int_{x_1}^{\infty} \mu_1(x) f_1(x) dx,$$

$$P_m = \int_{-\infty}^{\bar{x}_1} \mu_2(x) f_2(x) dx,$$

where $f_1(x)$ describes the statistics of the estimates of the feature when there is no reaction present, $f_2(x)$ the statistics of the estimates of the feature when the sodium/water reaction has commenced and \bar{x}_1 is the crisp value where \bar{x}_1 is *normal* (i.e., where the membership function is unity). The membership functions $\mu_1(x)$ and $\mu_2(x)$ describe the knowledge-based qualification of these statistics, i.e., the fuzzification of the decision boundary. Knowledge about the specifics of the actual system as well as constraints for the minimization of $(P_s + P_m)$, or the maximization of $(1 - P_s) \times (1 - P_m)$ may be reflected in the form of $\mu_1(x)$ and $\mu_2(x)$. The reaction has commenced when the threshold \bar{x}_1 , a fuzzy number, has been exceeded. The above formulation retains crisp values for the probability of a spurious indication and the probability of missing a valid event in order to facilitate comparison with results obtained by other methods.¹⁾

The approach considered for computing the membership functions $\mu_1(x)$ and $\mu_2(x)$ relies on the use of a neural network to derive the knowledge contained within the signals themselves as well as imposing additional rules reflecting plant-specific constraints. It uses TILGen³⁾ to generate a set of fuzzy rules and calculate $\mu_1(x)$ and $\mu_2(x)$. TILGen utilizes a neural network to learn an input-output function and a proprietary technique to decode the neural network and generate the fuzzy rules. The rules can subsequently being modified and/or added to by the developer of the decision-making logic. Furthermore, when additional data is available and/or the performance of the system as reflected in integrated spurious trip rates or probabilities to meet demand has been degraded, the network may be retrained. The decision for retraining may be based on the fuzzy variance of the threshold value. When the fuzzy variance is exceeded by a predetermined amount the rule-base ought to be re-tuned.

In order to generate the feature signal we consider filtering and twice squaring the original signal as in previously done in JAERI for the detection of boiling.¹⁾ During training, however, different zones of the spectrum of the original signal are to be considered resulting in different rules for computing the membership functions.

The above may be generalized to the case when the signal processing technique relies on more than one features derived from one or more signals. In such a case we would have an n dimensional decision boundary defined by specifying the threshold values of x_1, x_2, \dots, x_n as well as appropriate membership functions. In such a case also P_s and P_m would be conjointly dependent on the decision boundary and the form of $f_1(x)$, $f_2(x)$, $\mu_1(x)$ and $\mu_2(x)$. Again, as far as P_s and P_m are concerned, each can separately be made as small

as desired at the expense of the other. The objective of the proposed methodology is to incorporate the n-dimensional fuzzy decision boundary into the overall detection algorithm.

References

- 1) International Working Group on Fast Reactors, *Signal Processing Techniques for Sodium Boiling Noise Detection, Final Report and Proceedings of a Coordinated Research Programme*, Report IWGFR/68, International Atomic Energy Agency, Vienna (1989).
- 2) Ragheb M. and Tsoukalas L.: "Monitoring Performance of Devices Using a Coupled Probability-Possibility Method", in *International Journal of Expert Systems*, 1, 111 (1988).
- 3) *TILGen User's Manual*, Togai Infralogic, Irvine, California, USA (1991).

8.7 A Practical Module for Manipulator Mechanism Analysis

S.Sasaki

A determination of joint variable values corresponding to the prescribed hand positions is one of the most important topics in robot manipulation. Although a completely general robot with six degree of freedom does not have a closed form solution, certain important special cases can be solved. This implies manipulators in which three consecutive axes intersect at a point as shown in the existing industrial robots. If the last three joints are revolute and their axes intersect, then their point of intersection is only a function of motion in the first three joints and the constant link parameters, which represents three equations in three unknowns. The other possibilities—first three axes intersecting and three intermediate axes intersecting also lead to a soluble class. The problem is analyses of mechanisms without such a structural feature. In that case, it is desirable to introduce iterative methods under the problem formulation such that robotic architectures connected in series are separable into two subsystems consisting of the first three links and the remaining three links. While solving one subsystem, the joint variables of the other subsystem remain fixed. The manipulation is repeated till a certain criterion is satisfied. Such a two-stage procedure based on a reduction of dimensionality has a central role in coping with the complicated kinematic relationships.

According to the optimization principle, a computational process is reduced to a mathematical structure of minimizing the Euclidean norm of the residuals. And desired arm solutions can be derived with high precision using the non-linear least squares techniques—Levenberg and Marquardt method or quasi-Newton methods, which attach importance to dealing with a latent effect of non-linearity by means of more simplified procedures instead of making complex computations or to approximating the inversion of Hessian without the explicit use of second partial derivatives. In addition to these approaches, a compact linearization model with a self-tuning algorithm is of value for a practical use, where the reasonable step size is determined at each step in an automatic manner. With the aid of this heuristic algorithm, it is possible to obtain a rapidly converging solutions. Throughout a number of performance tests, the proposed strategies have been identified to be more superior to the conventional Newton method. Admitting that previous use has achieved a high degree of popularity because of simplicity of the algorithm, the computation of the Jacobian is generally fraught with numerical difficulties such as a rank deficiency. Hence, it is to be noted that our proposal made a great contribution to avoiding kinematic singularity as well as to widening the application range.

8.8 A Method for Improving Resolution of Ultrasonic Object Location

N. Ishikawa, Y. Fujii and Y. Shinohara

Introduction

Synthetic aperture imaging is a method widely used for the ultrasonic object location. This method gives an ideal resolution if an impulsive acoustic signal is transmitted. But such an impulsive acoustic signal cannot be obtained by using usual ultrasonic sensor having poor characteristics of electro-acoustic conversion. This causes degradation of measuring resolution. In this study, we apply deconvolution signal processing to the preprocessing of synthetic aperture imaging to improve the resolution.

Synthetic Aperture Imaging Method

Transmitter converts an electric signal $u(t)$ to an acoustic signal $p_i(t)$. This relation is expressed as $p_i(t) = x_T(t) * u(t)$, where $u(t)$ is the electric signal and $p_i(t)$ is the acoustic signal; the symbol $*$ represents the convolution operation with respect to time t . This acoustic signal propagates through the medium and reflected by the objects. Let $f(\mathbf{r})$ denote the reflectivity distribution of the objects, then the reflected wave observed by receiver at a position of \mathbf{r}_R is expressed as follows

$$p_o(t; \mathbf{r}_R) = \int f(\mathbf{r}) p_i(t - (L_T + L_R)/c) d\mathbf{r},$$

where $L_T(=|\mathbf{r} - \mathbf{r}_T|)$ represents the distance between the transmitter and an arbitrary position on the object; $L_R(=|\mathbf{r} - \mathbf{r}_R|)$ denotes the distance between the receiver and an arbitrary position on objects, and c denotes velocity of sound. The received acoustic signal is converted into electric signal. The converted electric signal can be represented by $g(t; \mathbf{r}_R) = x_R(t) * p_o(t; \mathbf{r}_R)$, where $x_R(t)$ is electric-acoustic conversion characteristics of receiver.

The synthetic aperture imaging is performed by evaluating reflectivity distribution $f(\mathbf{r})$ from receiving signals. The value is estimated by the following formula

$$f(\mathbf{r}) = \sum g(L(\mathbf{r})/c; \mathbf{r}_R),$$

where $L(\mathbf{r}) = L_T(\mathbf{r}) + L_R(\mathbf{r})$. For convenience of later explanation, let $x(t)$ denote the electro-acoustic conversion characteristics of both transmitter and receiver. The frequency domain expression of $x(t)$ is represented by

$$X(\omega) = X_T(\omega) X_R(\omega)$$

Deconvolution Signal Processing

We explain the way of designing deconvolution filter. The filter is to be designed so as to eliminate the effect of $x(t)$ and $u(t)$. To perform filter processing by digital manner, the receiving signals are sampled at certain sampling rate. We express the sampled signals in the vector form $g = [g_0, g_1, \dots, g_{L-1}]^T$. By designing deconvolution filter as an N -order FIR filter, the filter coefficients vector h can be obtained by solving the equation $[G] h = d$, where d is the desired output vector of the filter. $[G]$ is the lower triangular toeplitz matrix that consists of the elements of vector g .

Experiment and Result

The geometry of experimental setup is depicted in Fig.8.8.1, in which T denotes the transmitter and R_1, \dots, R_{12} denote the receivers; Q_1 and Q_2 denote the objects ($\phi 10\text{mm}$ pole) placed at the positions of $(-15\text{cm}, 85\text{cm})$ and $(-5\text{cm}, 65\text{cm})$ respectively. The transmitter is driven by 40kHz electric signal whose duration is 8 periods. The reflected signal is received at 12 positions along x -axis with spacing of 5cm. We estimate the positions of the objects from received signals by using synthetic aperture imaging method. The order of deconvolution filter is 128 and output of its filter is bandlimited by 6kHz.

Fig.8.8.2 shows the result of position estimation with direct use of the received signal, and Fig.8.8.3 shows the result with preprocessing of received signal by the deconvolution filter. The later provides the better resolution. The estimation of position is carried out by using the envelope of the signal. The envelope is calculated by following formula

$$s_e(k) = [s^2(k) + s'^2(k)]^{1/2},$$

where $s'(k)$ is the discrete Hilbert transformation of $s(k)$.

Conclusion

We apply the deconvolution processing as a preprocessing method for synthetic aperture imaging to improve the measurement resolution. The effectiveness of this method has been demonstrated by the experiment.

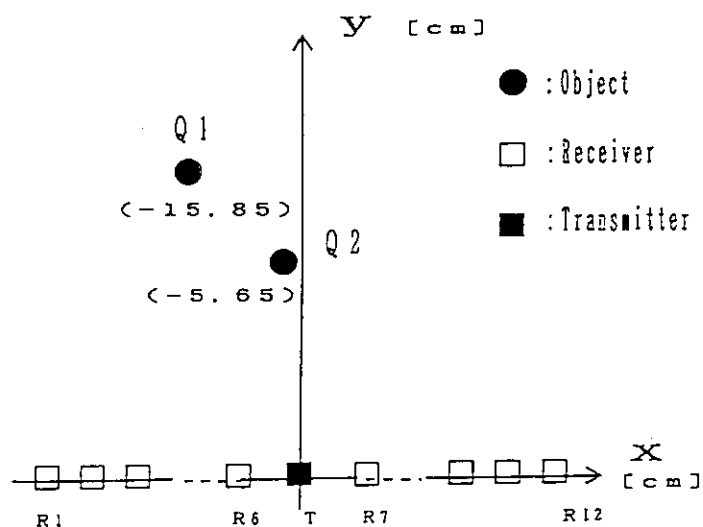
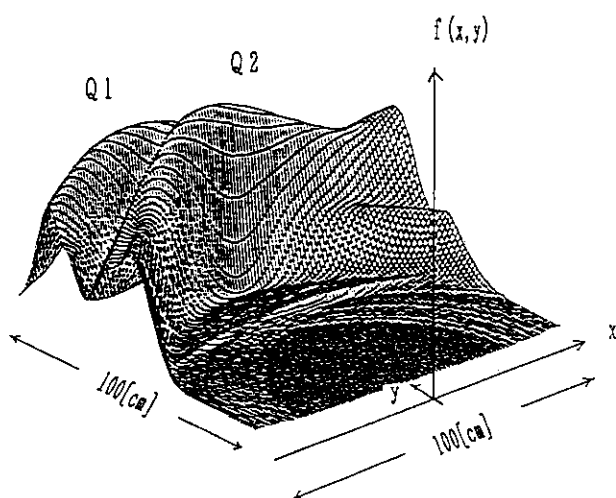
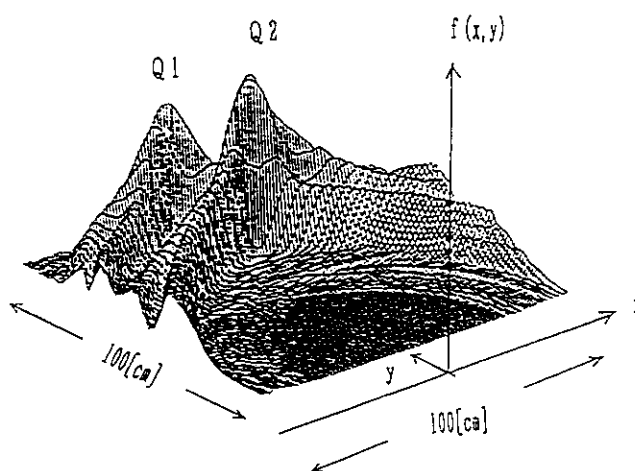


Fig.8.8.1 Geometry of experiment

Fig.8.8.2 Estimation of reflectivity
(Without preprocessing)Fig.8.8.3 Estimation of reflectivity
(With preprocessing)

9. Heat Transfer and Fluid Dynamics

There are three major fields of research involved in this chapter. The first one is related to development of best estimate codes for light water reactors. The REFLA/TRAC code is a three dimensional reactor transient analysis code with two-fluid model. The TRAC-PF1/MOD1 developed by the United States Nuclear Regulatory Commission (USNRC) is the frame of the REFLA/TRAC code and some models including the JAERI original model of built in the REFLA code for the reflood phase of a loss-of-coolant accident (LOCA) were replaced with the corresponding TRAC-PF1 models. In this year, predictive capability was assessed with the Cylindrical Core Test Facility (CCTF) reflood test, the Slab Core Test Facility reflood test, the ROSA-IV small break LOCA test and the ROSA-II large break LOCA test. The results show good predictability except for the ROSA-II case where the instrumentation quantity and quality are not enough to judge the cause of the discrepancy between the measured and the calculated. For accurate analysis of the thermal hydraulic behavior in the subchannels of the core, the COBRA-TF code has been improved. The code is a three field best estimate code and was also developed by the USNRC. Since predictability for low pressure is not accurate and the correlation was improved by referring the FIDAS code.

The second field is related to a fundamental study. In this time, the critical heat flux (CHF) is accurately predicted for the fuel bundles with the same configuration as already tested, however not reliable for those with new configuration. In the design of new light water reactors, a mechanistic CHF model is desirable, which can be applicable without performing many verification experiments. For developing a mechanistic model a visualization experiment was performed by means of the neutron radiography in the JRR-3 research reactor in the JAERI. In the test, experimental technique for visualization of two-phase flow was establishment, however higher resolution is expected for understanding of the CHF phenomena.

The third field is related to study on the advanced light water reactors. In this year, the departure of nuclear boiling ratio (DNBR) of a passive safety reactor concept, SPWR, was investigated under an accidental condition. Hydrodynamic behavior in a lower plenum of a pressure vessel was also investigated. The experience will be applied for studies on new light water reactors.

(Yoshi Murao)

9.1 Assessment of REFLA/TRAC Code for System Behavior during Reflood Phase in a PWR LOCA with CCTF Data

H. Akimoto, A. Ohnuki and Y. Murao

The REFLA/TRAC code is a best estimate code being developed at Japan Atomic Energy Research Institute (JAERI) for analyses of thermal hydraulic behaviors during postulated accidents in light water reactors. The REFLA/TRAC code uses the TRAC-PF1 code¹⁾ as the framework of the code and uses physical models developed at JAERI. Since 1984, several models have been implemented to the TRAC-PF1 code at JAERI including reflood model, condensation model, countercurrent flow model, interfacial and wall friction models, critical flow model through orifice plate, etc.²⁾ These models are synthesized in a program in order to assess predictive capability and understand the application limit of models. The REFLA/TRAC code was assessed for the system behavior during the reflood phase of a large break (LB) loss-of-coolant accident (LOCA) in a pressurized water reactor (PWR) using data from the Cylindrical Core Test Facility (CCTF).

The CCTF³⁾ is a test facility designed to provide information on thermal hydraulic behaviors during refill and reflood phases in a PWR LOCA with integral system simulation. The facility has a core with a full-height and 1/4.5 in radial direction and has four primary loops with reactor component simulations. The entire components of the facility were modeled in the calculation. The pressure vessel of the facility was modeled either by a three dimensional VESSEL component model or by a combination of one dimensional component models. Figure 9.1.1 shows the input schematics with a VESSEL component model. Measured water injection rates and water temperature into the cold legs, core power, and pressure at containment simulator tanks were used to specify the boundary conditions. The initial downcomer wall temperature was set at saturation temperature to prevent an oscillation in downcomer water head with a period of about 50 s arising from the overestimation of the evaporation rate at the lower part of the downcomer.

The REFLA/TRAC code predicted reasonably the water accumulation in the core, core cooling behavior, pressure drop through primary loops, heat transfer at steam generator and the condensation at the cold leg, although it slightly underestimated the

water carry-over to hot legs and overestimated the downcomer water head. As an example of comparisons between calculated and measured results for system behaviors, core inlet mass flow rate and its integral with respect to time are shown in Fig. 9.1.2. The REFLA/TRAC code predicts reasonably thermal hydraulic behaviors in the primary system.

For the core thermal hydraulic behaviors, both core water accumulation and cooling behaviors are predicted excellently, including quick water spread to the upper core, much water accumulation in the upper core, one-dimensional water accumulation regardless of steep radial power distribution and axi-symmetrical core cooling. Figure 9.1.3 shows an example of comparison of void fraction and clad temperature transients. Although the core heat transfer enhancement arising from the steep radial power profile is slightly underestimated, both void fraction and clad temperature transients are predicted well by the REFLA/TRAC code. The predicted peak clad temperatures were 1,149 K with one-dimensional model and 1,141 K with three dimensional model, while measured peak clad temperature was 1,119 K.

The effect of the system pressure, core power level and water injection rate on system behavior was also predicted well with the REFLA/TRAC code.

These assessment results confirm that the REFLA/TRAC code can predict system behavior during the reflood phase in a PWR LOCA with good accuracy.

References

- 1) Safety Code Development Group: TRAC-PF1/MOD1: An Advanced Best-Estimate Computer Program for Pressurized Water Reactor Thermal-Hydraulic Analysis, NUREG/CR-3858 LA-10157-MS R4, (1986).
- 2) Akimoto, H., et al.: Assessment of REFLA/TRAC Code for Various Postulated Accidents in PWR, Proc. of the Fifth International Topical Meeting on Reactor Thermal Hydraulics, September 21-24, Salt Lake City, UT, USA, pp.1797-1803.
- 3) Okubo, T., et al.: Evaluation Report on CCTF-II Reflood Test C2-4 (Run 62) - Investigation of Reproducibility -, JAERI-M 85-026, (1985).

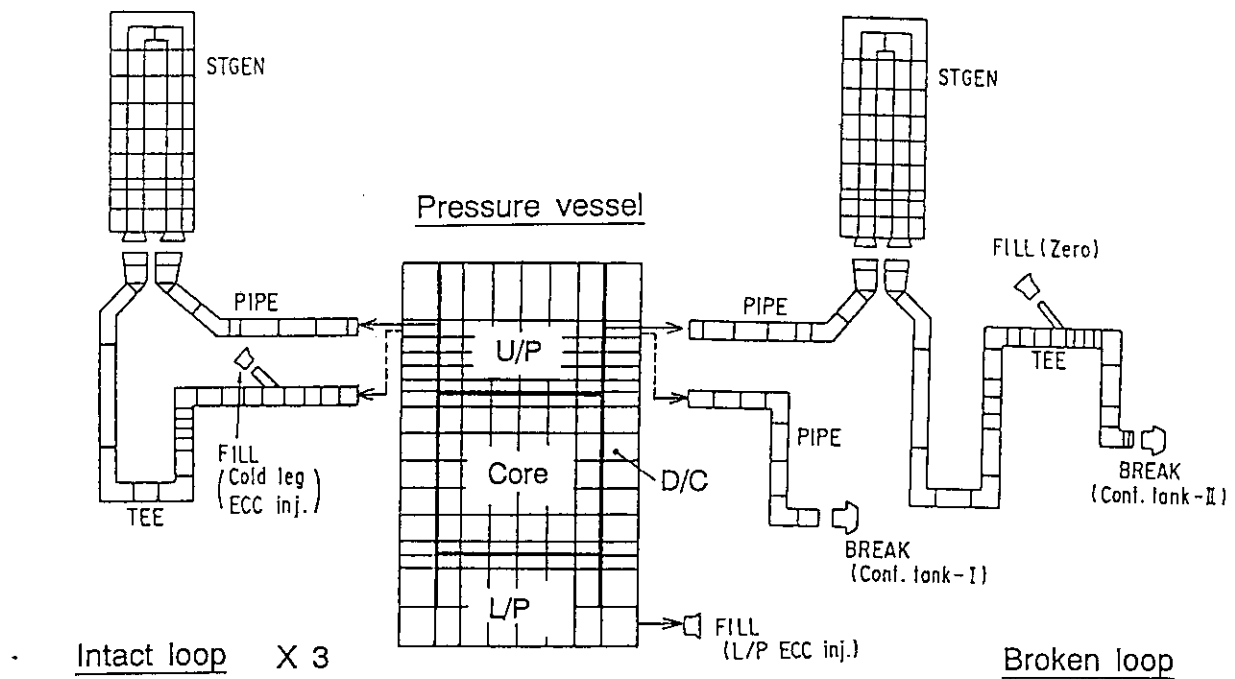


Fig. 9.1.1 Input schematics for CCTF system calculation with a VESSEL component

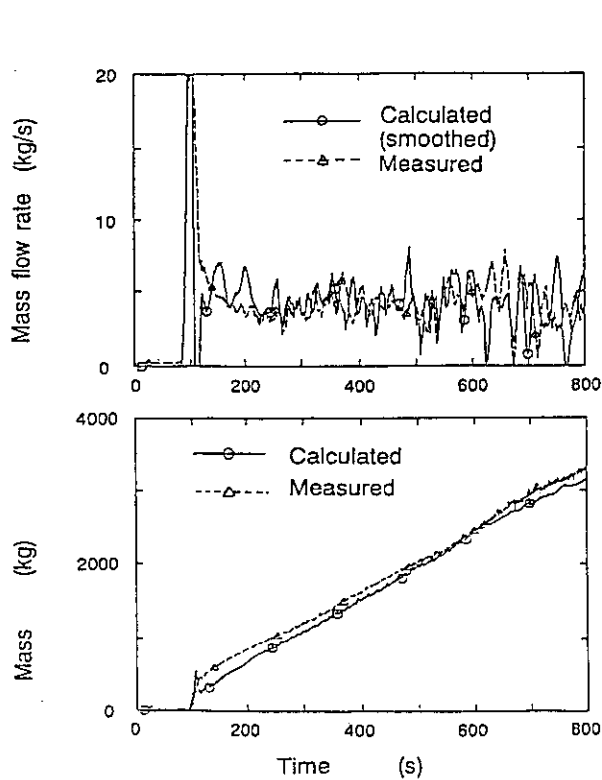


Fig. 9.1.2 Core inlet mass flow rate and its integral

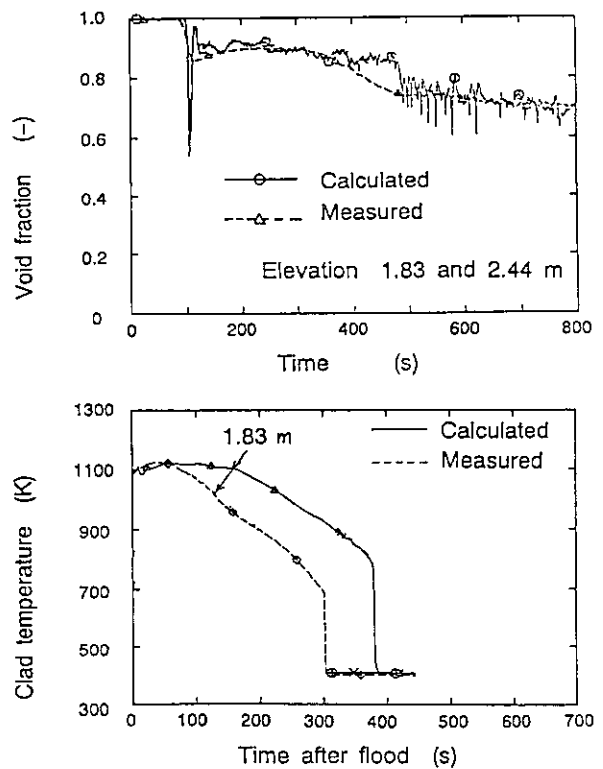


Fig. 9.1.3 Void fraction and clad temperature

9.2 Analysis of Multidimensional Thermal-hydraulic Behavior in Core during Reflood Phase of PWR-LOCA with REFLA/TRAC Code

A. Ohnuki, H. Akimoto and Y. Murao

The core heat transfer enhancement at a steep radial power distribution is very important to quantify the safety margin in PWR-LOCA. Although the heat transfer in higher power bundles was enhanced in large scale reflood tests at Japan Atomic Energy Research Institute¹⁾, the physical mechanism of the phenomenon has not been made clear yet. In this study, we analyzed the heat transfer enhancement phenomena with a multidimensional two-fluid model code, REFLA/TRAC²⁾, using data from the Slab Core Test Facility (SCTF) Test S2-16³⁾ which is a test of the large scale reflood tests. In the analysis, we expected that the heat transfer enhancement would be caused by the increase of local liquid velocity resulting from formation of flow circulation in the core.

Figure 9.2.1 shows the input noding used in the analysis. The pressure vessel of SCTF simulates a full height, full radius and one bundle width of an actual PWR. The pressure vessel was modeled by a two-dimensional VESSEL component of REFLA/TRAC code. In the Test S2-16, the radial power ratio was the highest in bundles 3 and 4 (1.2) and the lowest in bundles 7 and 8 (0.8) as shown in Fig. 9.2.1. The measured results were applied as boundary conditions for the ECCS conditions, the core supplied power and the pressure at the exit of hot leg.

Figure 9.2.2 shows a typical two-dimensional distribution of the calculated liquid mass flow rate in the core. The REFLA/TRAC code predicts higher upward liquid flow rate in higher power bundles and downward liquid flow in lower power bundles or a flow circulation in core. Figure 9.2.3 compares the magnitude in heat transfer enhancement with a factor of film boiling proposed by the authors⁴⁾. The factor of film boiling more than unity indicates that the heat transfer is enhanced due to a radial power distribution. The magnitude in heat transfer enhancement is predicted well where the distance from quench front, L_q , is less than about 0.5 m, although it is underestimated where L_q is between about 0.5 m and about 1.0 m. The good agreement in the region of L_q less than about 0.5 m was attained by a higher upward liquid velocity in higher power bundles. The prediction with the REFLA/TRAC code indicates that the increase of local liquid

velocity due to the formation of flow circulation is one of the important mechanisms which cause heat transfer enhancement in higher power bundles.

References

- 1) Iwamura T., et al.: Quantitative Evaluation of Heat Transfer Enhancement due to Radial Power Distribution during Reflood Phase of PWR-LOCA, J. Nucl. Sci. Technol., 26[4], 428-440 (1989).
- 2) Akimoto H., et al.: Assessments of REFLA/TRAC Code for Various Postulated Accidents in PWR, Fifth International Topical Meeting on Reactor Thermal Hydraulics (NURETH-5), Salt Lake City U.S.A. (1992).
- 3) Ohnuki A., et al.: Study on ECC Injection Modes in Reflood Tests with SCTF Core II -Comparison between gravity and forced feeds-, JAERI-M 91-001 (1991).
- 4) Ohnuki A., Akimoto H. and Murao Y.: Effect of Liquid Flow Rate on Film Boiling Heat Transfer during Reflood in Rod Bundle, J. Nucl. Sci. Technol., 27[6], 535-546 (1990)

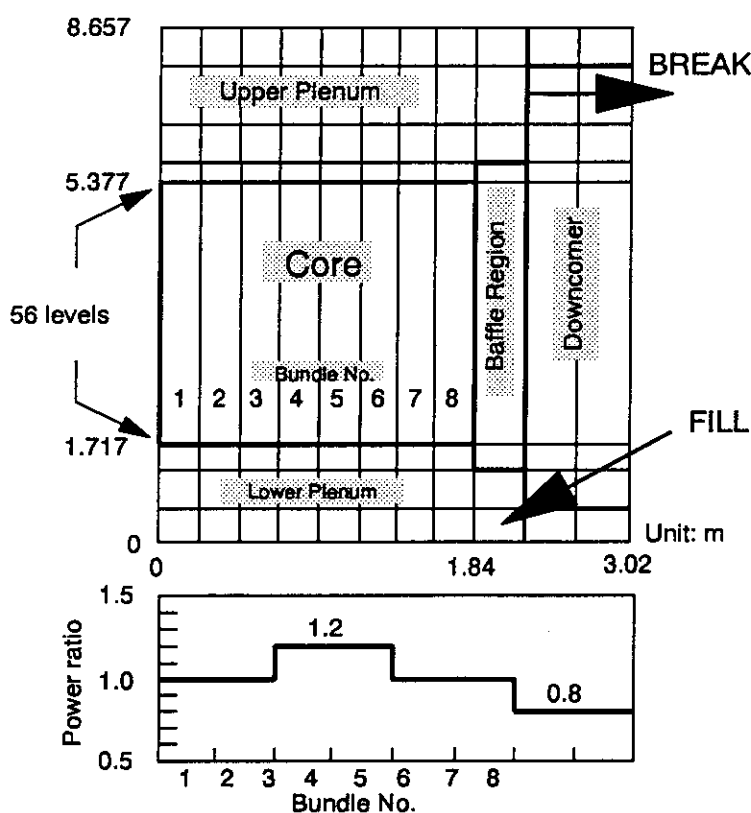


Fig. 9.2.1 Schematics of input noding

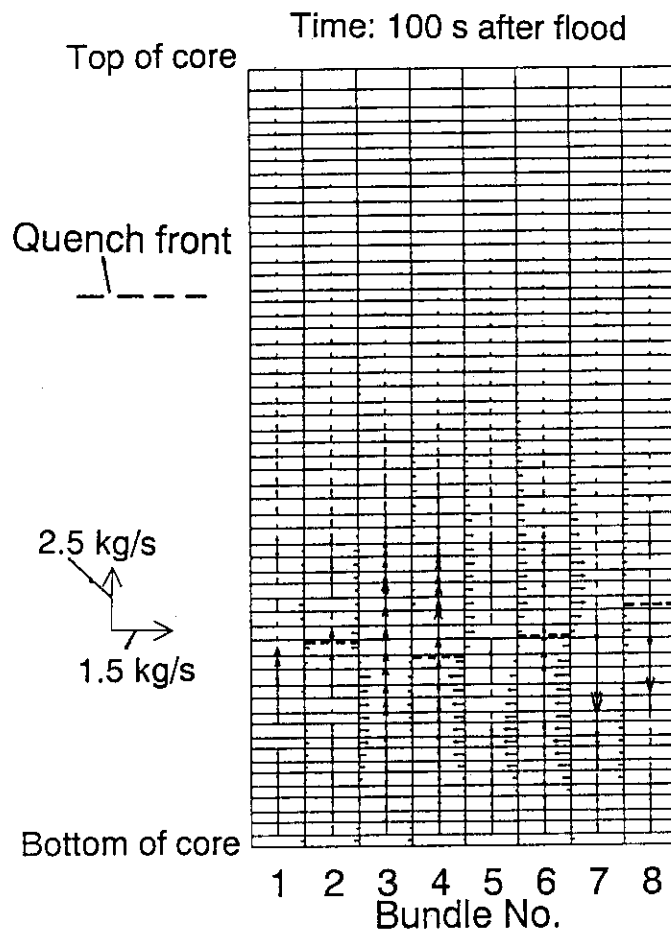


Fig. 9.2.2 Two-dimensional distribution of calculated liquid mass flow rate in core

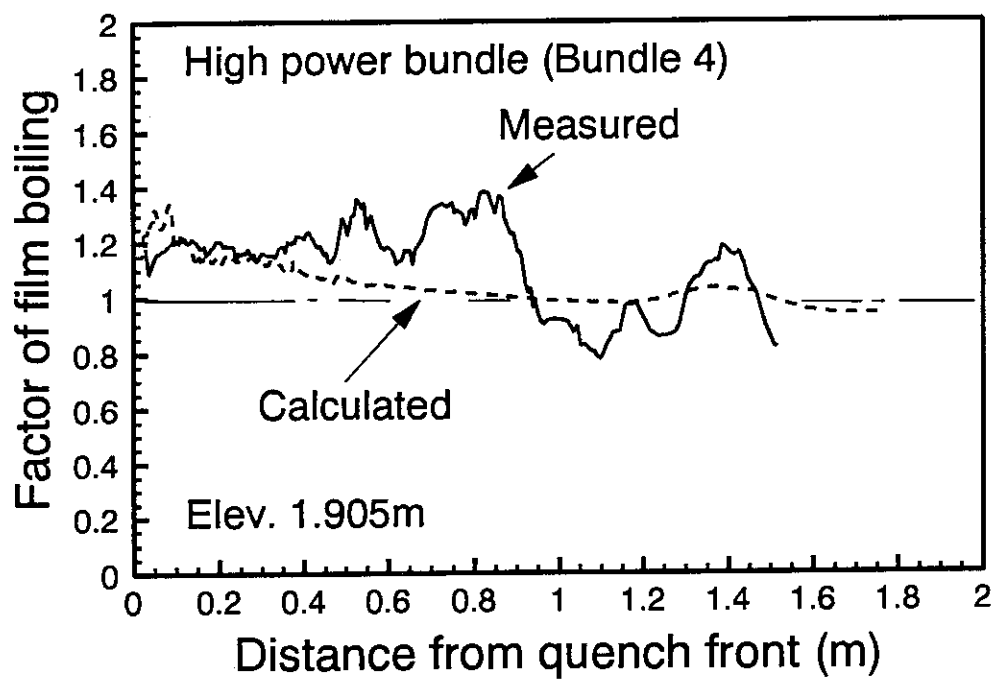


Fig. 9.2.3 Comparison of factor of convection term of film boiling heat transfer correlation

9.3 Applicability of REFLA/TRAC Code to a Small-break LOCA of PWR

A. Ohnuki, H. Akimoto and Y. Murao

The REFLA/TRAC code is a best-estimate code being developed at JAERI for the simulation of transient thermal hydraulic behaviors in light water reactors.¹⁾ The REFLA/TRAC code uses the TRAC-PF1 code²⁾ as the framework of the code and uses physical models developed at JAERI based on physical understanding of phenomena³⁾. Since the REFLA/TRAC code is expected to be used for the calibration of licensing codes and design of advanced light water reactors, it is important to assess the predictive capability for various transients encountered in light water reactors. This report presents assessment results of REFLA/TRAC code for the transient in a small break loss-of-coolant accident (SBLOCA) in a pressurized water reactor (PWR).

The assessment calculation was performed for Run SB-CL-05 (5% cold leg break SBLOCA test) of ROSA-IV Large Scale Test Facility (LSTF)⁴⁾. The LSTF is a large scale (1/48 of PWR based on volume scaling) integral test facility for the study of overall system behavior in PWR during SBLOCA's and anticipated transients. In the assessment calculation, the pressure vessel and the primary loops of LSTF were modeled with one-dimensional components of REFLA/TRAC code. The validity of the input model was confirmed by a steady state calculation which simulates the operational condition before the initiation of break. In the transient calculation, the following measured values were used as boundary conditions: core power, pump rotational speed, pressure at downstream of break location, fluid conditions (flow rate and fluid temperature) of ECCS and steam generator secondary conditions.

Figure 9.3.1 shows the comparison of break mass flow rate, core full height differential pressure and clad temperature at middle elevation of high power bundle. The core differential pressure almost equals to the collapsed liquid level in the core. In the test, the break was simulated with a sharp-edged orifice plate. Since the critical flow model in the TRAC code was reported to be unable to predict the flow through the orifice plate⁵⁾, the modified critical flow model by Asaka, et al.⁶⁾ was used in the REFLA/TRAC calculation. The REFLA/TRAC code gives better agreement with the data than the TRAC code for the break mass flow rate and the core differential pressure as

shown in Figs. 9.3.1(a) and 9.3.1(b), respectively. The REFLA/TRAC code with the TRAC critical flow model gave the same results as the TRAC code for the break mass flow rate and predicted the later depression of the core liquid level which was similar to the TRAC code prediction in the period between about 100 s and about 150 s. However, the REFLA/TRAC code gave better agreement for the core liquid level before about 100 s and after about 180 s regardless of the critical flow model.

The core heat-up was observed in the depression period of core liquid level in the test. Figure 9.3.1(c) compares the clad temperature. The data in the figure shows the highest temperature of high power bundle at the elevation. The REFLA/TRAC code predicts the higher temperature than that by the TRAC code and almost agrees with the measured data. The core heat-up was predicted in slightly later period by the REFLA/TRAC code with the TRAC critical flow model but nearly the same peak clad temperature was predicted.

The assessment results in this report indicate that the REFLA/TRAC code can apply to the SBLOCA transients with the accuracy more than that of the TRAC code. However, a suitable critical flow model should be used in order to predict the period of core heat-up due to the core liquid level depression.

References

- 1) Akimoto H., et al.: Assessments of REFLA/TRAC Code for Various Postulated Accidents in PWR, Fifth International Topical Meeting on Reactor Thermal Hydraulics (NURETH-5), Salt Lake City U.S.A. (1992).
- 2) Liles, D.R., et al.: TRAC-PF1/MOD1 Correlations and Models, NUREG/CR-5069 LA-11208-MS (1988).
- 3) Akimoto H. and Murao Y.: J. Nucl. Sci. Technol., 29[7], 642-655 (1992).
- 4) The ROSA IV Group: ROSA-IV Large Scale Test Facility (LSTF) System Description, JAERI-M 84-237 (1985).
- 5) Tasaka, K., et al.: The Effects of Break Location on PWR Small Break LOCA, Third International Topical Meeting on Nuclear Power Plant Thermal Hydraulics and Operations, Seoul Korea (1988).
- 6) Asaka, H., et al.: Experimental Thermal and Fluid Science, 3, 588-596 (1990).

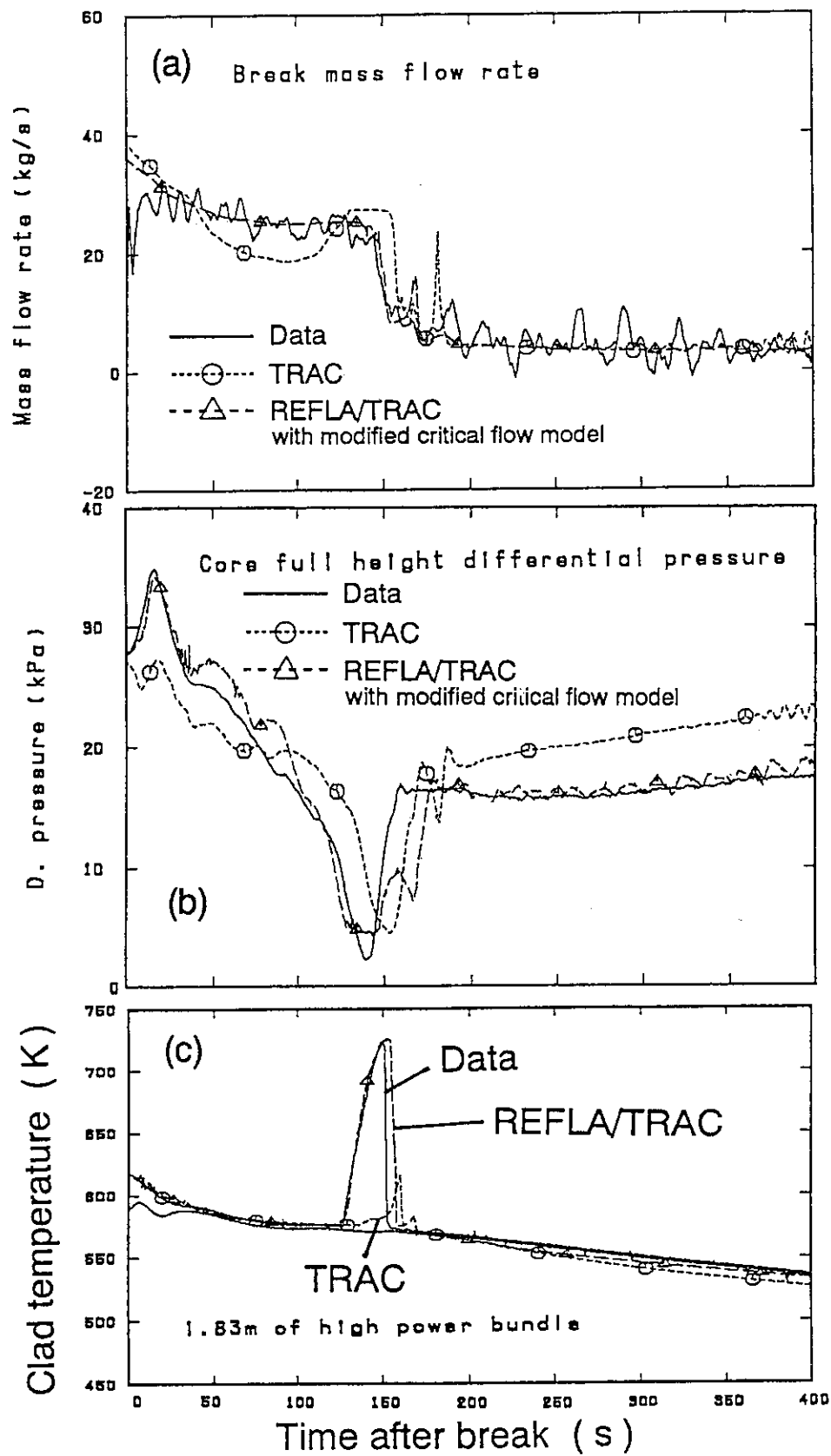


Fig. 9.3.1 Comparison of break mass flow rate (a), core full height differential pressure (b) and clad temperature (c)

9.4 Analyses for LOCA Experiments of ROSA-II Test Using REFLA/TRAC Code

M. Okazaki, H. Akimoto

As a part of REFLA/TRAC code assessment for predictive capability of thermal hydraulic phenomena in a large-break LOCA in PWR, analyses of ROSA-II test are made. ROSA-II¹⁾ test was conducted at JAERI to evaluate the effect of ECCS using the simulated facility (1/400 volumetric scale of PWR) for the blowdown and reflooding phenomena in PWR LOCAs. Three experiments which are varied on break location, injection point of ECCS and core heat power are chosen for the assessment. The discharge coefficient at each break point is tuned so that the history of pressure decrease and diminishing process of coolant in the core become similar to the experiments.

Input Model.

Main parts of input model consists of pressure vessel (PV), intact and broken primary loops, pressurizer (PR) and steam generators (SG). For the PV part, one-dimensional noding is used including downcomer, lower and upper plena and core.

RUN314²⁾ is the test simulating cold-leg double-ended large-break LOCA. ECC (Acc and LPCI) water is injected at lower plenum of PV and at broken loop cold leg. Experimental results show that the core is quenched due to reflooding of ECC water injected at lower plenum (Fig. 9.4.1), whereas calculated results show that core temperature continues to increase (Fig. 9.4.2). The causes of the differences between calculated and experimental results are considered as follows. First, the drop of downcomer head due to boiling is overestimated. Second, the velocity difference between vapor and liquid in the core is overestimated and the superficial level of water becomes so low that the upper part of core is almost covered by steam flow alone (Fig. 9.4.3), although the water head which is estimated from pressure difference through PV in the core is greater in the calculation than in the experiment (Fig.9.4.4).

RUN420³⁾ is the test simulating double ended large break LOCA of hot leg. Acc and LPCI water is injected at cold legs of broken and intact loops. Experimental results show

that flow stagnation occurs in the core at several seconds after blowdown initiation, and that the film boiling takes place in the middle part of the core resulting in rapid temperature rise in that place. Calculated results show the steep temperature rise immediately after blowdown initiation with the occurrence of flow stagnation and ensuing rapid development of void fraction in the core (Fig. 9.4.5). Water accumulation in the core is predicted to start earlier and to be by larger amount than in the experiment. But the predicted core cooling rate is worse than in experiment. To one of the causes of worse cooling, very high maximum heating rate of the core at initial condition in this RUN may be attributed ; i.e. 61.5 kW/m in RUN420 and 27.3 kW/m in other RUNs. Further study is needed for this problem. Because core power is turned off at 28 seconds, the void fraction starts to decrease.

RUN506⁴⁾ is the test simulating cold-leg double-ended large-break LOCA. Both Acc and LPCI water is injected at cold leg of intact loop and only Acc water is injected at cold leg of broken loop. The diminishing process of core coolant during blowdown is similar between experiment and calculation (Fig. 9.4.6). The appearance of film boiling in the core is predicted very early than in the experiments. It is about 6 seconds in the calculation and about 17 seconds in the experiment. Accordingly, film boiling heat transfer mode continues until core power is turned off at 80 seconds although the water accumulation in the core estimated from pressure difference through PV is greater in the calculation than in the experiment.

The REFLA/TRAC code tends to overestimate the cladding temperature. It is necessary to study more on wall heat transfer model.

References

- 1) Shiba, M., et al : JAERI-M 6247 (1975)
- 2) Reactor Safety Laboratory 1. ROSA Group : JAERI-M 6849 (1976)
- 3) idem : JAERI-M 7239 (1977)
- 4) idem : JAERI-M 7737 (1978)

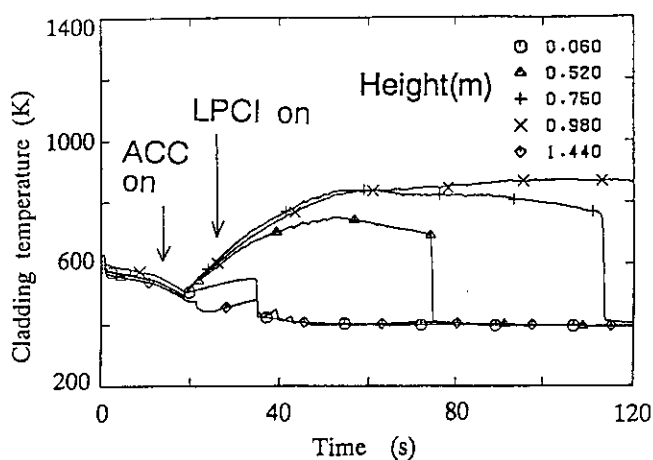


Fig.9.4.1
Cladding temp. of high heat flux rod (Exp.)
(Run 314)

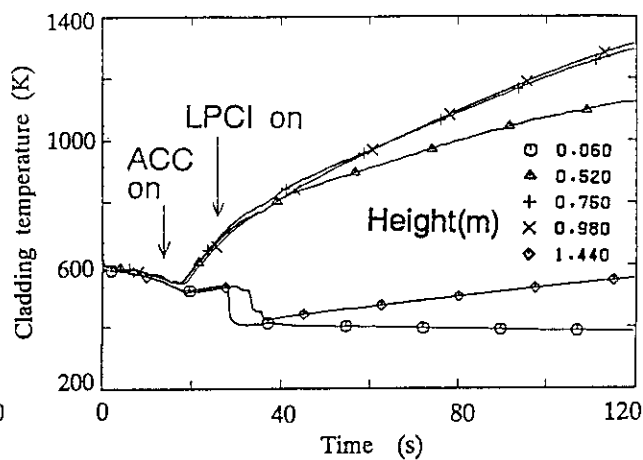


Fig.9.4.2
Cladding temp. of high heat flux rod (Calc.)
(Run 314)

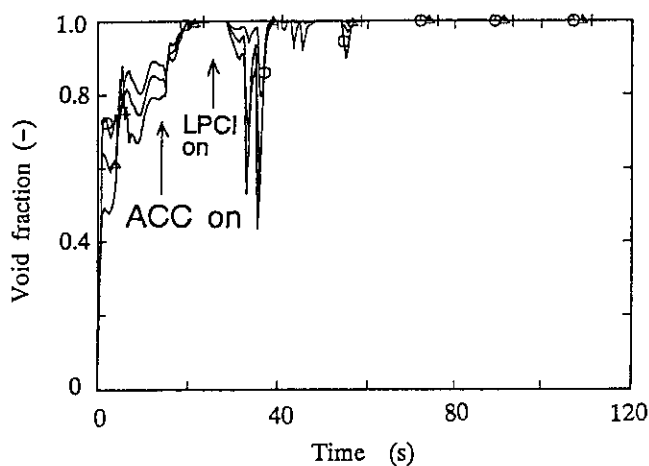


Fig.9.4.3
Void fraction in the upper core (Run 314)

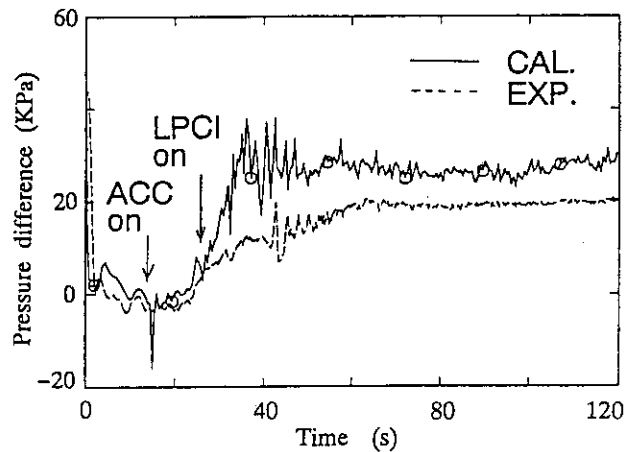


Fig.9.4.4
Pressure difference between PV bottom and Top (Run 314)

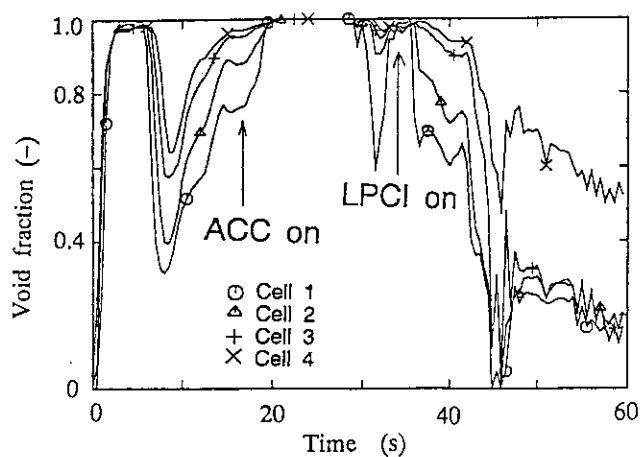


Fig.9.4.5
Void fraction in the lower core (Run 420)

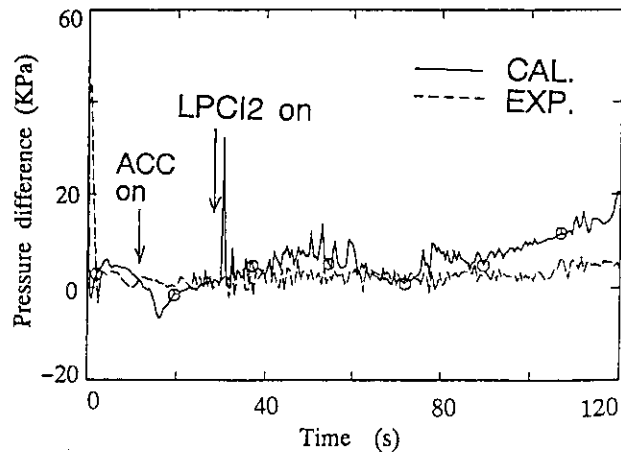


Fig.9.4.6
Pressure difference between PV bottom and Top (Run 506)

9.5 Improvement of Models in COBRA-TF Code for Liquid Entrainments in Film-mist Flow

T. Okubo, A. Ezzidi* and Y. Murao

The COBRA-TF code¹⁾ was developed to provide a detailed best estimate thermal hydraulic analysis of a Light Water Reactor (LWR) core for design basis accidents and anticipated transients. Since it provides a two-fluid three-field representation of the two-phase flow, *i.e.* continuous vapor, continuous liquid and entrained liquid, instead of the homogeneous representation used in the previous versions of the COBRA codes, it can appropriately analyze the film-mist flow behavior, which we are interested in from the point of view of the prediction of the film dryout phenomenon expected in the reactor core.

Prior to apply the code to the analyses on the film dryout phenomenon, some assessment calculations on the liquid entrainment and deposition models in the COBRA-TF code for the film-mist flow have been performed²⁾. This is because these models significantly affect the film dryout phenomenon. Through this study the following has been obtained :

- (1) The code can predict the entrainment flow rate well under high pressures of 3.4 and 6.9 MPa, but not under low pressures of 0.24 ~ 0.45 MPa (Fig. 9.5.1).
- (2) The main reason for the discrepancies at low pressures shown in Fig. 9.5.1 is considered to be that the Würtz's entrainment correlation used in the code, which was developed mainly based on his experimental data obtained at high pressures of 3 to 9 MPa, is not suitable for low pressure situations.
- (3) Sugawara's correlations used in the FIDAS code³⁾ are promising to improve the predictive capability of the code, since they can take account of low pressure situations.

Based on the investigation above, correlations for the entrainment and deposition have been changed in the COBRA-TF code in order to improve its predictive capability for the entrainment/deposition phenomenon at low pressures less than 0.5 MPa.

As the first step, Sugawara's correlations for the entrainment and the deposition,

* An STA Fellow during May, 1992 ~ May, 1993

which were used in the FIDAS code, were introduced into COBRA-TF. Although calculational results with these became in much better agreement with the concerned experimental data than before, the agreement was not yet satisfactory. Then, as the second step, the correlation for the interfacial friction factor was also changed to the Wallis' and this resulted in some more improvement in the calculational results. However, discrepancies between calculated results and the experimental data were still in the range of about 20 %. That is, it has been found the COBRA-TF code can not well predict the experimental data even with those correlations, with which the FIDAS code can predict them very well. This indicates the entrainment/deposition phenomenon is a very complicated process to be calculated and the phenomenon is not only determined with the entrainment and deposition relations but with many other factors, which are different from code to code.

In order to get a better agreement with the experimental data, a new entrainment correlation has been derived based on the Würtz's correlation and the Sugawara's ideas for modification factors. The new correlation has one more factor than the Sugawara's and this factor is a function of two Reynolds numbers for the liquid film and the relative motion between the vapor and the liquid film. The calculated results with the new entrainment correlation together with the Sugawara's deposition correlation and the Wallis' interfacial friction factor correlation are in very good agreement with the experimental data in a wide range of flow conditions, indicating a significant improvement on the predictive capability of COBRA-TF for the entrainment/deposition phenomenon. Figure 9.5.2 shows an example of the improvement at the low pressure of 0.24 MPa.

References

- 1) Thurgood, M.J. *et al.* : "COBRA/TRAC - A Thermal-Hydraulics Code for Transient Analysis of Nuclear Reactor Vessels and Primary Coolant Systems", NUREG/CR-3046 (1983).
- 2) Okubo T., Ezzidi A. and Murao Y. : "Assessment of Models in COBRA-TF Code for Liquid Entrainments in Film-Mist Flow", JAERI-M 93-069 (1993).
- 3) Sugawara, S., Miyamoto, Y. : "FIDAS : Detailed Subchannel Analysis Code Based on the Three-Fluid and Three-Field Model", *Nucl. Eng. Des.*, **120**, 147-161 (1990).

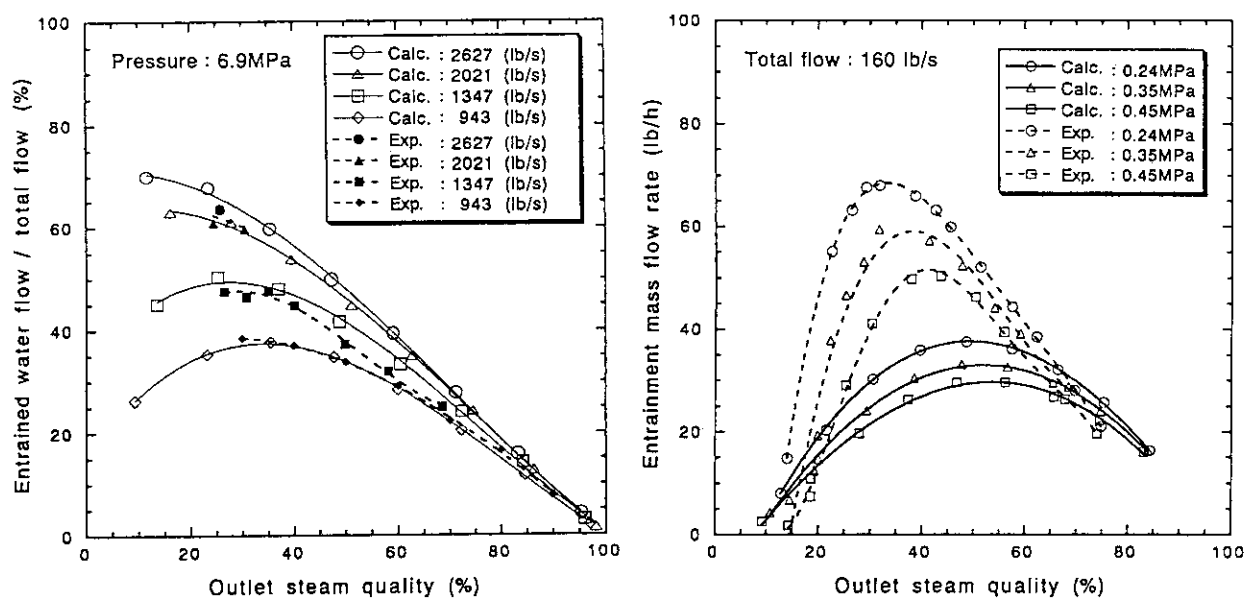


Fig. 9.5.1 Comparison of entrainment mass flow between the COBRA-TF calculation and experiment by Hewitt *et al.*

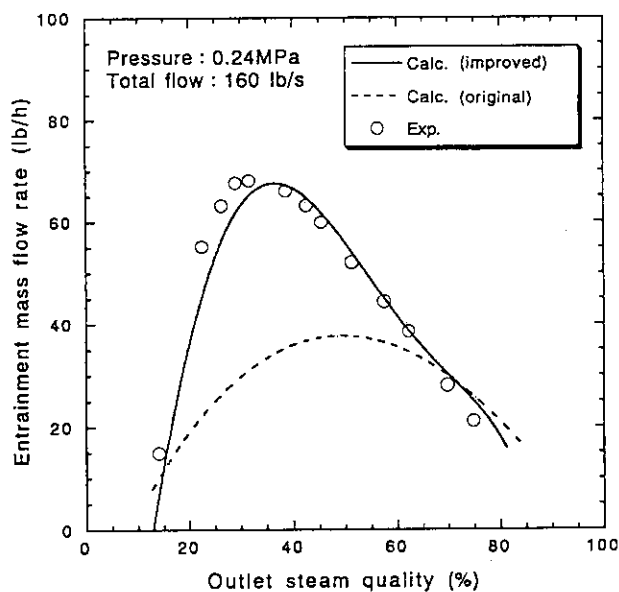


Fig. 9.5.2 Comparison of entrainment mass flow between the COBRA-TF calculation with improved models and experiment by Hewitt *et al.*

9.6 Visualization of Boiling Two-phase Flow and CHF Phenomenon with Real Time Neutron Radiography

T. Iwamura, H. Watanabe and Y. Murao

Microscopic observation of the CHF phenomenon on a heated surface is essentially important to establish a reliable CHF mechanistic model. Neutron Radiography (NRG) technique is particularly useful for two-phase water flow in a stainless-steel flow shroud because hydrogen contained in water is very efficient element for attenuating neutrons and stainless-steel is practically transparent for neutron beam. In the present study, the NRG technique was applied to observe the CHF phenomenon on a heated surface inside a stainless-steel flow shroud.

The NRG facility installed at the JRR-3M was used for the two-phase flow observation study. The JRR-3M is a heavy water moderated and light water cooled pool-type research reactor with the operating thermal power of 20 MW. Figure 9.6.1 shows the schematic diagram of the NRG and image processing system. A thermal neutron flux of $1.5 \times 10^8 \text{ n/m}^2\cdot\text{s}$ is provided from the reactor through a divergent collimator. After penetrating the two-phase flow test section, the neutron beam reaches a LiF-ZnS(Ag) convertor screen which fluoresces when absorbing neutrons. A mirror reflects the fluorescent images to a silicon intensifier tube (SIT) high sensitivity TV camera.

The real-time NRG images were recorded on a video cassette tape recorder at a frame interval of 1/30 sec. Various image processing techniques such as frame averaging, pseudo-color image conversion, and intensity analysis were available. For some NRG observation experiments, Musashi dynamic image processing system (MDIPS) developed by Murata et al.¹⁾ was used to process the image data just before and after the onset of CHF.

Figure 9.6.2 shows the schematic diagram of the experimental flow loop. Major part of the flow loop is located at the reactor building floor and the test section is located at the NRG irradiation room. The horizontal cross section of the test section is shown in Fig. 9.6.3. The stainless-steel flow shroud contains a slab-type stainless-steel heating element with a convex-shaped cross section. The heating element is located parallel to the neutron beam inside a 10 X 10 mm square-shaped flow shroud. The outer side of the flow shroud facing

to the neutron beam is cut off to minimize the neutron attenuation by the shroud material. The heating element has an effective heating length of 260 mm and is uniformly heated. The maximum available heating power source is 20 kW. Two K-type thermocouples are attached at the surface of heating element to detect the onset of CHF. In order to utilize the maximum neutron flux for the visualization of the CHF phenomenon, the top part of the heating element is located at the center part of the irradiation field. Inside the flow shroud, water flows vertically upwards under the maximum pressure of 1.0 MPa.

Monochrome images of typical flow pattern are shown in Fig.9.6.4. The images were obtained by integrating over 200 frames. Figure 9.6.4(a) shows water single-phase flow in which most of neutrons are attenuated, resulting in the dark image. Since the neutron attenuation rate is very small in the vapor phase due to the sparse density of hydrogen, the NRG image becomes lighter as the void fraction increases. Figure 9.6.4(b) shows the image of subcooled boiling flow in which the thermal equilibrium quality at the exit of heated part is 0.0. Figure 9.6.4(c) shows saturated boiling flow with the exit equilibrium quality of 0.02. In this figure, a high intensity region is recognized between the heater element and the wall. A thin liquid phase is also seen near the surfaces of heater element and unheated walls.

Figure 9.6.5 shows the continuous images of CHF phenomenon processed from the digitally recorded data using the MDIPS. The time interval of each frame is 1/30 sec. It is shown from this figure that the flow pattern just before the onset of CHF is annular flow. The heater element was melt-down just after the onset of CHF as seen in the 4th frame because the temperature rising rate was so rapid that the safety shutdown system could not respond in time. The average heat flux at the surface of the heater element and the exit quality at the time of CHF is 4.99 MW/m^2 and 0.099, respectively. After the power shut-off, the flow channel was recovered with water.

Since the minimum resolution of the NRG image is greater than 0.1 mm, microscopic flow behavior near the heated surface was not clearly observed. Further improvement of the NRG system is required to obtain quantitative information on the CHF phenomenon.

Reference

- 1) Murata, Y., et al.: Musashi Dynamic Image Processing System, Neutron Radiography 4 (Proc. 4th World Conf., San Francisco) (1992).

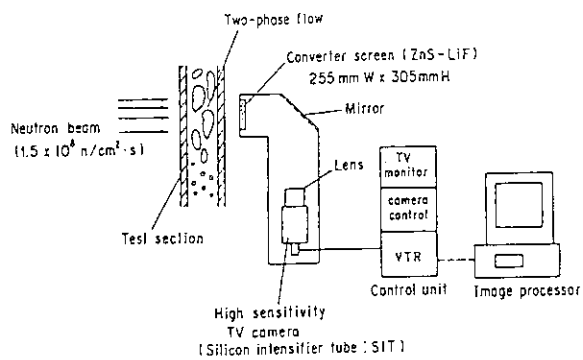


Fig.9.6.1 Neutron radiography system

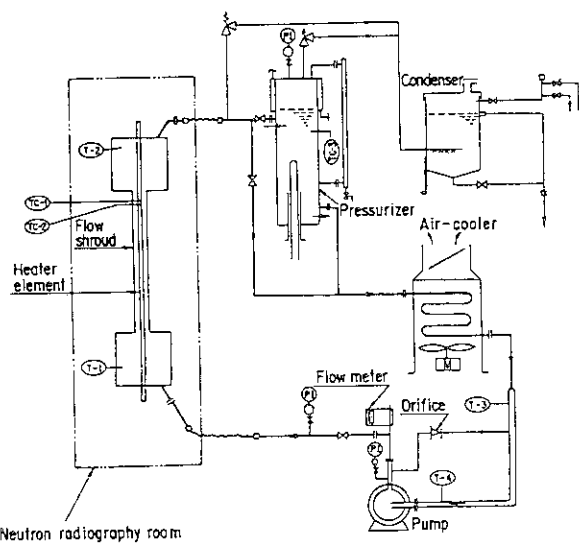


Fig.9.6.2 Schematic diagram of NRG observation test loop

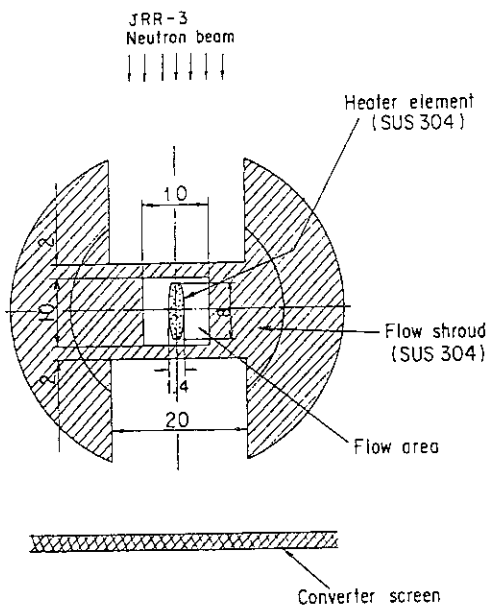


Fig.9.6.3 Cross section of NRG observation test section

Test conditions: $P = 0.95 \text{ MPa}$, $G = 1380 \text{ kg/s.m}^2$, $T_{in} = 160 \text{ }^\circ\text{C}$

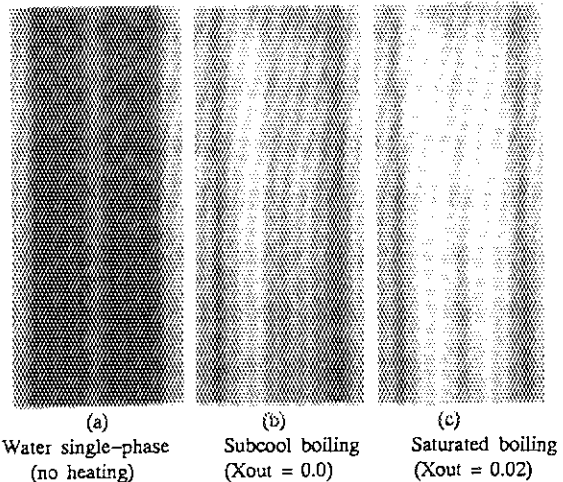


Fig.9.6.4 Observation results of boiling two-phase flow

Test conditions : $P = 1.0 \text{ MPa}$, $G = 820 \text{ kg/s.m}^2$, $T_{in} = 165 \text{ }^\circ\text{C}$
 $X_{out} = 0.099$, heat flux = 4.49 MW/m^2

: frame number, frame interval = 1/30 sec

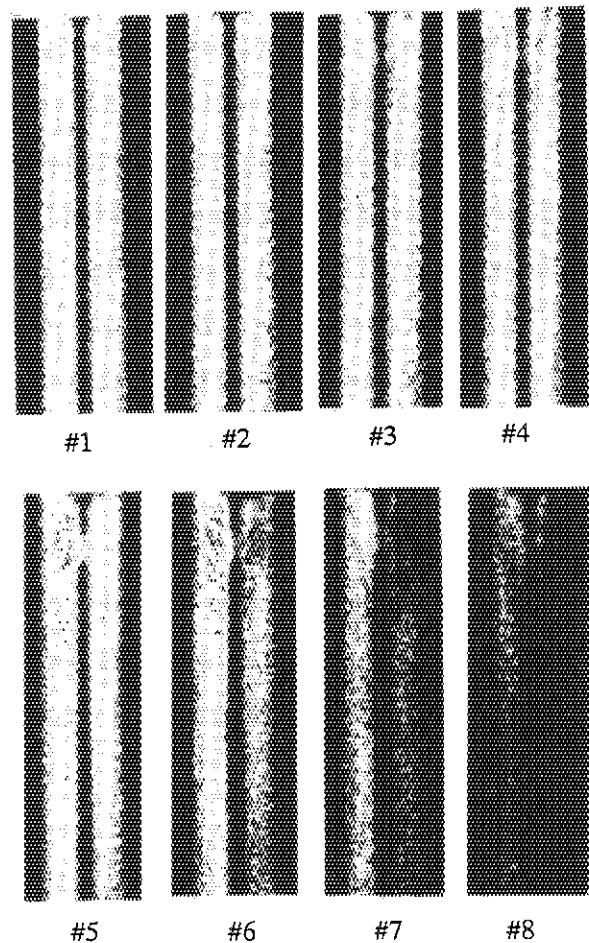


Fig.9.6.5 Observation results of CHF phenomenon

9.7 DNBR Analysis under Circulation Pump Seizure Accident for SPWR

T. Iwamura, F. Araya and Y. Murao

The SPWR (System-Integrated PWR) has been developed by Sako et al.¹⁾ to realize highly passive safety, good maintainability and economical competitiveness. The SPWR is an integrated reactor in which all the primary coolant system components including two units of steam generators, a main circulating pump and a pressurizer are located inside a single reactor pressure vessel. The reactor installs a poison tank filled with high concentration borated water for emergency shutdown system instead of control rod drive mechanism. In cases of abnormal situations such as station blackout, hydraulic pressure valves installed at the inlet of the poison tank are automatically opened and then the borated water in the tank flows into the core through the lower density lock by natural circulation. Consequently, the reactor is shut down within several seconds. The core consists of triangular-pitched fuel rod assemblies. The rod outer diameter and pitch are 9.5 mm and 14.0 mm, respectively. The average linear heat rate is as small as 11.6 kW/m. The flow reduction rate under the pump seizure accident for the SPWR is larger than that for a current PWR because the SPWR has only one circulation pump. Therefore, the pump seizure accident is considered to be the most severe event from the DNBR point of view. In the present study, transient DNBR analysis was performed to evaluate the safety margin of the SPWR design under the pump seizure accident condition.

The primary system transient calculation was performed with a best-estimate three-dimensional accident analysis code REFLA/TRAC²⁾, which is based on the TRAC-PF1 code³⁾ and incorporates some thermal-hydraulic models developed at JAERI. Figure 9.7.1 shows the REFLA/TRAC calculation results of the core inlet flow rate, reactor power, core inlet temperature and system pressure. In the present analysis, the hydraulic pressure valves were assumed to be inactive during the transient. The core inlet flow rate is rapidly reduced to 15% of the nominal flow rate within 1.5 s. The reactor power is reduced to 30% of the nominal value at 2 s due to the negative void reactivity coefficient. The core inlet water temperature is approximately constant during the transient. The system pressure increases up to 15.2 MPa which causes no problems for the intactness of the pressure boundary.

In order to obtain local flow parameters such as the mass velocity and enthalpy around a hottest rod, the time variations in the flow rate, core inlet temperature, system pressure and reactor power in Fig.9.7.1 were fed to the subchannel analysis code COBRA-IV-I⁴⁾. Figure 9.7.2 shows the radial noding schematics. The whole core was represented by the 1/12 sector due to the symmetrical configuration. The core has been analyzed in one-stage method using a fine mesh in a zone comprising the hottest rod and a coarse mesh outside this zone. Since the CHF correlation developed by Dalle Donne et al.⁵⁾ (KfK correlation) was found to be applicable to triangular-pitched fuel bundles,⁶⁾ the KfK correlation was incorporated into the COBRA-IV-I code to determine the DNBR using the local flow conditions. It should be noted that the change of fuel rod surface heat flux is delayed behind the change of reactor power under rapid transients due to the fuel rod thermal resistance. Therefore, the fuel rod model contained in the COBRA-IV-I was used to determine the surface heat flux transients.

The variation of minimum DNBR at the hottest rod is shown in Fig.9.7.3. The DNBR becomes minimum at 2.5 s and the value of the minimum DNBR is 1.5. The minimum DNBR is much higher than the conventional criterion of 1.3, indicating that an enough safety margin is assured under the pump seizure accident. Therefore, it is concluded that the present SPWR design is acceptable from a view point of the DNBR concern.

References

- 1) Sako,K., *et al.*:Passive Safe Reactor SPWR, *ANP'92 Oct.25-29, Tokyo* (1992).
- 2) Akimoto,H. *et al.*:Assessment of J-TRAC Code with CCTF/SCTF Test Data, *16th Water Reactor Safety Information Mtg.,Gaithersburg*, (1988).
- 3) Lilles,D.R.*et al.*:TRAC-PF1/MOD1: An Advanced Best-Estimate Computer Program for Pressurized Water Reactor Thermal-Hydraulic Analysis, *NUREG/CR-3858*,(1986).
- 4) Wheeler,C.L. *et al.*:COBRA-IV-I: An Interim Version of COBRA for Thermal- Hydraulic Analysis of Rod Bundle Nuclear Fuel Elements and Cores, *BNWL-1962*,(1976).
- 5) Dalle Donne,M. *et al.*:Critical Heat Flux Correlation for Triangular Arrays of Rod Bundles with Tight Lattices, Including the Spiral Spacer Effect, *Nucl. Technol.*,71,111,(1985).
- 6) Iwamura,T. *et al.*:CHF Experiments under Steady-State and Transient Conditions for Tight Lattice Core with Non-Uniform Axial Power Distribution, *J. Nucl. Sci. Technol.*, 30[5],413, (1993).

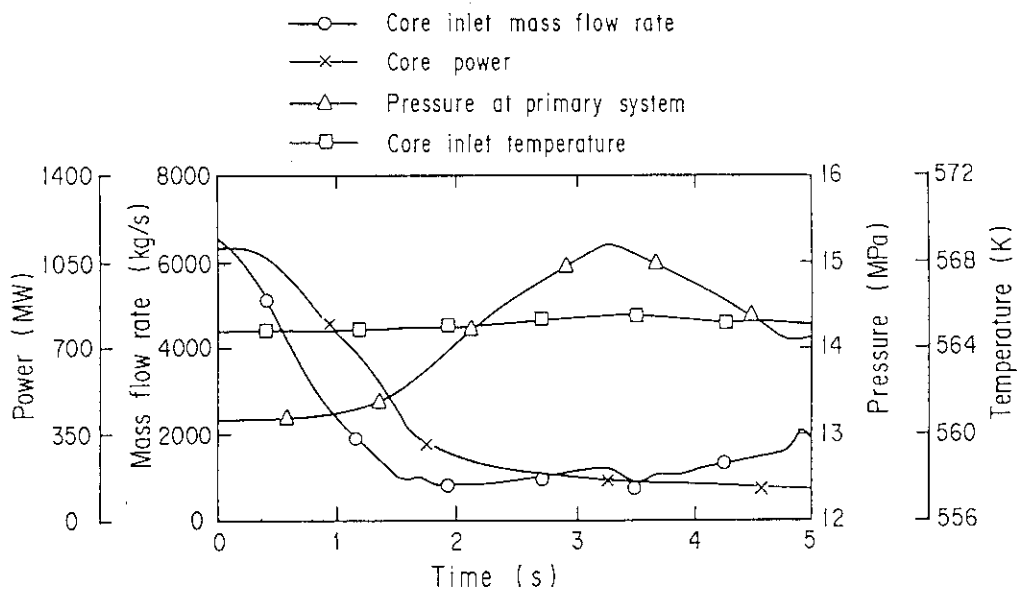


Fig.9.7.1 REFLA/TRAC analysis results

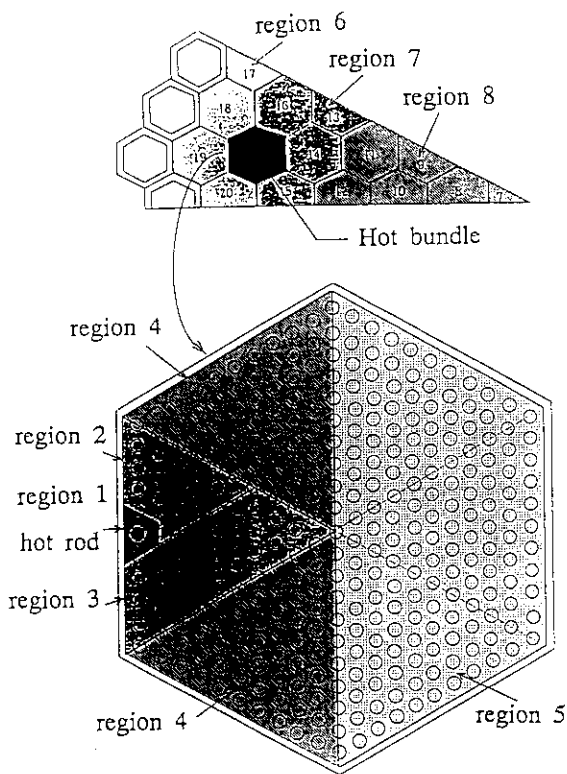


Fig.9.7.2 Subchannel noding model for COBRA-IV-I analysis

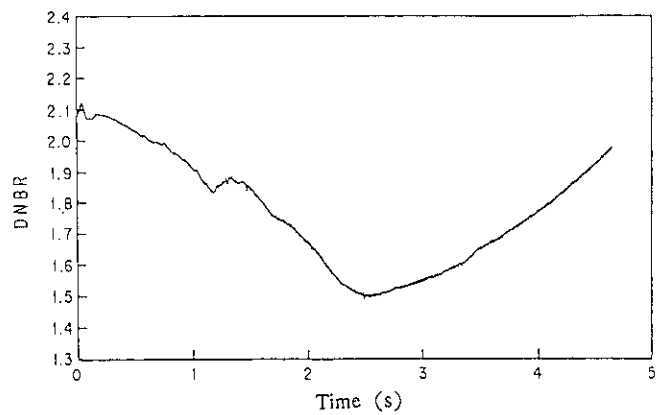


Fig.9.7.3 DNBR analysis result

9.8 Experimental Investigation on Non-uniform One-phase Flow in Lower Plenum Through Perforated Plate

K. Kunii, T. Iguchi, H. Watanabe and Y. Murao

As a part of conceptual design on the High Conversion Pressurized Water Reactor (HCPWR), a method to flatten the flow distribution at the core inlet has been developed. In the present study, an effect of hole size of the lower core support plate on the flow distribution in the lower plenum was experimentally investigated.

Figure 9.8.1 shows the experimental apparatus. The test section is a rectangular vessel (0.45m wide \times 0.025m depth \times 0.55m height) consisting of lower plenum, core and downcomer simulation parts scaled by 1/4 in radius compared to a reference HCPWR. The flow resistance in the core was simulated by installation of a perforated plate at the core part in the vessel. A similarity of fluid dynamics was obtained by using the identical Euler numbers for core inlet flows both in HCPWR and the experiment.¹⁾ Another perforated plate working as an orifice plate was positioned under the core perforated plate to investigate the effect of hole size on the flow pattern modification in the lower plenum. The perforated plate has 14 holes in same size. The ratio of open cross section of the lower plate to that of the core plate (ϕ ratio) was changed from 1/12 to 1.0 as an experimental parameter. The measurement of flow pattern in the lower plenum was performed by the methods of flow visualization and flowing particle image velocimetry²⁾.

The experimental results are summarized as follows:

- (1) Distribution of core inlet flow rate: The core inlet flow ratios from the center ($x=7/12$) to the downcomer side ($x=2/12$) were smaller and those in the contrary side ($x=8/12-11/12$) were larger, as shown in Fig.9.8.2. As the ϕ ratio decreases, the distribution of core inlet flow ratios tends to become uniform, though the effect of perforated plate is not significant. Especially, in the case of $\phi=1/12$ the flow ratio ranged within $\pm 10\%$, while the flow ratio ranged $\pm 20\%$ in the case of $\phi=1.0$.
- (2) Flow pattern in lower plenum: A circulating flow, which was including a zone of larger velocities along the outer wall (vessel), appeared in the lower plenum. The flow pattern in the case with perforated plates is shown in Fig.9.8.3. The similar flow pattern was observed in the case without perforated plates.

(3) Distribution of the deviation from the average to the local pressures (measured) at the core inlet: The ϕ ratio has little effect on the distribution of pressure deviation at the core inlet as shown in Fig.9.8.4. This result dynamically implied little difference in flow patterns in the lower plenum. Therefore the fact that the more uniform distribution of inlet flow ratio was obtained in the smaller ϕ case is considered as a result of the more increase of average static-pressure in smaller ϕ case caused by narrowing the flow cross section with the perforated plates.

Based on the experimental results, it was made sure that little differences appeared both on the flow pattern in lower plenum and on the distribution of deviation from average pressure at core inlet zone, even if the distribution of core inlet flow ratio became more uniform by narrowing the flow cross section using the orifice plates. Therefore it is concluded that the uniform flow distribution at the core inlet can be established by adjusting the hole sizes of the core supporting plate without disturbing the flow pattern in the lower plenum.

References

- 1) L.S.Tong and J.Weisman: "Thermal Analysis of Pressurized Water Reactors", ANS, 209 (1979).
- 2) Japan Soc. of Flow Visualization: "Handbook of Flow Visualization", Asakura Books, (1986) (in Japanese).

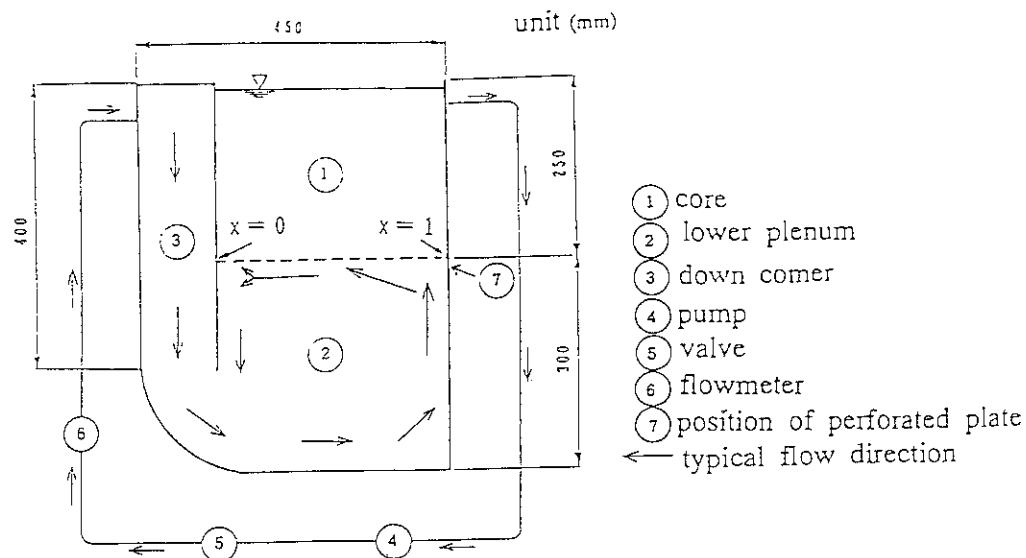
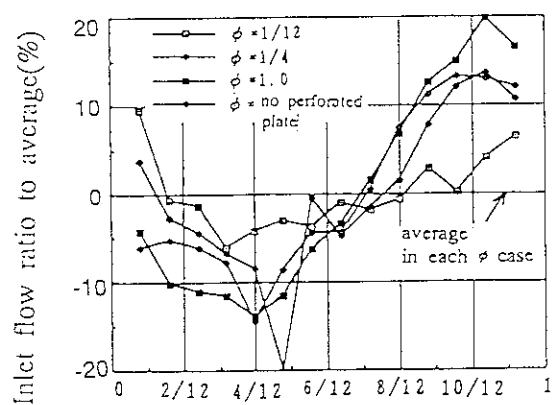


Fig.9.8.1 Experimental apparatus



Measurement position of inlet flow rate

Fig.9.8.2 Distribution of core inlet flow rate

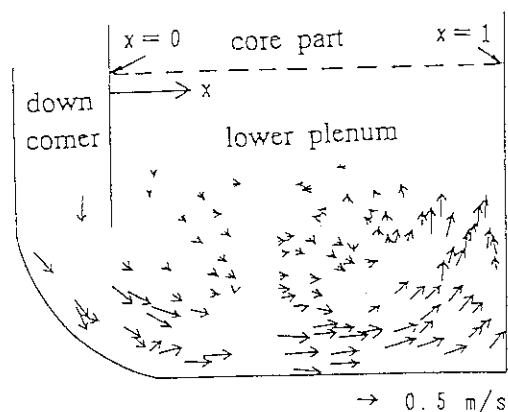
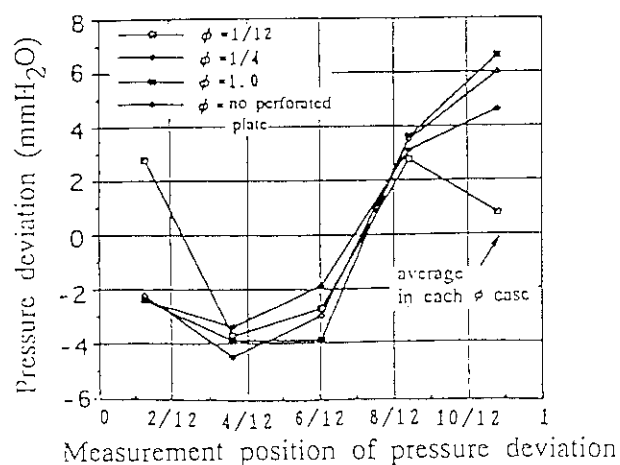
Fig.9.8.3 Flow pattern in lower plenum
(in a case of no perforated plate)

Fig.9.8.4 Distribution of pressure deviation

10. Development of Proton Linear Accelerator and Transmutation Target System

The conceptual design studies have been continued for an accelerator-driven minor actinide (MA) transmutation systems as a part of the OMEGA project (Options Making Extra Gains of Actinides and Fission Products). Two types of the systems, a sodium-cooled subcritical reactor system with actinide alloy fuel/tungsten target and a chloride molten-salt core/target system have been examined simultaneously. These systems are required to process annual rate of about 250 kg of actinides and to produce 800 MW thermal power in the studies. Several technical items such as configuration of the spallation target, thicknesses of the concrete shielding, capacity of the heat exchanger etc. were investigated to improve the transmutation efficiency and assure the system realization.

In the nuclear cascade simulation code NMTC/JAERI, the algorithm for pion generation was checked and the basic data for nucleon-nucleon elastic cross section were evaluated based on the new experiments and compilations. Benchmark studies of three high energy codes (NUCLEUS, ALICE-F and MCEXCITON) were performed to evaluate the accuracy of the calculated cross sections of aluminum, lead and bismuth.

Integral experiments have been made in order to obtain spallation neutron yield, nuclide productions in a lead assembly and to evaluate the validity of the simulation code system at the beam dump room of the 500 MeV booster proton synchrotron facility of National Laboratory for High Energy Physics (KEK). The experimental data obtained from the induced γ -ray activities in the assembly were in reasonable agreement with the calculated results. Neutron differential scattering for (p,n) reactions was also measured in the GeV region with the time-of-flight method at the KEK 12 GeV proton synchrotron facility.

For the mock-up test of the high intensity proton accelerator ETA (Engineering Test Accelerator 1.5 GeV, 10 mA), the design studies and R&D works of the Basic Technology Accelerator (BTA 10 MeV, 10 mA) are in progress. Main accelerator components under development are an ion source, a radio frequency quadrupole (RFQ), a drift tube linac (DTL) and an RF source. A proton beam current of 140 mA (peak) was extracted by the multicusp ion source at the 100 kV. The observed normalized emittance of about 0.45 π mm.mrad (90%) and proton ratio of 80 % were obtained. The design studies of the 4 vane type RFQ and the machining of the vanes and tank were completed. The hollow conductor type focussing magnets for the DTL were fabricated and their magnetic field strength and central position were measured with a Hall element and a rotating search coil method, respectively. The design for one unit of the RF source with the 1MW tetrode (EIMAC 4CM2500KG) was completed. The control unit for frequency, phase and amplitude was provided and a first stage solid state amplifier were equipped.

(Motoharu Mizumoto)

10.1 A Progress in the High Intensity Proton Linear Accelerator Development

M. Mizumoto, K. Hasegawa, H. Yokobori, H. Oguri, Y. Okumura, J. Kusano, T. Ono, H. Murata, K. Sakogawa and M. Kawai*

The high intensity proton linear accelerator (ETA: Engineering Test Accelerator) with an energy of 1.5 GeV and an average current of 10 mA has been proposed for the accelerator-driven nuclear waste transmutation as a part of the OMEGA project. The development of the Basic Technology Accelerator (BTA) is being carried out for the purpose of the mock-up test in the low energy portion of the ETA. The R&D's for main accelerator components such as high current hydrogen ion source, radio-frequency quadrupole (RFQ), drift tune linac (DTL) and RF power source are in progress¹⁾ as shown in Fig.10.1.1.

In the case of high intensity accelerator, it is of particular importance to minimize beam losses to avoid damage and activation of the accelerator structures. Heat removal problem from the accelerator structures is also an important issue for the mechanical design, because of the high beam current and high duty operation. Temperature distribution and thermal stresses should be carefully studied with the three dimensional modeling codes. The major progresses made in FY1992 are summarized in the following.

Ion source

The ion source was constructed in collaboration with the group of the NBI (Neutral Beam Injectors) Heating Laboratory for Fusion Research. The source consists of a multicusp plasma generator and a two stage extractor. The dimension of the plasma chamber is 20 cm in diameter and 17 cm in length. The chamber is surrounded by 10 columns of SmCo magnets with the field strength of about 2 kG at the inner surface. The high brightness hydrogen ion of 140 mA was extracted using the 100 kV high voltage power supply. The beam profile was measured with a multi-channel calorimeter and the observed normalized emittance was about $0.45 \pi \text{mm.mrad}$ (90%). The proton ratio and impurity were also obtained to be 80 % and less than 1 % respectively by a Doppler shifted spectroscopy method.²⁾

RFQ

The design study for the RFQ has been made for a four vane type resonator with the frequency of 201.25 MHz, the peak current of 110 mA and duty factor of 10 %³⁾. The beam

*Toshiba Corporation

dynamics calculation code, PARMTEQ was modified and use to examine the effects caused by two dimensional machining of the vane (circular cross section of the tip). The electromagnetic fields and power losses at the undercutting of the vanes in the end region were calculated with the three dimensional code system MAFIA. The temperature distribution and thermal displacement were calculated with the three-dimensional finite element code of ABAQUS. The machining of the vanes and RFQ tank has been completed and the ports for an RF coupler and vacuum devices are being fabricated by the Sumitomo Heavy Industries, LTD..

DTL

A resonant frequency, magnetic field strength and heat removal problem were investigated for DTL under the various mechanical constraints. A hollow conductor type coil with $5 \times 5 \text{ mm}^2$ was chosen for focussing magnet. Configuration of the quadrupole magnet is optimized under the condition on the coolant water (temperature rise 25°C in the coil, pressure drop 5 kgf/cm^2 and velocity 3.4 m/s). The beam dynamics design calculations for the DTL have been made using the computer code PARMILA. The MEBT consisting of four quadrupole magnets and one buncher is considered between the RFQ and the DTL to obtain matching. The hot test model with 9 cells, among which the #1 drift tube and the one at the front end plate are installed with the actual quadrupole magnets, is being fabricated by Mitsubishi Heavy Industries, LTD.. The magnetic field strength and center position, and higher harmonic field components have been measured with the conventional rotating search coil technique.

RF source

Three sets of 201.25 MHz RF sources with 1 MW peak class amplifier are required (641 kW for the RFQ and two 760 kW for the DTL) for the BTA. The tetrode 4CM2500KG (EIMAC), which was originally developed for fusion plasma heating, is used with multistage amplifier configuration. The high power amplifier (HPA) is driven by a 60 kW intermediate amplifier (IPA of RS2058CJ) which is fed by a master oscillator and a 3 kW solid state drive amplifier. The accelerator voltage and phase control loop are being prepared with an accuracy of $<0.1 \%$ in amplitude and $<1^\circ$ in phase. The RF source was designed and one set of the amplifier is being manufactured by the Sumitomo Heavy Industries, LTD.

Optimization Study for High β structure

The accelerator cavities and rf system for high β structures dominate the construction cost for the ETA. The conceptual and optimization studies for the ETA are performed

concerning proper choice of operating frequency, energy configuration, type of high β structure based on the beam dynamics and mechanical engineering considerations in collaboration with Los Alamos National Laboratory. RF source aspects on the trade-offs between large and small amplifiers are investigated.

References

- 1) Mizumoto M. et al.: "Intense Proton Accelerator for Nuclear Waste Transmutation", 1992 Linear Accelerator Conference Proceedings, 1992, August 24-28, Ottawa, Ontario, Canada, AECL-10728, p.749-751
- 2) Okumura Y. et al.: "Development of a High Brightness Ion Source for the Proton Linear Accelerator (BTA) at JAERI", *ibid*, p.645-647
- 3) Hasegawa K. et al.: "Design Study on an RFQ for the Basic Technology Accelerator in JAERI", *ibid*. p.314-316

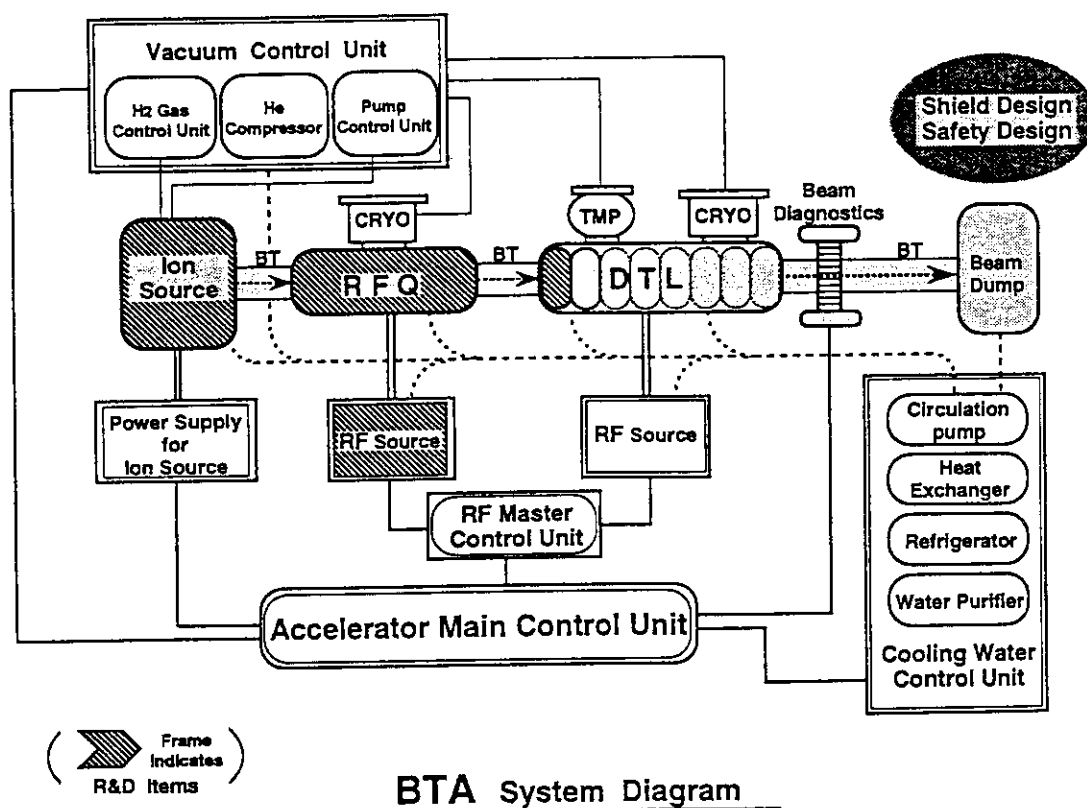


Fig.10.1.1 The BTA system diagram. The hatched items indicated four major R&D accelerator components.

10.2 Development of a High Brightness Hydrogen Ion Source for the Basic Technology Accelerator

—Beam Test at an Acceleration Voltage of 100 kV—

H. Oguri, Y. Okumura, J. Kusano, K. Hasegawa, H. Murata, K. Sakogawa, M. Kawai*, T. Ono and M. Mizumoto

The R&D work for construction of a high intensity proton linear accelerator has been carried out since 1991. A hydrogen ion source for the BTA is required to produce a high brightness (high current and low emittance) and high proton yield beam. The basic specifications of the ion source are listed in Table 10.2.1, and a cross-sectional view of the ion source is shown in Fig. 10.2.1. The ion source consists of a multicusp plasma chamber and a two-stage extractor. In the chamber, source plasma is produced by an arc discharge using tungsten filaments, and the plasma is confined by the strong cusp magnetic field of Sm-Co magnets for enough time to dissociate molecular ions so as to enhance the proton yield of the beam. Two-stage extraction system is adopted to obtain the convergent ion beam.

The ion source for the BTA has been designed and fabricated¹⁾. The first beam test was performed at an acceleration voltages up to 60 kV for the purpose to study the basic performance of the source²⁾. A new high voltage power supply of 100 kV and 200 mA was fabricated and the second beam test are being performed at full beam energy since the end of 1992.

In order to measure the beam optics of the ion source, a multichannel calorimeter was installed in the vacuum chamber. The calorimeter is made of copper buttons placed on a water cooled copper plate in the two perpendicular directions, and temperature distribution of the buttons gives the beam profile. Figure 10.2.2 shows a typical beam profile together with the Gaussian fitted curves (solid lines) at 100 kV. From the fitting, calculated beam divergence was 8.5 mrad, and assuming the beam diameter at the exit of the ion source is 5 mm, normalized emittance was estimated to be $0.5 \pi \text{ mm.mrad}(90\%)$. More precise emittance measurement are being performed by using an emittance scanner, and the data which support the estimation are obtained. Figure 10.2.3 shows the perveance characteristics of the ion source. The optimum beam current which gives the minimum beam divergence increases with the acceleration voltage, and achieved 140 mA at 100 kV.

Hydrogen ion beam consists of three species such as proton (H_1^+) and molecular ions (H_2^+ , H_3^+). The proton yield is more than 80 % at 50 mA which was measured by both

* Toshiba Corporation

momentum mass analysis and doppler-shifted spectroscopy in the first beam test²⁾. Moreover, the data from the latest measurement gives the proton yield as more than 85 % at 120 mA. Because the proton yield can be expected to reach 90 % at 140 mA from the previous measurement, proton beam of 126 mA will be obtained.

In this experiment, the filaments for the plasma production are worn and replaced every two months. The actual lifetime of the filaments is longer than that we expected. To extend the lifetime, if it is necessary, ECR or RF plasma production will be useful.

The aging process of the ion source is still continued for the stable extraction of the 100 kV beam without breakdown, and measurement of the detailed beam properties has been carried out. This ion source will be connected with the RFQ for 2 MeV proton beam acceleration test in the end of 1993.

References

- 1) Okumura Y. and Watanabe K.: "Design of a High Brightness Ion Source for the Basic Technology Accelerator (BTA)", JAERI-M 92-024 (1992)
- 2) Oguri H., et al.: "Development of a High Brightness Hydrogen Ion Source for the Basic Technology Accelerator (BTA)", JAERI-M 92-200 (1992), (in Japanese)

Table 10.2.1 Specifications of the ion source for the BTA

Energy	: 100 keV
Current	: 120 mA
Duty Factor	: CW
Emittance	: $0.5 \pi \text{ mm.mrad}$ (normalized 100%)
Proton Yield	: > 90%
Impurity	: < 1%

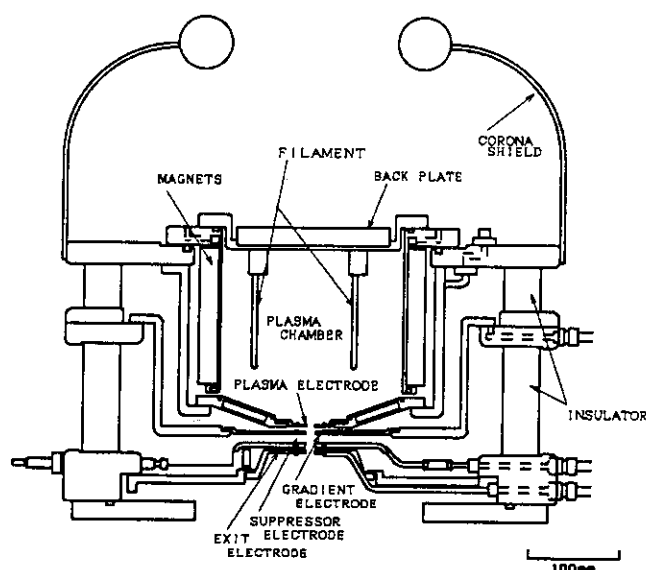


Fig. 10.2.1 Cross-sectional view of the ion source for BTA

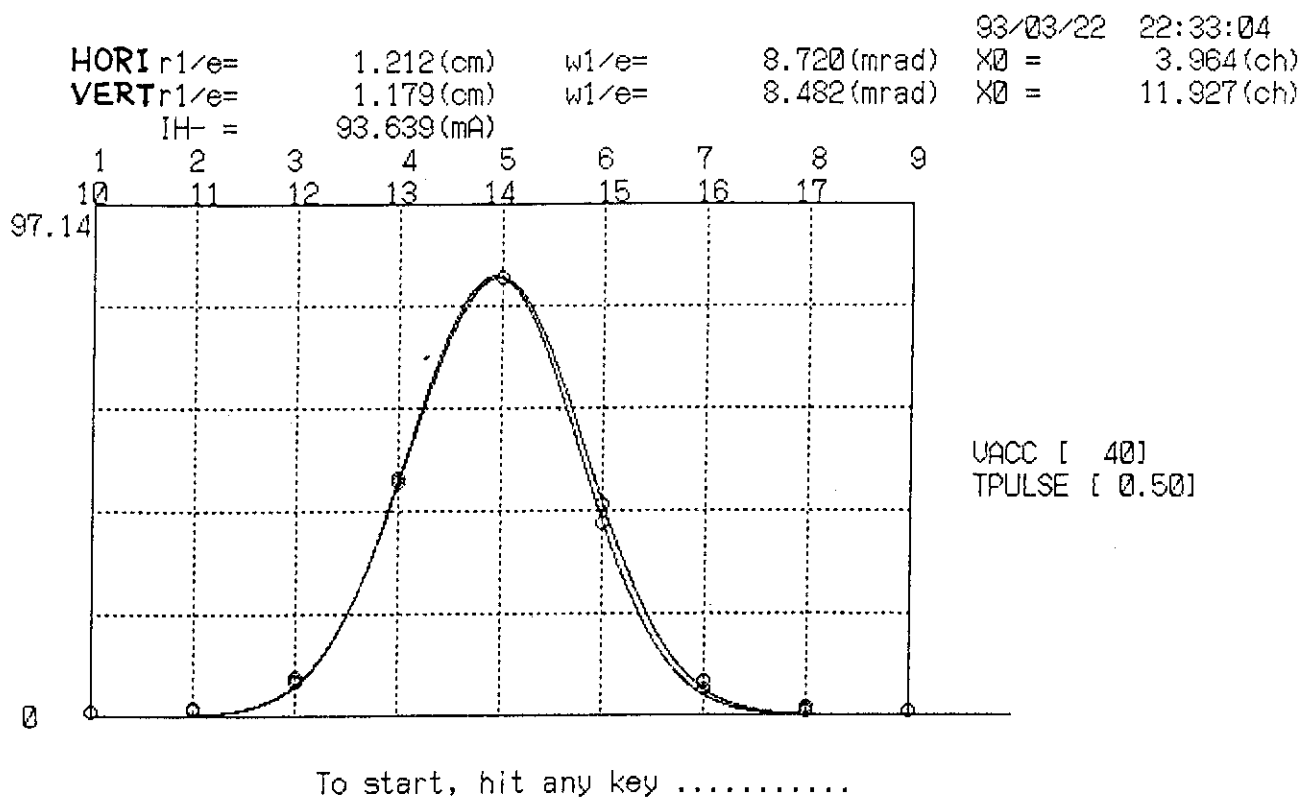


Fig. 10.2.2 Beam profile at 100 kV, 140 mA. The profile was measured by a multichannel calorimeter.

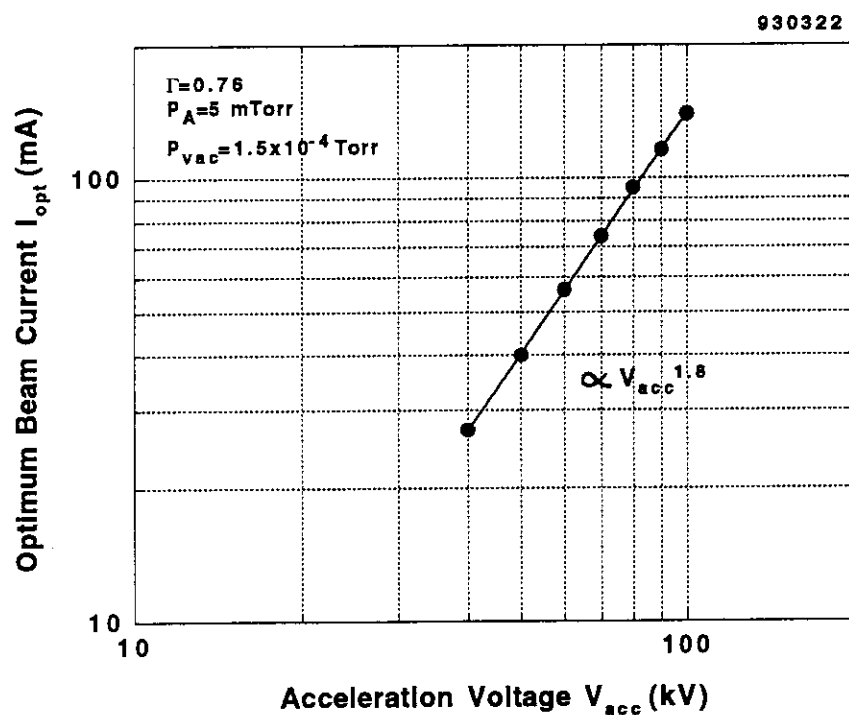


Fig. 10.2.3 Perveance characteristics of the ion source for the BTA

10.3 Development of a Radio Frequency Quadrupole for the Basic Technology Accelerator

—Study on an LEBT, Thermal Considerations and Mechanical Design—

K. Hasegawa, H. Murata, K. Sakogawa, M. Mizumoto, H. Oguri,
J. Kusano and M. Kawai*

A Radio Frequency Quadrupole (RFQ) for the Basic Technology Accelerator is designed to accelerate 10 mA (average) of protons up to 2 MeV.¹⁾ Development work for the RFQ has been continued. Study on a Low Energy Beam Transport (LEBT), thermal considerations and mechanical design have been carried out.

To obtain the desired transmission rate and the output emittance through the RFQ, the input beam emittance should be matched to the RFQ acceptance. The LEBT from the ion source to the RFQ was designed using the interactive code TRACE²⁾ for the first step. Since the beam from the ion source is axially symmetric and the RFQ requires a symmetric input, solenoids are used as the focusing elements in the LEBT. Although TRACE is convenient for the parameter search such as magnetic fields and distance between components, the emittance growth and its effects are not included in the calculations. Then the beam simulation including the emittance growth was performed with the modification version of PARMILA³⁾, which includes a DC beam simulation. Particle information from PARMILA was used as an input of the PARMTEQ code for the beam transport calculation of the RFQ. The magnetic fields of the two solenoids were determined to obtain the best transmission rate and emittance through the RFQ. The beam envelope in the LEBT and the x-x' emittance diagrams at the output positions of the ion source, LEBT and RFQ are shown in Fig.10.3.1. Transmission of 94 % through the RFQ was predicted, where the fields of the two solenoids are 0.368 T and 0.378 T, respectively.

Because of the high duty factor of 10 %, heat removal problem from the accelerator structures is an important issue for the mechanical design. By using the three-dimensional electromagnetic calculation code system of MAFIA, dissipation of the RF power loss density was calculated. Obtained relative values were normalized to the cavity wall point from the SUPERFISH results. Figure 10.3.2 shows the peak power loss density along the surface of the vane. With the heat load distributions specified by the MAFIA and SUPERFISH codes, a finite element modeling code of ABAQUS was used to study the thermal behavior for the mechanical structure design. Vanes are made of oxygen free copper with two cooling water channels ($\phi 22$ mm and $\phi 15$ mm). Water flow through each channel is 30 l/min, and average temperature is 25.5°C. Figure 10.3.3 shows a temperature distribution and displacement on the surface of the vane. Calculated maximum temperature is 39.1°C, and displacement in the

* Toshiba Corporation

transverse and longitudinal directions are $33\mu\text{m}$ and $99\mu\text{m}$, respectively. These deformations have no significant effects on the frequency tuning and for the beam dynamics.

After the design work based on the beam dynamics, electromagnetic and thermal aspects, mechanical design of the RFQ tank was carried out. Figure 10.3.4 is a cross sectional view of the RFQ tank. The inner diameter and the length are 36.6 cm and 334.8 cm, respectively. Two turbo-molecular pumps and two cryogenic pumps with the pumping speed of 500 l/sec and 700 l/sec, respectively, are equipped for the vacuum system to keep the pressure of 10^{-4} Pa during the operation. RF power is fed through the input coupler and the resonant frequency of the tank is tuned by the four automatic tuners.

The machining of the vanes and the tank has been completed. The high power test and beam test will be conducted in 1993 using a single unit of 1 MW RF source.

References

- 1) Hasegawa K., et al.: "Design Study on an RFQ for the Basic Technology Accelerator in JAERI", 1992 Linear Accelerator Conference, Ottawa, Canada, AECL-10728, pp.314-316 (1992)
- 2) Crandall K. R. and Rusthoi D. P.: "Documentation for TRACE: An Interactive Beam-Transport Code", LA-10235-MS (1985)
- 3) Boicourt G. and Merson J.: "PARMILA Users and Reference Manual", LA-UR-90-127 (1990)

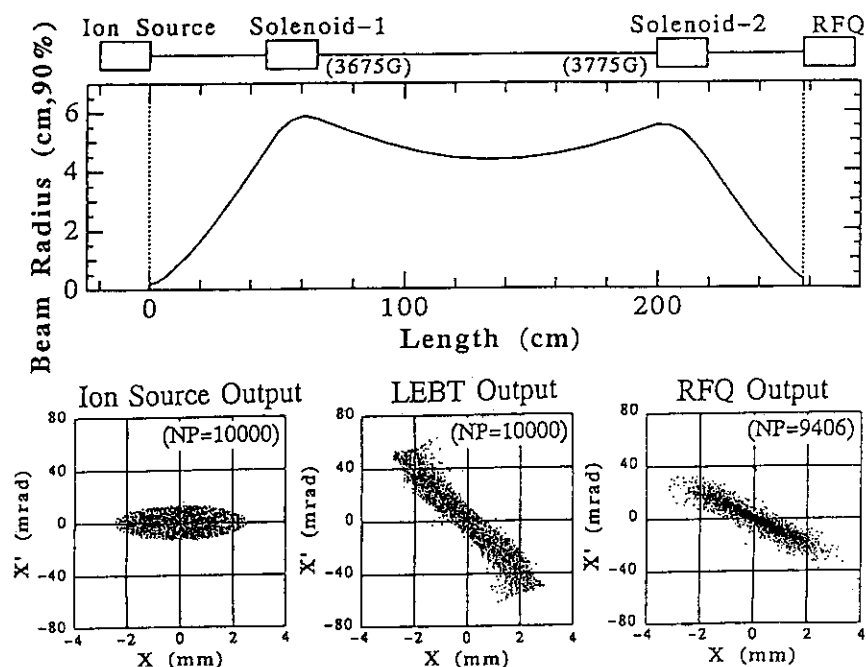


Fig.10.3.1 Beam envelope in the LEBT, and x - x' emittance diagrams at the output positions of the ion source, LEBT and RFQ

10.4 Development of a Drift Tube Linac for the Basic Technology Accelerator —Measurement of the Quadrupole Magnets—

K. Hasegawa and K. Sakogawa

Development work of a Drift Tube Linac (DTL) for the Basic Technology Accelerator (BTA) is being continued. An electromagnetic quadrupole using a hollow conductor (5mmx5mm) is chosen for the focusing magnet and excited with DC current, which is provided for the future cw operation. In order to use a quadrupole lens as a beam optical element, there are some characteristics that should be measured experimentally. These characteristics are

- (1) The field excitation as a function of exciting current
- (2) The field distribution
- (3) Displacement from the mechanical center to the magnetic field center
- (4) The intensity of the higher harmonic components.

In the R&D of the DTL, two quadrupole magnets (#0 and #1) were fabricated and examined. Measured data of the quadrupole magnets are summarized in Table 10.4.1.

Magnetic field as a function of exciting current is measured with a Hall effect transducer and 3-dimensional positioning machine. Figure 10.4.1 shows the excitation function measured at 5 mm from the center position of the magnet. Field gradient of 80 T/m is obtained at current of 785 A and 743 A for the magnet of #0 and #1, respectively. Figure 10.4.2 shows a field distribution in the transverse direction. Good linearity over the adequate range ($-15 < x < 15$ mm) is obtained, that satisfies the specification of the magnet since the beam bore radius is 10 mm.

A conventional rotating search coil and the Fast Fourier Transformer (FFT) technique is used to measure the magnetic center position and the harmonic field components. A testing apparatus was constructed with the modification of the milling machine. A fine adjusting stage, which can be moved in the two rectangular horizontal directions (X and Y) and its positioning accuracy is 1 μ m, is used for the magnet positioning. The induced voltage in the search coil is fed to a signal analyzer (HP35665A) and frequency spectrum is obtained. The magnetic center position, where the induced dipole voltage is minimum, is searched. The displacements from the mechanical center to the magnetic center are 12 μ m and 27 μ m for the #0 and #1 magnet, respectively. Figure 10.4.3 shows the measured induced dipole voltages as a function of Δy for five Δx cases.

The higher multipoles in the quadrupole magnet arise from the physical structure of the magnet (mechanical asymmetry etc.) and these components bring about an unwanted beam divergence. In many cases, the strengths of the harmonic field components are expressed relative to the quadrupole component. Figure 10.4.4 shows the voltage spectrum obtained from the FFT. For this magnet, higher multipoles are less than 1 % of the quadrupole components, and have not significant effects to the beam dynamics.

Table 10.4.1 Measured data of the quadrupole magnets

		Q-magnet #0	Q-magnet #1
I_Q at 80 T/m (A)		785	743
Displacement(*) (μm)	Δx	-6	-11
	Δy	+11	+25
Percentage relative to the quadrupole (n=2) signal	n=1	0.05	0.1
	n=2	100	100
	n=3	0.5	1.0
	n=4	0.05	0.03
	n=5	0.06	0.06
	n=6	0.7	0.7

(*) Displacement from the mechanical center to the field center

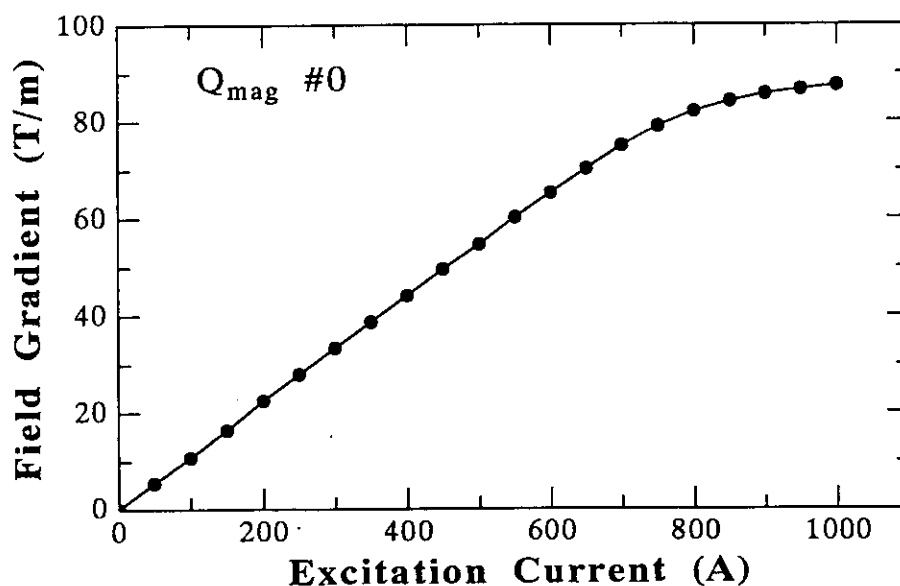


Fig.10.4.1 Field gradient as a function of excitation current

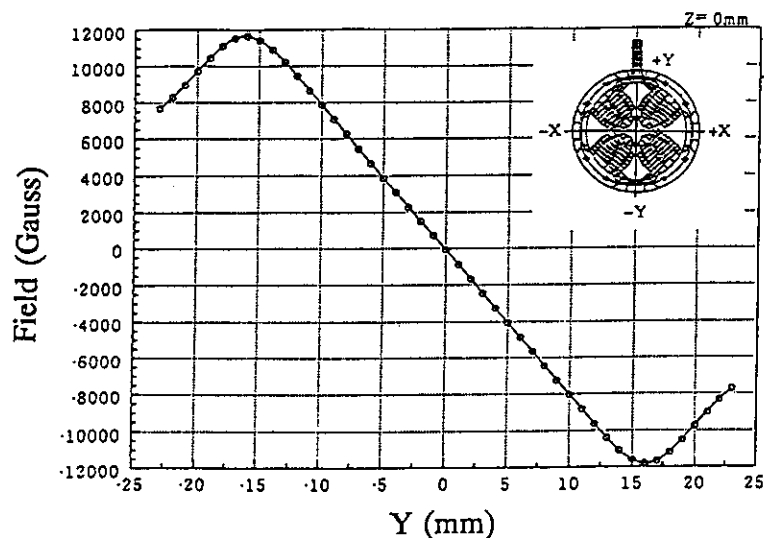


Fig.10.4.2 Field distribution in the Y direction (#0 magnet)

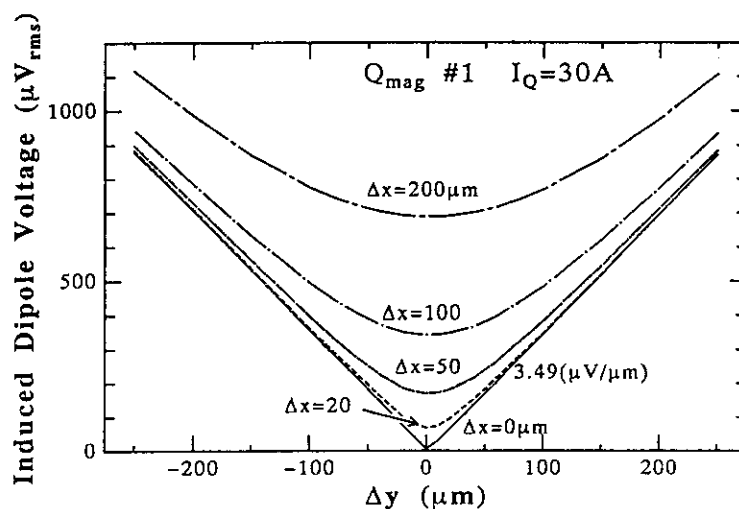
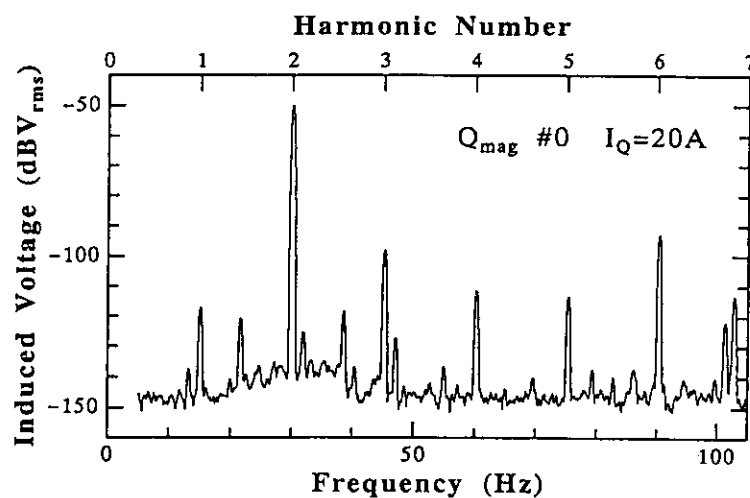
Fig.10.4.3 Induced dipole voltage in the rotating coil as a function of the distance from the magnetic center Δy for five Δx cases

Fig.10.4.4 Harmonic voltage spectrum (#1 magnet)

10.5 Improvements of the Spallation Cascade Code NMTC/JAERI

T. Nishida, Y. Nakahara, H. Takada, H. Kadotani *, N. Yoshizawa ** and S. Iwai ***

For the improvement of the spallation cascade code NMTC/JAERI, the algorithm calculating the pion generation option in the high energy region has been checked and the cutoff energy in the intranuclear cascade calculation has been adjusted. As the result the dependence of the number of spallation neutrons in a bulk target on the incident proton energy was considerably improved and showed the good agreement with those calculated at the relevant laboratories in USA and Europe.

Nucleon-nucleon elastic scattering cross sections used in the intranuclear cascade calculation have been estimated on the basis of the recent data. The old cross section data compiled in NMTC/JAERI tens years ago have been replaced by these new data. Nucleon-nucleon elastic scattering cross sections obtained in many experiments have been translated to the phase shift parameter δ_l at each reaction energy by the partial wave analysis method. Arndt et al.^{1),2)} estimated the δ value for ~ 5400 np and ~ 7200 nn data at the 22 energy points in the range of 20 MeV \sim 1.1 GeV. Total and differential cross sections for the nucleon-nucleon elastic scattering have been calculated as the sum of Legendre components dependent on these δ_l s, using the well known equations

$$d\sigma/d\Omega = 1/k^2 \left| \sum (2l+1) \exp(i\delta_l) \sin \delta_l P_l(\cos \theta) \right|^2 \quad (1)$$

and

$$\sigma = 2\pi/k^2 \sum (2l+1) \sin^2 \delta_l, \quad (2)$$

where k : incident particle's momentum.

Furthermore the values of parameters A, B and m in the equation (3) were determined as a function of the incident particle energy by applying the least mean squares method to these differential cross sections to be compiled in NMTC/JAERI.

$$d\sigma/d\Omega = A + B \mu^m, \quad (3)$$

$\mu = \cos \theta$, θ : scattering angle, m : integer

Figure 10.5-1 shows the comparison of the present curve fitted to the differential cross section data for the proton-proton elastic scattering at 1000 MeV with the Bertini's one compiled in NMTC. It is apparent that the Bertini's curve gives relatively lower cross section in the forward direction than the present curve. But this discrepancy has little influences on the calculation the spectra of neutrons escaped from the heavy metal target such as a bulk tungsten.

* Century Research Center, Inc. ** Mitsubishi Research Institute, Inc.

*** Mitsubishi Atomic Power Industry, Inc.

When calculating the internuclear cascade process in the present version of NMTC/JAERI code, the nucleon elastic scattering with nucleus is not taken into accounts. However the elastic scattering effects can not be ignored in the nuclear reaction calculations below several hundreds of MeV, especially in calculating the heat deposition distribution inside the metallic target and the number of neutrons escaping from the target surface to the shielding. The heat deposition distributions calculated by another cascade code HETC/KFA2 with and without the elastic scattering process were compared each other in the case of a Pb target irradiated by 1 GeV protons as seen in Fig.10.5.2. The NMTC/JAERI code has been modified to be able to treat the nucleon - nucleus elastic scattering process and the corresponding cross sections. Table 10.5.1 summarizes the nuclides for which the elastic scattering cross sections of proton and neutron in the high energy range are compiled in each data library. Figure 10.5.3 shows the dependence of elastic cross sections on the neutron energy for Pb, Fe, Al and C nuclides. By this improvement it is expected to upgrade the accuracy of the prediction on the heat generation distribution and the shielding of high energy particles in the transmutation system.

The benchmark studies were carried out using NMTC/JAERI for examining the nuclide production cross section in the high energy nuclear reaction. The results reveal the trend that the charge exchange reaction is overestimated in the bombardment of protons with the energy of 10~1000 MeV on a thin target of the light nucleus such as Al and the production cross section of a nuclide with the atomic number apart from one of target nuclide in the periodic table is underestimated. For the spectrum of neutrons generated in a thin target bombarded by protons with 25~1600 MeV the calculated value is larger than the experimental one in the forward direction of proton beams but smaller in the backward direction.

References

- 1) Arndt R. A. and L. D. Roper L. D. : Phys. Rev. D, 28(1), p.97 (1983).
- 2) Arndt R. A. et al. : Phys. Rev. D, 35(1), p.128(1987).

Table 10.5.1 Libraries of elastic scattering cross section for high energy nucleons

Particle	Library	Energy	Nuclide
Proton	NASA	100MeV~22.5GeV	He,C,O,Al,Ar,Fe,Br,Ag,Ba,Pb
Neutron	HILO	15MeV~100MeV	¹⁰ B,C,N,O,Na,Mg,Al,Si,S,K,Ca,Cr,Fe,Ni
	NASA	100MeV~22.5GeV	He,C,O,Al,Ar,Fe,Br,Ag,Ba,Pb

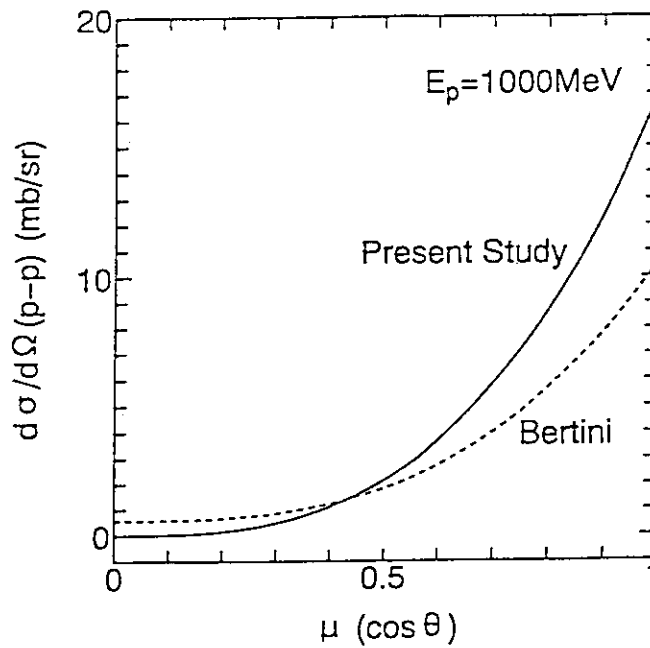


Fig.10.5.1

Curves fitted to differential cross section data for proton-proton elastic scattering at 1 GeV. The solid and broken lines represent the results in the present study and by Bertini respectively.

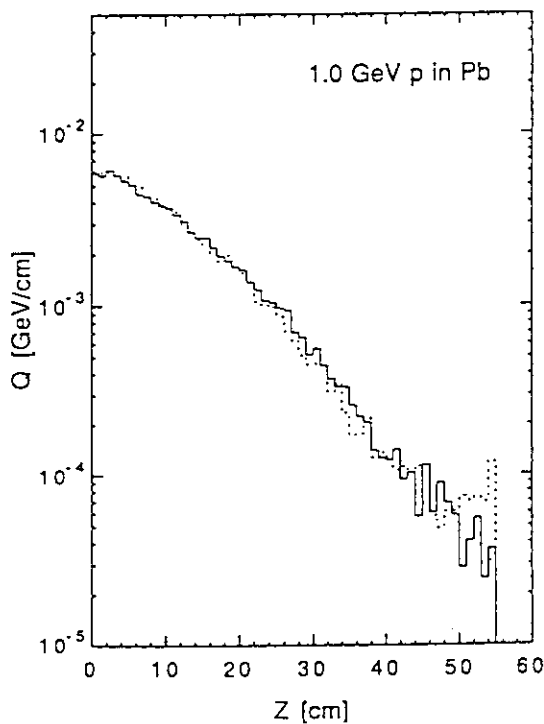


Fig.10.5.2

Heat deposition distributions in a Pb target irradiated by 1 GeV protons. The solid and broken histograms correspond to the results calculated by the HETC/KFA2 code with and without the elastic scattering process respectively.

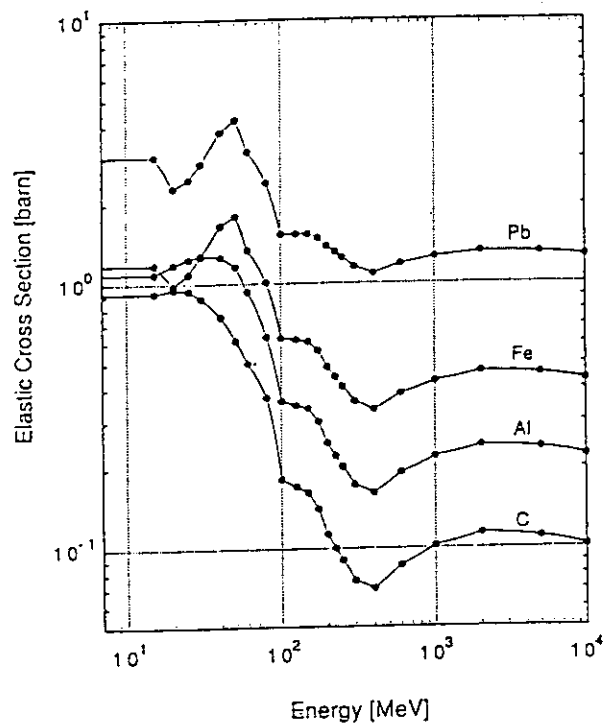


Fig.10.5.3

Dependence of elastic cross sections on the neutron energy for Pb, Fe, Al and C nuclides in the range of 15 MeV to 10 GeV.

10.6 Benchmark Calculations with Intranuclear Cascade Evaporation Model for Intermediate Energy Proton Induced Spallation Reactions

H.Takada, T.Fukahori and N.Kishida*

Nuclear data for the intermediate energy region are useful for the neutronics calculations of such facilities as the spallation neutron sources and the accelerator driven transmutation systems. Because evaluated nuclear data files are not available in this energy region yet except for a few nuclides^{1),2)}, the nucleon meson transport codes (NMTC/JAERI, HETC etc.) are usually employed in the neutronics calculation. The codes simulate the nuclear reaction by the intranuclear cascade³⁾ evaporation⁴⁾ (INCE) model including the high energy fission process⁵⁾ and also calculate the particle transport in a bulk medium at the same time.

From the point of view of estimating the neutronics performances of the system, it is of interest to verify the accuracy of the code on the various quantities relevant to the nuclear reaction in the intermediate energy region. As the first trial, benchmark calculations have been carried out by members of the Theoretical Calculation Code Working Group of the Japanese Nuclear Data Committee.⁶⁾ The proton induced nuclide production cross sections for aluminum, iron and bismuth have been selected as the subject because there were relatively a lot of experimental data in the energy region of 50 MeV to 1 GeV.

The codes NUCLEUS⁷⁾, ALICE-F⁸⁾ and MCEXCITON⁹⁾ were used in this benchmark calculation. NUCLEUS is based on the INCE model and corresponds to the nuclear reaction calculation part of NMTC/JAERI¹⁰⁾ which is employed in the neutronics calculations of the accelerator driven transmutation system in JAERI. The codes ALICE-F and MCEXCITON consist of the preequilibrium analysis part and the evaporation analysis part. For the preequilibrium process, the hybrid and the geometry dependent hybrid model are adopted in ALICE-F. On the other hand, the random walk exciton model is used in MCEXCITON. Major characteristics of the codes are summarized in Table 10.6.1.

In this work, calculations were made without any serious parameter adjustment. The results are given in Fig.10.6.1 to 10.6.3 for $\text{Al}(p,x)^{22}\text{Na}$, $\text{Fe}(p,x)^{52}\text{Mn}$ and $^{209}\text{Bi}(p,4n)^{206}\text{Bi}$, respectively. Roughly speaking, all of the calculated results show the similar tendencies and produce the differences of about a factor of 2 from the experiment in the intermediate energy region. As for the INCE model calculation, it is observed that the model can estimate the proton induced nuclide production with nearly the same accuracy as the preequilibrium and evaporation model in the intermediate energy region. Because the number

* CRC Research Institute Inc.

of experimental data is scarce above 200 MeV, more experimental data are required to investigate the accuracy of the calculation codes.

References

- 1) Pearlstein S.: J. Astrophys., **346**, 1049 (1989).
- 2) Fukahori T. and Pearlstein S.: JAERI-M 91-032 p106 (1992).
- 3) Bertini H.W.: Phys. Rev. **188**, 174 (1969).
- 4) Weisskopf V. F.: Phys. Rev. **52**, 296 (1937).
- 5) Nakahara Y.: Proc. of 4th Meeting of Int. Collaboration on Advanced Neutron Sources (ICANS-IV), KEK, Tsukuba, Japan p286 (1980).
- 6) Fukahori T. et al.: Proc. of 1992 Symposium on Nucl. Data, JAERI-M 93-046, p57 (1993).
- 7) Nishida T. et al.: JAERI-M 86-116 (1986).
- 8) Fukahori T.: JAERI-M 92-039, p114 (1992).
- 9) Kishida N. and Kadotani H.: Proc. Int. Conf. on Nucl. Data for Sci. and Technol. May/June 1988, Mito, Japan, p1209 (1988).
- 10) Nakahara Y. and Tsutsui T.: JAERI-M 82-198 (1982).

Table 10.6.1 Summary of the characteristics of calculation codes.

ITEMS	NUCLEUS	MCEXCITON	ALICE-F
Method	Monte-Carlo	Monte-Carlo	Analytic
INC Model	Yes	No	No
Direct Process	No	No	No
Preequilibrium	No	Random Walk Exciton Model	Hybrid Model, GDH
Equilibrium	Weisskopf-Ewing	Weisskopf-Ewing	Weisskopf-Ewing
Total Level Density	$\exp[2\sqrt{a(E-\Delta)}]$	$\exp[2\sqrt{a(E-\Delta)}]$	Fermi gas, Ramamurthy, Liquid Drop
p-h Level Density	Williams	Williams	Williams
Discrete Level	No	No	No
Angular Distribution	No	Phase-Space Approach	Pearlstein, Kalbach-Mann, Kalbach Syst.
γ -Emission	No	No	Yes
Other Functions	Fission	Recoil Energy Spectra of Residual Nuclei	Fission

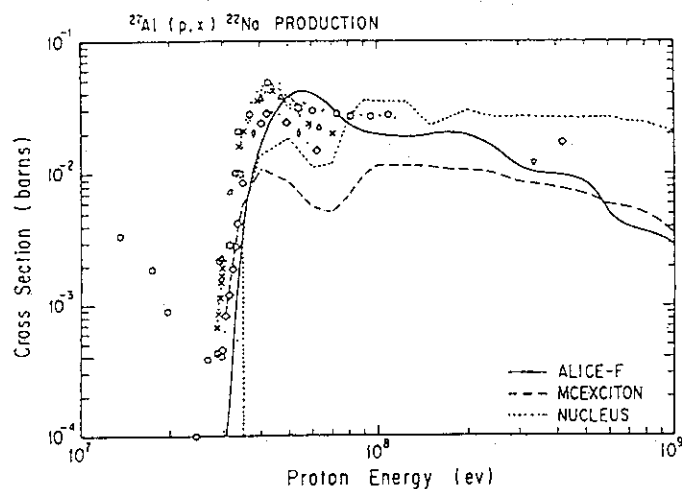


Fig.10.6.1 Cross section of the $\text{Al}(p,x)^{22}\text{Na}$ reaction. Ponit marks stand for the experimental data. The solid, the dashed and the dotted lines indicate the calculated results of ALICE-F, MCEXCITON and NUCLEUS, respectively.

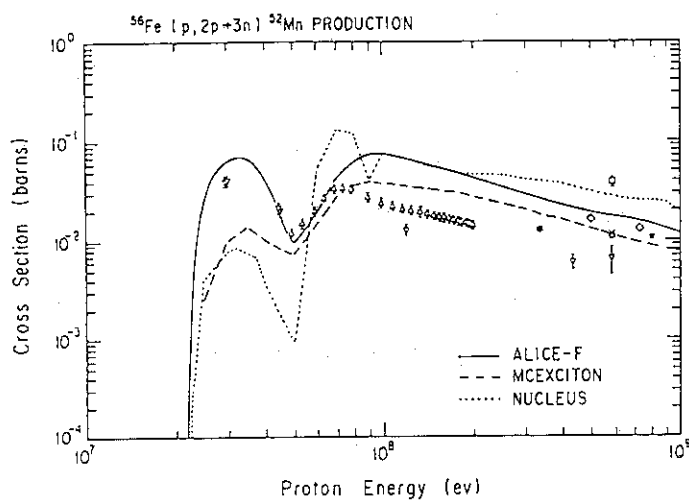


Fig.10.6.2 Cross section of the $\text{Fe}(p,x)^{52}\text{Mn}$ reaction. The marks are same as in Fig.10.6.1.

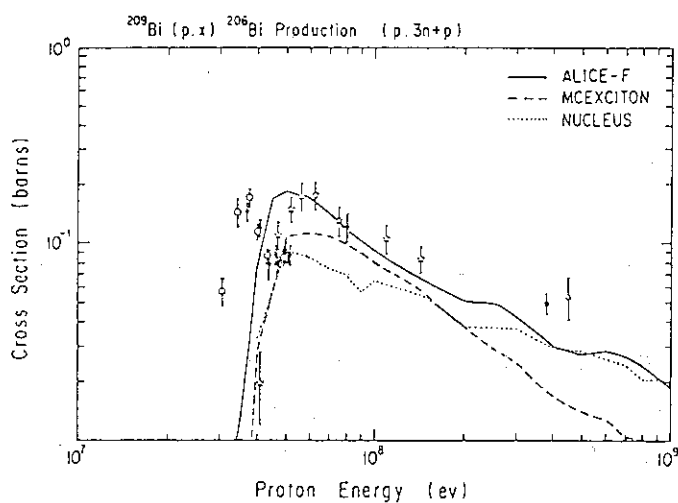


Fig.10.6.3 Cross section of the $^{209}\text{Bi}(p,x)^{206}\text{Bi}$ reaction. The marks are same as in Fig.10.6.1.

10.7 Integral Spallation Experiment with a Lead Assembly Irradiated with 500 MeV Protons

H. Takada, S. Meigo, K. Hasegawa, T. Sasa, M. Mizumoto,
M. Takeuchi, T. Ono and H. Yasuda

An integral spallation experiment with a lead assembly¹⁾ was performed using the 500 MeV booster proton synchrotron facility at National Laboratory for High Energy Physics. The tungsten target of 16 cm in diameter and 30 cm in length was installed in the assembly. In order to study the transport of the spallation neutrons in the assembly, the activation method with the high purity metallic samples of Fe(99.99%), Ni(99.9%) and Cu(99.99%) were employed. The samples were put into the metallic capsule of 50 cm in length and inserted in the lead assembly at the position of 0, 3, 6, 10, 15, 20 and 25 cm in the radial distance, r , along the proton beam axis, z . The capsule has the outer diameter of 9.4 mm with the thickness of 0.5 mm. In order to suppress the particle streaming through the samples as low as possible, the lead dummy samples were also used so that activation samples occupied only 10 to 20% of the entire space in the capsule. The numbers of induced reactions were obtained by measuring γ -rays with a 100 cc Ge-detector.

A preliminary calculation was made with the nucleon meson transport code NMTC/JAERI²⁾ assuming the assembly to be a uniform cylinder. In the calculation, the assembly was divided into some meshes in the r - z cylindrical geometry. The mesh interval corresponding to the position of samples was 2 cm in radial distance and 5 cm in axial one. The nuclide yields in the samples were estimated by multiplying the value of the neutron flux and the nuclide production cross section. Because there are few available evaluated nuclide production cross sections for the neutron induced reaction in the energy region above 20 MeV, we have calculated the cross sections with the code NUCLEUS³⁾ which is equivalent to the nuclear reaction calculation part of NMTC/JAERI.

The calculated nuclide yields in the case of the tungsten target are shown as a function of the axial position in Figs.10.7.1 and 10.7.2 for ${}^{\text{nat}}\text{Ni}(n,x){}^{57}\text{Ni}$ and ${}^{\text{nat}}\text{Ni}(n,x){}^{52}\text{Mn}$, respectively. It is seen that the calculated results reproduce well the experimental nuclide yield distributions in the radial position of 6 to 20 cm.

The comparison was also made on the nuclide yields in the case of the lead target. The nuclide yields are shown in Figs.10.7.3(a) and (b) for the copper sample inserted at 24 cm in depth on the axis. The results for the iron sample are shown in Fig.10.7.4. Because the 500

MeV proton was injected on the target surface which was located in the depth of 20 cm from the front surface of the assembly, the contribution of the proton induced spallation reaction was dominant in this position. It is observed that the calculated results agree with the experimental ones with a factor of 2 to 3. From the benchmark calculations⁴⁾, it was found that there existed the differences of a factor 2 to 3 between the value of the nuclide production cross sections calculated with NUCLEUS and the experimental ones. Consequently, the ambiguity included in the code seems to be imposed on the results seen in Figs.10.7.3(a), (b) and 10.7.4.

References

- 1) Takada H., et al.: JAERI-M 91-138, 232(1991), JAERI-M 92-039, 1(1992).
- 2) Nakahara Y. and Tsutsui T.: JAERI-M 82-198 (1982).
- 3) Nishida T. et al.: JAERI-M 86-116 (1986).
- 4) Fukahori T.: JAERI-M 92-039, p114 (1992).

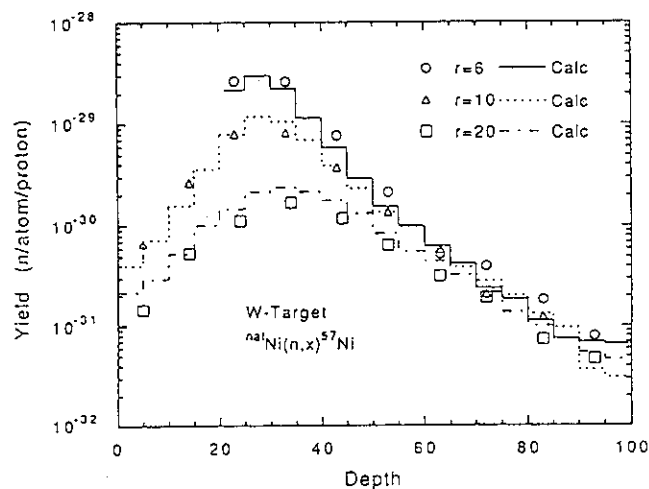


Fig.10.7.1 Comparison between the calculated and the experimental results of the yields of ^{57}Ni in the nickel samples for 500 MeV proton incident on the tungsten target installed in the lead assembly. The open marks indicate the experimental data and the lines represent the calculated results.

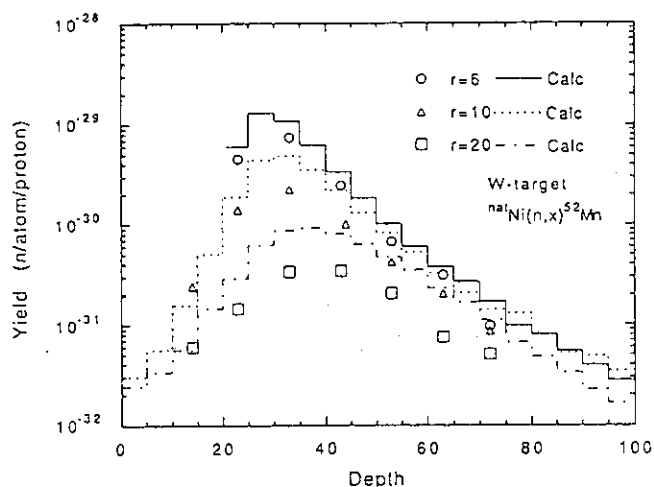


Fig.10.7.2 Comparison between the calculated and the experimental results of the yields of ^{52}Mn in the nickel samples for 500 MeV proton incident on the tungsten target installed in the lead assembly. The open marks and lines are same as in Fig.10.7.1.

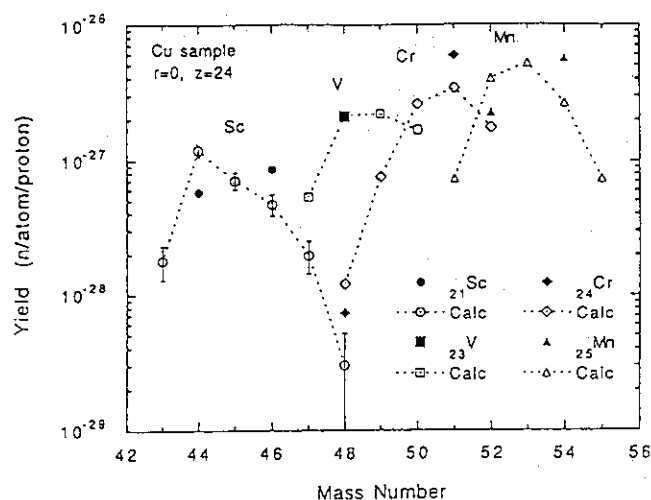


Fig.10.7.3(a) Yields of the nuclides with $21 < Z < 26$ produced in the copper sample placed at 24 cm on the axis for 500 MeV proton incident on the lead target installed in the lead assembly. The solid marks indicate the measured data. The open marks represents the calculated results.

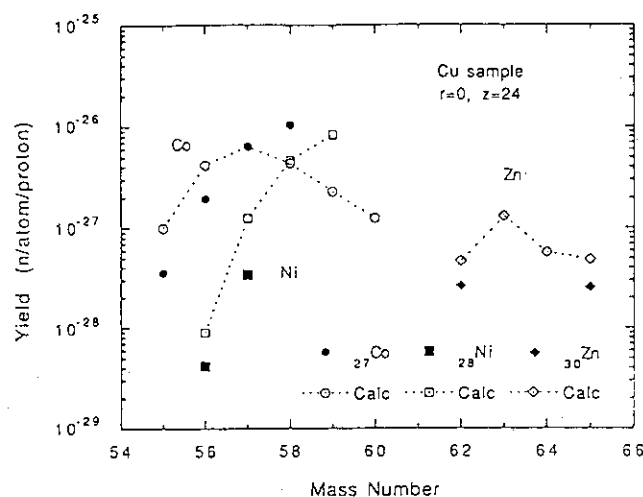


Fig.10.7.3(b) Yields of the nuclides with $27 < Z < 30$ produced in the copper sample placed at 24 cm on the axis for 500 MeV proton incident on the lead target installed in the lead assembly. The marks are same as in Fig.10.7.3(a).

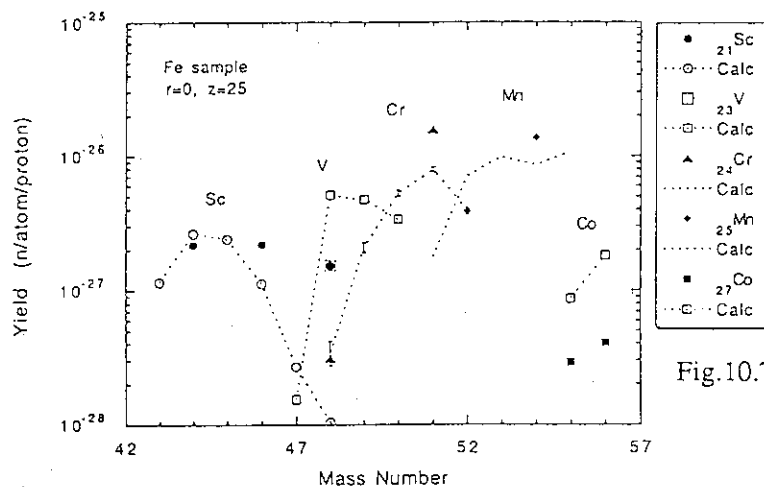


Fig.10.7.4 Yields of the nuclides produced in the iron samples placed at 25 cm on the axis for 500 MeV proton incident on the lead target installed in the lead assembly. The marks are same as in Fig.10.7.3(a).

10.8 Neutron Measurement for (p, xn) Reaction with Protons of GeV Range

S.Meigo, H. Takada, S.Chiba, K.Ishibashi*, T.Nakamoto*, N.Matsufuji*, K.Maehata*, S.Sakaguchi*, Y.Wakuta*, Y.Watanabe**, M.Numajiri***, Y.Yoshimura***, Y.Matsumoto† and T.Nakamura††

The neutron-emission cross section for the reaction (p,xn) by the proton in GeV region is required to ensure and improve the nucleon-meson transport calculation codes, such as NMTC and HETC, which are used for the neutronics calculation of the accelerator driven transmutation. Systematic data covering many targets have not been taken in the energy region above 800 MeV yet. Therefore the present experiment¹⁾ has been carried out with the targets of C and Pb using 0.8, 1.5 and 3 GeV protons which are supplied by the π 2 beam line at National Laboratory for High Energy Physics (KEK).

The time of flight (TOF) method was used to measure neutron spectra from the target. The thickness of the target was 10 cm for C and 1.2 cm for Pb, respectively. The NE-213 scintillators with two kinds of sizes ($\phi 5'' \times 5''$ and $\phi 2'' \times 2''$) were employed as neutron detectors. The larger detectors were used for making the neutron-detection efficiency as high as possible, in spite of a rather poor time resolution in the TOF measurement. The smaller ones exhibited the good neutron-gamma pulse-shape discrimination even in the neutron energy region below 1 MeV.

The experimental arrangement is illustrated in Fig. 10.8.1. The beam intensity of the proton was at a level of 10^5 particles/2.5 sec. Because the protons were obtained as the secondary particles generated by an internal target placed in the accelerator ring of the 12 GeV proton synchrotron, it was necessary to distinguish protons from pions by a pair of TOF scintillators (Pilot U) located at a separation distance. Incident particles were easily counted one by one by TOF scintillators. The time resolution was 0.35 nsec, and the 3.0 GeV proton was well discerned from the pion with a separation time of 1.7 nsec. Because of the low beam intensity, the flight path of the neutron TOF was limited to short distances. It was 1 to 1.5 m for $\phi 5'' \times 5''$ detectors, and 0.6 to 0.9 m for $\phi 2'' \times 2''$ ones. Veto plastic scintillators were installed in front of all neutron detectors in order to find charged-particle events in the neutron detectors.

The block diagram of the measurement circuit is shown in Fig. 10.8.2. When the

* Department of Nuclear Engineering, Kyushu University

** Department of Energy Conversion, Kyushu University

*** National Laboratory for High Energy Physics (KEK)

† Department of Management Information, Kyushu Teikyo Junior College

†† Cyclotron RI Center, Tohoku University

incident-beam coincidence took place at all the beam scintillators, the pulse with a typical width of 150 nsec was sent to the next coincidence module. Then, the signals of neutron detectors were accepted by this module for 150 nsec. The neutron-gamma pulse-shape discrimination was carried out by the two gate integration method. This method achieved the better neutron-gamma separation than the zero-cross method²⁾ for the wide neutron energy range. In this method anode signals of the photomultiplier were input into charge ADC's worked by different gate pulses. The ADC1 with the fast gate converted the initial peak of the photomultiplier signal, whereas the tail gate made ADC2 to accept only the slow tail portion thereof. The detection efficiency of the neutron detectors was calculated by the use of the Cecil code³⁾ of the Kent State University version.

The experimental data at 0.8 GeV are compared with those of LANL⁴⁾ in Fig.10.8.3. The present preliminary DDX agrees with the LANL data within 10 %. Further checks and corrections are in progress on such items as the detection efficiency and the multiple scattering effects in the target itself.

References

- 1) Ishibashi K., et al. : JAERI-M 93-046 p.82 (1992).
- 2) Plischke P., et al. : Nucl. Instrum. Meth., **139**, 579 (1976).
- 3) Cecil R.A., Anderson B.D. and Madey R. : Nucl. Instrum. Meth., **161**, 439 (1979).
- 4) Amian W., et al. : Nucl. Sci. Eng., **112**, 78 (1992).

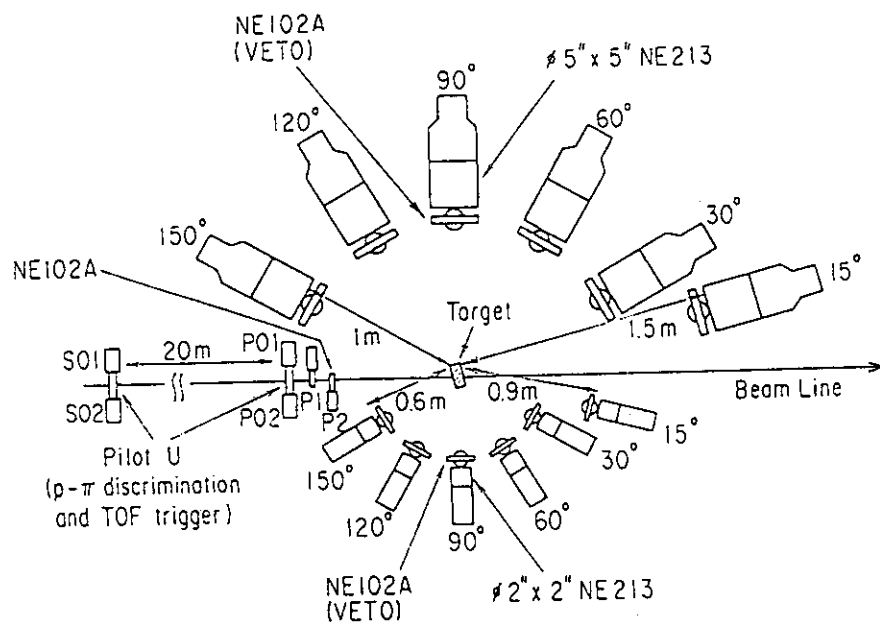


Fig.10.8.1 Illustration of the experimental arrangement.

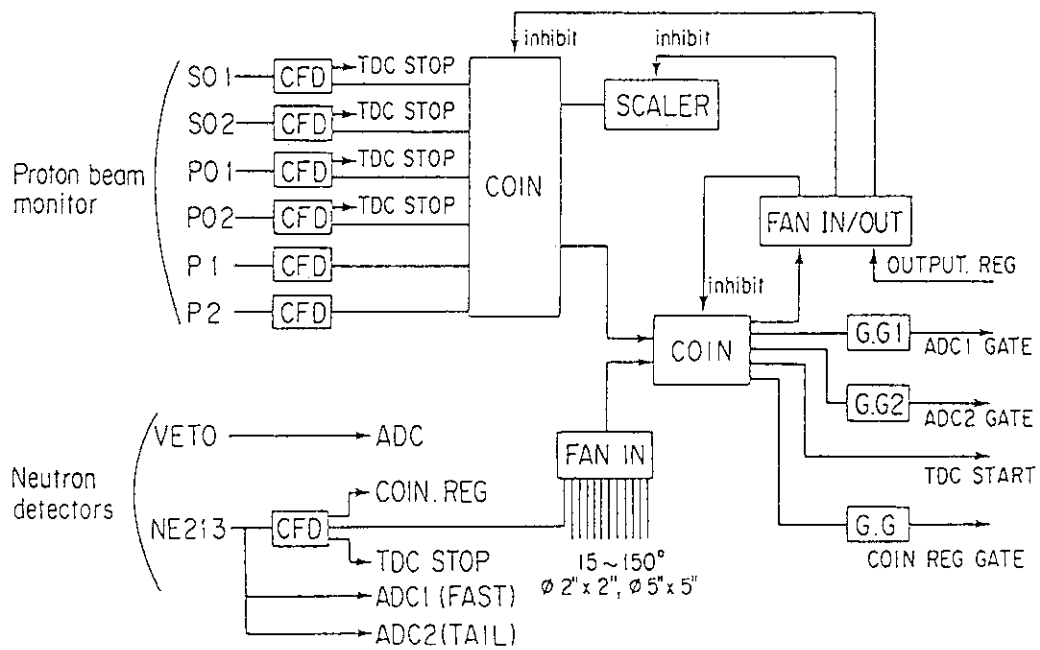


Fig.10.8.2 Block diagram of the electronics system.

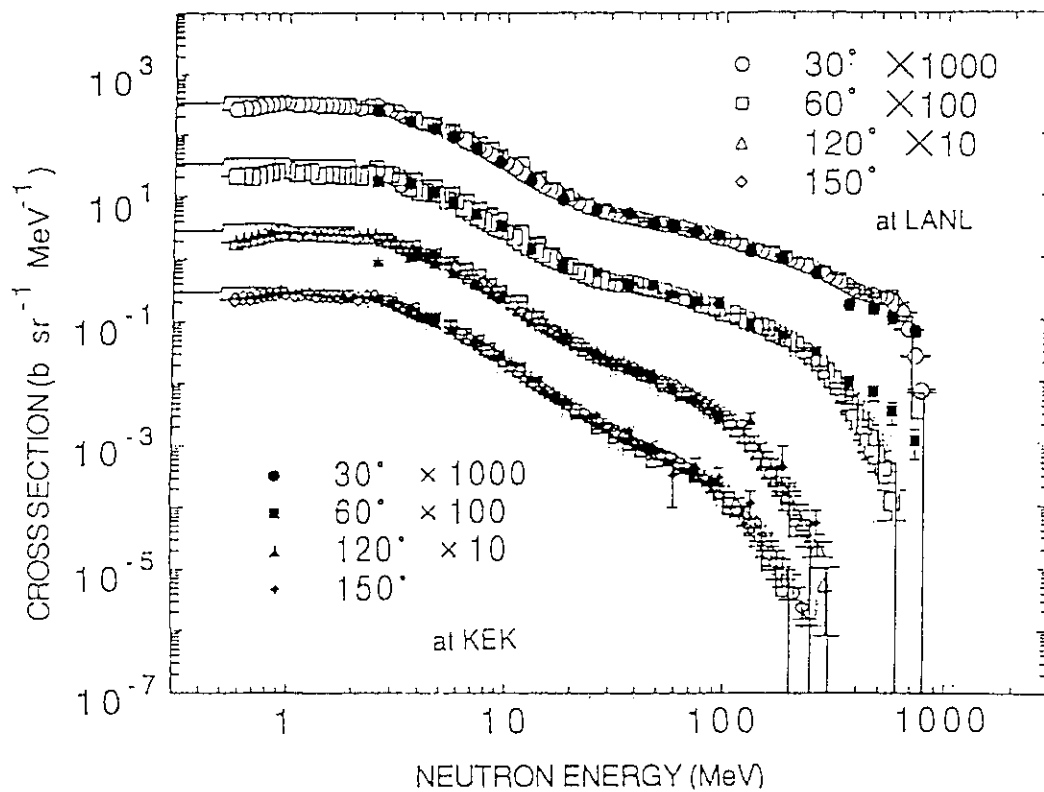


Fig.10.8.3 Double differential cross sections at 0.8 GeV for Pb, presented together with the results of LANL.

10.9 Neutronics and Thermal Hydraulics Calculations of Targets for the Proton Accelerator Driven TRU Transmutation System

S.Meigo, T.Takizuka, H.Takada and T.Nishida

Accelerator based incineration system is considered one of the candidates for the disposal schemes of long-lived transuranic nuclides (TRU). At JAERI, conceptual design studies have been made on the subcritical fast reactor driven by a 1.5 GeV proton accelerator¹⁾²⁾. In the core, proton beam is injected on the tungsten target surrounded by the pin bundle type metal alloy fuel. Both the tungsten target and the fuel pin are cooled with the liquid sodium. The neutronics and the thermal hydraulics calculations were made on the tungsten target to establish the feasible target design.

At first, we estimated the neutron yield dependent upon the configuration of the target. The following 3 types of the configuration were chosen; (a) Smeared geometry, (b) Disk geometry and (c) Pin geometry. The schematic view of the targets are illustrated in Fig.10.9.1. The target dimensions are 40cm in diameter and 130 cm in length. The volume ratio of the tungsten and sodium is assumed to be 1:1. Neutronics calculation was made on the condition that the 1.5 GeV proton beam was of uniform circular profile with the 40 cm diameter. In this calculation, a Nucleon Meson Transport Code NMTC/JAERI³⁾ was employed to simulate the spallation reaction and the particle transport for energies above 15 MeV in the target. MORSE-DD⁴⁾ was also employed to calculate neutron transport up to 15 MeV.

The calculated neutron yield from each geometry is indicated in Table 10.9.1. Figure 10.9.2 shows the lateral distribution of neutrons emitted from the cylindrical surface of the target. The disk geometry was chosen for the target because it gave the best neutron yield of all.

Secondary, the thermal hydraulics calculation was made to determine the size of the cooling channel in the tungsten disk. In the calculation, the heat conductivity and the heat transfer were estimated with the assumption that the simplified coolant flow was formed along the cooling channel. The conditions employed in the calculation are summarized in Table 10.9.2.

The specifications of the target were established based on the results of the neutronics and the thermal hydraulics calculations. The schematic view of the target is shown in the Fig.10.9.3. The lateral variation in the disk thickness can make relatively flat neutron distribution, as shown with the diamonds in Fig.10.9.2. The diameter of the cooling channel in each disk is 9 mm. The channel pattern of successive disks is a staggered arrangement such that the

proton beam which passes through channels should hit the next disk. This target produces 29.3 neutrons per proton and withstands the heat deposition of incident proton up to 68 mA. In order to estimate the total performance of the transmutation system, further study including the fuel region is in progressing.

References

- 1) Takizuka T., et al., "A study of Incineration Target System" : Proc. 5th Int. Conf. Emerging Nucl. Systems(Karlsruhe, 1989).
- 2) Takada H., et al. : JAERI-M 91-138 p226(1991).
- 3) Nakahara Y., Tsutsui T. : JAERI-M 82-198 (1982) .
- 4) Nakagawa M., et al. : JAERI-M 84-126(1984).

Table 10.9.1. Yield of the neutrons emitted from the target.

Geometry	Smeared	Disk	Pin
Neutrons /proton	34.3	35.3	26.8

Table 10.9.2. Conditions employed in the thermal hydraulics calculation.

Coolant conditions		Cooling channel condition	
Inlet temperature	<603K	Maximum temperature	<950K
Outlet temperature	<703K		
Flow speed	<8m/s		
Pressure depletion	<250kPa		

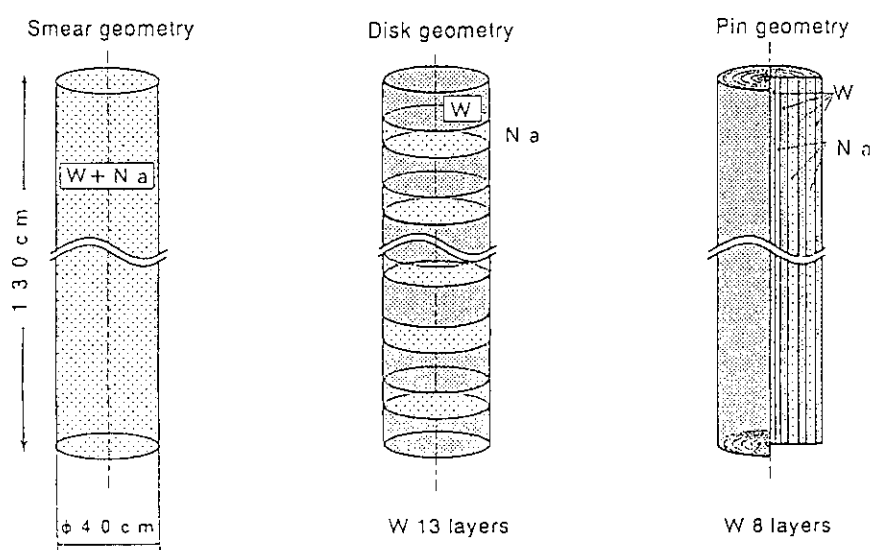


Fig.10.9.1 Target configurations were employed in the neutronics calculation.

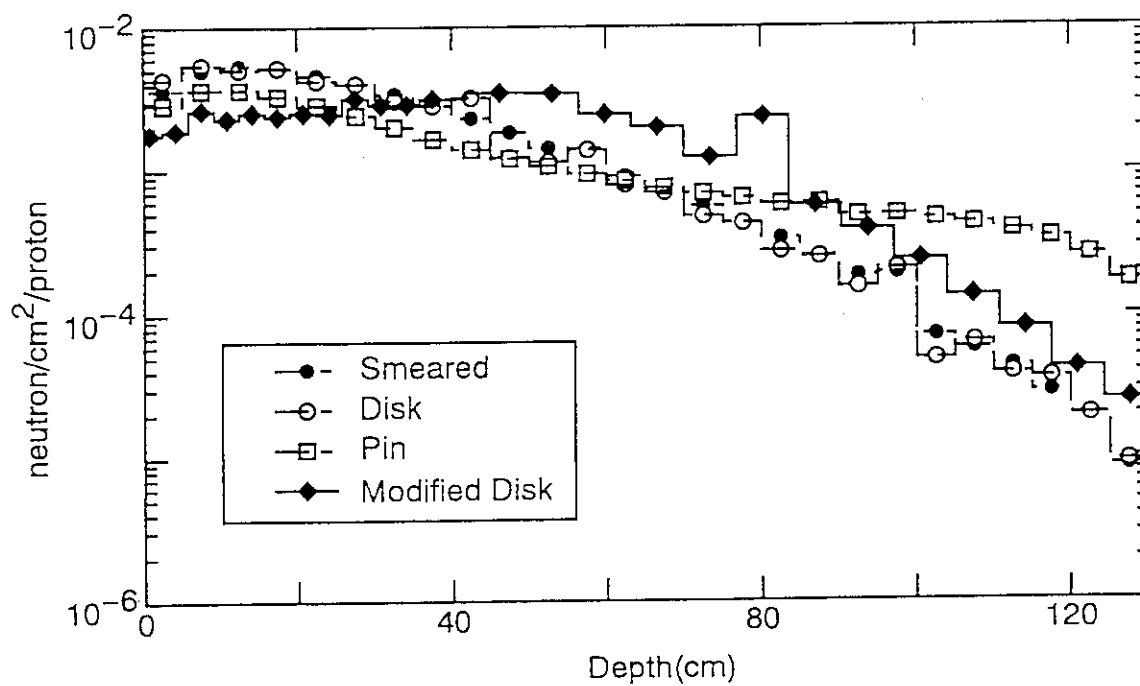


Fig.10.9.2 Flux distributions of the neutron emitted from the cylindrical surface.

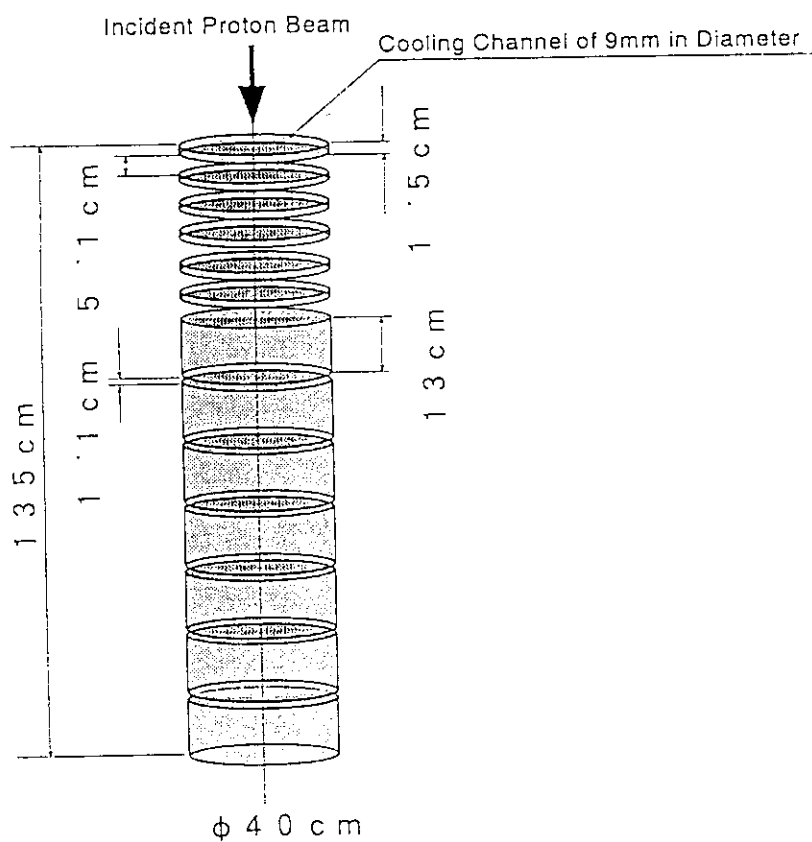


Fig.10.9.3. Tungsten target designed for the accelerator driven incineration system.

10.10 Conceptual Design Study on Accelerator-driven Minor Actinide Transmutation System

H. Takada, T. Takizuka, T. Nishida, S. Meigo, Y. Kato, H. Katsuta and M. Mizumoto

In improving the Minor Actinide(MA) alloy fuelled transmutation core, the nuclear design study for the target, which consists of tungsten disc layers, has been made to generate more effectively the spallation neutrons in the target than those in the former pin-bundle type target as reported in 10.9. Based on thermal hydraulic calculations the disc has been designed to have 19 holes, through which the sodium coolant flows up, with a diameter of 11.9 mm and a pitch of 15.4 mm under the condition of keeping the temperature at the hot spot in the target below the allowable temperature 650 °C(Fig. 10.10.1). It is proposed from the present work that the disc-type target assembly is fixed in a wrapper tube. That is because the pressure drop through this assembly would become relatively larger than the one in the pin-bundle type fuelled core. When the coolant flow rate through the target is controlled to cause the same order of pressure drop as one in the core, the coolant velocity becomes about 6.6 m/s. Then the coolant has the sufficient ability to completely remove the heat deposited in the discs.

On the other hand, the rough estimation of the shielding thickness for the high energy particles from the target and the core in the MA metal fuel transmutation system have been made to ascertain the realization of the accelerator-based transmutation system as an engineering plant from the point of view of hazard. The allowable maximum value of the dose rate, which we should keep, is 6.25 $\mu\text{Sv/h}$ (for the non-controlled region) outside the shielding structure covering the system. The cascade process calculations using the NMTC/JAERI code¹⁾ showed that when the proton beams with 1.5 GeV, 39 mA and 800 MeV, 87 mA injected on the target in the core, neutrons of $2.39 \times 10^{16}\text{n/sec}$ and $1.80 \times 10^{16}\text{n/sec}$ with the energy above 100 MeV are leaked out from this transmutation core respectively. The thicknesses of the ordinary concrete (2.3 g/cc), the heavy concrete (4 g/cc) and the iron (7.84 g/cc) materials for shielding these high energy neutrons were calculated by solving the equations such as Tesch's and Moyer's ones for the simplified neutron source (a uniform cylinder). The thicknesses requested for the ordinary concrete, the heavy concrete and iron have been determined 1300~1450 cm, 850~970 cm, 520~590 cm, respectively. These data have been compared with the heavy concrete thickness of ~ 600 cm which is given under the permissible dose rate 25 $\mu\text{Sv/h}$ outside the radial shielding around the accelerator at LAMPF

²⁾, where the proton linac with 800 MeV and 1 mA is being operated at present. Both JAERI and LANL data show relatively the good agreement because the LAMPF value recalculated for our condition of 87 mA and 6.25 μ Sv/h is about 830 cm.

The code system SPACE has been extended to examine the burnup and transmutation characteristics of the accelerator-based MA alloy transmutation system. The one group cross section libraries of actinides for the burnup calculation in Table 10.10.1 have been produced by degenerating the 295 group JSSTD cross section libraries with the neutron spectra computed by one dimensional transport code ANISN. The new version of the burnup code COMRAD was prepared to speed up the computation.

The conceptual design study of an accelerator based MA molten salt transmutation system ³⁾ has been performed on the heat balance between the core and the heat exchanger. This system has the core with 170 cm in height and 105 cm in radius and the stainless steel reflector with the thickness of 20~40 cm, including the inner heat exchanger to reduce the MA inventory as reported in the last Annual report⁴⁾. The MA chloride molten salt NaCl-MA Cl_3 (64-36 mol%, 453°C: melting point) with the higher solubility of MA acts as a target and fuel salts and as the primary coolant in this system and the fluoride molten salt NaBF $_3$ -NaF is selected as the secondary coolant. The heat removed from the core by the compact heat exchanger, which is installed just outside the active region of the core, is too small on comparison to thermal power 800 MW generated when MA~250 kg/y from ten units of 3 GWt LWR is transmuted. So in this design study the temperatures 650°C/550°C at hot/cold legs on the primary cooling system have been changed to 720°C/570°C respectively, while the corresponding temperatures 600°C/500°C in the secondary cooling system have been changed to 580°C/500°C. The plate-fin type compact heat exchanger was adopted to have the heat conducting area wider than 100 m² per m³. Three cold-leg type pumps, which are axial flow type ones, are arranged among three heat exchangers as shown in Fig. 10.10.2.

References

- 1) Nakahara Y. and Tsutsui T. : JAERI-M 82-198 (1982).
- 2) Cochran D. R. F. et al. : CONF -651109 (LA-DC-7522).
- 3) Kato Y., et al. : Proc. OECD/NEA Specialist Meeting of Accelerator-based Transmutation (1992).
- 4) Takada H., et al. : JAERI-M 92-125, p.221(1992).

Table 10.10.1

One group cross sections for actinides

No.	nuclide	1G cross section	
		fission	(σ , γ)
1	^{232}Bi	0.0	$3.81891\text{E}-3$
2	^{232}Th	$1.87832\text{E}-2$	$7.90494\text{E}-1$
3	^{231}Pa	$2.88055\text{E}-1$	$1.05396\text{E}+0$
4	^{232}U	$2.01400\text{E}+0$	$1.34495\text{E}-1$
5	^{233}U	$2.31354\text{E}+0$	$1.90150\text{E}-1$
6	^{234}U	$4.59225\text{E}-1$	$3.56662\text{E}-1$
7	^{235}U	$1.53459\text{E}+0$	$3.76665\text{E}-1$
8	^{236}U	$1.66707\text{E}-1$	$2.89453\text{E}-1$
9	^{238}U	$7.55165\text{E}-2$	$2.13378\text{E}-1$
10	^{237}Np	$4.77271\text{E}-1$	$9.93841\text{E}-1$
11	^{238}Np	$1.74019\text{E}-1$	$2.57555\text{E}-2$
12	^{239}Np	$6.41264\text{E}-1$	$1.16634\text{E}+0$
13	^{236}Pu	$8.71822\text{E}-1$	$6.11663\text{E}-1$
14	^{237}Pu	$3.27345\text{E}+0$	$1.24686\text{E}-1$
15	^{238}Pu	$1.22739\text{E}+0$	$4.08971\text{E}-1$
16	^{239}Pu	$1.67862\text{E}+0$	$2.79550\text{E}-1$
17	^{240}Pu	$5.14387\text{E}-1$	$3.55312\text{E}-1$
18	^{241}Pu	$2.07378\text{E}+0$	$3.26694\text{E}-1$
19	^{242}Pu	$3.90294\text{E}-1$	$2.97399\text{E}-1$
20	^{243}Pu	$7.41536\text{E}-1$	$2.26553\text{E}-1$
21	^{241}Am	$4.27689\text{E}-1$	$1.09733\text{E}+0$
22	^{242}Am	$2.57420\text{E}+0$	$4.55428\text{E}-1$
23	^{242m}Am	$2.56066\text{E}+0$	$3.83988\text{E}-1$
24	^{243}Am	$3.21913\text{E}-1$	$9.81039\text{E}-1$
25	^{244}Am	$2.57477\text{E}+0$	$6.78106\text{E}-1$
26	^{242}Cm	$8.90337\text{E}-1$	$3.10913\text{E}-1$
27	^{243}Cm	$2.45447\text{E}+0$	$2.46459\text{E}-1$
27	^{244}Cm	$5.81983\text{E}-1$	$4.39389\text{E}-1$
29	^{245}Cm	$2.19856\text{E}+0$	$2.52544\text{E}-1$
30	^{246}Cm	$4.08702\text{E}-1$	$2.01636\text{E}-1$
31	^{247}Cm	$2.07302\text{E}+0$	$3.47057\text{E}-1$
32	^{248}Cm	$4.28751\text{E}-1$	$1.64859\text{E}-1$
33	^{249}Cf	$2.07487\text{E}+0$	$3.98412\text{E}-1$
34	^{250}Cf	$6.48432\text{E}-1$	$3.91375\text{E}-1$
35	^{251}Cf	$2.50411\text{E}+0$	$1.89027\text{E}-1$
36	^{252}Cf	$1.50314\text{E}+0$	$1.97775\text{E}-1$

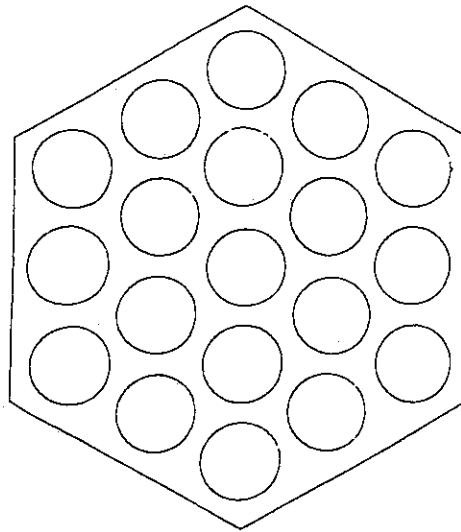


Fig.10.10.1

Arrangement of flow holes on a tungsten disc in the target

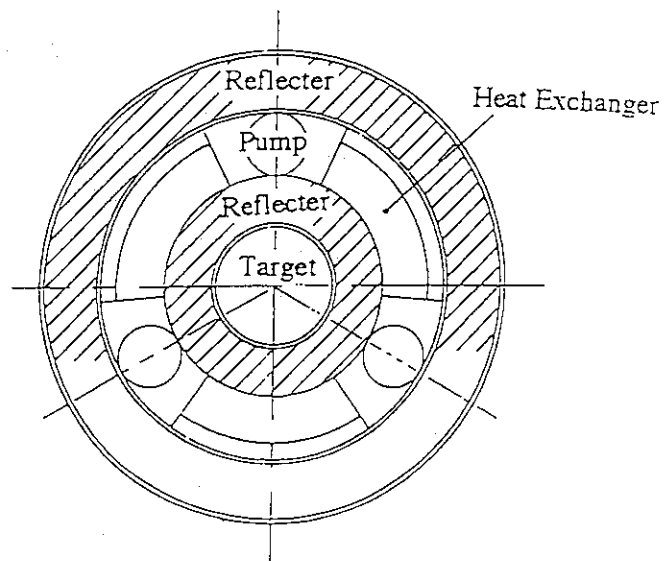


Fig.10.10.2

Cross section of the MA molten salt transmutation core.

11. Facility Operation and Technique Development

Operations of four reactor engineering facilities were carried out as scheduled, such as Fast Critical Assembly (FCA), Very High Temperature Critical Assembly (VHTRC), Fusion Neutron Source (FNS) and Heat Transfer and Liquid Flow Facility. Main activities of each facility covered in this period are summarized briefly below.

- (1) FCA was operated according to various purposes of experiments, and recored the opration time of 685 hours. As for maintenance activities, besides annual and monthly inspections, the cooling system was overhauled and the surveylance system in the reactor room was renewed. In connection with safeguards, monthly inspections and the physical inventory verification were carried out without problem by IAEA and STA.
- (2) VHTRC was operated as scheduled for experiments aiming at the verification of the calculation accuracy for HTTR, and recorded the operation time of 246 hours. As for a maintenance activity, two neutron absorption rods were fabricated newly to assure safety of the facility. A counter drive mechanism and a data base network system were equiped for improvement of experiment efficiencies.
- (3) FNS was operated as scheduled according to various requirements of experiments including bulk shielding experiments for the ITEA R/D program, and recorded the operation time of 608 hours. In those operations, used ten small-sized and two large-sized targets of which nominal tritium activity was 3.7×10^{11} Bq (10 Ci) and 2.96×10^{13} Bq(800 Ci), respectively. Exhaust tritium gas in the use of those targets was processed in safe by the tritium absorption plant (TAP). As for technique developments, improvement of cooling performance of a target disk was continued, and a development was commenced to establish the optimum structure for vacuum seals of a high speed rotating target.
- (4) Heat Transfer and Liquid Flow Facility was operated for various experiments such as critical heat flux tests using the high pressure small loop, two-phase fluid flow tests and subchannel fluid mixing tests. Because all tests have terminated using the facility, Large-scaled Reflood Test Facility was disassembled completely in order to establish newly a multi-dimensional fluid flow mock-up loop.

(Akio Ohno)

11.1 Operation Report of FCA

K. Satoh, A. Ohno, K. Hayasaka, H. Sodeyama, K. Kurosawa and H. Watanabe

The FCA XVI-2 and XVII-1 cores were assembled to obtain benchmark data on the "Metallic Fuel FBR" core. Operations have been performed as scheduled, without any major trouble.

Operations of 101 times were carried out in 81 days. No scram was recorded during the operations. The total operating time was 685 hours and the integrated power 5695.68 Wh. A total number of 4746 criticality operations has been recorded at the end of this fiscal year since the first achievement of criticality on 29 April 1967. Following to the safety regulation for operation, two days were devoted to the monthly inspection and about 10 weeks to the annual inspection from March in 1992 year. Routine maintenance activities were done in these days to provide maximum operation days for the experiments.

As for maintenance activity, the core cooling device which have been used over 10 years was overhauled. Bearings of motor were renewed. On March 1993, number of TV cameras was increased to make better observational capacity in the reactor room. Some of detection part in the physical protection system (P-P) were also renewed, and their sensitivity and the functions were examined and calibrated.

In connection with safeguards, IAEA and NSB(*) carried out monthly inspection under the international treaty. The physical Inventory Taking (PIT) of the fuels was performed from June 16 to June 19 by means of item counting, weighing and non-destructive assay. IAEA and NSB made the physical Inventory Verification (PIV) from June 22 to June 26. No anomaly was confirmed.

(*)NSB : Nuclear Safety Bureau

11.2 Operation Report of VHTRC

S. Fujisaki, M. Takeuchi, T. Ono, M. Seki and H. Watanabe

The VHTRC-6 and VHTRC-4 cores were assembled to obtain experimental data for the verification of the HTRR design accuracy. The operations for this purpose were completed as scheduled without any problems disturbing execution of the experiment.

Main experiment items were power distribution measurements of VHTRC-6 and VHTRC-4 cores and preliminary measurements of thorium fuel reactivity worth at the VHTRC-4 core.

The results of the operation were as follows;

- 1) Operations of 163 times in 48 days,
- 2) Critical operations of 159 times,
- 3) Total operation time of 246 hours,
- 4) Integrated power of 143 WH.

No scram was recorded during the operations. The integral operation time is 3,375 hours at the end of this fiscal year since the first achievement of criticality on May 13, 1985.

According to the safety regulation for operation, one day was devoted to the monthly inspection and about 8 weeks to the annual inspection from September to November.

The major activities relating to the maintenance were as follows;

- 1) Installation of the newly two neutron absorption rods for the control and safety rod drive mechanism which were made at this fiscal year,
- 2) Continuation of the data base work relating to the operation and the experiment data,
- 3) Development of the axial counter drive mechanism for reaction rate distribution measurements.

As for fuel management, Physical Inventory Taking (PIT) was carried out by item-counting each fuel rod. IAEA and NSB made the Physical Inventory Verification (PIV) under the international treaty on May 11. No anomaly was confirmed. The maintenance activity was also taken on the physical protection(p-p) system. The sensitivity and function of the system were examined and calibrated.

11.3 Operation Report of FNS

S. Tanaka, J. Kusano, C. Kutsukake, Y. Abe, M. Seki, H. Watanabe

General Accelerator Operation

Operation of the Fusion Neutronics Source (FNS) has been carried out to execute a variety of experiments and a series of bulk shielding experiments relevant to ITER R&D, as scheduled without serious trouble. The total operation time was 608 hours in this fiscal year.

Inspections of the control circuit of the accelerator were performed as the regular maintenance work every four month. A part of the pneumatic control system for ion sources was replaced with a fiber optic cable control system. The beam profile monitor with nitrogen gas cooling system was replaced with an electronic cooling system. It was essential because the parts of former system was not available. The inside of cooling pipe made of copper was cleaned chemically. After this work, the flow of cooling water increased by 30 % or more.

Tritium Handling

Ten pieces of tritium targets with 370 GBq per piece were used for experiments at the 80° beam line. Two pieces of tritium targets with 24 TBq per piece were used for heavy irradiation experiments and a nuclear heating measurement at the 0° beam line. The works for target exchange are conducted with a special care to avoid any contamination of tritium.

A total amount of 3.9 TBq tritium in exhaust gas from the vacuum system of the accelerator was processed by the Tritium Adsorption Processor (TAP) system. A total amount of 390 MBq tritium was released to environment from stack. A thermocouple in the catalyzer tube was replaced to make proper temperature indication. Radioactive wastes born in the irradiation experiments and tritium target handling as well as the used tritium target were canned in order to be transferred to the waste processing facility.

Development

The tritium targets were delivered for the first time from VALDUC center of France Commissariat a L'Energie Atomique. They were tested in terms of neutron generation rate and life-time. It was found that some of those exhibited very poor neutron yield and extreme short lives. Further investigation is under way to develop a new tritium target. An experiment on depth profile of tritium reduction was performed to investigate basic tritium target characteristics. The result is reported in this annual report 5.8. In addition, an R&D for advanced target substrate has been continued on a new cooling system with complex coolant channels. Several tests were made to realize good bonding between the target disk and another disk with coolant channels. So far, the vacuum diffusion technique was applied. An electroplating method is under consideration.

11.4 Operation Report of Heat Transfer and Fluid Flow Facility

K. Nakajima, H. Watanabe and H. Watanabe

In FY-1992, operating management of the Heat Transfer and Fluid Flow Facilities has been performed without any major troubles.

For the operations of the test facilities, following three tests have been performed;

- 1) Subchannel Fluid Mixing Test
- 2) Two-phase Fluid Flow Test
- 3) Critical Heat Flux Test with both High Pressure Small Loop and Neutron Radio Graphy Loop

For the maintenance of the test facilities, the annual inspections of the pressure vessels located in both of Large Scale Reflood Test building and Chemical/Mechanical Engineering building have been carried out for 1st-class pressure vessels etc.. As a result, those pressure vessels have passed the inspection by the Labor Standards Office.

The works on the disassembling and the removal of the Large Scale Reflood Test Facility have been finished, and the audit by the government authorities has been carried out. On the remained site, the Multi-Dimensional Fluid Flow Mock up Loop is being constructed.

The disposal procedure for radioisotopes used in the Large Scale Reflood Test Facility is also being proceeded.

12. Activities of the Research Committee on Reactor Physics

T. Hiraoka, K. Tsuchihashi, H. Maekawa and S. Tanaka

During the FY1992, there were held two meetings of the Research Committee on Reactor Physics(RCRP). The first (the 61st meeting) was devoted to review the work relating to the reactor physics on the nuclear ship MUTSU, the Japanese first nuclear ship, and also to the distribution of the information discussed at the first meeting of NEA NSC(Nuclear Science Committee) held at OECD Headquarters, Paris FRANCE, 18-19 Dec 1991. For the former item, the following two topics were presented and discussed. The first was the outline of experimental navigation intended to collect the fundamental data for the MUTSU plant performance on the several navigation conditions, which had been actually performed 4 times (to simulate the real conditions of voyages) through one year period. The second was reactor physics topics on the MUTSU plant about the three dimensional characteristics in the temperature coefficients of moderator, interference effects of control rods and about applicability of the newly developed digital reactivity meter. In this meeting, it was also reminded that RCRP was requested to strengthen the domestic research works on the reactor physics area through the works under the subcommittees of RCRP independent on the restructuring of NEA NSC.

The second one (the 62th meeting) of RCRP was held in November 1992 to review the recent FCA measurements on FBR physics and to report the 2nd and 3rd Meeting of NEA NSC, which was held in Paris on 3-4 June and 3-4 Nov 1992, respectively. For the former, the experimental works on advanced type FBR using metallic fuel were presented. To check data and method, the FCA-XVI-1 and 2 cores were set up and analyzed on the main core parameters crucial to the design. From the study, current data and methods are confirmed except for the Doppler reactivity coefficient. It is concluded that the upper limits of unresolved resonance energy range of JENDL is too low for the accurate prediction of the Doppler effects. As to the NEA NSC, the two benchmark results were presented in detail. They were "3-D LWR Core Transient Benchmark" and "Power Distribution within LWR Assemblies". It was also reported that the outline of the 8th Topical Meeting on Nuclear Code Development held at JAERI Tokai, 11-12 Nov, whose topics were the next generation nuclear reactor design system and advances of the nuclear fuel reprocessing safety analysis codes.

The 35th meeting of the Subcommittee on Reactor System was held in June 1992 to where the multi-band theory and the application to cell calculation was presented. Modification of the core management software at Shikoku Electric Power Co. was also introduced. On the 36th meeting held in November, evolution of three deterministic 3-D transport codes in Japan was reviewed. After the review of design efforts to reduce the positive void coefficient of FBR, importance of power coefficient was emphasized. The 37th meeting was held March 1993 with the topics of NEANSC benchmark on 3-D LWR Core transient, measurement of effective delayed neutron fraction, and software development of α -flow.

The 38th meeting was held on September 8, 1992. There were several meeting reports; (1) on the Japan/US workshop on fusion neutronics experiment and the technical meeting of JAERI/USDOE collaboration on fusion neutronics held at UCLA, (2) on the 10th ANS Topical Meeting on Fusion Technology in Boston, (3) on the IAEA-RCM on Double Differential Cross Section at Chulalongkorn University of Thailand. It was announced that the formal signing of ITER/EDA was made in July, 1992. In the framework of ITER/EDA, various R&D tasks will be conducted for coming 6 years with 300 M\$. A concept for an international collaboration on fusion neutronics under IEA auspice was presented from a JAERI's stand point.

The 39th subcommittee meeting was held in March, 1993. The present status of ITER/EDA was reported. Importance of harmonizing domestic activity was pointed out for realization the ITER building site promotion in Japan. The prospect was given for the IEA international collaboration, signing of an agreement among Japan, US, Canada and EC. A technical talk was presented on the development of vectorized fast Monte Carlo transport calculation code, GMVP and MVP. The excellent capability for calculation with high speed was highlighted. A summary talk on Cold Fusion was given with reviewing international research activities. Emphasizing recent results observed at Osaka University, it was stressed that the correlation between excess heat generation and nuclear reaction products has been clearly established. It was agreed that a working group is to be organized for executing integral test of JENDL-3.2 and JENDL Fusion File.

The activity of the Subcommittee on Shielding has been focused on the issue of high energy accelerator shielding. In the 33rd meeting held in July, high energy neutron cross

sections and typical experiments for accelerator shielding were discussed, and besides a working group started to embody the specialist meeting on shielding aspects of accelerator, targets and irradiation facilities which was a project proposed at the NSC. In the 34th meeting in March 1993, benchmark problems which were prepared and discussed by the working group were presented to evaluate the data and methods for high energy accelerator shielding together with related cross sections, and the radiation safety of the 8 GeV synchrotron radiation facility (Spring-8) was introduced.

Publication List

1. Nuclear Data and Group Constants

- 1) Fukahori T., Chiba S., Takada H., Watanabe Y. and Yamamuro N.: "Benchmark Calculations of Theoretical Calculation Codes for Nuclear Data Evaluation in the Intermediate Energy Region.", Proc. of the 1992 Symposium on Nucl. Data, JAERI-M 93-046 p57 (1993)
- 2) Ishibashi K., Nakamoto T., Matsufuji N., Maehata K., Sakaguchi S., Wakuta Y., Watanabe Y., Takada H., Meigo S., Chiba S., Numajiri M., Yoshimura Y., Matsumoto Y. and Nakamura T.: "Neutron Measurement for (p, xn) Reaction with Protons of GeV Range.", JAERI-M 93-046 p82 (1993)
- 3) Ishibashi K., Higo K., Sakaguchi S., Matsumoto Y., Wakuta Y., Takada H., Nishida T., Nakahara Y. and Kaneko Y.: "Moving Source Model Analysis of Neutron Production Cross Section for Proton Induced Spallation Reactions." Nucl. Sci. Technol., Vol. 26, No. 6, 499 (1992)
- 4) Kosako K., Oyama Y., Maekawa H.: "FSXLIB-J3 MCNP Continuous Cross Section Library Based on JENDL-3", Proc. ANS Topical Mtg. on New Horizons in Radiation Protection and Shielding, April 26 May 1, 1992, Pasco, Washington., pp357-363,(1992)
- 5) Oyama Y., Maekawa H. and Kosako K.: "Measurements and Analysis of Angular Neutron Flux Spectra on Liquid Nitrogen, Liquid Oxygen and Iron Slabs, "Proc. Int'l Conf. Nucl. Data for Sci. and Technol., Jülich, Germany, 13-17 May 1991, pp337-340
- 6) Ikeda Y., Konno C., Mizumoto M., Hasegawa K., Chiba S., Yamanouchi Y. and Sugimoto M.: "Activation Cross Section Measurement at Neutron Energy Range from 9.5 to 13.2 MeV Using $^1\text{H}(^{11}\text{B},n)^{11}\text{C}$ Neutron Source at JAERI," *ibid.*, pp294-296
- 7) Ikeda Y., Kumar A. and Konno C.: "Measurements of Long-Lived Activation Cross Sections by 14MeV Neutrons at FNS," *ibid.*, pp364-366

2. Theoretical Method and Code Development

- 1) Fujimura T. and Tsutsui T.: "Manual for JSSL(JAERI Scientific Subroutine Library), 4th edition", JAERI-M 92-121 (1992) (in Japanese)
- 2) Mori T., Nakagawa M. and Sasaki M.: "Vectorization of Continuous Energy Monte Carlo Method for Neutron Transport Calculation", J. Nucl. Sci. Technol. 29, 4, 325(1992)
- 3) Mori T., Nakagawa M. and Sasaki M.: "Point Detector Estimator for a Vectorized Monte Carlo Code", *ibid*, 29, 12, 1224(1992)
- 4) Nakagawa M., Fujii S., Uno M. and Ogawa H.: "Design Window Search Based on AI Technique", *ibid*, 29, 11, 1116(1992)
- 5) Kugo T.: "Applicability of Avery's Coupled Reactor Theory to Estimate Subcriticality of Test Region in Two Region System", *ibid*, 29, 6, 513(1992)
- 6) Kugo T., Nakagawa M. and Tsuchihashi K.: " Solutions to NEACRP Benchmark Problems on Power Distribution within Assemblies(PDWA) Using SRAC and GMVP", JAERI-M 92-117(1992)(in Japanese)
- 7) Kugo T., Tsuchihashi K., Nakagawa M. and Mori T.: " Intellectual Reactor Design System IRDS", Proc. of the 8th Topical Mtg. on Nuclear Code Development, Nov. 11-12, 1992, Tokai, JAERI-M 93-033, 127(1993)(in Japanese)
- 8) Tsuchihashi K., Nakagawa M., Mori T. and Kugo T.: " Development of Intellectual Reactor Design System IRDS", Proc. Int. Conf. on Design and Safety of Advanced Nuclear Power Plants, Oct. 25-29, 1992, Tokyo, Vol.III, 32.1-1(1992)
- 9) Morimoto Y. and Okumura K.: "Development of a BWR Core Burn-up Calculation Code COREBN-BWR", JAERI-M 92-068(1992)

3. Reactor Physics Experiment and Analysis

- 1) Mukaiyama T. : "Partitioning and Transmutation research and Development Program (OMEGA) in Japan", Proc. Specialists Mtg. on Use of Fast Reactors for Actinide Transmutation (Obninsk, Sept., 1992), IAEA-TECDOC-693, p30(1993)
- 2) Mukaiyama T., Yoshida H. and Ogawa T. : "Minor Actinide Transmutation in

Fission reactors and Fuel Cycle Consideration", *ibid.* p86

- 3) Mukaiyama T., Gunji Y., Ogawa T., Takizuka T. and Yoshida H. : "Minor Actinide Transmutation in Fission Reactors and Fuel Cycle Consideration", Proc. OECD/NEA 2nd Information Exchange Mtg. on Actinide and Fission Products Partitioning and transmutation (ANL Chicago, Nov., 1992)
- 4) Mukaiyama T. : "Transmutation of Long-lived nuclides in Fission Reactors", Report of Mtg. on Separation, Analysis and Nuclear Reaction of Long-lived radioactive Nuclides (Editor, Furuya, H), p81(1993),(in Japanese)
- 5) Mukaiyama T. : "Status of Transmutation Research and Development", Report on Technology of Radioactive Waste Transmutation (Editor, Kato , T), p11(1993) (in Japanese)
- 6) Okajima S., Oigawa H. and Mukaiyama T. : "Measurement of Doppler Effect up to 2000°C at FCA (3) -Development of a Cell Code, PEACO-X, with Ultra-fine Group Structure-", JAERI-M 92-185, (1992) (in Japanese)
- 7) Okajima S., Oigawa H., Mukaiyama T., Hayano M., Kasahara Y. and Kudough F.: "Measurement of Doppler Effect up to 2000°C at FCA", Trans. Am. Nucl. Soc., 66 523-524 (1992)
- 8) Okajima S., Oigawa H. and Mukaiyama T.: "Measurement of Doppler Effect up to 2000°C at FCA ", Proc. of the 1992 Symposium on Nuclear Data, JAERI-M 93-046, 135-141(1993)
- 9) Oigawa H., Okajima S., Mukaiyama T. and Satoh K.: "Experimental Study of ^{238}U Doppler Reactivity Worth in FCA XVI-1 and XVI-2 Cores", JAERI-M 92-113, (1992), (in Japanese)
- 10) Iijima S., Oigawa H., Bando M. and Nakano M. "Benchmark Physics Experiment of Metallic-Fueled LMFBR at FCA - Core Design of FCA Assembly XVI-1 and Criticality -", JAERI-M 92-196, (1992) (in Japanese)

4. Advanced Reactor System Design Studies

- 1) Akie H., Ishiguro Y. and Morimoto Y.: "Water Moderated Th/U Breeder Reactor", Proc. Int. Specialists Mtg. on Potential of Small Nuclear Reactors(SR/TIT), Oct. 23-

- 25, 1991, Tokyo, 197(1992)
- 2) Morimoto Y. and Okumura K.: "Performance Evaluation of a High Conversion Boiling Water Reactor Core with Axially Heterogeneous Core Concept", JAERI-M 92-067(1992)
 - 3) Sako k. et al.: "Passive Safe Reactor SPWR", Proc. Int. Conf. on Design and Safety of Advanced Nuclear Power Plants, Oct. 25-29, 1992, Tokyo(1992)

5. Fusion Neutronics

- 1) Maekawa H., Oyama Y., Tanaka S.: "A Review of Shielding Experiments for Fusion Reactor at FNS/JAERI" *ibid.*, pp611-618 (1992)
- 2) Mori T. and Nakagawa M.: "Benchmark Calculation for Deep Penetration Problem of 14MeV Neutrons in Iron", *J. Nucl. Sci. Technol.*, 29, 11, 1061(1992)
- 3) Maekawa F., Konno C., Kosako K., Oyama Y., Ikeda Y. and Maekawa H.: "Analysis of Bluk Shielding Experiment on Large SS316 Assemblies", 10th ANS Topical Mtg. on Technol. of Fusion Energy, June 7-11, 1992, Boston., *Fusion Technol.* 21[3], pp2107-2111 (1992)
- 4) Konno C., Maekawa F., Ikeda Y., Oyama Y., Kosako K. and Maekawa H.: "Bluk Shielding Experiments on Large SS316 Assemblies", *ibid.*, pp2169-2173 (1992)
- 5) Kumar A., Abdou M.A., Youssef M.Z., Ikeda Y., Konno C. and Oyama Y.: "Measurements of Decay Radioactivity of Long Lived Isotopes", *ibid.*, pp2180-2189 (1992)
- 6) Ikeda Y., Konno C., Kosako K., Oyama Y., Maekawa F., Maekawa H., Kumar A., Youssef M.A. and Abdou A.: "Measurements and Analysis of Nuclear Heating Deposition in Structural Materials Induced by D-T Neutrons", *ibid.*, pp2190-2196 (1992)
- 7) Noda K., Sugimoto M., Kato Y., Matsuo H., Watanabe K., Kikuchi T., Usui H., Oyama Y., Ohno H. and Kondo T.: "Capability of Energy Selective Neutron Irradiation Test Facility (ESNIT) for Fusion Reactor Materials Testing and Status of ESNIT Program", *J. Nucl. Materials*, 191-194 pp1367-1371 (1992)
- 8) Oyama Y., Konno C., Ikeda Y., Yamaguchi S., Tsuda K., Maekawa H., Nakamura T.,

Kosako K., Nakagawa M., Mori T., Kumar A., Youssef M.Z., Abdou M.A., Watanabe Y., Porges K.G., Bennett E.F. and Mattas R.F.: "Phase-II C Experiments of the JAERI/USDOE Collaborative Program on Fusion Blanket Neutronics ü\Experiments and Analysis of the Heterogeneous Fusion Blanketü\ Vol. I : Experimental Results", JAERI-M 92-182; UCLA-FNT-63/UCLA-ENG-93-18 (1992).

- 9) Nakagawa M. et al.: "PhaseIIC Experiments of the USDOE/JAERI Collaborative Program on Fusion Blanket Neutronics -Experiments and Analysis of Heterogeneous Fusion Blankets, Vol.II: Analysis, JAERI-M 92-183(1992)
- 10) Oyama Y., Yamaguchi S., Kosako K. and Maekawa H.: "Calculation of Neutron Field Generated at Thick Li-Target Bombarded with 10-40 MeV Deuterons for Energy Selective Neutron Irradiation Test Facility" JAERI-M 92-191 (1992)
- 11) Maekawa F. and Maekawa H.: "Second International Comparison on Measuring Techniques of Tritium Production Rate for Fusion Neutronics Experiments (ICMT-2)", JAERI-M 93-017;NEACRP-L-340, NEA/NSC/DOC(92)6 (1993)
- 12) Ikeda Y., Kumar A., Konno C., Kosako K., Oyama Y., Nakamura T., Maekawa H., Youssef M.Z. and Abdou M.A.: "Joint Report of JAERI/USDOE Collaborative Program on Fusion Neutronics -Induced Radioactivity Measurements in Fusion Neutron Environment-" JAERI-M 93-018;UCLA-FNT-53/UCLA-ENG-91-32 (1993)

6. Radiation Shielding

- 1) Iwai S., Uehara T., Sato O., Yoshizawa N. and Tanaka S.: "Evaluation of Quality Factors for High Energy Radiations", Genshikaku Kenkyu, Vol.36(6), 145(1992)(in Japanese)
- 2) Tanaka S., Kotegawa H., Suzuki T. and Hasegawa A.: "Shielding Data and Methods for Evaluating 1-cm Depth Dose Equivalent of Photons, β -rays(Electrons) and Neutrons Based on ICRP-26 Recommendation", Proc.of ANS Topical Meeting in Pasco,595(1992)
- 3) Harima Y., Hirayama H., Sugiyama M. and Tanaka S.: "The Behavior of Gamma-Ray Buildup Factors in Stratified Shields", Proc.of ANS Topical Meeting in

Pasco,473(1992)

- 4) Suzuki T., Hasegawa A., Tanaka S. and Nakashima H.: "Development of BERMUDA : A Radiation Transport Code System Part I, Neutron Transport Codes", JAERI 1327(1992)
- 5) Nariyama N., Tanaka S., Namito Y., Yoshizawa M., Hirayama H., Ban S., Nakashima H. and Nakane Y.: "Calculations of Absorbed Dose Distributions in Phantoms Irradiated with Gamma and Low Energy X-rays", Proc. of the Second EGS4 User's Meeting in Japan, KEK-Proc-92-16, 31(1992)
- 6) Hasegawa A.: "Development of a Common Nuclear Group Constants Library System : JSSTD L-295n-104 γ Based on JENDL-3 Nuclear Data Library", Proc. Int. Conf. on Nuclear Data for Science & Technology in Julich, 232(1992)
- 7) Roussin R.W., Hasegawa A., Takano H. and et al.: "International Evaluation Cooperation Subgroup 7 : Multigroup Cross Section Processing", Proc. Int. Conf. on Nuclear Data for Science & Technology in Julich, 860(1992)
- 8) Sato O., Uehara T., Yoshizawa N., Iwai S. and Tanaka S.: "Evaluation of Fluence to Dose Equivalent Conversion Factors for High Energy Radiation (I), Preparation of Code System and Basic Data", JAERI-M 92-126(1992)(in Japanese)
- 9) Harima Y. and Sakamoto Y.: "New Gamma-Ray Attenuation Factors and Buildup Factors", Isotope News 460, 44(1992)(in Japanese)
- 10) Hirayama H., Tanaka S., Nakashima H. and et al.: "Accelerator Shielding Benchmark Problems", KEK Report 92-17(1993)
- 11) Kotegawa H., Nakane Y., Hasegawa A. and Tanaka S.: "Neutron-Photon Multigroup Cross Sections for Neutron Energies up to 400 MeV: HILO-86R -Revisions of HILO86 Libraries-", JAERI-M 93-020(1993)(in Japanese)

7. Reactor and Nuclear Instrumentation

- 1) Yamagishi H., Wakayama N., Itoh H. and Sakasai K. : "Measurement of Dynamic Neutron Flux Change in the AVR by Use of High Temperature In-core Fission Chamber", in Proceedings of the OECD/NEA-IAEA International Symposium on Nuclear Power Plant Instrumentation and Control, Paper #9.3, Tokyo, Japan, 18-22

May,(1992)

- 2) Kakuta T., Iida T., Matsubara T., Sanada K. and Tanaka H. : "Radiation Resistant Optical Fibers and Their Applications in Nuclear Power Plants", in Proceedings of the OECD/NEA-IAEA International Symposium on Nuclear Power Plant Instrumentation and Control, Paper #11.6, Tokyo, Japan, 18-22 May,(1992)
- 3) Kakuta T. : "Fusion Neutron Irradiation Effects in Optical Fibers", in Proceedings of the A US/Japan Workshop on Dynamic Effects of Irradiation in Ceramics, Santa Fe, New Mexico, USA, 11-14 Nov., pp.279-287, (1992)
- 4) Katagiri M., Hatakeyama M., Satoh F., Itoh H. and Wakayama N.: "Telescopic Measuring Method for Specific Activities of Structural Components in a Reactor Pressure Vessel", J. Nucl. Sci. Technol., 29, 735(1992)
- 5) Katagiri M., Itoh H. and Wakayama N.: "Nondestructive and Quantitative Method for Measuring Radioactivity from Crud, Liquids and Gases in a Contaminated Pipe", ibid, 29, 831(1992)
- 6) Katagiri M., Kishimoto M., Itoh H. et al: "Real-time High-sensitivity Fuel Failure Detection for HTGR", ibid, Technol., 29, 957(1992)
- 7) Katagiri M., Itoh H. and Wakayama N.: "Development of Nondestructive Measurement System for Quantifying Radioactivity from Crud, Liquids and Gases in a Contaminated Pipe", JAERI-M 92-184(1992)
- 8) Ara K., Katagiri M., Itoh H. and Sakasai K.: "Ac Magnetization of a $\text{Bi}_2\text{Sr}_2\text{CaCu}_2\text{O}_x$ Disk by a Planar Coil and Magnetic-Flux Penetration", IEEJ, MAG-92-124(1992) (in Japanese)
- 9) Sakasai K., Kishimoto M. and Ara K.: "Experiment for Directional Detection for Magnetic-flux Sources with High Tc Superconductors", IEEJ, MAG-92-125(1992) (in Japanese)
- 10) Sakasai K., Kishimoto M. and Ara K.: "Directional detection of magnetic dipoles by a hybrid system of a perfect diamagnetic device and a magnetic-flux sensor", in Proceedings of the Fourth International ISEM Symposium on Nonlinear Phenomena in Electromagnetic Fields, Nagoya, Japan, 26-29 Jan., pp.85-88, (1992)
- 11) Ara K., Sakasai K. and Kishimoto M.: "Understanding of spatial transfer function between magnetic fields and their sources in connection with forward and inverse

problems", *ibid*, pp.193-196 (1992)

- 12) Sakasai K., Kishimoto M. and Ara K.: "Experiment for Directional Detection of Current Dipoles with a combined system of high Tc superconducting parallel plates and a magnetometer", IEEJ, MAG-92-234(1992) (in Japanese)
- 13) Kishimoto M., Sakasai K. and Ara K.: "The application of genetic algorithm to inverse problems in electro-magnetics", IEEJ, MAG-92-235(1992) (in Japanese)
- 14) Ara K., Katagiri M., Itoh H. and Sakasai K.: "Ac magnetic flux penetration in a sample disk-type sintered $\text{Bi}_2\text{Sr}_2\text{CaCu}_2\text{O}_x$ under low magnetic field applied by a planer coil", J. Appl. Phys., 73(1), 471(1993)
- 15) Sakasai K., Ara K., Itoh H., Kishimoto M., Katagiri M. and Matsumura K.: "Magnetic Characteristics of a Co-Fe-Si-B Amorphous wire at Very Low Temperature and Its Application to a Multivibrator-type Magnetometer", IEEJ, MAG-93-9(1993) (in Japanese)
- 16) Ara K., Sakasai K. and Kishimoto M.: "Measurement of Magnetic Fields from Human Body in Connection with Inverse Problems", IEEJ, MAG-93-91(1993) (in Japanese)

8. Reactor Control, Diagnosis and Robotics

- 1) Inamata S. and Suzuki K.: Study of Concurrent Calculation with a Multitransputer Network, JAERI-M, 92-084 (1992) (in Japanese)
- 2) Suzuki K., Shimazaki J. and Shinohara Y.: Design of H_∞ Optimal Estimator for Time-invariant System, JAERI-M 93-040 (1993) (in Japanese)
- 3) *idem*: Application of H_∞ Optimal Estimator to Reactivity Estimation of Fast Breeder Reactor, JAERI-M 93-062 (1993) (in Japanese)
- 4) Suzudo T.: Reactor Noise Analysis based on Nonlinear Dynamic Theory-Application to Power Oscillation, Nucl. Sci. Eng., 113, 145 (1993)
- 5) Konno H., Hayashi K. and Shinohara Y.: Nonlinear Dynamics of Reactor with Time Delay in Automatic Control System and Temperature Effect, J. Nucl. Sci. Technol., 29, 530 (1992)
- 6) Hayashi K., Shinohara Y. and Konno H.: Identification of Nonlinear Autoregressive Model Based on GMDH and Its Special Analysis, J. SICE, 28, 1216 (1992) (in

Japanese)

- 7) Hayashi K.: Development of Preprocessing System for Non-stationary Reactor Noise Data Recording, J. At. Energy Soc. Japan, 34, 971 (1992) (in Japanese)
- 8) idem: Study on Statistical Analysis of Nonlinear and Nonstationary Reactor Noise, JAERI-M 93-041 (1993) (in Japanese)
- 9) Ishikawa N., Fujii Y. and Shinohara Y.: Basic Experiment on Preprocessing of Ultrasonic Signal by Inverse Filtering Technique, JAERI-M, 92-171 (1992) (in Japanese)

9. Heat Transfer and Fluid Flow Dynamics

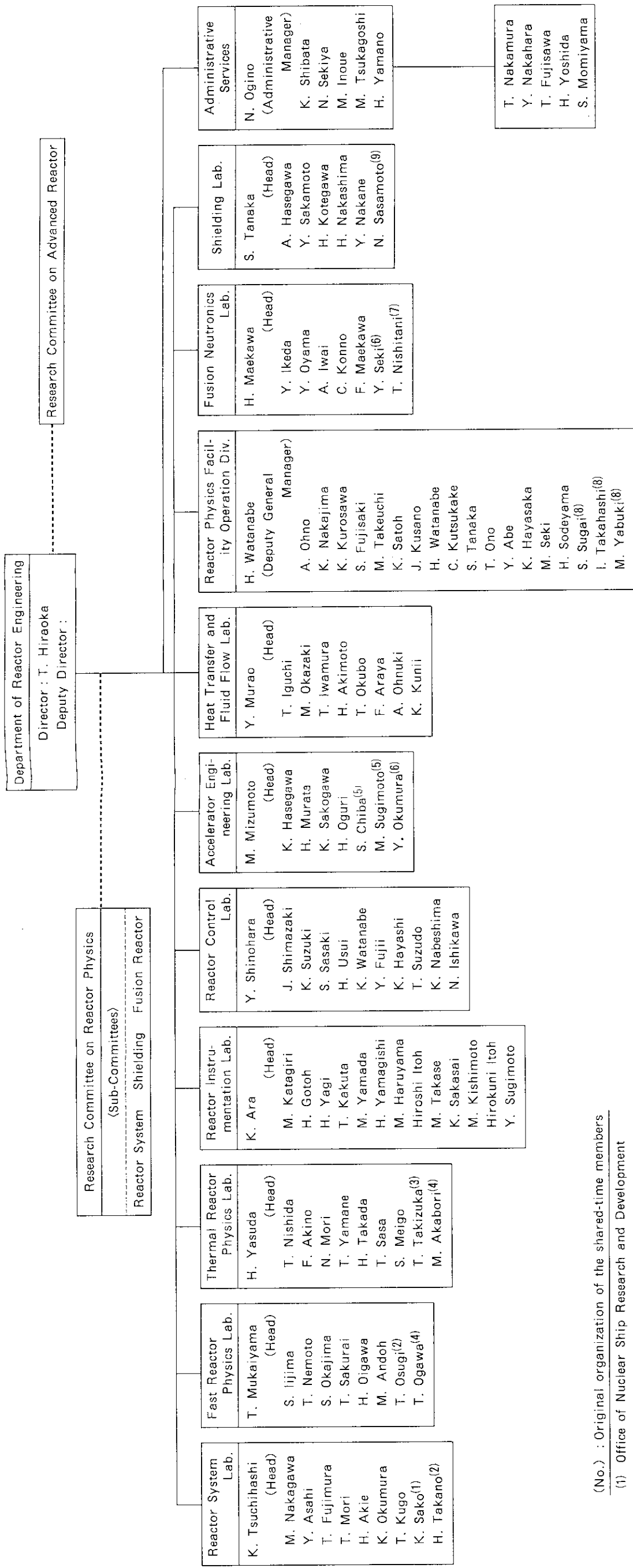
- 1) Araya F., Iwamura T., Okubo T., Akimoto H. and Murao Y. : "Feasibility Study of Double-Flat-Core Type HCPWR for Reactivity Initiated Accidents", J. At. Energy Soc. Japan, Vol.34, No.8 (1992) (in Japanese)
- 2) Araya F., Hirano M., Yoshida K., Matsumoto K., Yokobayashi M. and Kohsaka A., : "Development of Method to Determine Instability Threshold with RETRAN code", ibid., Vol.34, No.9 (1992) (in Japanese)
- 3) Ohnuki A.: "Study of Two-Phase Flow under Low Velocity in PWR-LOCA", JAERI-M 92-150 (1992)
- 4) Akimoto H., Ohnuki A. and Murao Y.: "Implementation of JAERI's Reflood Model into TRAC-PF1/MOD1 Code", JAERI-M 93-027 (1993)
- 5) Akimoto H., Ohnuki A., Abe Y. and Murao Y.: "Assessment of TRAC-PF1/MOD1 code for Large Break LOCA in PWR", JAERI-M 93-028 (1993)
- 6) Akimoto H., Ohnuki A., Kikuta M. and Murao Y.: "Assessment of TRAC-PF1/MOD1 Code for Core Thermal Hydraulic Behavior during Reflood with CCTF and SCTF data", JAERI-M 93-032 (1993)
- 7) Akimoto H., Ohnuki A., Abe Y. and Murao Y.: "Assessment of TRAC-BF1 1D Reflood Model with CCTF and SCTF Data", JAERI-M 93-045 (1993)
- 8) Okubo T., Ezzidi A. and Murao Y.: "Assessment of Models in COBRA-TF Code for Liquid Entrainments in Film-Mist Flow", JAERI-M 93-069 (1993)

10. Development of Proton Linear Accelerator and Transmutation System

- 1) Mizumoto M., Hasegawa K., Yokobori H., Mino H., Murata H., Sakogawa K., Oguri H., Okumura Y., Takada H., Nishida T. and Takizuka T.: "High Intensity Proton Accelerator for Nuclear Waste Transmutation", Proc. of 1992 Linear Accelerator Conference, Ottawa, AECL-10728, 749 (1992)
- 2) Okumura Y., Inoue T., Oguri H. and Tanaka H.: "Development of a High Brightness Ion Source for the Proton Linear Accelerator (BTA) at JAERI", *ibid*, 645 (1992)
- 3) Hasegawa K., Mizumoto M., Murata H., Sakogawa K. and Yokobori H.: "Design Study on an RFQ for the Basic Technology Accelerator in JAERI", *ibid.*, 314 (1992)
- 4) Mizumoto M., Hasegawa K., Yokobori H., Oguri H., Murata H., Sakogawa K., Kawai M., Kusano J. and Okumura Y.: "Development of the JAERI Basic Technology Accelerator (BTA)", Proc. of the 17th Linear Accelerator Meeting in Japan, 121 (1992) (in Japanese)
- 5) Okumura Y., Inoue T. and Oguri H.: "Development of a High Brightness Ion Source for the Proton Linear Accelerator (BTA)", *ibid*, 94 (1992)
- 6) Oguri H., Okumura Y., Inoue T. and Tanaka H.: "Development of a High Brightness Hydrogen Ion Source for the Basic Technology Accelerator (BTA)", JAERI-M 92-200 (1992) (in Japanese)
- 7) Takada H., Hasegawa K., Sasa T., Meigo S. and Kanno I.: "Integral Spallation Experiment with a Lead Assembly Irradiated with 500 MeV Protons.", JAERI-M 93-046 p72 (1993)
- 8) Nishida T., Takada H., Nakahara Y., Yoshizawa N. and Iwai S.: "Benchmark Study on the Computational Model in the Accelerator Based Transmutation Simulation Code." PSI-Proc. 92-02, p535, ISSN 1019-6447 (1992)
- 9) Nishida T.: "Development of Accelerator Based Transmutation Research at JAERI." Nuclear Data News, No.44, p49, ISSN 0385-4876, (1993) (in Japanese)

Appendix I Department of Reactor Engineering Organization Chart

March 1993



(No.) : Original organization of the shared-time members

- (1) Office of Nuclear Ship Research and Development
- (2) Advanced LWR Technology Development Program Team
- (3) OMEGA Program Team
- (4) Department of Fuels and Materials Research
- (5) Department of Physics
- (6) Department of Fusion Engineering Research
- (7) Department of Fusion Plasma Research
- (8) Department of Engineering Services
- (9) Office of Synchrotron Radiation Facility Project

Appendix II Abbreviations

CCTF : Cylindrical Core Test Facility

The CCTF is an experimental facility to study overall primary system response as well as the in-core behavior during the refill and reflood phase of a large cold leg break LOCA.

ECCS : Emergency Core Cooling System

FCA : Fast Critical Assembly

The FCA is a split-table type facility of horizontal matrix structure designed for studying nuclear characteristics of fast reactor. The construction of the FCA was started in 1965 and the first core went critical on 29th April, 1967.

The main features of the facility are summarized as follows:

Type : Split-table type of horizontal matrix structure

Size : 2.8 m × 2.8 m × 1.3 m (each half assembly)

Fuel : Enriched uranium and plutonium

(Plate type)

Other material : Sodium, stainless steel, aluminum
oxide (Al_2O_3), polystyrene etc.

(Plate type)

Maximum power : 2 kW

Assembly name constructed : FCA-I ~ FCA-XVII

Critical experiments using enriched uranium cores were made in 1960s for investigating basic characteristics of fast reactor cores. Mock-up experiments were extensively made in 1970s for the Fast Experimental Reactor JOYO and the Prototype Fast Breeder Reactor MONJU. In 1980s, the main subjects of experiments were the investigation of the core characteristics of an axially heterogeneous large fast breeder reactor and the core physics study on a high conversion light water reactor. From 1989, the reactor physics experiments of metallic-fueled LMFBR have been carried out

using the FCA-XVI and XVII cores.

FER : Fusion Experimental Reactor

A next fusion device designed and planned at JAERI.

FNS : Fusion Neutronics Source

The FNS is an accelerator based D-T neutron source installed for the purpose of investigating the neutronics on the D-T fusion reactor blanket and shielding. It provides following three functions to meet experimental requirements:

- 1) High intensity DC point source
- 2) DC point source with wide variation of neutron yield rate
- 3) Pulsed neutron source

The D-T neutrons are generated via ${}^3\text{T}(\text{d},\text{n}){}^4\text{He}$ reaction. There are two beam lines; one is so called 0° line for high current operation, and the other is so called 80° line for rather low current operation. The major specifications of the FNS accelerator are shown in the following Table.

<<Table>>

Items	0°	80°
●Beamcurrent	>20 mA	3 mA
●Beamsize	<15 mm ϕ	<15 mm ϕ
●Pulsewidth	--	< 2 ns
●Frequency	--	2 MHz
●Peakcurrent	--	40 mA
●Targetassembly	Rotating (Water cooled)	Stationary (Water cooled, Air cooled)
●Amountof ${}^3\text{T}$	<37T Bq	370G Bq
●Neutronyield	$4 \times 10^{12}/\text{s}$	$5 \times 10^{11}/\text{s}$

The major experimental subjects are as follows:

- 1) Tritium production rate in the various blanket configurations
- 2) Nuclear heating rate in the structural materials
- 3) Shielding performance for D-T neutrons in the various structure configurations
- 4) Induced effects on the structural materials by D-T neutrons

HCLWR : High Conversion Light Water Reactor

HTTR : High Temperature engineering Test Reactor

JAERI is constructing the HTTR to carry out the necessary R&D for establishing and upgrading the HTGR (High Temperature Gas-cooled Reactor) technology basis, and to conduct various innovative basic researches on high-temperature technologies such as ceramics and fusion reactor materials. The HTTR consists of a core of 30 MWt, a main cooling circuit, an auxiliary cooling circuit and related components. The reactor pressure vessel is 13.2 m high and 5.5 m in diameter and contains the core graphite reflectors, metallic core support structure and radial restraining devices.

<<Table>> Specification of HTTR

Thermal power	30 MW
Outlet coolant temperature	850°C/950°C
Inlet coolant temperature	395°C
Fuel	Low enriched UO ₂
Fuel element type	Prismatic block
Direction of coolant flow	Downward-flow in core
Pressure vessel	Steel
Number of main cooling loop	1
Heat removal	IHX and PWC (parallel loaded)
Primary coolant pressure	4 MPa
Containment type	Steel containment
Plant lifetime	20 years

- ITER : International Thermonuclear Experimental Reactor
A next fusion device. The ITER Project is conducted by four parties, i.e., Japan, USA, Russia and EC under the framework of IAEA.
- JENDLE-3 : The Japanese Evaluated Nuclear Data Library, version 3, released in 1989.
- JMTR : Japan Materials Testing Reactor
- LOCA : Loss of Coolant Accident
- NSRR : Nuclear Safety Research Reactor
- SCTF : Slab Core Test Facility
The SCTF is an experimental Facility to study two-dimensional effect on thermal hydraulics in the core of full radius during reflood phase of LOCA.
- TRU : Trans-Uranium element (Transuranic nuclide)
- VHTRC : Very High Temperature Reactor Critical assembly
1. Purpose
Neutronics design verification of Very High Temperature Reactor
 2. Main features of VHTRC
 - Type : Split table type of hexagonal graphite block structure
 - Size : Height; 2.4 m
Length; 2.4 m
 - Fuel : Coated particle fuel compact (pin in block)
 - Size; 36, 18 mm outer, inner diameters, 36 mm height
 - Coated particle; 920 μm overall diameter
 - (600 μm UO_2 kernel coated with pyrolytic carbon and SiC)
 - Enrichment; 2, 4 and 6 wt%
 - Moderator and reflector : Graphite

Core temperature : Room temperature to 210°C by electric heaters

Maximum power : 10 W

Auxiliary equipments :

(1) Sample heating device (Up to 800°C)

(2) Pulsed neutron source